Ceria-Based Engine Exhaust Catalysts

Rood, Shawn

Award date:
2019

Awarding institution:
University of Bath

Ceria-Based Engine Exhaust Catalysts

submitted by

Shawn Chung Ming Rood

For the degree of Doctor of Philosophy

University of Bath

Centre for Sustainable Chemical Technologies

Department of Chemical Engineering

August 2019

Signed on behalf of the Doctoral College ……..……..

Abstract

Ceria and ceria-based materials are a significant component of automotive three-way catalyst washcoats. Fossil fuel-powered vehicles emit pollutants such as carbon monoxide, nitrogen oxides, and unburnt hydrocarbons from fuel, and three-way catalysts are a critical technology in reducing emissions of these pollutants. Air quality issues around the world, particularly in urban areas with high vehicle density, are a major public health concern, and improving three-way catalyst performance is a significant component in addressing this concern. This thesis addresses two potential routes for improving the performance of ceria-based catalysts – doped ceria for improved low-temperature performance and graphene oxide-templated ceria to improve catalyst stability at high temperatures.

The effect of doped transition metals on ceria nanorod catalysts has been examined and tested in CO oxidation and NO reduction reactions, both relevant to three-way catalysis. In particular, the use of copper and chromium as co-dopants is shown to have a synergistic effect, with significant improvement in reducibility and oxygen storage capacity compared with single-dopant and undoped ceria nanorod catalysts. Due to this, enhanced low-temperature activity for both CO oxidation and NO reduction is seen, beyond that of typical three-way catalyst designs which rely on platinum group metal catalysts.

Graphene oxide has been utilised as a sacrificial template to synthesise two-dimensional ceria nanoflakes. Due to this morphology, ceria nanoflakes demonstrate improved resistance to sintering at high temperatures compared to untemplated ceria particles and retain higher levels of reducibility and oxygen storage capacity. This correlates with a higher catalytic performance for CO oxidation. Additionally, using ceria nanoflakes as a catalyst support for metal particles results in a more stable catalyst than using untemplated ceria. This is demonstrated for copper/ceria catalysts with CO oxidation and nickel/ceria catalysts for dry reforming of methane.

Acknowledgements

I would like to express my sincere gratitude to my supervisor Salvador Eslava for his guidance and support throughout my PhD. A further thank you goes to everyone in the Eslava group – for your support over the past few years and for being a great group of people to work with. I would also like to thank Laura Torrente-Murciano, for supervision during my master's degree and continued support during my PhD.

Thank you to everyone else who has helped me during my time at Bath – this includes but is not limited to Ursula Potter, John Mitchels, Philip Fletcher, Gabriele Kociok-Köhn, Rémi Castaing, and Sheila Apps. And the chemical engineering technical team deserve acknowledgement for all they do to keep the department running – we wouldn't be able to do our research without you! In particular, I would like to acknowledge Fernando Acosta for his assistance in a wide variety of laboratory matters.

To the CSCT 2014 cohort, thank you for a fantastic first year at Bath and in the UK.

And finally, a very big thank you to the Illuminati HQ office – Sonia, David, and Olivia – for the board game nights, political discussions, and friendship.

Declaration of Authorship

I am the author of this thesis, and the work described therein was carried out by myself personally, except where explicit reference is made regarding the input of others.

Chapter 5

Some of the synthesis and catalyst testing of the Mn-doped and Cu-doped ceria nanorods was conducted by Man Cheng, Oriol Pastor Algaba, or Albert Tosca Princep under my guidance. TPR experiments were performed by Laura Torrente-Murciano and Bruce Pinho at the University of Cambridge. XPS measurements were performed by Mark Isaacs at the EPSRC National Facility for XPS at Harwell.

Chapter 6

Graphene oxide was synthesised by Salvador Eslava. Some of the ceria nanoflakes synthesis was conducted by Anais Gomez-Ramon. Synthesis of ceria-zirconia nanoflakes was conducted by Lloyd Couzens-Sharpe under my guidance. The majority of TPR experiments were performed and analysed by Laura Torrente-Murciano at the University of Cambridge.

Chapter 7

Nickel loading of the ceria nanoflakes and untemplated ceria particles, DRM testing, XRD, and TGA of Ni-ceria catalysts was performed by Huseyin B. Ahmet and Tomas Reina at the University of Surrey.

Table of Contents

Dissemination of Thesis

- S.C. Rood, H.B. Ahmet, A. Gomez-Ramon, L. Torrente-Murciano, T.R. Reina, S. Eslava, *Enhanced ceria nanoflakes using graphene oxide as a sacrificial template for CO oxidation and dry reforming of methane*, Applied Catalysis B: Environmental. 242 (2019) 358–368. doi:10.1016/j.apcatb.2018.10.011.
- S. Rood, S. Eslava, A. Manigrasso, C. Bannister, *Recent advances in gasoline three-way catalyst formulation: A review,* Proceedings of the Institution of Mechanical Engineers, Part D: Journal of Automobile Engineering. (2019) doi:10.1177/0954407019859822.
- *Co-doping ceria nanorods with Cu and Cr: synergy for CO oxidation and NO reduction* (submitted to Applied Catalysis B: Environmental)

- S.C. Rood, A. Gomez-Ramon, L. Torrente-Murciano, T.R. Reina, S. Eslava. *Improved ceria catalysts via doping and graphene oxide templating strategies*.
  Oral presentation presented at: The 8th Tokyo Conference on Advanced Catalytic Science and Technology (TOCAT8); 2018 Aug 5-10; Tokyo, Japan.
- S.C. Rood, H. Ahmet, A. Gomez-Ramon, L. Torrente-Murciano, T.R. Reina, S. Eslava. *Enhanced ceria nanoflake catalysts using graphene oxide as a sacrificial template*. Poster presented at: CSCT Summer Showcase; 2018 Jun 25-26; Bath, UK.
- S.C. Rood, S. Eslava, L. Torrente-Murciano. *PGM-free automotive catalysts for CO oxidation*. Poster presented at: CSCT Summer Showcase; 2017 Jul 10-11; Bath, UK.
- S.C. Rood, S. Eslava, L. Torrente-Murciano. *PGM-free automotive catalysts for CO oxidation*. Poster presented at: UK Catalysis Conference; 2017 Jan 4-6; Loughborough, UK.
- S.C. Rood, S. Eslava, L. Torrente-Murciano. *Ceria-based engine exhaust catalysts*. Poster presented at: CSCT Summer Showcase; 2016 Jul 11-12; Bath UK.
- S.C. Rood, S. Eslava, L. Torrente-Murciano. *Ceria-based engine exhaust catalysts*.
  Poster presented at: Winter Process Conference; 2015 Dec 14-16; Bath, UK.

Thesis Structure

Chapter 1

This chapter provides an overview of three-way catalysis and the importance of catalytic converters for maintaining air quality standards, the shortcomings of present-day three-way catalyst designs, and the importance ceria plays as a component in catalyst formulations. The influence of oxygen vacancies, and how nanomorphology and doping can affect oxygen vacancy concentration, is also reviewed. The mechanism of three-way catalysis, particularly the Mars-van Krevelen mechanism, is reviewed. Finally, the performance of various doped ceria catalysts for CO oxidation, NO reduction, and hydrocarbon oxidation is assessed and compared.

Chapter 2

The article in Chapter 2 was written to review recent advances in three-way catalyst washcoat formulations. The effect of different ratios of ceria, zirconia, and alumina on three-way catalyst performance, as well as that of rare earth and alkaline metal promoters, is considered. The use of zeolites as a cold trap for pollutants at ambient temperatures is also reviewed. Platinum, palladium, and rhodium loading levels and ratios are examined, and the design of more efficient monoliths is also briefly considered. The data collected in this literature review was used to design a research project with an automotive OEM, with the goal of identifying better low-temperature catalyst formulations.

Chapter 3

The research objectives of this thesis are outlined in this chapter.

Chapter 4

This chapter provides the materials and methods used in this thesis. Synthetic techniques and characterisation methods are outlined, and the background theory behind each characterisation technique is briefly reviewed.

Chapter 5

In this chapter, the experimental results of doping ceria nanorods with transition metals (Mn, Cu, or Cr) are examined. These doped ceria catalysts demonstrate enhanced low-temperature activity for CO oxidation and NO reduction. The synergistic effect of co-doping ceria with two dopants simultaneously is also studied. These materials are fully characterised (TEM, XRD, Raman, XPS, H_2-TPR, N_2 adsorption) to relate their physical and chemical properties to their performance as catalysts.

Chapter 6

The use of graphene oxide as a sacrificial template for the synthesis of ceria nanoflakes is reported in this chapter. Compared to unstructured ceria particles, these nanoflakes are shown to demonstrate an improved resistance to sintering and retention of reducibility after exposure to high temperature calcination. Due to this, they show improved catalytic activity for CO oxidation and NO reduction. Ceria-zirconia mixed oxide nanoflakes are also synthesised to investigate if further improvements in thermal stability are possible, and copper-loaded ceria nanoflakes are tested as catalysts as well.

Chapter 7

In this chapter, nickel-loaded ceria nanoflakes are used as catalyst for the dry reforming of methane. The catalysts are characterised both pre- and post-reaction to examine changes between the fresh and spent catalyst materials and to identify the source of catalyst deactivation during long-term stability tests. It is shown that ceria nanoflakes inhibit sintering of the loaded nickel particles compared with nickel loaded onto untemplated ceria.

Chapter 1

Introduction

Outdoor air pollution is a major public health concern, particularly in urban areas. In the United Kingdom, 23,500 – 40,000 early deaths per year are attributed to exposure to outdoor air pollution, and exposure to airborne pollutants is estimated to reduce UK life expectancy by six months. The cost to UK health services, businesses, and society at large is estimated to be over £20 billion per year. [1,2] Worldwide, over 3.5 million deaths per year are attributed to outdoor air pollution, a figure which is increasing. Exposure to air pollution leads to increased risk of a range of health issues, including stroke, heart disease, lung cancer, and respiratory diseases such as asthma. [3]

Vehicle emissions account for approximately 50% of the health impact of air pollution in OECD countries, making this the single largest negative influence on air quality. [3] Vehicle exhaust contains a range of pollutants detrimental to human health – these include carbon monoxide, which is poisonous, and unburnt hydrocarbons from fuel and nitrogen oxides, which react with sunlight to form photochemical smog. Uncontrolled, these pollutants are typically be emitted at levels up to 90 g CO/mile, 15 g HC/mile, and 6 g NO_x/mile from a typical passenger vehicle. Particulate matter emissions from diesel vehicles is also a concern. [4]

Today, vehicle emissions are controlled with a catalytic converter, located downstream of the engine. Modern petrol vehicle catalytic converters are also known as three-way catalysts (TWCs). A TWC simultaneously oxidises carbon monoxide and hydrocarbons to carbon dioxide and water, and reduces nitrogen oxides to nitrogen gas (Equations 1-3).

$$2CO + O_2 \rightarrow 2CO_2 \quad (1)$$

$$C_xH_{2x+2} + (1.5x+0.5)O_2 \rightarrow xCO_2 + (x+1)H_2O \quad (2)$$

$$2NO_x \rightarrow xO_2 + N_2 \quad (3)$$

However, even with modern control measures in place, 56% of major cities in high-income nations do not meet World Health Organization air quality guidelines. This rises to 98% of cities in low- and middle-income nations. [5] Clearly, current catalytic converter designs are not sufficient.

Modern three-way catalysts consist of a metal foil substrate or extruded cordierite monolith, which supports a washcoat of alumina and ceria-based oxygen storage material, and the active metal nanoparticle catalyst. The oxygen storage component of the three-way catalyst consists of a ceria-based mixed oxide. Ceria helps stabilise the alumina at high temperatures, stabilises platinum group metal (PGM) nanoparticle dispersion, and, most importantly, provides oxygen storage capacity – storing and releasing oxygen under 'rich' and 'lean' exhaust conditions. This material is usually a mixed oxide; generally ceria-zirconia and other promoters such as yttrium or lanthanum. [6–8]

The alumina component has several roles – it binds the catalyst layer to the substrate, absorbs poisons such as sulphur dioxide, and helps the catalyst maintain surface area when exposed to high temperatures. Platinum group metal nanoparticles are dispersed on top of the washcoat, and act as the active catalyst. Generally, Pt/Rh or Pd/Rh formulations are used. [6] A typical vehicle incorporates approximately 2.5-5 g of PGM content. [7,9] However, reliance on PGMs for three-way catalysis has led to a number of performance, economic, and sustainability-related drawbacks that must be overcome to improve TWC design.

Performance-wise, TWCs suffer at both very low and very high temperatures. From a cold engine start, petrol vehicle exhaust is approximately 250-300°C when it reaches the catalytic converter. However, TWCs do not become active until they reach 300°C. Because of this, there is a period of approximately two minutes when an engine is first started in which the catalytic converter is not active. [7] Higher emissions during this 'cold start' account for between 10-30% of total automotive emissions, and this figure may rise to 50% in dense urban areas, where shorter trips are the norm. [10]

At very high temperatures, the metal nanoparticle catalysts sinter and agglomerate over time – this leads to loss of surface area and activity. [8,11] Catalytic converters are routinely exposed to exhaust temperatures of up to 850°C, and temperatures can rise to over 1000°C. [7,8,12] Furthermore, over the lifetime of a catalytic converter, metal leaches out of the system and is lost to the environment. Because of this, modern catalytic converters become less effective over the lifetime of a vehicle. Loss of metals over time is also a potential health concern – the health risks of long-term exposure to environmental PGM particulate matter in urban areas are not well-understood. [13]

The sustainability and economic issues with TWC designs are mainly due to the relative scarcity of PGMs worldwide. Annual platinum demand has risen every year since 1980, mainly driven by catalytic converter production – 40% of platinum production and 76% of palladium production is dedicated to automotive catalysts. [14,15] The rising number of vehicles operated worldwide and increasingly restrictive emissions legislation mean that this trend is likely to continue. Because catalytic converters are such a large percentage of a relatively small PGM market, they are highly exposed to what are often highly volatile prices – for example, ruthenium spiking in price from $1000/ounce to $12000/ounce. Furthermore, given that PGMs are several thousand times more expensive than common metals, there is a clear economic incentive to reduce dependence on PGMs. [16] By some estimates, there are about five decades of remaining reserves, but this assumes that there will be no increased demand from other growing industries (which include wind turbines, fuel cells, and electronics). [9,17]

Therefore, new catalytic converter designs need to meet three requirements: increased low-temperature performance, higher resistance to sintering and loss of activity at very high temperatures, and reduced dependence on platinum group metals. Achieving this has the potential to significantly improve outdoor air pollution and save thousands of lives annually in the UK and millions worldwide.

1.1 Overview of ceria

Using ceria as a direct catalyst in the relevant TWC reactions – carbon monoxide oxidation, hydrocarbon oxidation, and nitrogen oxide reduction, has been examined in the literature, but pure ceria alone is not active enough at low temperatures to match the performance of PGM catalysts. Formulating ceria to act as the catalyst would allow for the removal of PGMs from catalytic converter designs. However, this will require a very good understanding of ceria's physical and chemical properties.

Ceria (CeO_2) is a rare earth oxide with a fluorite cubic crystal structure (Figure 1). It consists of a face-centred cubic unit cell of Ce^{4+} cations with eight O^{2-} anions in the interstitial sites. [18]

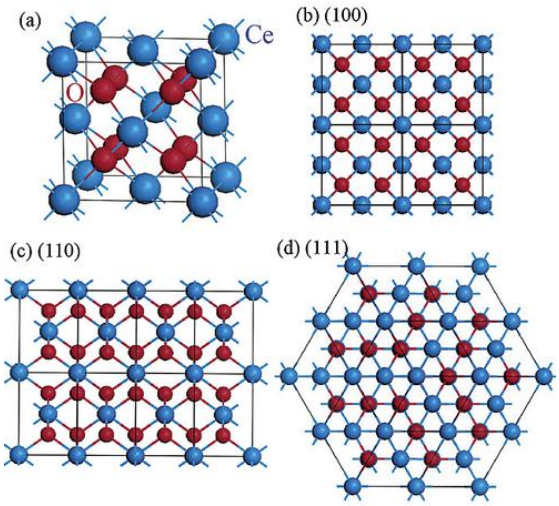

Figure 1. (a) Ceria unit cell, where blue circles are cerium atoms and red circles are oxygen atoms. (b)-(d) (100), (110), and (111) crystal planes of ceria, respectively. Reprinted with permission from Ref. [19]. Copyright 2003 American Chemical Society.

Ceria is well-known for its ability to easily undergo repeatable reduction-oxidation cycles. Ceria can be reduced by the removal of an oxygen atom from the lattice structure, creating an oxygen vacancy which is accompanied by two Ce^{3+} cations. [20] This may be written in Kröger-Vink notation, as shown in Equation 4:

$$O_o + 2Ce_{Ce} \rightarrow 0.5O_{2(g)} + V_{o^{\cdot\cdot}} + 2Ce'_{Ce} \qquad (4)$$

Where O_o is an oxygen atom in the crystal lattice, Ce_{Ce} is Ce^{4+} in the lattice, $V_{o}^{\cdot\cdot}$ is an oxygen vacancy in the lattice, and Ce'_{Ce} is the reduced Ce^{3+} ion. Depending on the environmental conditions, ceria can rapidly undergo reduction-oxidation cycles in which oxygen vacancies are formed and healed, providing an oxygen storage capacity. [18,21] Depending on the partial pressure of oxygen, the lattice structure of pure ceria can accommodate a reduction of CeO_{2-x} with x up to a value of 0.25. [20] In a three-way catalyst, this means ceria can provide oxygen for carbon monoxide and hydrocarbon oxidation and take up oxygen from nitrogen oxide reduction (Figure 2).

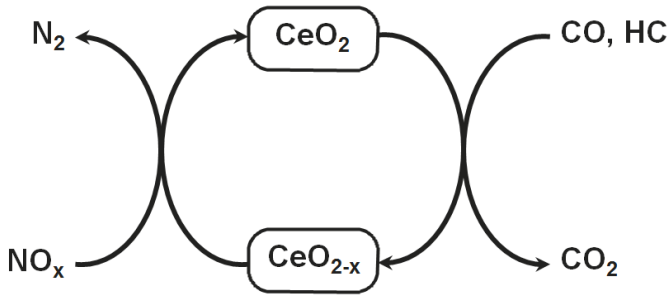

Figure 2. Ceria's reduction-oxidation cycle within a three-way catalyst.

Ceria's unique redox capabilities and high oxygen storage content are the key to its role in a wide variety of applications. In addition to automotive catalysts, these include solid oxide fuel cells, oxygen sensors, glass polishing, and various biomedical applications. [22–26] Other catalytic applications which rely on ceria's redox properties such as methane reforming, photocatalytic generation of hydrogen via water splitting, and photodegradation of pollutants in wastewater have been reported as well. [27–30]

1.2 Synthesis of ceria

Numerous synthetic methods for the production of ceria have been reported in the literature. Different synthesis procedures may be employed for better control of the final nanostructure, selective exposure of different crystal faces, ease of doping, or more 'green' methods which use less harsh solvents and lower synthesis temperatures. [31,32] Methods can be divided into various approaches: oriented growth of nanoparticles

directed by crystallographic structure, oriented nanoparticle growth directed by capping agents, particle growth dictated by a template, and other methods. [33] Some of the more common synthesis methods reported in literature are briefly outlined below.

1.2.1 Precipitation and co-precipitation synthesis

Precipitation and co-precipitation syntheses are amongst the simplest methods for the production of nanoscale ceria. Typically, a base is used to precipitate a cerium salt (often cerium nitrate), followed by heat treatment. [34] Reaction parameters such as the choice of base, precipitation time, reaction temperature, and aging temperature can be manipulated to adjust the morphology of the final product. [31] While this method is widely used in industry, the obtained ceria nanoparticles are often non-uniform in size and easily aggregate upon heat treatment. [33] Co-precipitation syntheses may be used for the production of mixed oxides, such as ceria-zirconia. Precipitation may be combined with other synthetic methods, such as hydrothermal synthesis. [35]

1.2.2 Hydrothermal and solvothermal synthesis

Hydrothermal and solvothermal methods for the production of ceria and ceria-based materials allows for a simple, one-pot batch synthesis procedure of template-free nanostructured ceria. Torrente-Murciano *et al* and Mai *et al* report similar shape-selective hydrothermal methods, in which variations in the base concentration and reaction temperature result in the production of ceria nanopolyhedra, nanorods, or nanocubes (Figure 3). While the nanopolyhedra mainly exposed (111) facets, the nanorods selectively exposed ceria's (110) and (100) facets, and nanocubes (100) facets. [36,37] Other morphologies reported in the literature include hollow nanospheres and "flower-like" particles. [38,39] The reaction may be further controlled by varying or changing the reaction medium, which can affect crystal growth and improve dispersion to avoid particle agglomeration. [40] Hammond *et al* report a solvothermal synthesis using the deep eutectic solvent reline to control the morphology and porosity of ceria

nanowires. [41] While morphological control is generally improved compared with precipitation techniques, size distribution is usually poor.

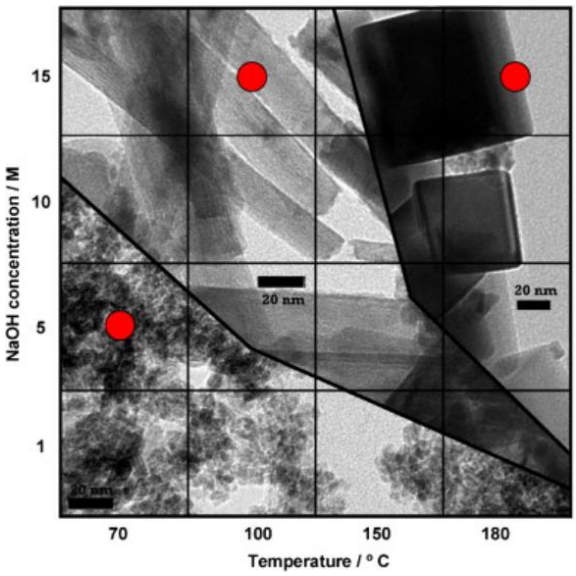

Figure 3. TEM images of hydrothermally synthesised ceria nanoparticles, nanorods, and nanocubes. Reprinted from Ref. [37] with permission from Elsevier.

1.2.3 Sol-gel synthesis

In sol-gel synthetic methods, a starting material is converted into a colloidal solution, the 'sol', which further forms into a gel. The gel is then dried and heat applied to form the final metal oxide product. [42] Similarly to hydrothermal methods, good shape selectivity can also be achieved with sol-gel. Yu *et al* report a procedure for the selective production of ceria nanospheres, nanowires, or 'tadpole-shaped' nanowires, while Laberty-Robert *et al* report the production of porous nanoarchitectures. [43,44]

1.2.4 Template synthesis

A wide variety of ceria morphologies may be achieved using templating agents. Templates such as carbon spheres (Figure 4) or nanotubes, polystyrene spheres, and silica, amongst others, have been used to produce ceria with varying morphology. [33,45] Some of the more novel templates used to synthesise ceria are natural polymers or biologically derived structures such as DNA, chitosan, or tobacco leaves. [46–48] 'Soft' template

methods employing surfactants such as CTAB or PVP may also be used to promote the formation of ceria rod, sphere, flower, cube, and plate morphologies. [33] While templated synthesis methods offer good control of morphology, the addition of a template removal step in the synthesis may result in a more complicated procedure than other methods.

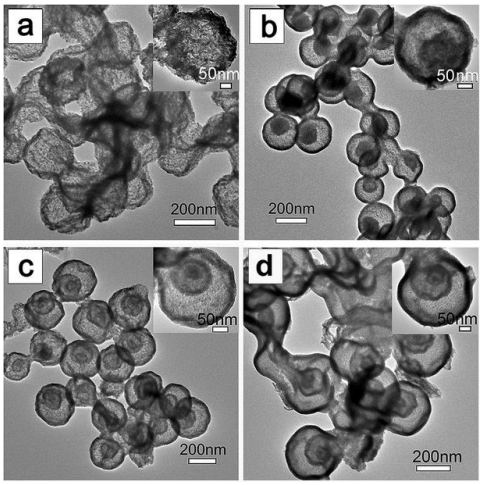

Figure 4. Hollow ceria nanospheres synthesised with a carbonaceous sphere template. Republished with permission of the Royal Society of Chemistry from Ref. [49]; permission conveyed through Copyright Clearance Center, Inc.

1.2.5 Combustion synthesis

In combustion synthesis, also known as self-propagating high-temperature synthesis, heat is applied to precursor materials to trigger a self-propagating exothermic reaction, leading to the formation of the final product. [50] While this may be done with solid state precursors, this method does not easily allow for the controlled production of nanoparticles. [51] Therefore, solution combustion synthesis has been developed and reported for the production of nanoscale ceria. [52,53] While these methods are quite simple in comparison to others such as template or hydrothermal synthesis, control of final morphology is much more limited.

1.3 Oxygen vacancies and oxygen storage capacity

The creation and healing of oxygen vacancies within ceria is directly related to its oxygen storage capacity. This plays a key role in its potential as both a catalyst and catalyst support. Ceria oxygen vacancies can form in both the bulk crystal structure and at the surface. The formation and healing of these vacancies is affected by a range of variables, including the presence of other elements within the crystal structure and which crystal planes are exposed at the surface. [18,54,55] Much of the literature regarding oxygen vacancies in ceria focuses on improving its reducibility – while the rate of ceria oxidation (healing of vacancies) proceeds very quickly, ceria reduction (creating vacancies) in pure ceria does not. [12]

While there is some variation in the literature regarding the calculation of the energy of oxygen vacancy formation, there is general consensus about the mechanism – in which the removal of an oxygen atom from the lattice structure results in the closest two Ce ions reducing from a 4+ to 3+ oxidation state. [56,57]

1.3.1 Nanostructured ceria and oxygen vacancies

The quantity of oxygen vacancies in a ceria-based material is strongly influenced by its morphology, particularly at the nano scale. Simply decreasing the size of ceria nanoparticles can lead to more oxygen vacancy formation, due to the higher surface-to-volume ratio. This has been employed, using ceria nanoparticles of 3-4 nm, to directly utilise ceria as a catalyst for CO oxidation, and also as a catalyst support to supply more reactive oxygen to metal nanoparticle catalysts. [21]

Depending on nanomorphology, different crystal planes may be exposed on the surface of a ceria nanoparticle – three of the most commonly reported are the (111), (110), and (100) surfaces, shown in Figure 1. These crystal planes have different oxygen vacancy formation energies and consequently, different reactivities when employed as a catalyst.

The relative stability of these three surfaces is generally acknowledged to be (111) > (100) > (110), due to how the bulk lattice structure terminates at each surface (Figure 5). [54]

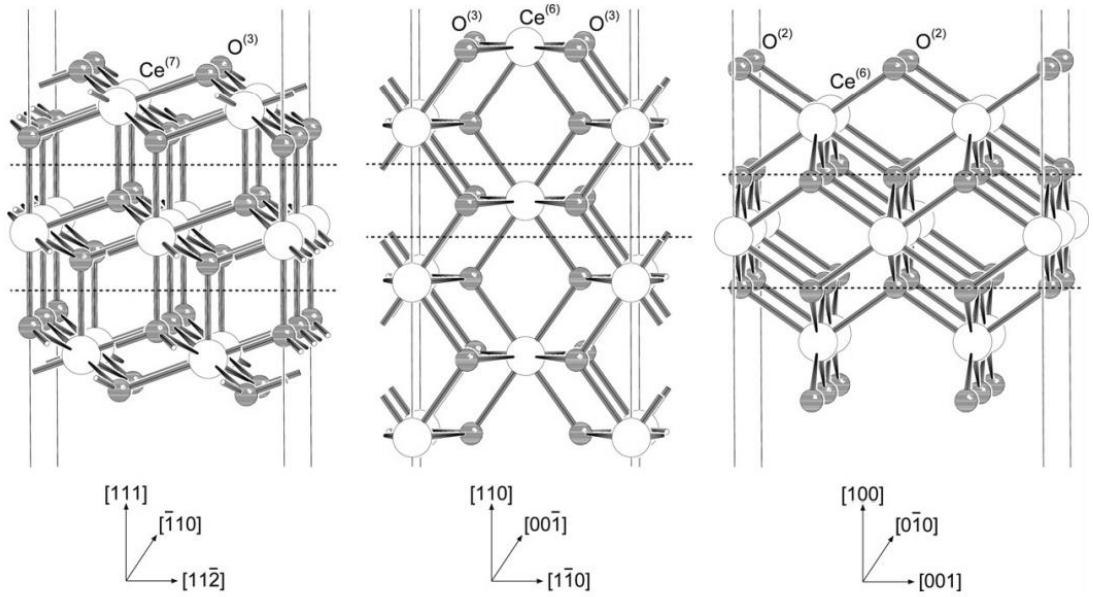

Figure 5. Bulk ceria truncated at the (111), (110), and (100) surfaces. Large circles represent cerium atoms and small circles represent oxygen atoms. Reprinted from Ref. [54] with permission from Elsevier.

There are a number of computational reports in the literature regarding how different ceria surfaces affect oxygen vacancy formation. Sayle *et al* investigated the surface stability and oxygen vacancy formation at the (111), (110), and (310) ceria surfaces. In addition to finding that oxygen vacancy formation is more thermodynamically favourable at the surface than in the bulk, Sayle determined that the (111) surface was the most stable, followed by (110) and then (310). Lower surface stability correlated with a lower energy of reduction and lower vacancy formation energy – calculated to be 16.06 eV, 15.65 eV, 14.56 eV, and 13.59 eV for bulk, (111), (110), and (310) oxygen vacancies, respectively. When calculated together with the adsorption of CO and oxidation to CO_2 using an oxygen atom from the ceria lattice, the overall reaction energy was shown to be exothermic for the (110) and (310) surfaces. Sayle concluded that ceria morphologies that selectively exposed those surfaces would result in the highest oxidative activity. [56]

A number of different groups have reported DFT investigations of the (111), (110), and (100) surfaces of ceria. Generally, these calculations involved vacancy formation energies

of a single vacancy on different ceria surfaces. Nolan *et al* showed that the removal of an oxygen atom led to some surface distortion and the reduction of two cerium atoms from 4+ to 3+. This surface distortion was lowest for the stable (111) surface. Vacancy formation energies were calculated to be 3.30 eV, 2.69 eV, and 2.97 eV for the (111), (110), and (100) surfaces, respectively. [57] Mayernick *et al* calculated the vacancy formation energies to be 2.76 eV, 2.10 eV, and 2.26 eV for the (111), (110), and (100) surfaces. [58] Yang *et al* calculated oxygen vacancy formation energies of 3.39-3.98 eV for the (111) surface and 2.48-3.17 eV for the (110) surface. The large variation was attributed to the calculated surface energy being strongly dependent on the size of the CeO_2 cluster used for calculations. [59] Fabris *et al* calculated the vacancy formation energies to be 2.15-2.92 eV for the (111) surface and 1.57-2.33 eV for the (110) surface. [60] In general, while there is some disagreement amongst different groups about the values of vacancy formation energy, the overall trend is the same: oxygen vacancy formation energy is lowest for ceria's (110) surface, followed by (100) and then (111).

Experimentally, ceria of various nanomorphologies has been synthesised to selectively expose different crystal faces and assess the resulting catalytic activity. Zhou *et al* report that ceria nanorods were shown using high-resolution TEM to expose (110) and (100) surfaces, compared with ceria nanoparticles exposing the (111) surface. Despite having a lower BET surface area, the nanorods demonstrated a significantly higher CO oxidation activity than the nanoparticles. Furthermore, the nanorods demonstrated greater stability than the ceria nanoparticles upon calcination at 600°C. [61] These results were corroborated by Tana *et al*. [62]

Mai *et al* and Torrente-Murciano *et al* report that ceria nanoparticles expose (111) and (100) crystal surfaces, ceria nanorods expose (110) and (100) crystal surfaces, and ceria nanocubes expose the (100) surface. Both groups synthesised their ceria samples with similar untemplated hydrothermal methods. [36,37] Mai *et al* calculated the oxygen storage content of ceria nanorods, nanocubes, nanoparticles, and bulk ceria to be 554, 353, 318, and 109 μmol O/g respectively. Normalised to BET surface area, this became 5.1, 9.1, and 10.6 μmol O/m^2 for nanoparticles, nanorods, and nanocubes, respectively. Mai concluded that (110)/(100) dominated ceria morphologies such as nanorods and

nanocubes are idea for catalysing oxidation reactions. [36] Torrente-Murciano *et al* used XPS to determine the surface oxidation state of different ceria morphologies, correlating this to the level of surface oxygen vacancies. The percentage of Ce^{3+} on ceria's surface was calculated to be 16.4%, 13.9%, and 13.6% for nanorods, nanocubes, and nanoparticles, respectively. The total oxidation of naphthalene was used to assess catalytic activity – nanorods were shown to be the most active, followed by nanocubes and then nanoparticles. [37]

In contrast, using the same hydrothermal synthesis procedure to produce ceria nanorods, Agarwal *et al* found that although ceria nanorod growth is along the (110) direction, only (111) facets were observed on the nanorod surface. [63] Silva *et al* corroborate this, reporting that fresh, hydrothermally synthesised nanorods mainly expose (111) facets, while a post-synthesis comminution process results in the exposure of (110) facets, which improves catalytic activity. [64] Therefore, post-synthesis treatment may be necessary to achieve the best morphology.

Zhang *et al* report that ceria nanorods exposing the (110) surface have a surface area-adjusted catalytic activity three times as high as (111)-exposing nanooctahedra and four times as high as (100)-exposing nanocubes for the oxidative coupling of ketones and primary alcohols. [65] Bezkrovnyi *et al* report the synthesis of ceria nanocubes with (100) faces, but small (110) and (111) faces at the edges and corners, representing <10% of the total surface area. Upon calcination at 500 °C in a reducing atmosphere, these (110) edges were reconstructed into (111) edges. This was accompanied by a significant loss in activity for CO oxidation, showing the importance of the (110) surface in oxidation reactions. [66]

In addition to being more active, nanorods have been shown to be more selective for full oxidation to CO_2 than other morphologies. Zhou *et al* report that ceria nanorods demonstrate both higher conversion rates and CO_2 selectivity at low temperatures for the oxidation of ethanol than ceria nanocubes. Zhou attributes this to the greater availability of active oxygen species on the (110) surface of the nanorods. [67]

Overall, the trend is clear – ceria morphologies, particularly nanorods, that selectively expose the (110) crystal surface enhance surface reducibility and oxygen vacancy formation. This has been shown to correlate with higher catalytic activity for a range of oxidative reactions. However, there is some disagreement with regard to the particular crystal facets exposed by hydrothermally synthesised ceria.

1.3.2 Doped ceria and oxygen vacancies

Another strategy for improving oxygen vacancy formation in ceria is introducing other elements into the crystal lattice. The replacement of cerium atoms with elements of lower valence can lead to oxygen vacancies being created to compensate for the charge difference. [18] Alternatively, the presence of other elements can lead to lattice distortions and defects, which can also result in oxygen vacancies. [55] There have been many computational studies reported in the literature regarding how different dopant properties affect oxygen vacancy formation and thus catalytic activity of the final ceria-based material.

Nolan has reported a DFT study examining how dopant ionic radius affects the energy of oxygen vacancy formation on the (110) surface of doped ceria. Al, Sc, In, Y, and La (ionic radii of 0.39, 0.75, 0.80, 0.96, and 1.16 Å, respectively) were examined. In comparison, the ionic radius of Ce^{4+} is 0.97 Å. Nolan found that dopants with radii close to that of cerium were easily accommodated within the crystal lattice. However, aluminium, with a much smaller ionic radius, and lanthanum, with a much larger ionic radius, both strongly distorted the lattice structure. The formation energy of charge-compensating oxygen vacancy formation was calculated to be -0.13, 0.00, -0.18, +0.47, and +0.65 eV for Al, Sc, In, Y, and La, respectively, meaning that dopants with ionic radii smaller than cerium had the most favourable vacancy formation energies. However, it was noted that these calculations were performed at 0 K and that under more realistic environmental conditions, oxygen vacancy formation was likely to be favourable for all of the dopants in question. [68]

Balducci *et al* also looked at the effect of dopant ionic radius – this time with regard to how it affects the reducibility of cerium atoms within the bulk crystal structure. Mn^{2+}, Zn^{2+}, Ca^{2+}, Mn^{3+}, Sc^{3+}, Y^{3+}, Gd^{3+}, and La^{3+} were chosen as sample dopants. They determined that larger ionic radii resulted in a lower energy of reduction for reducing Ce^{4+} to Ce^{3+}. This was rationalised by the larger dopant ionic radii assisting in relieving the stress of lattice expansion accompanied by the reduction of Ce^{4+} to Ce^{3+} (in which cerium's ionic radius expands from 0.97 to 1.143 Å). [69] Although this appears to contradict Nolan's results, this study did not specifically look at oxygen vacancy formation energies, only the Ce^{4+} reduction energy.

Krcha *et al* report a comprehensive DFT study in which the first three rows of transition metals in the periodic table from groups IV – XII are examined as ceria dopants. This study looked at how different dopants affected oxygen vacancy formation as well as catalytic activity for dissociative methane adsorption. In general, it was found that transition metals in groups IV and V altered the reducibility of cerium atoms, while dopants from groups X – XII became reduction centres themselves, reducing from 4+ to 2+ upon surface reduction and oxygen vacancy formation. This matches the results of Balducci's experiments, in which dopants with larger ionic radii tended to be better at reducing cerium in the lattice. Gold was a partial exception to this trend, instead reducing to 3+ upon oxygen vacancy formation, with a single cerium atom also reducing from 4+ to 3+ to compensate for the charge. The calculated oxygen vacancy formation energy decreased when moving from left to right across the periodic table, when moving up a column in the periodic table, and with lower atomic radii. [70] (Figure 6) This trend is the same as that identified by Nolan. [68]

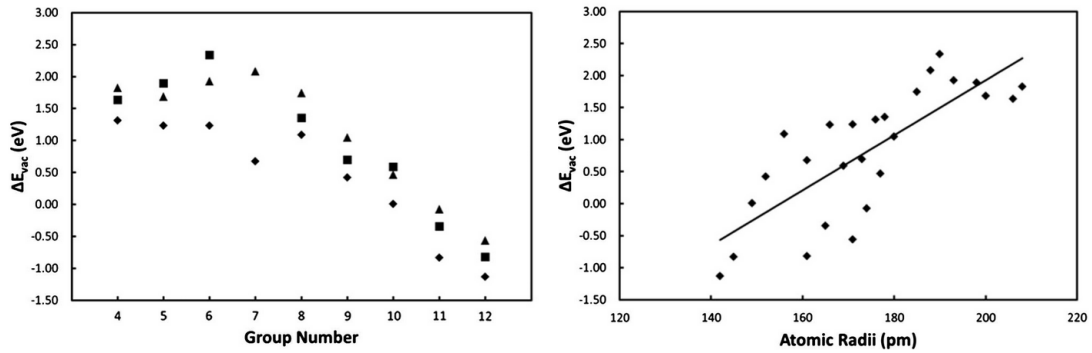

Figure 6. Energy of oxygen vacancy formation vs periodic table group number (left) and atomic radius (right). Reprinted from Ref. [70] with permission from Elsevier.

Because dopants that decrease the energy of oxygen vacancy formation will correspondingly *increase* the energy of oxygen vacancy healing, Krcha *et al* propose that dopants that reduce oxygen vacancy formation energies to between -0.5 eV and 1.0 eV (from pure ceria's 2.76 eV) provide the best balance between improved oxygen vacancy formation and easily healing those vacancies to complete the TWC catalytic cycle. They suggest the use of Ag, Au, Ni, Co, Pt, Pd, and Mn as potential ceria dopants. [70]

In another DFT study, Gupta *et al* report that doping ceria with transition metals and rare metals (Mn, Fe, Co, Ni, Cu, Pd, Pt, Ru) significantly enhance the reducibility of ceria and oxygen storage capacity, while rare earth dopants (La and Y) do not improve oxygen storage capacity. This is attributed to how the dopants are incorporated into the lattice structure – when a transition or rare metal dopant replaces a cerium atom in the lattice structure, significant lattice distortion occurs. This results in the formation of 'long' and 'short' dopant-oxygen bonds, where the longer bonds lead to weakly bound oxygen atoms with a bond valence of approximately -1.5 instead of -2. Because these oxygen atoms are 'underbonded,' they are more reactive, meaning the overall system is more reducible. This phenomenon was not seen with La- or Y-doped ceria – here, only minimal lattice distortion was observed. [55]

Experimental trends have been reported as well, with a wide range of dopants being reported in the literature – mainly transition metals or other lanthanides. [71–73] Hegde *et al* corroborate Gupta's DFT results by attributing increased oxygen mobility in Zr- and Ti-substituted ceria to lattice distortion leading to long and short cation-oxygen bond lengths. In contrast, pure ceria does not show any variation in cerium-oxygen bond length. [74] Sugiura reports that the inclusion of Zr within the ceria lattice structure improves overall oxygen storage capacity because Zr has a smaller ionic radius than Ce^{4+}, which gives neighbouring cerium ions 'space' to expand when they reduce to Ce^{3+}. [75] Min *et al* also report that smaller dopant ionic radii improve oxygen vacancy concentrations in ceria, testing Hf and Sn dopants. [76]

Liu *et al* propose a correlation between dopant electronegativity and CO oxidation activity. They note that both redox potential and ionic radius, both shown to be relevant

to oxygen vacancy formation in computational studies, are related to the ability of an atom to attract or lose electrons. Furthermore, electronegativity strongly influences a transition metal oxide's metal-oxygen bond intensity. Liu *et al* examined ceria doped with Cu, Co, Mn, Ti, Zr, and Tb. They report that dopants with higher Pauling electronegativity values resulted in ceria materials with higher active lattice oxygen (the oxygen active in the CO oxidation), as well as higher catalytic activity at lower temperatures. (Figure 7) Higher dopant electronegativity resulting in a more distorted lattice structure, and therefore more oxygen vacancies, is given as the explanation for this phenomenon. [71]

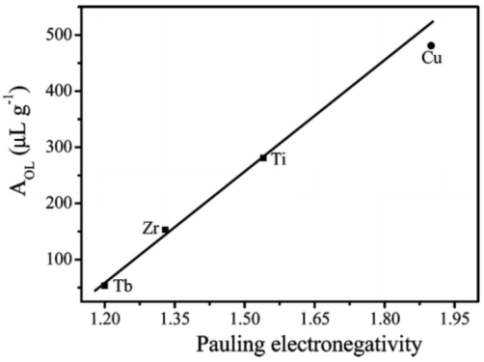

Figure 7. Active lattice oxygen vs. Pauling electronegativity for ceria dopants. Reprinted with permission from Ref. [71]. Copyright 2010 American Chemical Society.

Xiao *et al* report improved CO oxidation activity for ceria doped with Sn or Pr, but reduced CO oxidation activity for ceria doped with Y, Zr, La, or Gd. They propose this is due to dopants with stable valence states 'dampening' the Ce^{4+}/Ce^{3+} redox cycle and thus adversely affecting oxygen vacancy formation. In contrast, Sn and Pr have a variable 4+/2+ oxidation state, which can promote ceria reduction and higher oxygen storage content. [73]

Shehata *et al* report that doping ceria with 3+ lanthanides (Sm, Nd, Ho, Er) does not necessarily aid in oxygen vacancy concentration within ceria. Here, the quantity of reduced Ce^{3+} was correlated with the measured bandgap. Sm and Nd were found to reduce the bandgap compared with undoped ceria, resulting in a higher ratio of Ce^{3+} to Ce^{4+} atoms and thus more oxygen vacancies. The opposite effect was found for Ho and Er. [72]

There is some agreement amongst these computational and experimental results. The reported computational experiments are in relatively good agreement. Liu's proposed relationship between dopant electronegativity and oxygen vacancy formation agrees well with Gupta's DFT results. However, the results of Xiao *et al* and Shehata *et al* do not necessarily agree with Gupta's, as they demonstrated that at least some lanthanide dopants were able to improve oxygen vacancy formation in ceria. Overall, some of the proposed trends – such as the electronegativity/vacancy formation relationship and taking more careful consideration of dopant valence states – will likely be useful for guiding future experimental investigations. Nevertheless, much more work will be necessary to strongly identify dopant trends.

1.3.3 Creation of oxygen vacancies – other methods

In Sections 1.3.1 and 1.3.2, selectively exposing ceria crystal faces and doping ceria with other metals to create ceria-based materials with higher intrinsic levels of oxygen vacancies than pure cerium oxide have been discussed. However, it is also possible to induce higher oxygen vacancy concentrations in ceria via chemical or thermal methods. For instance, Lan and Sohn report that the high-temperature treatment of ceria nanoparticles in hydrogen results in the creation of oxygen vacancies and the formation of a Ce_2O_3 phase, compared with ceria nanoparticles treated in air. [77] This is due to the consumption of oxygen from the ceria lattice by hydrogen, a phenomenon which can be replicated with other reducing agents as well. However, the effect of particle size, discussed in Section 1.3.1, can have a stronger effect due to sintering at high temperatures. Wan *et al* report that while heating ceria nanoparticles under hydrogen up to 445 °C, reduction of Ce^{4+} to Ce^{3+} by hydrogen takes place, but is entirely mitigated by the growth in particle size at high temperatures, leading to a net decrease in Ce^{3+} levels and oxygen vacancy concentration. [78]

A low partial pressure of oxygen can also affect oxygen vacancy levels in ceria, without the presence of a reducing atmosphere. Choudhury *et al* report that annealing ceria nanoparticles in air at 200 °C reduces oxygen vacancy concentration and lattice strain, but

annealing in vacuum at 200 °C sharply increases oxygen vacancy levels and lattice strain. [79]

Qiu *et al* have reported that Ar^+ ion sputtering or irradiation of ceria with x-rays can induce the creation of oxygen vacancies and reduction of Ce^{4+} to Ce^{3+}. [80] Because of this, characterisation techniques such as XPS (x-ray photoelectron spectroscopy) have the capacity to reduce ceria samples, depending on the beam strength. [81]

1.3.4 Quantification of oxygen vacancies in ceria

Spectroscopic and chemical methods may both be used to characterise ceria. XPS is commonly used to analyse the oxidation state of ceria and ceria-based materials due to the ability to distinguish between Ce^{4+} and Ce^{3+} ions in the Ce 3d spectra, although deconvolution of overlapping peaks is complex. [82] However, this technique is only useful for surface measurements. The use of synchrotron radiation, as opposed to the typical Al Kα or Mg Kα radiation sources, has also been reported for XPS analysis, providing a higher photon flux and tuneable excitation energy. X-ray absorption spectroscopy (XAS) also utilises synchrotron radiation to identify surface adsorbates on ceria materials, although infrared spectroscopy can also be used to identify surface species. [83]

Raman spectroscopy may be used to examine oxygen vacancy concentration. Ceria Raman spectra typically show a main band at 465 cm^{-1}, attributed to vibrations in the Ce-O bonds in the fluorite-type lattice structure. In pure ceria, shifts in this bond may be attributed to oxygen vacancy levels and quantified. [77,84] Additionally, a second band at approximately 595 to 600 cm^{-1} is related to higher levels of oxygen vacancy concentration.

Due to the difference in mass between CeO_2 and CeO_{2-x}, the bulk oxygen deficiency in a ceria sample can be determined using thermogravimetric methods. By measuring the gain in mass while heating the sample under an oxidising atmosphere, the quantity of oxygen

taken up by the sample can be measured. A reducing atmosphere may also be used to determine the reductive capacity of a ceria material. [85]

1.4 Three-way catalyst reaction mechanisms

The Mars-van Krevelen (MvK) mechanism is commonly reported in the ceria-catalysed oxidation of carbon monoxide to carbon dioxide. [71,86,87] The oxidation of various hydrocarbons in exhaust gas is also thought to proceed via a MvK mechanism. [88–91] In general, the characteristic feature of a MvK-catalysed heterogeneous reaction is that a reactant adsorbs to the surface of a catalyst, and the reaction product leaves the catalyst surface containing a constituent of the catalyst lattice structure. [92] In contrast, in other surface-catalysed reaction models such as Eley-Rideal or Langmuir-Hinshelwood, the reaction occurs between two elements originally in the gas phase. [93]

According to the MvK mechanism, for CO and hydrocarbon oxidation, oxygen atoms are removed from the lattice to oxidise the reactants. This forms an oxygen vacancy and can be shown in equation form:

$$CO + \bullet \rightarrow CO\bullet \quad (5)$$

$$CO\bullet + O_L \rightarrow COO_L\bullet \quad (6)$$

$$COO_L\bullet \rightarrow \bullet + CO_2 + V_L \quad (7)$$

$$0.5O_2 + V_L \rightarrow O_L \quad (8)$$

Here, CO adsorbs to the surface of the ceria lattice at adsorption site • and reacts with a surface oxygen O_L to form an intermediate, $COO_L\bullet$. This intermediate desorbs from the surface as CO_2, leaving behind an oxygen vacancy V_L, which can be healed by atmospheric oxygen. To complete the catalytic cycle, the oxygen vacancy left by CO or hydrocarbon oxidation may also be healed by the reduction of a nitrogen oxide. [94]

Although this is a surface-catalysed reaction, internal oxygen vacancies within ceria's bulk lattice structure can also contribute to the reaction. This is possible because oxygen

atoms are able to migrate through the lattice structure via a vacancy hopping mechanism between neighbouring oxygen sites. This phenomenon is very rapid, allowing bulk oxygen to migrate to the surface of ceria to aid in catalytic oxidation reactions. There are a wide range of possible activation energies of oxygen diffusion through the lattice, dependent on sample, morphology, and the exact stoichiometry. [95,96] Lattice distortion and higher quantities of oxygen vacancies contribute to higher oxygen mobility throughout the lattice. [97]

1.4.1 CO and HC oxidation: the Mars-van Krevelen mechanism

The MvK mechanism is a somewhat general description – consequently, various computational experiments have been conducted to gain a more detailed understanding of CO oxidation on ceria's surface. Nolan and Watson report a DFT study that looks at the surface dependence of CO oxidation on different crystal planes, focussing on the (111), (110), and (100) crystal surfaces. They found that CO only weakly interacts with the (111) surface, with an adsorption energy of -0.26 eV. For both the (110) and (100) surfaces, the CO molecule formed a bond with two adjacent surface oxygen atoms, forming a carbonate-like intermediate. For the (110) surface, the CO adsorption energy was -1.95 eV, with an overall CO→CO_2 energy gain of -1.17 eV. For the (100) surface, the CO adsorption energy was higher (-3.21 eV), but the energy gain of the overall reaction was lower (-0.87 eV). Only physisorption was observed for the (111) surface, while chemisorption was observed for the (110) and (100) surfaces. [98]

This difference is attributed to the different atom configurations on each crystal plane. Oxygen atoms in the (111) surface are three coordinate and relatively far apart – for a CO molecule to bond to two surface oxygens, the oxygen atoms would need to be displaced by 0.90Å. For the (100) surface, the oxygen atoms are displaced by 0.65Å, and for the (110) surface, they are displaced by 0.25Å. Therefore, the (110) surface is most favourable to CO adsorption and oxidation to CO_2. [98] A separate DFT study by Huang and Fabris confirm these results for the (111) and (110) surfaces.[99] Scanlon *et al* separately confirm the CO_3 intermediate adsorption process for the (110) surface. [100]

CO oxidation on doped ceria surfaces has also been investigated. Nolan *et al* report a DFT study of CO adsorption and oxidation on Au-doped ceria (110) and (100) surfaces. The adsorption energies were calculated to be -4.70 eV and -3.90 eV for the (110) and (100) surfaces, respectively. These compare favourably with the adsorption energies calculated for undoped ceria. [101] In other experiments, Nolan reports that the adsorption energy for CO adsorbed on doped ceria's (110) surface is -4.30, -4.31, -4.10, and -2.42 eV for ceria doped with Ti, Zr, Hf, and La, respectively. [102,103]

Shapovalov and Metiu also examined CO oxidation with gold-doped ceria, comparing an undoped and gold-doped ceria (111) surface. As with Nolan's study, CO oxidation on the gold-doped ceria surface was much more favourable than on the undoped ceria surface. [86] Chen reports that Ru-doping improves CO adsorption on the ceria (111) surface, allowing for chemisorption in addition to the physisorption seen on the pure ceria (111) surface. [104] X-S. Liu *et al* report that Fe doping also improves CO adsorption and CO_2 formation on the (111) surface. [105] Yang *et al* report that CO adsorption and CO_2 formation is more favourable on the (110) surface of a Ce-Zr mixed oxide than pure ceria. [106]

B. Liu *et al* report a modified carbonate-mediated MvK mechanism for the (110) surface of cobalt-doped ceria. (Figure 8) Here, CO (1) adsorbs onto a surface cobalt site, (2) reacts with an adjacent lattice oxygen to form a 'bent' CO_2 intermediate, (3) interacts with another adjacent lattice oxygen to form a carbonate intermediate, and (4) the carbonate intermediate reacts with another adsorbed CO and desorbs as two linear CO_2 molecules, leaving behind two oxygen vacancies. In contrast, a conventional MvK mechanism was reported for cobalt-doped (111) and (100) surfaces, in which CO is adsorbed on the site of a lattice oxygen, forming a linear CO_2 intermediate which can readily desorb, leaving behind a single oxygen vacancy. [107]

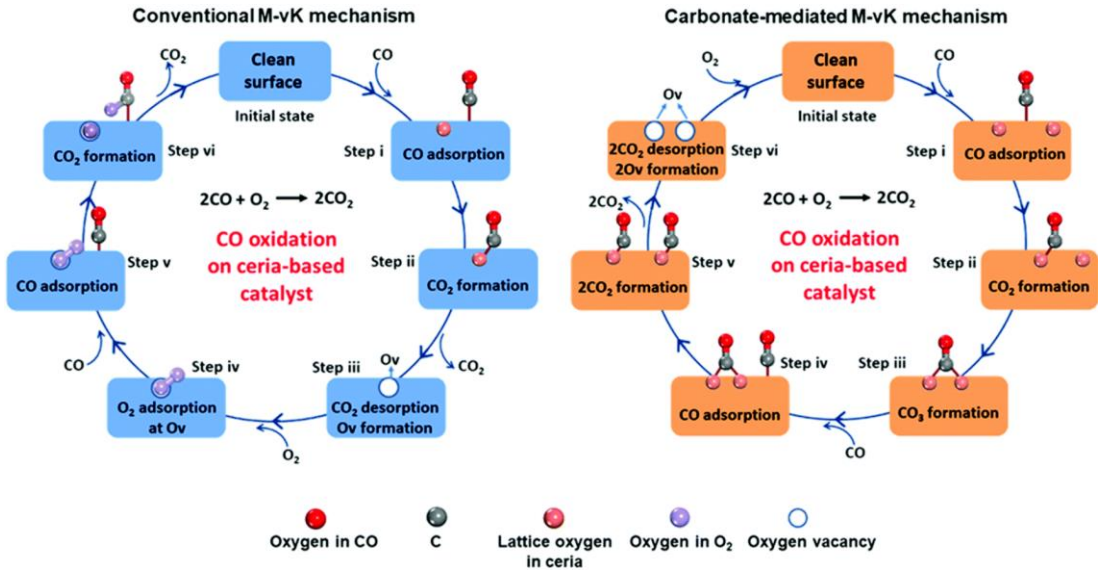

Figure 8. Convention and carbonate-mediated Mars van Krevelen mechanisms for the oxidation of CO to CO_2. Republished with permission of the Royal Society of Chemistry from Ref. [107]; permission conveyed through Copyright Clearance Center, Inc.

Computational studies have also been reported that look at ceria-catalysed hydrocarbon oxidation. Knapp and Ziegler look at the oxidation of methane to water and carbon dioxide on the ceria (111) surface. This reaction is more complicated than CO oxidation, involving disassociation of the methane molecule's hydrogen atoms and adsorption at surface oxygen sites and conversion of the carbon atom to CO. While the disassociation of methane on the surface was found to be exothermic (-1.86 eV), desorption of the hydrogen atoms as H_2 or H_2O was calculated to be highly endothermic (+4.47 eV). [108]

Krcha *et al* report dopant trends in regard to the disassociative adsorption of methane on doped ceria's (111) surface. The first three rows of transition metals in the periodic table from groups IV – XII are examined as potential dopants. They report that the methane activation energy and energy of oxygen vacancy formation are correlated. For doped ceria materials with the lowest (most favourable) vacancy formation energies, hydrocarbon oxidation is only limited by the refilling of oxygen vacancies. For doped ceria with unfavourable vacancy formation energies, methane activation is the rate-limiting step. The potential dopants identified as the most promising for hydrocarbon oxidation were Ag, Au, Ni, Co, Pt, Pd, and Mn. [70]

Mayernick and Janik report a DFT study looking at methane activation over the (111), (110), and (100) surfaces of Zr- and Pd-doped ceria. Both Zr-doped ceria and Pd-doped ceria were calculated to have more favourable adsorption energies than undoped ceria, for all three surfaces. For the (111) surface, adsorption energies were -0.76, -1.00, and -1.93 eV for CeO_2, Zr-CeO_2, and Pd-CeO_2, respectively. For the (110) surface, adsorption energies were -1.22, -1.60, and -2.50 eV for CeO_2, Zr-CeO_2, and Pd-CeO_2, respectively. For the (100) surface, adsorption energies were -1.52, -1.67, and -2.05 eV for CeO_2, Zr-CeO_2, and Pd-CeO_2, respectively. [58]

Wu *et al* use DFT to examine the oxidation of formaldehyde on the (111) surface of undoped and Mn-doped ceria. They report that for stoichiometric ceria (doped or undoped), the reaction proceeds with a MvK pathway – the formaldehyde adsorbs and interacts with surface lattice oxygen atoms, and post-oxidation and desorption of CO_2, the oxygen vacancy is healed by atmospheric oxygen. The presence of Mn dopant reduces the adsorption energy from -0.86 eV to -1.98 eV. However, under typical conditions, Mn-doped ceria will contain numerous oxygen vacancies. For nonstoichiometric Mn-doped ceria with oxygen vacancies, Wu *et al* instead report a Langmuir-Hinshelwood reaction mechanism, in which atmospheric O_2 adsorbed on the site of an oxygen vacancy interacts with an adjacent adsorbed formaldehyde molecule. They report that overall, this reaction pathway is more favourable than the MvK mechanism of the stoichiometric ceria surface. [109]

Overall, these results correlate well with both the computational and experimental oxygen vacancy formation energy results. Papers that look at different crystal facets are in general agreement that the (110) surface is most favourable for oxidative catalysis. Regarding dopants, while there are still many areas that need investigation, the oxygen vacancy trends identified in Section 1.3 seem to hold true in the DFT studies discussed here.

1.4.2 NO_x reduction: oxygen vacancy healing

Nitrogen oxides react with reduced ceria to heal oxygen vacancies. Yang *et al* report a DFT study in which they examine the adsorption of NO on ceria (111) and (110) surfaces. For stoichiometric, unreduced ceria, NO only weakly interacts with either surface, and will not disassociate to form N_2. When an oxygen vacancy is present, NO adsorbs much more strongly, with adsorption energies of -1.82 and -1.33 eV for the (111) and (110) surfaces, respectively. For both surfaces, the oxygen adsorbs at the vacancy site, resulting in a lengthening of the N-O bond. If two NO molecules adsorb on adjacent oxygen vacancy sites, their nitrogen ends will interact to form a N-N bond as an intermediate to disassociating as a free N_2 molecule. This overall interaction resulting in a healed ceria surface and free N_2 is thermodynamically favourable, with a calculated energy gain of -2.73 eV for both the (111) and (110) surfaces. [110]

Mihaylov *et al* report different adsorption behaviour for the interaction between NO and the reduced ceria (111) surface. They report that this interaction can lead to the 'deep reduction' of NO to form N_3^- azide species, which are intermediates in the conversion of NO to nitrogen gas. This process is highly exothermic as it involves the simultaneous healing of three oxygen vacancies. These findings were supported by both DFT calculations and experimental data, using FTIR spectra of adsorbed NO species on commercially provided ceria powders. [111]

Nolan *et al* report a DFT study of the interaction between NO_2 and reduced ceria (111), (110), and (100) surfaces. In all cases, the NO_2 adsorption proceeds by one of its oxygen atoms adsorbing at and occupying the oxygen vacancy site, resulting in an elongated N-O bond (from 1.21 Å to 1.36, 1.31, and 1.44 Å, respectively). The adsorption energy was calculated to be -2.40, -2.25, and -2.32 eV for the (111), (110), and (100) surfaces, respectively, while the overall reaction energy (resulting in NO and a healed oxygen vacancy) was calculated to be -1.52, -0.93, and -1.20 eV, respectively. This is an expected result – the ease of oxygen vacancy formation on these surfaces is (110) < (100) < (111), as discussed in Section 1.3.1, so it is logical that the easy of vacancy healing is the opposite. Nevertheless, all surfaces showed an exothermic reaction. But despite this being the case,

spontaneous decomposition of the adsorbed NO_2 to NO and a healed oxygen vacancy were not observed on any surface, implying a necessary energy cost to break the N-O bond. [112]

Scanlon *et al* report a slightly more complicated model of NO_2 adsorption on the reduced ceria (110) surface. They report two possible modes of adsorption. NO_2 can adsorb to the surface via an oxygen atom at the site of an oxygen vacancy in the ceria lattice. Alternatively, the two NO_2 oxygen atoms coordinate to the reduced Ce^{3+} atoms around an oxygen vacancy, with neither actually occupying the vacancy site. Both options are exothermic and favourable, with adsorption energies of -1.83 and -1.94 eV, respectively. However, the 'split' adsorption mode is more favourable. The overall reaction energy gain for reducing NO_2 to NO and healing the oxygen vacancy was calculated to be -0.44 eV; significantly smaller than that calculated by Nolan *et al* but still exothermic. [100]

While ceria doping is a good strategy for oxidative reactions because it improves reducibility and oxygen vacancy formation, the trade-off is reduced favourability for reoxidising and healing of the oxygen vacancies. Complementing Nolan's previous study on NO_2 adsorption and reduction on different ceria surfaces, further work was undertaken looking at the adsorption energy of NO_2 at an oxygen vacancy on the (110) and (100) surfaces of Au-doped ceria. Here, the adsorption energy was calculated to be -1.46 and -1.97 eV for the (110) and (100) surfaces, respectively (compared with -2.25 and -2.32 eV for the undoped surfaces). So while doping ceria with gold somewhat reduced the favourability of NO_2 adsorption, the interaction was still favourable. [113]

Koizumi *et al* report a mechanism for the reduction of NO with CO using a Cu and Cr co-doped ceria (111) surface (Figure 9). Similarly to previous experiments, they report a MvK mechanism for CO oxidation. Here, CO adsorbs on the surface near a Cu site, followed by reaction with a surface lattice oxygen, desorption as CO_2, and the creation of an oxygen vacancy. DFT experiments show that the presence of Cr enhances the adsorption of NO on Ce sites, followed by interaction with neighbouring oxygen vacancies. This exposes the N to interaction with another adsorbed NO molecule,

allowing for formation of N_2 and the healing of the oxygen vacancy. Koizumi *et al* also use FTIR experiments to support their DFT results. [114]

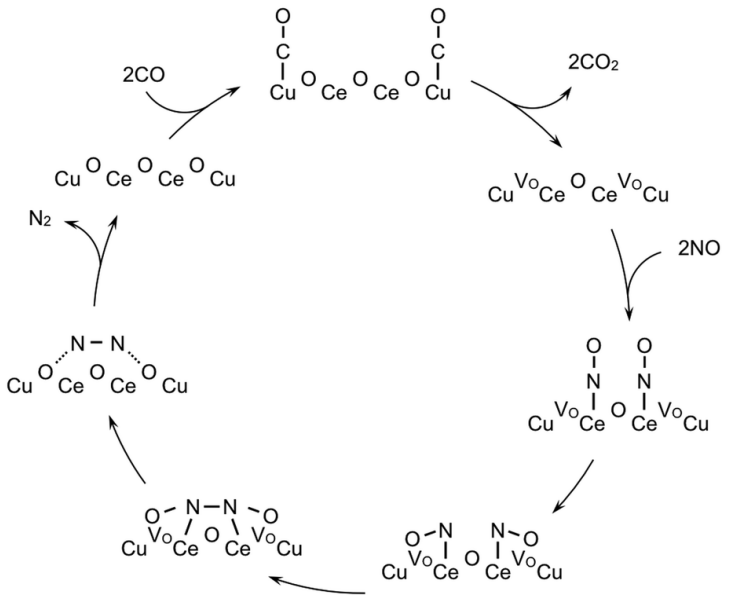

Figure 9. Reaction mechanism for CO-NO reaction with a Cu-Cr/CeO_2 catalyst reported by Koizumi *et al*. Republished with permission of the Royal Society of Chemistry from Ref. [114]; permission conveyed through Copyright Clearance Center, Inc.

There is some disagreement amongst these computational studies regarding the precise mode of NO_x adsorption and reduction on ceria's surface. Nevertheless, they are in general agreement that the overall reduction reaction is exothermic, and therefore favourable. This remains true even when ceria is doped with elements that improve oxygen vacancy formation and make vacancy healing less favourable.

1.5 Thermal resistance of ceria-based materials

Ceria exposed to high temperatures (800°C and above) experiences severe degradation of its ability to easily reduce and reoxidise, which greatly impairs ceria's ability to act as a three-way catalyst or catalyst support. This is problematic for its use in three-way catalysts, as under realistic driving conditions, catalytic converters are routinely exposed to temperatures of up to 850°C and are occasionally heated to over 1000°C. [7,8] While pure ceria was initially used as the oxygen storage support material in PGM-based

three-way catalysts, this was replaced with ceria-zirconia mixed oxides in the 1990s because of its improved performance after exposure to high temperatures. [12,115]

1.5.1 Ceria-zirconia mixed oxides

Pulse neutron diffraction and temperature programmed reduction experiments of ceria and ceria-zirconia mixed oxides treated at up to 800°C by Mamontov and Egami show that its high-temperature degradation is due to a permanent loss of oxygen vacancies. In pure ceria calcined at 500°C, there are an equal quantity of detected oxygen vacancies and interstitial oxygen atoms, an indication of a mobile, 'active' species of oxygen which is only weakly bound to the lattice structure. This active oxygen, mainly located in the bulk lattice structure, can migrate to the surface to participate in reactions. However, in the course of heating ceria up to 800°C, the concentration of these defects irreversibly starts to fall at approximately 760°C. This results in a permanent loss of activity. It is also an indication that oxygen storage content is not necessarily connected to surface area – ceria heated to 760°C has already lost most of its surface area, experiencing only minimal changes between 760-800°C. However, this is the temperature range in which the loss of oxygen vacancies is seen. [116]

This decline in oxygen vacancy concentration and loss of activity is not seen in a $Ce_{0.7}Zr_{0.3}O_2$ mixed oxide prepared with the same synthesis method. Here, a much higher concentration of oxygen vacancies, up to 8%, was detected compared with interstitial oxygen – this indicates that Ce^{3+} ions are present to balance the charge. Therefore, the presence of zirconium in the lattice keeps the ceria in a slightly reduced state. Furthermore, this higher concentration of oxygen vacancies compared with pure ceria is maintained after treatment at 800°C. Mamontov and Egami speculate that, because zirconium has a much smaller ionic radius than cerium, this creates 'compressive stresses' at the oxygen vacancy sites, making it more difficult for interstitial oxygen to recombine with the vacancies. [116] These results indicate that the bulk properties of the mixed oxide material, not just surface morphology or area, is important in maintaining a high OSC.

These experimental results are supported by computational work by Balducci *et al*, who report that incorporation of Zr^{4+} into the lattice decrease the Ce^{4+}/Ce^{3+} reduction energy in the bulk lattice structure. [117] The importance of the bulk structure, rather than surface effects, is further emphasised with experimental work by Bozo *et al* and Balducci *et al*, who report that calcined Ce-Zr samples with severe loss of surface area still maintain oxygen storage capacity. [118,119] More recently, Fernandes *et al* examined a commercial catalytic converter monolith loaded with Ce-Zr support and a Pd/Rh catalyst to examine the effect of high temperature on deactivation and degradation of catalytic ability. Even after calcination at 1200°C and degradation of BET surface area to ~1 m^2/g, the catalyst retained significant activity, with T_{50} values of 285 °C and 485 °C for CO oxidation and propane oxidation, respectively. [120]

The ratio of cerium to zirconium in Ce-Zr mixed oxides affects the oxygen storage content, and a wide range of different compositions have been reported in the literature that still maintain the fluorite lattice structure. [121] Cuif *et* al show that oxygen storage capacity is highest with a Zr content of 20-40%, while Graham *et al* report the best ratio is 70% cerium, 30% zirconium (when used as a support for a Pd catalyst). [121,122] The difference in OSC compared with pure ceria is quite significant. Hegde *et al* report that while approximately 5% of pure ceria's oxygen can be reversibly exchanged, this rises to 25-30% for ceria-zirconia mixed oxides. [74]

Doping ceria-zirconia with small amounts of other metals can also improve thermal stability. Li *et al* report a $Ce_{0.67}Zr_{0.33}O_2$ sample doped with 3 wt. % NiO for use as a palladium catalyst support. Upon calcination at 1000°C for four hours, the Pd/nickel-ceria-zirconia material demonstrated improved oxygen storage content compared with undoped Pd/ceria-zirconia. [123]

1.5.2 Ceria-zirconia-other mixed oxides

Ceria-zirconia mixed oxides experience a degree of phase separation at high temperatures, and this is more likely for Zr-rich compositions. [122] Bozo *et al* report that for all Ce-Zr mixed oxides with 16-83 mol % cerium content, strong phase separation

occurs at 1200°C with the emergence of a tetragonal Zr-rich phase on the material surface. [118] Chuang *et al* report phase separation in Ce-Zr mixed oxides at 1100°C, also noting that high-temperature calcination results in a tetragonal, Zr-rich surface phase. They attribute this to zirconium's smaller ionic radius – smaller atoms can diffuse more easily through the fluorite structure, and migrate to the surface to lower the overall surface energy. [124]

Catalytic converter designs somewhat alleviate this problem by physically separating individual Ce-Zr crystallites with alumina. By using alumina particles as a 'diffusion barrier' phase between Ce-Zr particles, the Ce-Zr is prevented from sintering into larger particles, as shown in Figure 10. [75] While it is not entirely clear if this strategy prevents Zr phase separation within particles as well, Morikawa *et al* report that after treatment at 1000°C, oxygen storage capacity decreases for both Ce-Zr and Al/Ce-Zr materials, but is much less significant for the material with incorporated alumina particles. [125]

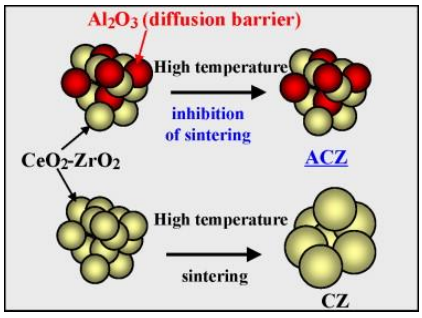

Figure 10. Al_2O_3 diffusion barrier to prevent sintering and preserve oxygen storage capacity of Ce-Zr mixed oxide. Reprinted from Ref. [125] with permission from Elsevier.

In a study by Chang *et al*, Johnson Matthey report an alumina-ceria-zirconia mixed oxide for use as a catalyst support with improved thermal stability and improved oxygen storage capacity. Also making use of the alumina diffusion barrier strategy, they report the deposition of Ce/Zr particles on Al_2O_3 in solution. Compared with mechanically blended Ce/Zr and alumina powders, this material demonstrated a higher thermal stability (both in terms of maintaining surface area and resisting Ce/Zr phase separation) and improved ease of reducibility. This material was developed as a support for a Pd catalyst. [126]

Recently, aluminium-doped Ce-Zr-Al mixed oxides have been reported. Dong *et al* report a $Ce_{0.5}Zr_{0.5-x}Al_xO_y$ solid solution with an improved thermal stability and oxygen storage capacity after 1000°C calcination, compared with pure ceria and $Ce_{0.5}Zr_{0.5}O_2$. Unlike the studies mentioned above, aluminium atoms were directly incorporated into the fluorite lattice structure, demonstrated by XRD patterns only showing ceria peaks with a decreased lattice parameter (proportional to the amount of Al included). [127]

The incorporation of other lanthanides (Y, Nd, Pr, or La) into the crystal lattice has also been shown to improve the lattice stability, 'delaying' phase separation by 100-150 °C. Rohart *et al* report a proprietary synthesis process for Ce-Zr mixed oxides with incorporated La, Nd, or Pr which maintain a single fluorite phase when calcined up to 1100°C, while materials prepared according to a previous synthesis method, or without La, Nd, or Pr doping, experience phase separation at 1000°C. These materials also maintain BET surface areas of 14-23 m^2/g after calcination at 1100°C and up to 6.5 m^2/g after calcination at 1200°C. [128]

1.5.3 Thermally stable PGM-free catalysts

Much of the work discussed in this literature review has been undertaken to develop oxygen storage materials to support PGM catalyst designs, and have only been tested as catalyst supports, not catalyst materials in their own right. Nevertheless, it is also useful for informing future work in developing ceria-based, PGM-free three-way catalysts. Various groups have reported the performance of doped and undoped Ce-Zr mixed oxide materials in CO oxidation, hydrocarbon oxidation, and nitrogen oxide reduction reactions. This will be discussed further in Section 1.6.

As discussed in Sections 1.3.1 and 1.4.1, it is advantageous for ceria-based catalysts to selectively expose ceria's (110) crystal plane for the best performance in oxidative reactions. However, much of the work undertaken on Ce-Zr mixed oxides does not focus on this, as PGM ceria support materials are usually unstructured nanoparticles, with no focus on specific morphology. There is limited work investigating doped Ce-Zr materials

with a structured morphology, compared with the broad range of literature investigating different ceria morphologies.

Xiao *et al* report the synthesis of a mesoporous 'flowerlike' $Ce_{0.9}Zr_{0.1}O_y$ material – these 'flowers' are particles 2 μm in diameter with a surface that has the appearance of tightly packed, wrinkled petals. [73] Zhang *et al* report the synthesis of $Ce_{0.6}Zr_{0.3}Y_{0.1}O_2$ materials with a nanorod, microsphere, micro-'bowknot' or micro-octahedral morphology, dependent on the reaction conditions and surfactant used in an assisted hydrothermal synthesis. However, for all morphologies, the authors determined that the dominant exposed surface was (111), based on lattice spacing measurements from HRTEM images. [129]

1.6 Doped ceria catalyst performance in TWCs

There is a large body of literature regarding the performance of doped, PGM-free ceria materials for catalytic CO oxidation or hydrocarbon oxidation. However, the number of reports that look at doped ceria for nitrogen oxide reduction is much smaller. In a Web of Science search of 'doped ceria catalyst', 93 papers published between 1995 and 2018 were found that examined the performance of PGM-free, doped ceria used as a catalyst (and not catalyst support for a separate metal phase) for at least one TWC reaction. Of these, 71 papers reported results for CO oxidation, 22 for oxidation of hydrocarbons, and 8 for reduction of NO_x. Additionally, only one (Mei Li *et al*) examines the simultaneous TWC performance of doped ceria materials simulated exhaust. [130] A potential reason for this discrepancy may be the difficulty in performing HC oxidation or NO reduction using PGM-free ceria catalysts. Compared with CO oxidation, the HC oxidation and NO reduction reactions in three-way catalysis depend more strongly on the PGM content in catalytic converters. Due to this, much higher light-off temperatures are typically reported for HC oxidation or NO reduction with doped ceria catalysts.

Mei Li *et al* report the doping of $Ce_xZr_{1-x}O_2$ with La, Y, or Pr, and subsequent catalytic activity with varying air-fuel ratios to assess simultaneous CO, hydrocarbon, and NO_x

conversion. [130] Samples were aged at 900°C or above, demonstrating thermal stability. Compared with an undoped $Ce_{0.7}Zr_{0.3}O_2$ sample, ceria-zirconia catalysts doped with Y or La exhibited lower light-off temperatures (up to 28°C lower), and slightly higher conversion rates of CO, HC, and NO_x at 450°C at all the air-fuel ratios tested. A sample simultaneously doped with Y, La, and Pr demonstrated an even lower light-off temperature, but lower reactant conversion rates at 450°C. These results show that Y, La and Pr doping of ceria-zirconia can improve catalytic activity, but obvious improvements compared with traditional PGM-loaded catalysts are not seen, as even the best reported catalyst did not achieve full conversion of reactants at 450°C.

Shanlong Li *et al* report the catalytic performance of a Cu-doped ceria porous nanostructure for both CO oxidation and NO reduction in the presence of CO. However, these reactions are examined separately and simultaneous CO oxidation/NO reduction activity is not reported. Their catalyst demonstrated very good CO oxidative activity; with a T_{10} value of 50°C and full conversion by 110°C. For the reduction of NO in the presence of CO, activity was poorer, with full conversion not reached until 450°C. [131]

Other than this, papers for doped ceria catalytic activity generally examine single-reaction performance. This area of literature is somewhat lacking, as simultaneous TWC catalytic assessment with simulated exhaust is commonly reported for PGM-loaded ceria materials (and ceria loaded with other metal particles). [132–134]

1.6.1 Doped ceria: CO oxidation

CO oxidation is the most commonly tested TWC reaction for literature reporting doped ceria catalysts. These papers cover a wide variety of dopants, morphology (nanoscale or otherwise), and synthesis methods. While examining the details of every single paper goes beyond the scope of this report, some general trends can be drawn from the collated results.

Shown below in Figure 11 is a graph of T_{10} values (temperature at which 10% conversion of CO to CO_2 is achieved) vs. dopant Pauling electronegativity for single-dopant ceria

catalysts. A lower T_{10} value means a catalyst has higher activity at lower temperatures. Each point represents the best reported value for ceria doped with that element. [48,71,73,135–145] While there is a loose correlation between higher electronegativity values and lower T_{10} values, the R-squared value is below 0.5. It should be noted that large differences in preparation methods and experimental parameters can account for much of the difference in reported catalyst performance. Nevertheless, these results may support the relationship between electronegativity and dopant effectiveness proposed by Liu *et al*, discussed in Section 1.3.2, as well as trends in ionic radius identified by Krcha *et al* and Nolan. [68,70,71,146,147] In general, lanthanide-doped ceria materials were less effective at improving CO oxidative activity, while transition metal-doped ceria showed more significant improvement. This is in agreement with the DFT study by Gupta *et al* discussed in Section 1.3.2. [55]

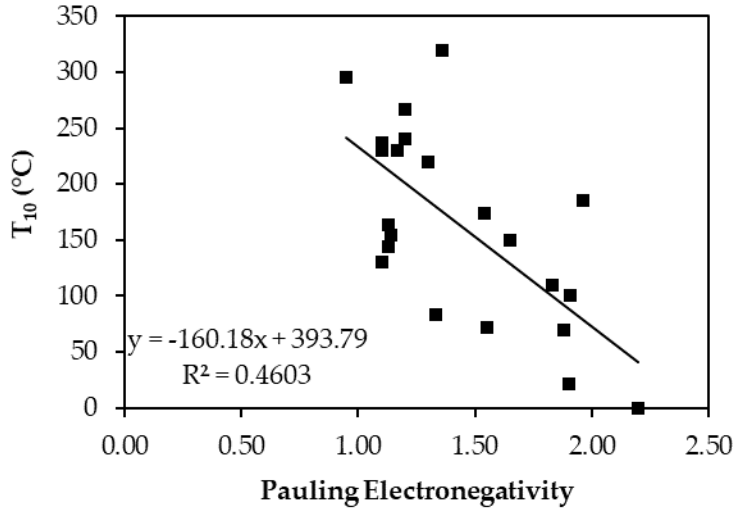

Figure 11. CO oxidation T_{10} values vs. Pauling electronegativity for various single-dopant ceria compounds, showing the best T_{10} value reported in literature for each dopant.

It should be noted that these results come from papers that use different synthesis techniques and calcination temperatures and products with a wide range of morphologies. A further drawback of making comparisons across several papers like this is that the catalyst test conditions are not always very directly comparable. Different research groups will use widely differing CO flowrates, CO/O_2 ratios, catalyst loadings, and catalyst bed configurations. While it is better to directly compare the turnover frequency (s^{-1}) or rate (mol g^{-1} s^{-1}) of catalyst samples, which will show the quantity of

converted reactant per mass of catalyst or number of active sites, papers often do not report enough experimental data to calculate this. Therefore, direct comparisons are often not possible, with the exception of materials made by the same research group using the same experimental conditions.

Widely varying results have been reported for the same dopants. For instance, ceria materials doped with lanthanides such as La, Gd, or Pr are commonly reported to demonstrate decreased catalytic activity for CO oxidation compared with undoped ceria [148–151], while other reports show improved activity. [136,152,153] Venkataswamy *et al* report a comparison of sol-gel, coprecipitation, and hydrothermal synthesis methods for the production of Mn-doped ceria nanoparticles, with widely varying results. They report that the hydrothermal synthesis resulted in a final Mn-doped ceria catalyst with smaller pores, a larger surface area, and higher surface concentration of reduced Ce^{3+} than catalysts produced via sol-gel or coprecipitation methods with the same quantity of Mn. Regarding CO oxidation, the hydrothermally synthesised material demonstrated a T_{10} value of 290 °C, compared with 347 and 371 °C for the sol-gel and coprecipitation synthesis products, respectively. [154]

Several papers report the comparison of catalyst performance after calcination at two different temperatures, generally 500 °C and 800 °C. Ceria doped with Zr, La, Eu, Sm, Mn, Fe, La, and Tb have been reported by Reddy *et al* and Katta *et al* with an average performance reduction (in terms of T_{10}) of approximately 18% when calcined at the higher temperature. [135,148,155–160]

1.6.2 Doped ceria: hydrocarbon oxidation

Fewer dopants and ceria morphologies have been reported for doped ceria catalysts tested for hydrocarbon oxidation in comparison with CO oxidation catalytic activity. Furthermore, a wide range of model hydrocarbons are used, meaning results are often not comparable. Ceria-catalysed oxidation reactions of methane, ethane, ethene, propane, propene, butane, hexane, benzene, toluene, naphthalene, methanol, and acetone have all been reported. [161–169]

The best T_{10} results per dopant for the more commonly reported reactants, methane and propane, are shown below in Figure 12. [138,161,163,170–174] However, these results are much less comprehensive than the CO oxidation T_{10} results shown in Figure 11. Unlike the CO oxidation results, many of the dopants shown here are only reported in one or two papers, and often only a single dopant level is reported. As it is unlikely that many of the reported materials have optimised dopant levels, these results should be considered preliminary. Because of this, while it appears that, as with CO oxidation, dopant electronegativity appears to (at least weakly) correlate with lower T_{10} values, more experimental results should be published to support this.

In certain cases, dopants reduced HC oxidative activity in comparison with identically prepared pure ceria materials. Zhao *et al* report that Sm-doped ceria performs more poorly than pure ceria for the oxidation of n-butane. For the oxidation of methane, the results were more ambiguous – Sm-doped ceria had a higher T_{10} value but lower T_{50} and T_{90} values. [170] This matches the trends identified in previous sections – as a lanthanide, Sm is much less electronegative than most of the dopants reported.

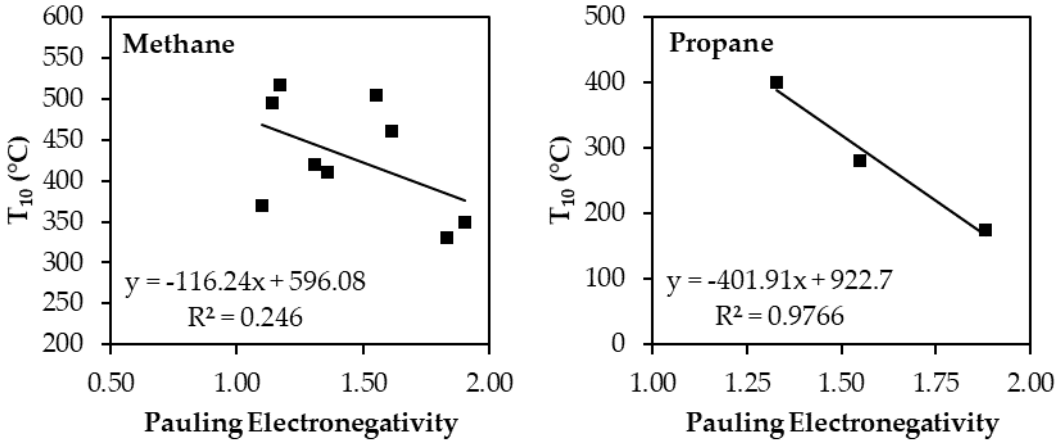

Figure 12. Methane (left) and propane (right) T_{10} values vs. Pauling electronegativity for various single-dopant ceria materials, showing the best T_{10} value reported in literature for each dopant.

1.6.3 Doped ceria: NO_x reduction

Only eight papers were found that report testing PGM-free doped ceria for nitrogen oxide reduction. [131,171,175–180] Similarly to CO and HC oxidation, the best results are shown (T_{10} vs. electronegativity) in Figure 13. Results here are very limited - nevertheless, some preliminary trends may be identified.

Interestingly, the same trend of improved catalytic activity for dopants with higher electronegativity is seen, as with CO and HC oxidation. This was not necessarily an expected result, as it has been proposed that improving oxidative activity in a catalyst material may be associated with reduced performance in reduction reactions. [113] The best-performing dopants for NO_x reduction – Sn, Mn, and Cu, have also been previously shown to improve oxidative activity in ceria, meaning that catalytic activity for both reactions can simultaneously be improved with the same dopant.

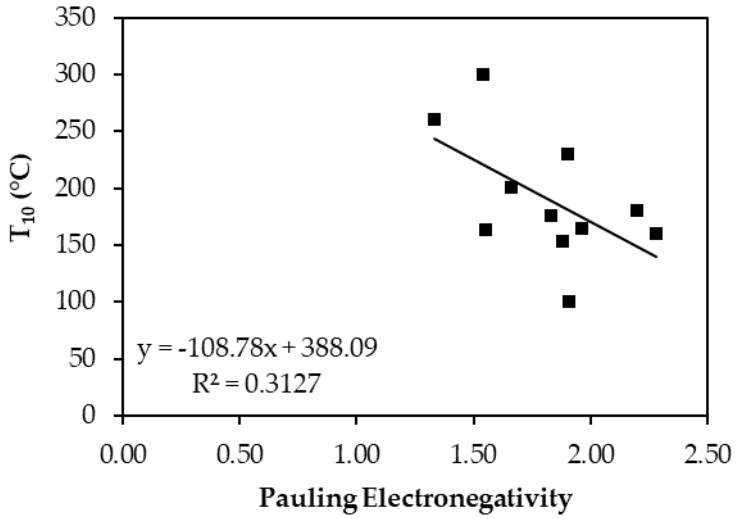

Figure 13. NO_x reduction T_{10} values vs. Pauling electronegativity for various single-dopant ceria materials, showing the best T_{10} value reported in literature for each dopant.

Overall, the reported catalysts generally required higher temperatures to achieve acceptable conversion rates for removal of NO_x, compared with CO oxidation.

1.7 Current state of literature and further investigation

While the available literature concerning ceria-based materials for three-way catalysis is extensive, there are still many areas which would benefit from further investigation.

The present-day understanding of how ceria crystal planes affect catalytic performance is fairly comprehensive. Both the reported computational and experimental literature is in general agreement that the (110) ceria surface aids in oxidation reactions, and that morphologies that selectively expose this surface, such as nanorods, show higher catalytic activity for oxidation reactions. However, while the surface chemistry has been well-investigated computationally for nitrogen oxide reduction, this area is lacking in experimental data.

A wide range of lanthanides, transition metals, and other elements have been reported as successful ceria dopants, and many have been catalytically tested, at least for CO oxidation. General trends in dopant properties have been identified – however, a more complete understanding that could guide ceria-based catalyst design is still lacking. More work is needed, particularly a focus on reactions beyond CO oxidation. There are fewer papers that report hydrocarbon oxidation compared with CO oxidation papers, and fewer still for the reduction of nitrogen oxides with PGM-free doped ceria catalysts. Furthermore, as with research into PGM- or precious metal-loaded ceria catalyst supports, more experimental work should be conducted using simulated exhaust streams to assess simultaneous three-way catalytic activity.

Thermal stability of ceria-based catalysts is another area which should be studied more. Many papers reporting catalytic performance only include a 500-600°C calcination step Occasionally calcination at 800°C is included for comparison. While this is useful, much more research is necessary in this area, and at higher temperatures, to gain a better understanding of how these materials will behave when exposed to 'real-world' high-temperature conditions.

Ceria-based catalysts show great promise as a replacement three-way catalyst technology. Materials have been reported that show a significantly improved light-off temperature (at least for CO oxidation) that also eliminate or reduce dependence on platinum group and other precious metals. Moving forward, experimentally demonstrating improved thermal stability and simultaneous three-way catalytic performance will be vital in improving the sustainability and performance of PGM-based catalysts.

Chapter 2

Literature Review – TWC Washcoats and PGM Loading

The following work has been adapted from the accepted manuscript of the literature review titled "Recent Advances in Gasoline Three-Way Catalyst Formulation – A Review".

2.1 Commentary

This chapter contains a review of recent published automotive catalyst literature, with a focus on washcoat formulations for gasoline three-way catalysts. The purpose of this literature review was to identify options for improving low-temperature reactivity of catalytic converters to reduce light-off times and thus lower overall vehicle emission during testing. Reducing the light-off time and improving low-temperature performance is important because a large percentage of total pollutant emissions during vehicle testing occur during the first few minutes after a cold start. [10] This work has been used to guide research into new catalyst washcoat formulations to develop improved three-way catalyst designs.

The literature review is divided into three main sections. First, variations in washcoat composition are considered. Typically, three-way catalyst washcoats are predominantly synthesised from alumina, ceria, and zirconia, with additional promoters such as barium and lanthanides included to improve performance or stability. [181] An unlimited number of possible material variations exist, so recent literature on this topic is reviewed to identify the best formulations and ratios, in terms of light-off temperature. The inclusion of zeolites in washcoat compositions as a low-temperature trap for hydrocarbons and NO_x is also briefly examined. Second, PGM catalyst loading rates and ratios are reviewed. Modern TWC designs often utilise a Pt/Rd or Pd/Rd formulation,

with cost and performance both dictating the choice in elements. [6] The performance of bimetallic alloys and the inclusion of Ir are also examined in this section. Third, the design of monoliths – cordierite, metallic, and extruded zeolite – is briefly reviewed.

2.2 Statement of Authorship

<table>
<tr><td colspan="10">This declaration concerns the article entitled:</td></tr>
<tr><td colspan="10">Recent Advances in Gasoline Three-Way Catalyst Formulation – A Review</td></tr>
<tr><td colspan="10">Publication status</td></tr>
<tr><td>Draft manuscript</td><td></td><td>Submitted</td><td></td><td>In review</td><td></td><td>Accepted</td><td></td><td>Published</td><td>✓</td></tr>
<tr><td>Publication details</td><td colspan="9">S. Rood, S. Eslava, A. Manigrasso, C. Bannister, Recent advances in gasoline three-way catalyst formulation: A review, Proceedings of the Institution of Mechanical Engineers, Part D: Journal of Automobile Engineering. (2019) doi:10.1177/0954407019859822.</td></tr>
<tr><td>Candidate's contribution to the paper</td><td colspan="9">The candidate contributed to/ considerably contributed to/predominantly executed the…

Formulation of ideas (25 %):
All authors contributed.

Design of methodology (50 %):
Chris Bannister and Shawn Rood identified the areas of research to cover and developed an outline to guide the literature search.

Experimental work (100 %):
Shawn Rood conducted the literature search and gathered experimental data from the papers cited.

Presentation of data in journal format (95 %):
This manuscript and the tables presented in its appendices were written by Shawn Rood.</td></tr>
<tr><td>Statement from Candidate</td><td colspan="9">This paper reports on original research I conducted during the period of my Higher Degree by Research candidature.</td></tr>
<tr><td>Signed</td><td colspan="5"></td><td>Date</td><td colspan="3"></td></tr>
</table>

2.3 Article

2.3.1 Abstract

Development of three-way catalyst (TWC) technology has been critical in maintaining air quality regulations for gasoline engines via the conversion of pollutants from the internal combustion engine exhaust. The development of improved TWC formulations is an important challenge for automotive industry. Indeed, in order to meet increasingly stringent environmental regulations around the world, the development of more efficient catalysts depends on a complete understanding of the many parameters related to TWC design. In this review paper, some of these parameters are examined in relation to TWC performance, and especially low temperature activation performance, with a focus on more recently published work. In particular, washcoat composition, platinum group metal ratios and loading, and substrate design are considered. The effect of these parameters with regard to the conversion efficiency of carbon monoxide, unburned hydrocarbons, and nitrogen oxides pollutants is summarised.

2.3.2 Introduction

Global air pollution caused by human activities and industries has been a major public health concern, particularly in urban areas. The impact to health services and society at large is significant, and the majority of cities worldwide do not meet World Health Organization (WHO) air quality guidelines. [2,5] Recognition of this problem led to the introduction of legislations controlling and imposing limitations on pollutant emissions at the exhaust of vehicles. These legislations led to the development of catalytic converter technology in the 1970s to control and treat these pollutants. While gasoline engine exhaust composition can vary based on design and driving conditions, typical operating conditions are 0.5 vol. % CO, 3500 ppm HC, 900 ppm NO_x, 0.17 vol. % H_2, 10 vol. % H_2O, 10 vol. % CO_2, 0.5 vol. % O_2, and the balance N_2. [182] Initially, Pt/Pd or Pt/Rh oxidation catalysts were developed to limit hydrocarbon and carbon monoxide emissions, later developing into three-way catalysts (TWCs) which also convert NO_x emissions. [6]

While carbon monoxide levels are controlled because of its very high toxicity, hydrocarbons and NOx are dangerous because they react to form photochemical smog in the presence of sunlight:

$$\mathrm{HC} + \mathrm{NO}_x + h\nu \rightarrow \mathrm{O}_3 + \text{other} \quad (9)$$

Satisfactory emission control is achieved within a three-way catalyst via the simultaneous oxidation of carbon monoxide and hydrocarbons to carbon dioxide and water, and the reduction of nitrogen oxides to nitrogen gas. [6] However, other reactions, such as the water-gas shift reaction or reaction of pollutants with water or hydrogen, can occur as well. [182]

$$2\mathrm{CO} + \mathrm{O}_2 \rightarrow 2\mathrm{CO}_2 \quad (10)$$

$$\mathrm{C}_x\mathrm{H}_y + \mathrm{O}_2 \rightarrow \mathrm{CO}_2 + \mathrm{H}_2\mathrm{O} \quad (11)$$

$$2\mathrm{NO} \rightarrow \mathrm{O}_2 + \mathrm{N}_2 \quad (12)$$

Three-way catalyst design consists of a monolith substrate, high surface area washcoat with oxygen storage promoter materials, the active catalyst (platinum-group metals, or PGMs), and promoter materials. The substrate has a honeycomb structure and is usually made from cordierite, but metallic foil substrates have been developed as well. The washcoat contains a doped alumina-based material (Al_2O_3) due to its high surface area and good thermal stability and resistance to sintering. Ceria (CeO_2) or ceria-based materials are used as a promoter due to ceria's oxygen storage capacity (OSC). Without any OSC function, the ratio of oxygen to fuel needs to be tightly controlled with a specific stoichiometric ratio to achieve the best conversion rates, typically an air-to-fuel ratio of 14.7:1 (Figure 14). [181,182] This is because while CO and hydrocarbons are converted to CO_2 under oxidising conditions, the reduction of NO_x to N_2 only shows good conversion efficiency under reducing conditions. However, cerium ions can easily switch between 3+ and 4+ oxidation states via the creation and regeneration of oxygen vacancies, which allows the ceria-containing catalyst material to store oxygen from the exhaust stream when it is in stoichiometric excess, promoting conversion of NO_x, as well as release oxygen to the exhaust stream when it is deficient, promoting conversion of CO and

hydrocarbons to CO_2. This expands the air-to-fuel ratio 'window' under which acceptable catalyst performance is achieved for all three reactants. [82] Typically, a CeO_2-ZrO_2 blend is used to improve thermal stability. Pt or Pd are used as the active phase, with Rh included for the reduction of NO_x to N_2.

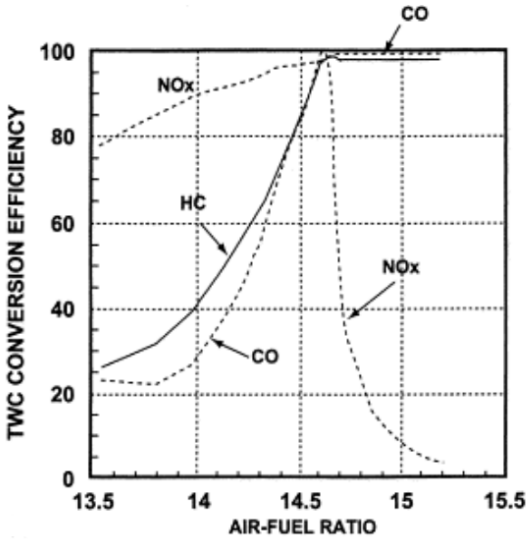

Figure 14. Three-way catalyst performance in terms of CO, HC, and NO_x performance as a function of air/fuel ratio. Reproduced from Ref. [183] with permission from Elsevier.

In addition to promoting reducibility, ceria stabilises the noble metal catalysts in a dispersed state, hindering sintering at high temperatures via the formation of oxidised Pt-O-Ce bonds in presence of oxygen. Because cerium can easily cycle between oxidation states, it allows the Pt to return to a more catalytically active metallic state during stoichiometric conditions (Figure 15). In contrast, a similar mechanism does not exist for Pt/alumina systems. [184]

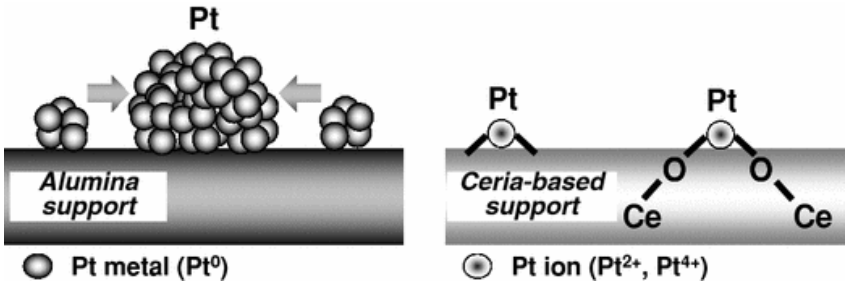

Figure 15. Sintering inhibition on Pt/ceria compared with Pt/alumina support. Reproduced from Ref. [184] with permission from Springer.

A significant shortcoming in modern TWC design is cold-start performance during the initial minutes of a vehicle journey. TWCs depend on the elevated temperatures provided by the engine exhaust to operate with satisfactory conversion rates. During this start-up period, the low engine exhaust temperature (typically <250 °C) only slowly raises the temperature of the catalyst itself. [8] However, good conversions are typically only achieved at temperatures > 300 °C. [115] Cold-start emissions can account for a high proportion of total trip emissions – sometimes up to 50% in urban areas where shorter trips are the norm. [10,185] Therefore, strategies to either enhance low-temperature catalytic performance or heat the three-way catalyst more quickly will have the largest impact on improving overall TWC performance.

The focus of this review will be on the design of three-way catalysts to enhance light-off temperatures and low-temperature catalytic performance. In particular, the effect of washcoat composition, precious metal catalyst loading (Pt, Pd, and/or Rh), and substrate design will be examined.

2.3.3 Washcoat composition

Alumina (Al_2O_3) is the main material in most TWC washcoat formulations due to its stability at high temperatures. A ceria (CeO_2)-based material is typically dispersed over or incorporated into the alumina layer to provide oxygen storage capacity to the TWC, enhancing conversion rates. Generally, a ceria-zirconia (CeO_2-ZrO_2) solid solution is used instead of pure ceria – the inclusion of zirconium ions into ceria's crystal lattice can enhance the material's oxygen storage capacity and improve thermal stability. [115] This is important because TWCs can be exposed to extremely high temperatures (800-1000 °C) for extended periods of time. Exposure of ceria to these temperatures leads to severe sintering phenomena. This can cause a number of issues that affect TWC performance: loss of surface area, loss of available reactive oxygen within the ceria lattice, further sintering of the active metal catalyst, and reduction in contact area between the ceria and alumina washcoat. However, using ceria-zirconia somewhat mitigates these issues. Additionally, the 'controlled deposition' of ceria-zirconia onto alumina can prevent its transformation from high surface area γ-alumina to its low surface area α form. [181,182]

Thermal stability of TWC materials can be further improved by the addition of other 'promoter' elements, such as alkaline earth metals or any of the trivalent rare earth metals. [186] While $Ce_xZr_{1-x}O_2$ solid solutions with a composition of x = 0.4-0.6 have been shown to have good OSC values compared with other Ce/Zr ratios, these materials also undergo phase separation after long-term (>100 h) aging at 1000 °C. However, the introduction of trivalent rare earth metals (Y, La, Pr, Nd) can stabilise the material – resulting in an improved surface area and higher OSC value after long-term aging. Dopants can also improve ceria's oxygen storage capacity. [187]

The type of oxide support can influence the oxidation state and dispersion of Pt, Pd, or Rh catalysts, and thus affect performance. This can inform which washcoat layer a particular metal catalyst will be deposited onto. For instance, ceria and titania supports improve the reducibility of Pd particles to form metallic Pd, which generally provides better low-temperature performance than Pd/Al_2O_3. [188] On the other hand, Rh has the potential to interact too strongly with Ce-rich supports, forming Rh-O-Ce bonds. ZrO_2 has been reported as a more beneficial support for preserving catalytically active metallic Rh after aging in air. [189]

Below, various aspects of washcoat composition are discussed, and results from literature are summarised in Table A11 in the Appendix. Results are shown in terms of light-off temperature (T_{10} and/or T_{50}) for conversion of CO, HCs, and NO_x. T_{10} and T_{50} are defined as the temperatures at which 10% and 50% conversion are achieved, respectively. Experimental parameters are summarised in Table A12 in the Appendix, with select values shown in Figure 16.

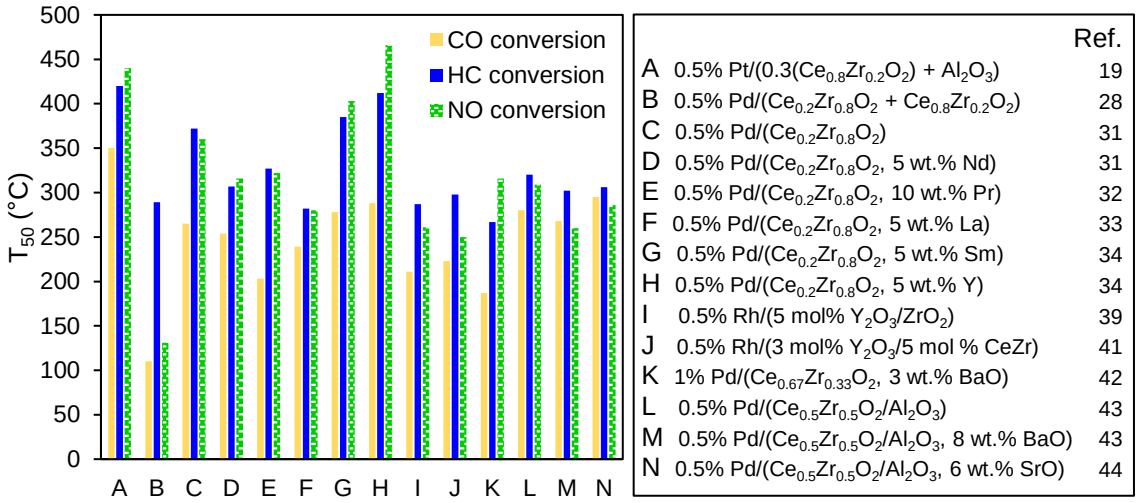

Figure 16. Select T_{50} values of CO oxidation, hydrocarbon oxidation, and NO reduction for catalysts with various washcoat compositions.

Addition of ceria-zirconia to washcoat

Compared with pure alumina washcoats, ceria-zirconia shows many improvements for three-way catalysis. Lang *et al* examined the effect of using either CeO_2-ZrO_2 or Al_2O_3 as a support material for a Pd catalyst, finding that for CO oxidation, the Ce-Zr catalyst showed clear improvements in terms of light-off temperature. [190] For HC oxidation, while light-off performance was similar, the Ce-Zr catalyst was able to achieve full conversion at a lower temperature than the alumina catalyst. Zheng *et al* performed a similar study, using commercial BASF washcoat materials and a Rh-based catalyst. [191] They found that Rh and alumina had strong metal-support interactions, leading to the formation of rhodium aluminate and catalyst deactivation, while Rh-CeZr interactions were weaker and more reversible, allowing the Rh to remain in its catalytically active Rh^0 state. For both metals, deposition on CeZr was advantageous compared with deposition on Al_2O_3 due to prevalence of oxygen vacancies (Figure 17). Because CeZr can create oxygen vacancies by releasing oxygen from its lattice structure, it can quickly provide this oxygen to react with CO and hydrocarbons, allowing them to oxidize to CO_2. In contrast, Al_2O_3 does not have the capability to generate oxygen vacancies, so reactions proceed more slowly by reacting directly with oxygen adsorbed on the surface of Pd.

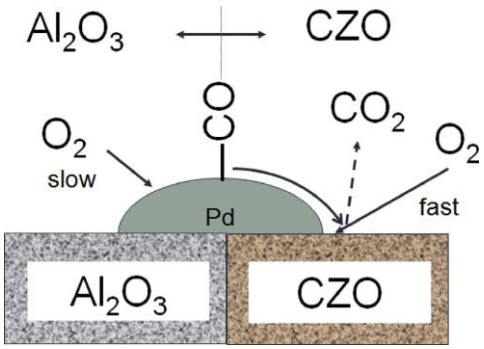

Figure 17. Oxidation of CO on Pd/Al_2O_3 vs. Pd/CeO_2-ZrO_2. Reproduced from Ref. [190] with permission from Elsevier.

Ozawa *et al* looked at modification of alumina with ceria, producing three catalysts: Pt/Al_2O_3, $Pt/(CeO_2+Al_2O_3)$, and $Pt/(Ce_{0.8}Zr_{0.2}O_2+Al_2O_3)$. [192] Here, the incorporation of ceria and zirconia into the washcoat material improved light-off performance for HC and NO oxidation. The ceria-zirconia both inhibited sintering of Pt and provided additional OSC. While this study looked at the addition of CeZr materials to already-synthesised alumina, Chen and Chang developed a novel $Al_2O_3/CeO_2/ZrO_2$ mixed oxide material, in which Ce, Zr, and Al precursor materials were simultaneously coprecipitated into a single material. [193] This was compared as a washcoat material for a Pd-based catalyst with a more traditional CeO_2/ZrO_2 mixed oxide physically blended with Al_2O_3. They found that the $Al_2O_3/CeO_2/ZrO_2$ washcoat was more thermally stable – inhibiting sintering of both the Pd particles and the ceria-zirconia component of the washcoat, which improved low-temperature catalytic performance. In a 'real-world' test, Chen and Chang attached the catalysts to a 3.5 L GTDI engine on a 2010 model vehicle with low-temperature exhaust. Here, while both materials showed similar performance for NO_x removal, the $Al_2O_3/CeO_2/ZrO_2$ was superior in terms of HC conversion.

The choice of where to deposit PGM catalysts on the washcoat can have a significant influence on TWC performance. Yamamoto and Tanaka explored this by designing a TWC containing both Al_2O_3 and a CeZr component, but only depositing Pd particles on either the alumina or ceria-zirconia, not both. [194] They found that under static operating conditions, the Pd-Al_2O_3 catalyst performed better due to improved dispersion of Pd particles on the washcoat, but under dynamic conditions (more realistic – with fluctuating

concentrations of O_2, H_2, and CO), the Pd-CeZr catalyst showed better performance because it had enhanced resistance to sintering.

Ceria-zirconia ratio

Many different ceria-zirconia ratios have been employed in TWC designs. [75,195] In the first generation of CeZr-based washcoat materials developed in the late 1980s, Zr was introduced in quantities up to 20 mol % to provide thermal stability. This limitation was due to the chosen production method – impregnation of already-synthesised ceria powders in an aqueous zirconium nitrate solution. Several years later, second-generation CeZr materials were developed in which any molar ratio of ceria and zirconia could form nearly perfect solid solutions. In 1998, third-generation alumina-ceria-zirconia materials were developed, using Al_2O_3 particles interspersed amongst CeZr particles to inhibit sintering (Figure 18). This design uses the more thermally stable Al_2O_3 particles as a 'diffusion barrier' between CeZr particles, preventing them from sintering and agglomerating into larger particles at high temperatures. This preserves the oxygen storage capacity of the washcoat material, which would otherwise decrease with sintering and loss of surface area upon high temperature exposure.

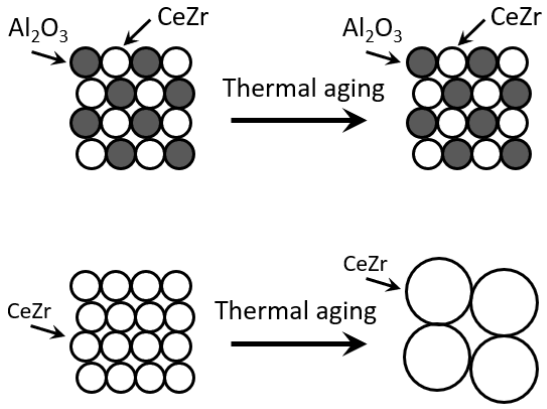

Figure 18. Sintering behaviour of CeZr and CeZr/Al_2O_3 particles upon aging.

Typically ceria-zirconia materials with approximately 40-60% ceria content are considered to have the highest OSC, and thus enhanced catalyst performance. [186,196] Priya *et* al find that $Ce_{0.6}Zr_{0.4}O_2$ has the highest OSC, while Madier *et al* report that

$Ce_{0.63}Zr_{0.37}O_2$ has the highest OSC. [197,198] In a more complex mixed oxide experiment, Priya *et al* also synthesised a series of $Ce_{0.6}Zr_{(0.4-x)}Al_{1.3x}O_2$ oxides (x = 0, 0.1, 0.2, 0.3, and 0.4), finding that $Ce_{0.6}Zr_{0.2}Al_{0.26}O_2$ had the highest oxygen storage capacity. [199]

However, such materials can undergo phase separation into separate Ce-rich and Zr-rich particles at high temperatures. Lan *et al* examined this phenomenon by synthesising $Ce_{0.2}Zr_{0.8}O_2$, $Ce_{0.5}Zr_{0.5}O_2$, $Ce_{0.8}Zr_{0.8}O_2$, and a physical mixture of $Ce_{0.2}Zr_{0.8}O_2$+$Ce_{0.8}Zr_{0.2}O_2$, as a support for a Pd-based TWC. [200] They found that using a physical mixture of Ce-rich and Zr-rich particles from the beginning was advantageous compared with the 50-50 CeZr material (which would separate into Ce-rich and Zr-rich phases anyway). This material contained numerous interfacial boundaries between different crystallites, which both hindered high-temperature sintering and provided more lattice defects, improving OSC.

Other design considerations can inform Ce-Zr ratio choice as well. For instance, while materials with higher Ce levels can store and release the most oxygen, they do so more slowly than Zr-rich materials, which release smaller amounts of oxygen, but more quickly. Aoki *et al* proposed a system in which the front half of a TWC contains a Zr-rich washcoat and the rear half a Ce-rich formulation. [201]

Rare earth and alkaline metal promoters

In addition to Ce, Zr, and Al, rare earth and alkaline earth metals are often used as promoters to further improve OSC and thermal stability. Guo *et al* synthesised a series of $Ce_{0.35}Zr_{(0.65-x)}Nd_xO_2$ supports for use with a Pt-Rh catalyst. [202] The inclusion of Nd in the washcoat improved OSC and catalytic activity up to 15 mol % Nd – with higher levels of Nd, performance declined. $Ce_{0.35}Zr_{0.5}Nd_{0.15}O_2$ was shown to be the best-performing washcoat material out of those tested.

Wang *et al* examined the addition of Nd, Pr, La, Sm, or Y dopants in a Zr-rich Pd/$Ce_{0.2}Zr_{0.8}O_2$ catalyst (3-10 wt. % dopant levels). [203–206] In agreement with Guo *et al*, Nd improved catalyst performance, although here 5% Nd-$Ce_{0.2}Zr_{0.8}O_2$ was the washcoat

material with the best low-temperature performance. The addition of La (5 wt. %) and Pr (8-10 wt. %) also improved catalytic activity, but Sm and Y-doped catalysts performed poorly, resulting in higher light-off temperatures than the undoped Pd/CeZr catalyst. Of the materials examined in these studies, the Pr-doped Pt/CeZr catalyst showed the best performance – with fresh catalyst light-off temperatures (T_{50}) of 152, 200, 174, and 157 °C for CO, HC, NO, and NO_2 removal, respectively. After calcination at 1100 °C for 4 h, light-off temperatures were 203, 332, 336, and 203 °C for CO, HC, NO, and NO_2, respectively.

The same group also examined the same dopants for a Ce-rich Pd/$Ce_{0.67}Zr_{0.33}O_2$ catalyst (molar ratio of dopant to Ce – 1:8). [207] All dopants improved catalytic activity compared to the undoped Pd/CeZr, due to improved interactions between PdO and the catalyst support. Out of the five dopants, Pr and Nd showed the best low-temperature activity. This was attributed to a more homogeneous solid solution being formed, compared with the La, Sm, or Y-doped materials. The T_{50} of aged catalysts was as low as 267 °C for HC oxidation, 267 °C for NO reduction, and 186 °C for NO_2 reduction (Figure 19).

Zhou *et al* also looked at the effect of Y, Nd, and Pr dopants, synthesising a series of Pd/(0.4CeO_2/0.5ZrO_2/0.05La_2O_3/0.05M) catalysts (M = Y_2O_3, Nd_2O_3, or Pr_2O_3). [208] Light-off temperatures achieved were slightly higher than those reported for the ceria-rich Nd- or Pr-containing catalysts of Wang *et al*, despite a higher Pd loading (1 wt. % vs. 0.5 wt. %). This is potentially due to higher zirconia content reducing OSC in the washcoat material.

The effect of Y or La dopants on a Pt+Rh/CeO_2-ZrO_2-M_xO_y/(3 wt. % La_2O_3/Al_2O_3) catalyst was investigated by Jiaxiu *et al*. [209] The catalysts were hydrothermally aged for 5 h at 1000 °C. In agreement with Wang *et al*'s study on Ce-rich washcoat materials, both dopants improve metal dispersion and low-temperature catalyst performance, particularly after aging. This study shows that the beneficial effect of rare earth dopants is maintained even with alumina included in the washcoat composition.

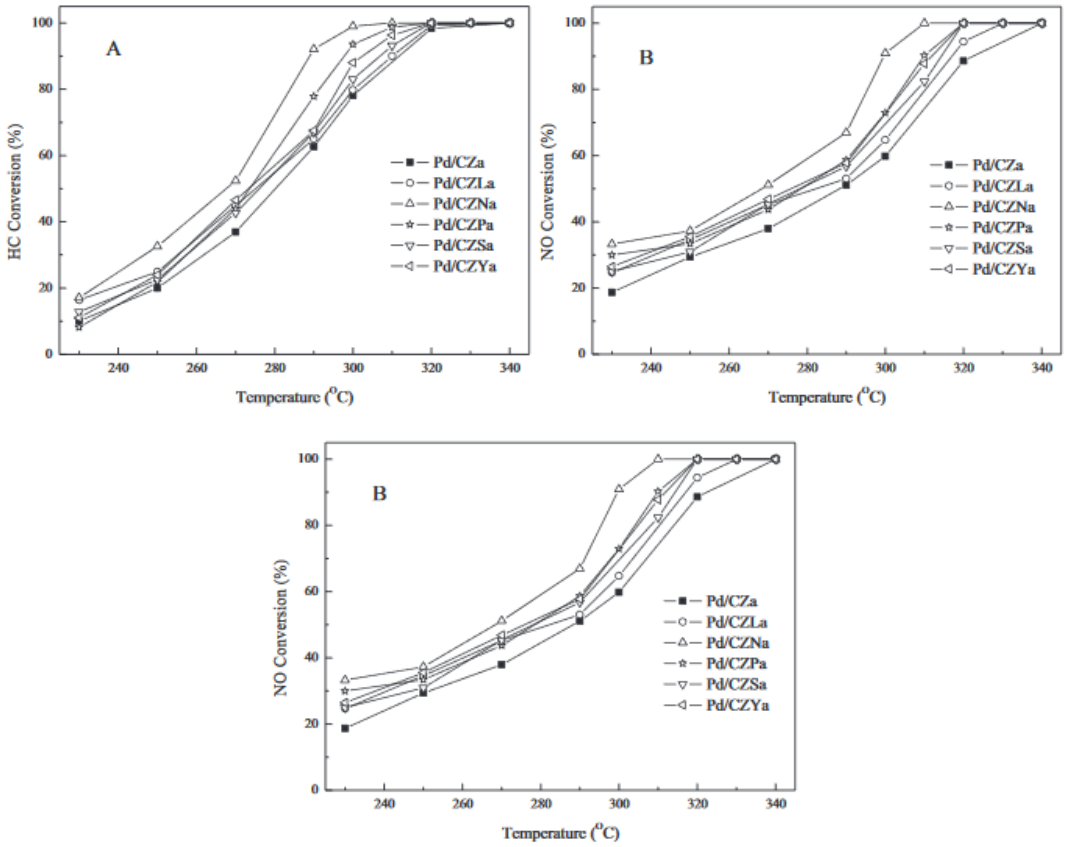

Figure 19. Conversion rates of HC, NO, and NO_2 for aged Pd/CeZrM catalysts (M = Nd, Pr, La, Sm, Y) under stoichiometric conditions. Reproduced from Ref. [207] with permission from Elsevier.

In a similar study, Papavasiliou *et al* compared the performance of a $Pt/Al_2O_3/Ce_{0.4}Zr_{0.5}La_{0.1}O_{1.95}$ catalyst with a commercial Pt-Rh TWC. [210] The synthesised catalyst had a Pt loading of 0.5 wt. %, while the commercial catalyst's metal loading was 2.25 wt. %. In this study, two versions of synthetic exhaust were used – one without H_2O and CO_2, as is often reported in the literature, and one with 10% each H_2O and CO_2 to simulate a more realistic 'real-world' exhaust. For the experiment including H_2O and CO_2, the synthesised Pt/AlCeZrLa catalyst showed better low-temperature performance than the commercial catalyst, despite a much lower metal loading. However, the opposite was true for the experiment without H_2O and CO_2 in the exhaust stream, underlining the need to make such experiments mirror real-world conditions as closely as possible (Figure 20).

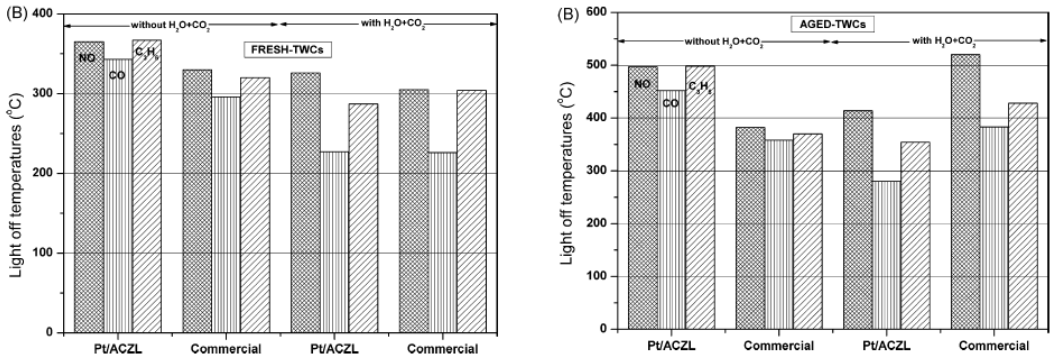

Figure 20. Light-off temperatures (T_{50}) of fresh and aged Pt/Al-Ce-Zr-La and commercial catalysts, under simulated exhaust conditions (with or without H_2O and CO_2). Reproduced from Ref. [210] with permission from Elsevier.

Zirconia-based oxides can be used to support Rh particles to avoid unfavourable interactions between Rh and ceria. Haneda *et al* examined the use of 5 mol % doped ZrO_2 as a support for a Rh catalyst. [211,212] La, Pr, Nd, Y, Ce, Sm, Gd, Tb, and Dy were chosen as potential dopants. In contrast to the ceria-based formulations discussed above, Haneda *et al* report that the inclusion of La, Pr, and Nd reduce catalyst performance for the Rh/ZrO_2 system. However, Y, Ce, Sm, Gd, Tb, and Dy improve catalytic activity. The best-performing catalyst support was Y-doped ZrO_2. The level of improvement compared with undoped Pd/ZrO_2 was correlated with the level of Rh dispersion. In particular, Rh interactions with Y_2O_3 helped stabilise the Rh particles in a dispersed state and prevent sintering, thus improving catalytic activity. Haneda *et al* have also reported that adding 5 mol % CeO_2 to the $Rh/Y\text{-}ZrO_2$ catalyst system further improves performance due to enhanced catalyst reducibility. [213] However, higher levels of Ce reduce performance by allowing for excessively strong Rh-ceria interactions which create stable, inactive oxidised Rh particles.

Yang *et al* and Lan *et al* looked at the addition of BaO to $Pd/CeO_2\text{-}ZrO_2$ and $Pd/CeO_2\text{-}ZrO_2\text{-}Al_2O_3$, respectively. [214,215] Yang *et al* found that it was possible to synthesise a homogeneous single-phase Ce/Zr/Ba solid solution with enhanced reducibility. For catalysts aged in air for 4h at 1100 °C, the 5 mol % BaO catalyst showed the best performance for HC and NO removal. However, CO oxidation was negatively impacted due to the Ba doping inhibiting Pd-CO interactions, which decreased the number of active sites for CO oxidation on the catalyst surface. Including alumina in the

washcoat composition, Lan *et al* found that with lower (4-6 wt. %) BaO levels, the Ba would preferentially combine with Al_2O_3, acting as a stabiliser. At 8 wt. % BaO, some of the Ba enters the Ce/Zr phase, forming a solid solution with enhanced oxygen mobility, reducibility, and thermal stability. However, at 10 wt. % and above, segregation of a separate BaO phase occurs, which distorts the catalyst's physical structure and has a negative impact on catalytic activity. 8 wt. % was determined to be the ideal BaO level in the Pd/CeO_2-ZrO_2-Al_2O_3 system.

Lan *et al* also looked at the impact of incorporating SrO into a similar Pd/CeO_2-ZrO_2-Al_2O_3 TWC. [216] Similarly to BaO, SrO strongly interacts with the alumina phase to improve thermal stability. A two-phase $Ce_{0.5}Zr_{0.5}O_2$-SrO/Al_2O_3 nanostructure is formed, improving reducibility, stability, and Pd dispersion. However, while improvements in catalytic activity were seen compared to a Pd/CeZrAl catalyst, the SrO-doped TWC did not outperform the BaO-doped system in terms of light-off temperature. Yang *et al* also looked at other alkaline metal dopants, synthesising Mg, Ca, Sr, and Ba-doped Pd/CeO_2-ZrO_2 TWCs. [217] In agreement with Lan *et al*, they found Ba was the best-performing dopant, while the inclusion of Mg actually reduced thermal stability and catalyst performance.

Alternative washcoat materials – zeolites as a HC and NO_x trap

Zeolites can be included as a washcoat component as a 'cold trap' for reactants – adsorbing them in ambient conditions and releasing them at higher temperatures. Zeolites are a group of microporous, Al and Si-containing materials. Their large network of mesopores and micropores provide them with a good adsorption ability. HC trap designs utilising zeolite materials have been in use since the 1990s, with various systems demonstrating improved low-temperature performance. [218] Factors that can limit zeolite HC trap effectiveness include thermal stability, desorption below 200 °C (below light-off temperatures), reversibility of adsorption process, and different behaviour for different HCs. For instance, while higher molecular weight HCs (such as toluene) are taken up by zeolite materials to a high degree, lighter molecules such as propene are only lightly adsorbed, and can desorb from the trap at temperatures far below light-off. [219]

Kustov *et al* looked at using Li, Na, and K-modified ZSM-5 zeolite materials for toluene adsorption (Figure 21). [220] They found that Li or Na doping (to 5 wt. % and 2.5 wt. %, respectively) provided the largest advantages for toluene storage, as well as high-temperature desorption (between 200 and 400 °C). ZSM-5 was chosen for this study due to its higher thermal stability and good pore structure compared with many other common zeolites.

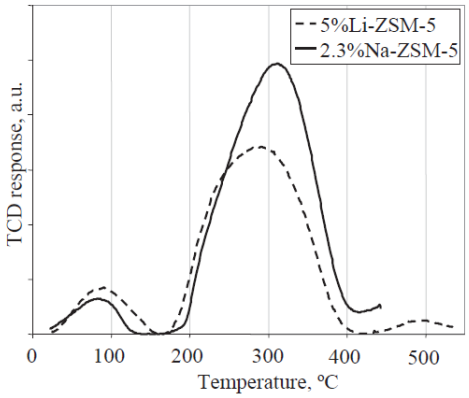

Figure 21. Temperature-programmed desorption of toluene from ZSM-5 zeolites. Reproduced from Ref. [220] with permission from Elsevier.

Design considerations for HC traps may need to take into account more than just successful HC uptake. Bugosh and Harad looked at the use of a BEA zeolite as a dodecane trap, as well as its performance incorporated into a Pt/Pd/BEA/Al_2O_3 TWC. [218] They found that while higher levels of BEA improved hydrocarbon adsorption, as expected, the adsorbed dodecane had an inhibitory effect of CO oxidation – higher levels of pre-adsorbed HCs shifted the light-off curve of CO to higher temperatures. Burke *et al* examined the effect of water in the exhaust stream on HC adsorption in Na-BEA and La-BEA zeolites. [221] They found that, compared with a H_2O-free test run, the presence of water significantly decreased the adsorption of propene and toluene, and adsorption of water was favoured. The authors suggest the incorporation of a more hydrophilic zeolite in combination with BEA may be a strategy for dealing with water in vehicle exhaust.

There are a large number of possible zeolite materials, and many have been used as HC trap materials, including Y zeolite, ZSM-5 (MFI), USY, BEA, mordenite, FAU, and FER with varying SiO_2/Al_2O_3 ratios of 1 to 150. [220] Therefore, a comprehensive examination of zeolite properties, correlated to performance, is desired. Westermann and Azambre looked at the effectiveness of six different zeolites for use in a HC trap: HY-15 and Hβ-12.5 (large pores), HZSM5-5.5 and 5A-2 (medium pores), HFER-10 (small pores with 2D structure), and HMOR-10 (large pores but 1D structure). [222] They used decane, toluene, and propene as representative heavy and light HC molecules. Their findings were that HY-15, 5A-2, and Hβ-12.5 preferentially adsorbed decane over toluene, while HFER-10 was skewed toward propene adsorption. However, HMOR-10 and HZSM5-5.5 showed less preferential 'single-file' adsorption behaviour and higher desorption temperatures, more favourable for cold-start applications. The behaviour of different zeolite materials was attributed to the quantity of acid sites, the Si/Al ratio, the degree of microporosity, and the pore size – the optimum pore size was determined to be 5.5 to 6 Å for toluene and 4 to 5 Å for propene. The relationship between acidity and microporous volume on hydrocarbon adsorption capacity is shown in Figure 22.

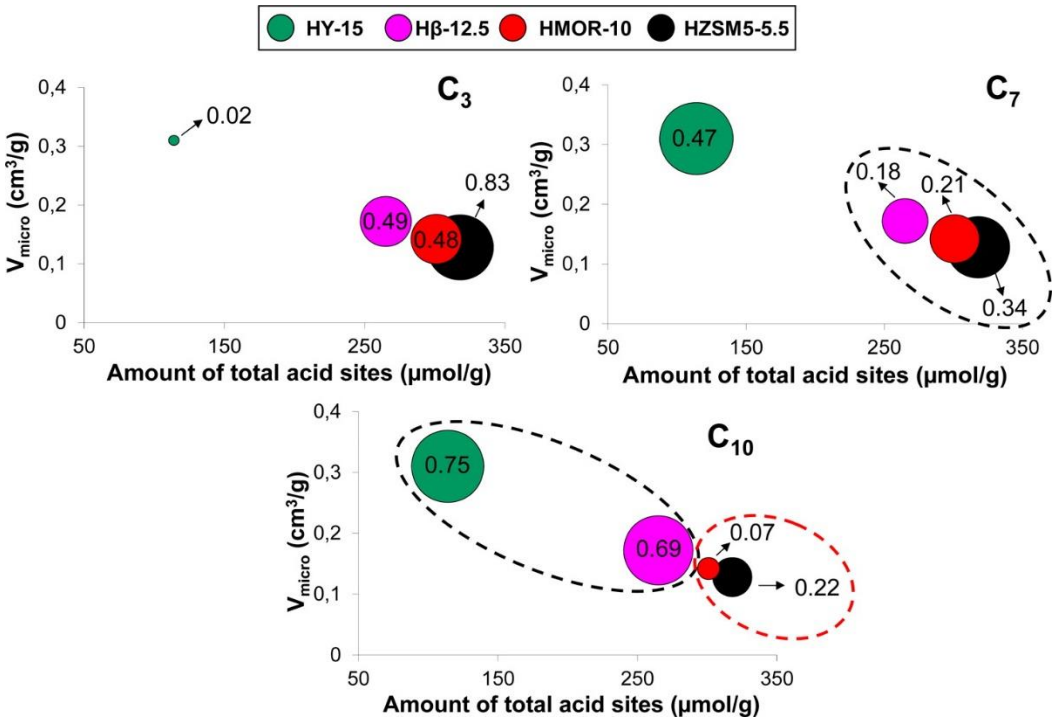

Figure 22. Influence of acidity and microporous volume on the total adsorptive capacity of various zeolite materials for propene (C_3), toluene (C_7), and decane (C_{10}). The absorptive capacity (mmol g^{-1}) is represented by the size of the circles. Reproduced from Ref. [222] with permission from the American Chemical Society.

More recent research has also focused on using zeolites as a NO_x cold-start trap. Murata *et al* report a study looking at 1 wt. % Pd, Pt, or Rh-loaded ZSM-5 zeolite for TWC use. [223] They found that Pd/ZSM-5 adsorbed NO up to 0.4 g_{NO} L_{cat}^{-1}, compared with approximately 0.03-0.04 g_{NO} L_{cat}^{-1} for Pt/ZSM-5, Rh/ZSM-5, and Pd loaded on other supports (Al_2O_3, ZrO_2, CeO_2). This adsorbed NO could be reduced to N_2 while heated under a slightly reducing atmosphere. In a real-world engine test using a traditional close-coupled Pt/Rh TWC and a Pd/ZSM-5 underfloor catalyst, NO_x emissions during the initial cold-start period were reduced from 200 to 50 ppm.

2.3.4 Platinum group metal loading

Platinum, palladium, and rhodium are the common platinum group metals (PGMs) employed as the active component in three-way catalyst designs. Pt and Pd are used for the oxidative component of three-way catalysis, while Rh is necessary to control NO_x emissions. The choice of using Pt or Pd is mainly economic – in the 1990s, Pd was more common because it was less expensive, but increasing demand for Pd led to a surge in price, and Pt-based formulations were developed instead. [224] It should be noted that Pd and Pt are not interchangeable without other design considerations – Pd is typically less stable than Pt, which must be accounted for. [194] Rh is the most expensive of the three metals, and 80% of global Rh demand is for TWC use. This has driven the development of low-Rh formulations. While rhodium-free Pd-only TWCs have been produced, they typically do not have very good NO_x removal capabilities. [224,225] Recent results are summarised below and in Table A13 in the Appendix.

PGM loading quantities and ratios

From Johnson Matthey, Cooper and Beecham reported a study comparing TWC activity across a range of Pt, Pd, and Rh loadings and relative ratios (Figure 23). [226] All catalysts tested were either Pd/Rh or Pt/Rh and were aged at 950 °C for 80 h (correlating to 160000 km of road use). Loadings were chosen to match the 'lower end' of PGM loadings in commercial catalysts. Their findings were that increasing Pt or Pd loading only slightly

improved the catalyst performance for HC and NO_x removal and decreasing the amount of Pt or Pd only slightly reduced catalytic activity. In contrast, increasing or decreasing the amount of Rh had a more significant benefit in improved catalytic activity (in terms of light-off temperature). Additionally, Pd slightly outperformed Pt under most testing conditions. The authors note that while low-Rh formulations have become common due to the high cost of rhodium, this may not make sense in terms of performance. Their conclusions are that increasing Rh levels should boost TWC performance, while Pd or Pt loadings can probably be decreased for cost savings, if necessary.

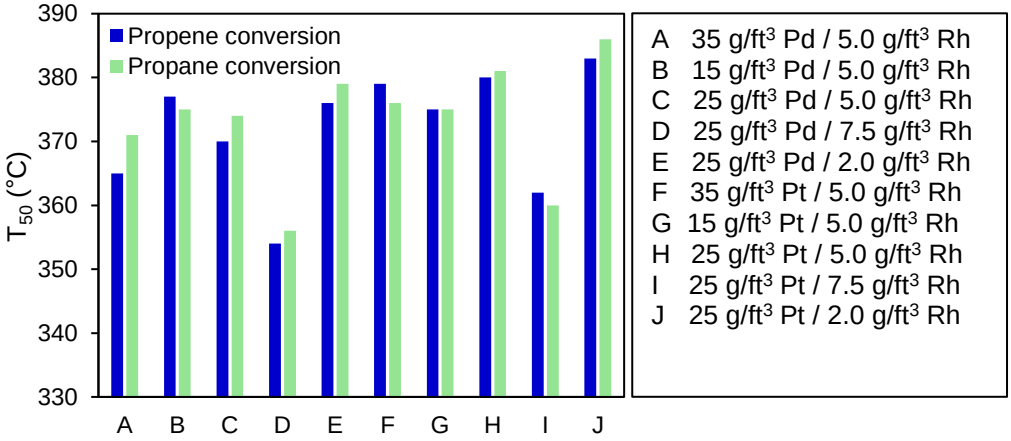

Figure 23. T_{50} conversion values of hydrocarbons for a catalyst with different Pt, Pd, or Pd loadings and ratios.

Alikin and Vedyagin examined different Rh loadings (0.01 to 1 wt. %) on a CeO_2-ZrO_2-Y_2O_3-La_2O_3 washcoat material for three-way catalysis. [227] As expected, they report that higher Rh loadings improve light-off temperatures. They also found that if the Rh loading is too low (0.1 wt. % or below), strong Rh-ceria interactions upon high-temperature aging lead to a loss of catalytic activity. For Rh levels higher than this, performance improves because most of the Rh remains catalytically active.

Theis *et al* looked at varying Pd loadings on Al_2O_3 catalysts (0 to 4 wt. % Pd). [228] They found that increasing the Pd loading from 0 to 2 wt. % led to an improvement in catalyst performance for CO, HC, and NO removal. However, this improvement was not linear – and the performance of the 4 wt. % sample was very similar to that of the 2 wt. % sample,

suggesting that under the experimental conditions used, there are only diminishing or no returns for adding Pd above 2 wt. %.

Kang *et al* also examined Pd loading's impact on TWC performance, looking at commercial catalysts with Pd loadings of 0.10 to 1.24 wt. % (20 to 240 g/ft^3) Pd. [229] The washcoats were alumina with 3% ceria and 1% each BaO and La_2O_3. Similarly to Theis, Kang found that TWC performance increased nonlinearly with increasing Pd content, finding only small differences in catalysts with more than 0.42 wt. % (80 g/ft^3) Pd.

Jeong and Choi looked at different ratios of Pd, Pt, and Rh in a TWC with a double-layer washcoat consisting of Al_2O_3 and an undisclosed amount of Ce, Zr, and La. (Figure 24) [230] Unlike many other reports in the literature, real exhaust gas (from a 5 hp gasoline engine) was used in this study. In agreement with Cooper and Beecham, they found that Pd-based catalysts had better light-off temperatures than Pt-based catalysts. The optimum Pd:Rh ratio in this study was 18:1 – this catalyst outperformed others with equivalent levels of Rh, but either higher or lower Pd loadings. However, this result does not necessarily contradict the results of Cooper and Beecham because catalysts with higher Rh loadings with equivalent Pd levels were not tested.

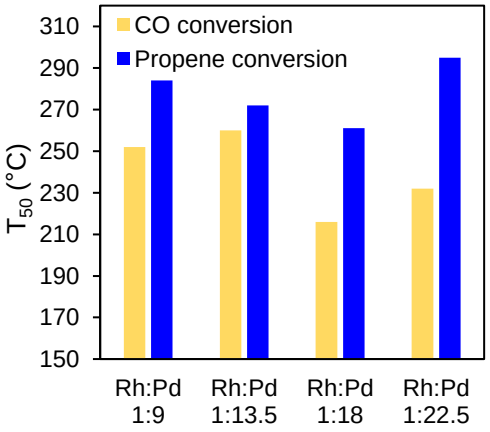

Figure 24. T_{50} conversion values of hydrocarbons for a catalyst with different Rh:Pd ratios.

In other studies in which only CO oxidation or NO removal with CO were considered, Phan and Kureti report that in a Pd/Al_2O_3 system for CO oxidation, the light-off temperature improves up to 2 wt. % Pd, with higher Pd levels not providing additional

performance. [231] Martínez-Arias *et al* report that, between 0.05, 0.5, and 1.0 wt. % Pd/Al_2O_3, increasing Pd provides improved performance for CO and NO removal. However, CO desorption from Pd is a rate-limiting step due to strong CO-Pd interactions. [232] Di Monte *et al* report that for a $Pd/Ce_{0.6}Zr_{0.4}O_2/Al_2O_3$ catalyst, 2.8 wt. % Pd provides better light-off performance for CO and NO removal than 0.7 wt. % Pd. [233] Finally, Anderson *et al* report that loading more Pt in a $Pt/Rh/Ce_{0.5}Zr_{0.5}O_2$ catalyst material improves performance for CO oxidation. [234]

Additional considerations for TWC metal loading

Three-way catalysts may be designed with distinct washcoat layers, with separated active metals either to improve activity or prevent sintering. Catalyst deactivation has been partially attributed to the formation of Pd-Rh alloys at high temperatures in catalyst formulations which originally had separate Pd and Rh particles. [235] For example, Rh can be placed in a top layer where it is exposed to the various reductant species in the exhaust gas, before the reactants diffuse to a lower Pt- or Pd-containing layer where oxidation takes place. [224] Jeong and Choi's TWC study, discussed in the previous section, employed a double-layer washcoat with Pd/Pt and Rh components in different layers. [230] In another experiment, Shinjoh *et al* reported a TWC in which Pt was supported on a ceria-based oxide material and Rh was supported on a zirconia-based oxide to prevent sintering after high-temperature aging. This was achieved through the high level of interaction between metal and support, with Pt-O-Ce and Rh-O-Zr bonds preventing high-temperature particle agglomeration. This design outperformed a conventional catalyst design in terms of light-off temperature. [236] It also avoided excessive Rh-Ce or Rh-Al interactions, which can cause the formation of a highly oxidised inactive form of rhodium. [213,237]

In contrast to designs with separate metal components, other recent research has shown that some bimetallic alloy designs can improve catalytic performance or stability, not just cause deactivation. Vedyagin *et al* developed an alloyed 0.2 wt. % $Pd\text{-}Rh/Al_2O_3$ catalyst (Pd:Rh ratio 3:2) which was more stable than an identical catalyst with separate Rh and Pd particles. [238] Interactions between Pd and Rh in the alloyed metal particles

prevented Rh from diffusing into the washcoat phase, a potential cause of rhodium deactivation. However, despite improved stability, the bimetallic alloy catalyst showed worse light-off performance than a similarly prepared Rh-only catalyst. This was explored further in a following study, looking at different Pd:Rh ratios (3:2, 7:3, and 4:1). [235] The catalyst with the highest level of Rh demonstrated the strongest Pd-Rh interactions, and thus the highest level of stability after aging at 1000 °C. However, it should be noted that in both studies, a similarly prepared Rh-only catalyst had better low-temperature performance than any of the alloyed catalysts – their only advantage is stability.

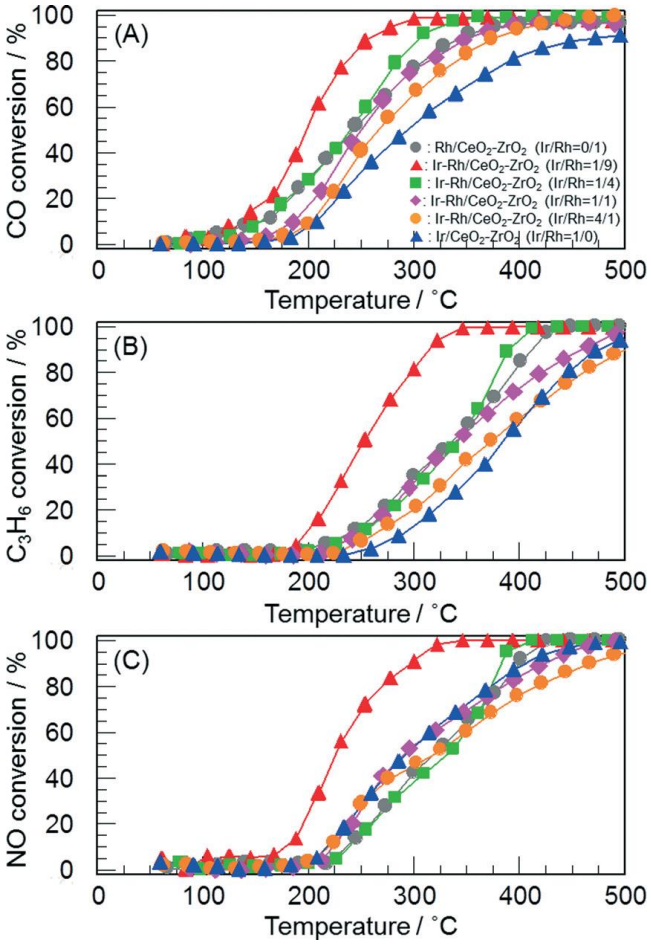

Figure 25. CO, HC, and NO conversion rates for Rh and Ir/Rh-based catalysts. Reproduced from Ref. [225] with permission from the Royal Society of Chemistry.

The reason why such alloy catalysts perform more poorly than pure Rh, despite better stability, is that Pt and Pd strongly interact with CO – adsorbing it to the point of hindering the other TWC reactions by blocking reaction sites. This interferes with Rh's

catalytic activity in Pt-Rh or Pd-Rh alloys. To mitigate this, Haneda *et al* designed an iridium-rhodium catalyst – Ir does not adsorb CO as strongly as Pt or Pd, so should not hinder HC/NO_x. [225] They found that the inclusion of Ir (unlike the Pd-Rh alloy catalysts above) at a 1:9 Ir:Rh ratio improved activity beyond that of a Rh-only catalyst, as well as enhancing stability (Figure 25). The authors state that the use of Ir could be a strategy to reduce Rh levels in TWC design. This could be useful from an economic point of view – Ir is less expensive than Rh. [239]

2.3.5 Monoliths

The two most common monolith designs for TWCs are cordierite ceramic or metallic foil. Extruded cordierite monoliths are the most popular design on the market due to their good thermal shock resistance, chemical resistance and low coefficient of thermal expansion – cordierite's melting temperature is approximately 1450 °C and it resists oxidation. [240] This makes cordierite a good material to withstand the harsh conditions TWCs are exposed to.

However, there are limits to how thin cordierite monolith walls can be manufactured. In contrast, metallic monoliths can have a frontal open area of about 90%. [240,241] This provides a higher geometric area per volume for catalyst deposition and allows lower flow resistance and back pressure. While cordierite monoliths are more common, metallic monoliths can be found in certain niche applications, such as large trucks or high-performance sports vehicles in which the low pressure drop is more desirable. An additional advantage of metallic monoliths is high thermal conductivity, allowing faster heating of the catalyst. However, their coefficient of thermal expansion is also larger than that of cordierite monoliths, meaning special bonding techniques must be employed to ensure the washcoat material adheres to the monolith.

Santos *et al* find that with identically prepared ceramic and metallic substrates, the ceramic monoliths provide better CO and HC conversions than metallic monoliths at low space velocities (< 50000-70000 h^{-1}). [240] However, at higher space velocities, metallic substrates provide better conversions due to a larger surface area and improved mass

transfer properties. This is because at higher space velocities the TWC reactions are mass-transfer limited, providing an advantage to the metallic substrate.

Reducing the mass of a monolith can improve its performance. Otsuka *et al* developed a 'super-light' monolith with a 20% increase in porosity levels. [242] This monolith had the same pressure drop and thermal stability as a conventional monolith, but provided extra surface area for washcoat deposition while maintaining the same wall thickness (2 or 3 mil) and cell size. Overall, emissions were reduced by approximately 10% compared with the conventional monolith. Kikuchi *et al* compared monoliths with 600, 900, and 1200 cells, with wall thicknesses of 4.3, 2.5, and 2.0 mil, respectively. [243] They found that maximising the number of cells and minimising wall thickness and overall substrate mass improved TWC performance.

Chang *et al* report a novel substrate made from an extruded zeolite material, instead of cordierite or metal foil. [126] This was done in the investigation of zeolites as a 'HC trap' washcoat material, which have been shown to be able to adsorb and store HCs below the light-off temperature and release them at a higher temperature. However, zeolites can only be loaded to approximately 2 g/in^3 on a traditional ceramic monolith because of increasing back pressure and processing constraints if the washcoat layer is too thick. Therefore, Chang *et al* developed an extruded zeolite-based monolith, containing about 4 g/in^3 zeolite material. When combined with a Pd/Al_2O_3-ZrO_2-CeO_2 catalyst and washcoat, TWC low-temperature performance was improved compared with a similar catalyst with a ceramic monolith. Additionally, the zeolite monolith catalyst trapped approximately 85% of HC emissions in a 30 second storage test, compared with 64% for a more traditional zeolite-on-cordierite catalyst.

2.3.6 Conclusions

Three-way catalytic converters are essential for reducing gasoline engine powered vehicle pollutants emissions to regulation levels. This review has shown the recent range of research investigating the numerous factors that impact the three-way catalyst design. One such factor is the design of washcoat formulations. Ceria-zirconia is added to

alumina washcoats to improve oxygen storage capacity. While ceria-zirconia materials with 40-60% ceria are typically used due to their high oxygen storage capacity, good results have also been achieved with other formulations, such as a mixture of Ce-rich and Zr-rich particles. An additional consideration is the use of Zr-rich formulations to avoid unfavorable interactions between Rh and ceria. Oxygen storage capacity and thermal stability of the washcoat can be further improved with the addition of low levels of rare earth or alkaline metal promoters, and the inclusion of zeolites to act as a hydrocarbon or NO_x cold trap should be considered as well.

Another key factor in three-way catalyst design is the loading and ratio of platinum group metals. Pt/Rh or Pd/Rh are the most commonly used metals – Pt or Pd for oxidative reactions, and Rh for NO_x reduction. While the use of Pt or Pd has often been based on economic decisions, performance differences mean the two metals are not interchangeable without other design considerations. While low-Rh designs have been introduced due to the higher cost of Rh, this may have a larger negative impact on catalyst performance than decreasing the loading of Pt or Pd. More novel catalyst designs such as the use of bimetallic alloys show potential in reducing Rh loading without sacrificing performance.

Monolith design choices also influence three-way catalyst performance. Metallic monoliths may be chosen instead of the more common cordierite-based monoliths in applications where a lower pressure drop is desirable. Highly porous cordierite monoliths have been shown to improve performance by increasing the surface area available for washcoat deposition, and novel zeolite-based monoliths offer a potential way to increase the total zeolite loading in a catalyst beyond that of what traditional cordierite monolith designs allow.

Overall, a good understanding of how various washcoat compositions, PGM particles, and the monolith interact to form an effective catalyst is necessary for the further development of three-way catalysts with better performance, particularly at low temperatures where current catalyst designs are not very active. While the development of this technology thus far has provided numerous environmental benefits, with

increasingly stringent air quality and emissions regulations in the US, Europe, China, and elsewhere, the need for further progress in emissions control technology is clear.

Chapter 3

Research Objectives

The overall aim of this research project is to investigate alternative ceria-based catalysts, primarily for automotive three-way catalysis applications. In particular, the areas of focus will be: improvement of low-temperature catalytic activity in PGM-free catalysts and enhancement of high-temperature stability. All materials synthesised will be fully characterised (TEM, BET, XRD, Raman, TPR, XPS, EDX) to relate their physical and chemical characteristics with their performance as catalysts.

The specific aims of this PhD thesis are:

(a) To hydrothermally synthesise transition metal-doped ceria nanorods to develop a platinum group metal-free catalyst with enhanced activity at low temperatures. These catalysts will be tested for both CO oxidation and NO reduction reactions to determine their suitability for three-way catalysis and characterised to understand how the dopants affect catalyst reducibility and performance.

(b) To investigate the use of graphene oxide (GO) as a template for ceria nanoflake synthesis. GO-templated and untemplated ceria catalysts will be calcined at a range of different temperatures and then tested for catalytic activity in CO oxidation and NO reduction reactions to determine their resistance to sintering.

(c) To explore the potential use of these catalysts in other non-automotive applications.

Chapter 4

Materials and Methods

4.1 Syntheses

4.1.1 Doped ceria nanorods

Pure and doped ceria nanorods were synthesised via a hydrothermal method. [37] For undoped ceria, a 15 mol L^{-1} aqueous solution of NaOH in deionised water was prepared. 120 mL of this solution was added to a Teflon-lined stainless-steel autoclave with a total capacity of 150 mL. 1.8 g of $Ce(NO_3)_3 \cdot 6H_2O$ was added to the autoclave, the solution was stirred for approximately 30 s, and the autoclave was sealed and placed in an air-circulating oven. The oven was heated to 100 °C at a ramp rate of 5 °C min^{-1}, held at this temperature for 10 h, and allowed to cool to room temperature.

To prepare doped ceria, a stoichiometric amount of the respective dopant precursor in aqueous solution was added to the autoclave with the cerium nitrate to achieve the desired wt. % of dopant. Dopant precursors were aqueous solutions of 0.25 mol L^{-1} $CuSO_4$, 0.3 mol L^{-1} $Cr(NO_3)_3$, or 1 mol L^{-1} $MnCl_2$.

Ceria-zirconia nanorods were prepared using the same procedure and a stoichiometric amount of $ZrO(NO_3)_2 \cdot 6H_2O$ partially replacing the Ce precursor to achieve the desired Ce/Zr ratio.

Post-synthesis, the solid product was separated from the sodium hydroxide solution via vacuum filtration and washed with 500 mL deionised water. The wet product was dried in a vacuum oven at 80 °C overnight, and the resulting powder was gently ground in an agate mortar and pestle.

4.1.2 GO-templated ceria nanoflakes

Graphene oxide was prepared by oxidising and exfoliating graphite using a modified Tour *et al* synthetic method. [244,245] 24 g of 100-500 μm natural graphite flakes were added to a concentrated acid solution (3 L H_2SO_4 : 0.3 L H_3PO_4) under vigorous stirring. 144 g of $KMnO_4$ was added gradually, then the reaction mixture was vigorously stirred for 18 h at 50 °C. After this, the reaction mixture was cooled to room temperature. 1.72 L of 2 wt. % aqueous H_2O_2 was added dropwise to stop oxidation reactions from continuing. The resulting suspension of GO was repeatedly isolated via centrifugation and redispersed in distilled water until the pH of the supernatant matched that of the original distilled water (typically after 16 washing cycles). Then, unexfoliated graphite particles were separated from the GO with two further lower speed (<1000 rpm) centrifugation cycles. The GO was stored as a 3 wt. % suspension in water.

Ceria nanoflakes were prepared with a room temperature precipitation reaction. [65] 3 mL of the GO solution described above was added to 600 mL of deionised water. Aqueous ammonia solution (30 %) was added to adjust the pH to 11. 150 mL of 0.05 mol L^{-1} $Ce(NO_3)_3 \cdot 6H_2O$ in deionized water was added to the GO/ammonia solution while stirring. The reaction mixture was left to stir for 3 h under ambient conditions, after which three cycles of centrifugation and redispersion in deionized water were performed to wash the product. The wet powder was freeze-dried at -60 °C.

Post-synthesis, the product was calcined at 400 °C for 3 h to remove the GO. Different samples were prepared by subsequent calcination at 600, 800, 900, or 1000 °C for 3 h. Calcination was performed in air under static conditions with a ramp rate of 5 °C min^{-1}.

Untemplated ceria particles were synthesised using the same procedure, without the addition of GO prior to pH adjustment with ammonia.

Nickel-loaded ceria nanoflakes and ceria particles were prepared by dispersing bare ceria catalysts (calcined at 400 °C) in ethanol with a corresponding amount of $Ni(NO_3)_2 \cdot 6H_2O$ to achieve a loading of 10 wt. % Ni. This mixture was stirred for 30 min, then the solvent

was remove by drying under vacuum in a rotary evaporator. The product was dried in an oven at 80 °C overnight, then calcined at 700 °C for 4 h in air under static conditions.

4.2 Characterisation and catalyst testing

Powder X-ray diffraction (XRD) was performed with a Bruker D8-Advance or X'Pert Pro PANalytical instrument using Cu Kα radiation. Sample analysis was conducted in the 2θ range of 20 to 90° with a step size of 0.0164° and 0.25 s per step, or 5 to 80° with a step size of 0.05° and 0.16 s per step. Crystallite sizes were calculated using the Scherrer equation and unit cell parameters were calculated using Bragg's law.

Nitrogen adsorption measurements were performed with a Micromeritics 3Flex Surface Characterization Analyzer. Samples were degassed under vacuum at 200 °C for 90 min. Specific surface areas were calculated using the Brunauer-Emmett-Teller (BET) method.

Thermogravimetric analysis (TGA) was performed in a TA Instruments Discovery TGA, Q50. Approximately 3 mg of sample was combusted under 40 mL min^{-1} of air from 50 to 900 °C at 10 °C min^{-1}.

Raman analysis was performed with a Renishaw inVia Raman Microscope with a 532 nm green laser, and spectra were obtained with 2-10 s exposure time at 1-10% laser power.

Transmission electron microscopy (TEM) was performed with a JEOL JEM1200EXII or JEOL JEM-2100Plus microscope. Samples were prepared for analysis by dispersing dried powders in ethanol, letting 1-2 drops of the ethanol solution dry on the surface of a copper TEM sample grid, and storing the TEM grids overnight under vacuum. Energy-dispersive X-ray spectroscopy (EDX) analysis was performed with an Oxford Instruments large area EDX detector integrated into the TEM instrument.

Temperature-programmed reduction (TPR) experiments were performed with a Micromeritics AutoChem II 2920. 0.1 g of each sample was heated from room temperature

to 900 °C at a rate of 10 °C min^{-1}, under flow of 50 mL min^{-1} of 5 % hydrogen in argon. A thermal conductivity detector was used to analyse the outlet gas.

X-ray photoelectron spectroscopy (XPS) analysis was performed using a Kratos SUPRA XPS instrument with monochromated Al Kα x-rays (1486.69 eV). Survey scans were recorded with a pass energy of 160 eV, while high resolution spectra were recorded with a pass energy of 20 eV.

Catalytic activity experiments for CO oxidation and NO reduction were performed in a U-shaped quartz tube reactor (10 mm ID). In a typical experiment, 15 mg of ceria particles were dispersed in a catalytic bed of 4 cm^3 silicon carbide particles. In the quartz tube reactor, this bed was secured at both ends with high-temperature quartz wool. For CO oxidation, the reactant feed consisted of 2000 ppm CO and 2000 ppm O_2 in nitrogen, with a total flow rate of 50 mL min^{-1}, achieving a weight hourly space velocity (WHSV) of 200 L g^{-1} h^{-1}. For NO reduction, the reactant feed consisted of 1667 ppm NO and 2667 ppm CO in nitrogen, with a total flow rate of 45 mL min^{-1}, achieving a WHSV of 180 L g^{-1} h^{-1}. For both reactions, the reactor was enclosed in a tube furnace and heated between room temperature and 500 °C with a ramp rate of 2.5 °C min^{-1}. The outlet gas, including CO_2, was measured with a Hiden mass spectrometer, and CO concentration was measured with a Fuji Electric ZRH Infrared Gas Analyzer. The mass spectrometer and infrared analyser were used simultaneously to allow the measurement of both CO and CO_2 to ensure a complete carbon balance. Data points shown in charts in this thesis are the mean of ten continuously logged data points, and error bars shown represent the standard deviation of these points. Therefore, error bars represent instrumental variation.

Blank reactor tests were performed to determine the non-catalytic contributions to conversion, which was insignificant. A representative example is shown in Figure 26.

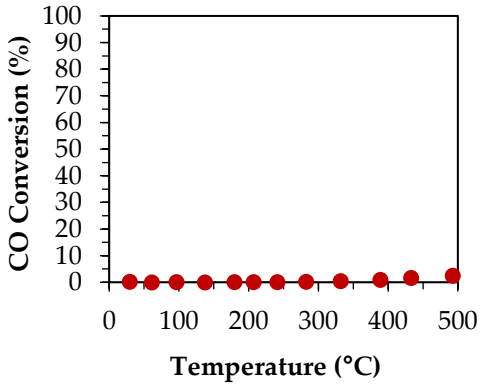

Figure 26. Blank reactor test for CO oxidation.

Catalytic activity experiments for dry reforming of methane (DRM) were performed in a tubular quartz reactor (10 mm ID). Prior to the reaction, catalysts were reduced in a H_2 atmosphere (10 vol. % H_2 and 90 vol. % N_2) at 850 °C for 1 h. In a typical experiment, 100 mg of Ni-ceria catalyst was loaded into the reactor on a bed of quartz wool. The reactant feed consisted of a 1/1/6 ratio of $CH_4/CO_2/N_2$, with a total flowrate of 100 mL min^{-1}, achieving a WHSV of 60 L g^{-1} h^{-1}. Reactants and products were monitored with an on-line gas analyser (ABB AO2020) with both IR and TCD detectors. Catalysts were tested between 550 and 850 °C. Long-term stability tests were performed at a constant temperature of 800 °C for 20 hours.

4.3 Characterisation theory

4.3.1 Powder x-ray diffraction

Powder x-ray diffraction (XRD) is a technique used to analyse the structure of crystalline materials. [246] Diffraction of light will occur if the wavelength of the light in question is similar to the separation of the diffracting material. X-rays are electromagnetic waves with a wavelength (λ) of 0.1 to 100 Å, which is a range comparable to the spacing between atoms in many crystalline materials. The most common source of radiation in a powder XRD machine is a Cu Kα x-ray tube, which produces x-rays with a wavelength of 1.5406 Å.

In x-ray diffraction, x-rays are fired at a sample material and are scattered by electrons bound to atoms. Depending on the spacing of atoms in the crystal lattice of the material and the angle of interaction, some x-rays will positively interfere with each other, producing a high intensity signal. The x-ray beam is rotated around the sample to change the angle at which the x-rays interact with the sample material, producing a pattern of diffraction angle vs. signal intensity. Bragg's law (Equation 13) can be used to relate the angle of diffraction with the lattice spacing. This is shown in Figure 27, where θ is the angle of incidence, λ is the x-ray wavelength, d is the spacing between parallel crystal lattice planes, and n is an integer value.

$$n\lambda = 2d\sin(\theta) \tag{13}$$

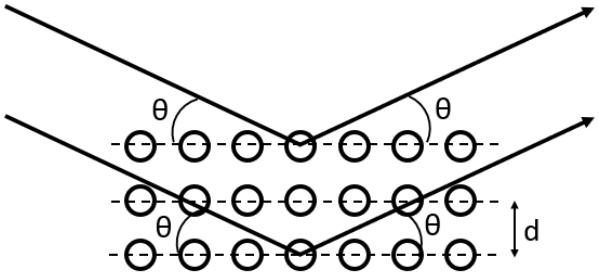

Figure 27. Illustration of geometry used for Bragg's law.

The Scherrer equation is widely used to calculate sample crystallite size. [247] While this equation actually relates peak broadening with the coherent diffraction domain size, the phrase 'crystallite size' will be used in this thesis to maintain consistency with the majority of the literature. [248] Shown in Equation 14, τ is crystallite size, K is a shape factor (usually approximated as 0.9), λ is x-ray wavelength, β is the full width at half maximum of the diffraction peak, and θ is the Bragg angle in radians.

$$\tau = \frac{K\lambda}{\beta\cos(\theta)} \tag{14}$$

While this equation is widely used to approximate the crystallite size of powder samples, it should be noted that other factors can also contribute to peak broadening in powder

XRD patterns, such as experiment resolution and microstrain. As instrumental peak broadening from the x-ray diffractometer can differ from machine to machine, this broadening contribution can be determined for a particular instrument by measuring a standard such as NIST Standard Reference Material 660b (LaB_6 powder) and correcting for this contribution in subsequent XRD measurements.

4.3.2 Nitrogen adsorption – BET surface area

The adsorption of nitrogen on the surface of porous materials at 77 K (nitrogen's boiling point) can be used to determine the specific surface areas of nanopowders and mesoporous materials. [249,250] The Brunauer-Emmett-Teller (BET) method relates the amount of adsorptive gas required to completely cover the external surface and any accessible internal pores with a single monolayer of adsorbed gas. In a nitrogen BET experiment, nitrogen gas is injected into a sealed sample container held at a constant 77 K. The amount of nitrogen adsorption is measured in equilibrium with nitrogen pressure P and plotted against relative pressure P/P_o to provide an adsorption isotherm. IUPAC classifies different isotherm shapes (types I – VI), which correspond to microporous (type I), nonporous/microporous (types II, III, and VI), or mesoporous (types IV and V).

In the 1930s, it was discovered that the amount of nitrogen adsorbed at the beginning of the plateau of a type I isotherm corresponded with completion of a monolayer of adsorbed nitrogen. For type II and IV isotherms the beginning of this linear, nearly flat section was found to be in good agreement with the changeover from monolayer to multilayer adsorption, and thus could be used to determine the specific surface area of measured samples.

4.3.3 Thermogravimetric analysis

Thermogravimetric analysis (TGA) is a technique used to measure the mass of a sample over time, with changing temperature. This analysis can take place in air, or under the flow of a different inert or reactive gas and can be used to quantify characteristics such as

the loss of water, loss of solvent, oxidation, carbon content, or decomposition vs. temperature. Typically, a TGA instrument will contain a highly sensitive microbalance that continuously measures the mass of a sample as it is continuously heated.

4.3.4 Raman spectroscopy

Raman spectroscopy is a vibrational spectroscopy technique that uses lasers in the visible, near-infrared, or near-ultraviolet wavelength range to analyse materials. [251] While most light is scattered elastically (with no loss of energy or change in wavelength), Raman scattering relies on the very small percentage of photons which are inelastically scattered. This phenomenon occurs because during the scattering process, some light interacts with molecular vibrations, changing the energy. Therefore, Raman spectroscopy is used to measure the nature of these molecular vibrations, which are sensitive to changes in the structure and chemistry of crystal lattices.

In a typical setup, a monochromatic light source is focused and used to illuminate a sample. Most of this light is scattered elastically, but this is filtered out using a notch filter, which is designed to strongly adsorb radiation at the wavelength of the filter but transmit all other wavelengths. The remaining radiation is Raman scattered light, which is detected by a charge-coupled device (CCD), an array of silicon-based semiconductor pixels that generate an electric charge when hit with photons. This signal is used to create a Raman spectrum.

4.3.5 Transmission electron microscopy

Transmission electron microscopy (TEM) is a microscopic technique that transmits a beam of electrons through a sample to generate an image. [252] Due to the smaller wavelength of electrons compared with photons, transmission electron microscopes can achieve much higher resolution than traditional light microscopes, down to the sub-nanometre level.

Electrons are generated under vacuum by a filament, or electron gun, made from a material such as lanthanum hexaboride (known for its high electron emissivity). The beam of electrons is focused with an electromagnetic condenser lens into a thinner, more coherent beam, and further restricted by an aperture, which restricts high angle electrons. This beam of electrons hits the sample, and, depending on sample thickness and transparency to electrons, parts of the beam transmit through the sample and hits a detector. This creates an image which is enlarged through intermediate and projector lenses, hits a phosphor screen, generating a visible light image.

4.3.6 Energy-dispersive x-ray spectroscopy

Energy-dispersive x-ray spectroscopy (EDX) is an elemental analysis technique that identifies characteristic emitted x-rays from a sample specimen. [253] When a material is bombarded with high-energy particles, it emits x-rays characteristic which can be detected and assigned to specific elements. EDX analysis is often paired with electron microscopy, because such characteristic x-rays are generated when the microscope's electron beam bombards the sample.

When a sample is bombarded by a high-energy beam of electrons, atoms have some of their electrons ejected. This creates electron vacancies in the inner shell of the atom. These vacancies are filled by electrons from a higher state, and this is accompanied by the creation of an x-ray photon to balance the difference in energies. The energy of this x-ray photon is characteristic to the element of the atom in question.

4.3.7 Temperature-programmed reduction

Temperature-programmed reduction (TPR) is a characterisation technique used to determine the reduction conditions of a material. [254] In a typical procedure, an oxidised material is subjected to a controlled temperature increase while under flow of a reducing atmosphere – usually a mixture of hydrogen diluted in nitrogen or argon. At the outlet, the decrease in hydrogen concentration is monitored and can be plotted vs. temperature.

The detector used to measure hydrogen concentration is typically a thermal conductivity detector (TCD). A TCD measures changes in the thermal conductivity of the gas flow. When compared to a reference thermal conductivity value of the inlet gas, this can be used to determine the change in hydrogen concentration.

4.3.8 X-ray photoelectron spectroscopy

X-ray photoelectron spectroscopy (XPS) is used to analyse the surface chemistry of solid materials. [255,256] Samples are analysed by bombarding the surface with monochromatic x-rays in a vacuum. Al Kα or Mn Kα are commonly used as x-ray sources. When an x-ray photon hits an atom, it can transfer its energy to a core electron, which is ejected with a kinetic energy dependent on the x-ray's energy and the binding energy of its initial atomic orbital. These energies are determined by the photoelectric effect (Equation 15), where E_k and E_b are the kinetic energy and binding energy of the electron, respectively, and hv is the energy of the incident x-ray.

$$E_k = hv - E_b \tag{15}$$

The energy of these emitted electrons can be used to identify different elements, and the intensity of the signal at different energy levels can be used to quantify the relative concentration of the elements present in a sample.

XPS is a surface technique, with a typical analysis depth of ~10 nm for Al Kα, because the intensity of the x-rays decreases with increasing sample depth and ejected electrons near the surface have a higher chance of escaping past the surface and reaching the detector. In comparison to EDX, which is more of a bulk analysis technique, XPS provides information about surface and near-surface chemistry and can provide additional information about oxidation states.

Chapter 5

Ceria-Based Catalysts for Low-Temperature Vehicle Exhaust Conditions

This chapter reports on the synthesis, characterisation, and catalyst performance of transition metal-doped ceria nanorods for the improvement of low-temperature catalytic activity. Catalysts were tested using CO oxidation and NO reduction as model reactions to investigate the applicability of synthesised materials for automotive catalyst applications.

As discussed in Section 1.3.1 in the literature review, different ceria morphologies strongly influence the nature of exposed crystal faces, which influences the performance of ceria materials as catalysts. Previous work by Torrente-Murciano *et al* reports that different ceria morphologies such as nanorods or nanocubes can be easily produced by modifying the reaction parameters of a template-free hydrothermal synthesis. Ceria nanorods have been shown to improve catalytic activity compared with ceria nanocubes and unstructured ceria in various reactions, including the total oxidation of toluene, hydrogenation of CO_2 for the production of hydrocarbons, and the water-gas shift reaction. [257–259] In all cases, the selective exposure of the (110) crystal plane by ceria nanorods played a significant role in the improved catalytic activity.

The goal of this project was to investigate the potential of PGM-free ceria materials doped with low levels of transition metals in automotive catalytic applications, while using the prior experience of Torrente-Murciano *et al* with hydrothermal ceria synthetic procedures. Herein, the characterisation and catalytic performance of ceria nanorods doped with Mn, Cu, Cr, or Cu+Cr in CO oxidation and NO reduction reactions is reported. Mn, Cu, and Cr were selected as dopants due to their high potential based on parameters discussed in the literature review (Section 1.3.2) as well as the catalytic performance of other reported copper-doped ceria materials (Section 1.6). All three dopants are transition metals with

smaller ionic radii than cerium, as well relatively high Pauling electronegativity values, trends reported in the literature to identify good dopants for ceria-based catalysts in terms of improved reducibility and activity for oxidative reactions. [68,70,71] Additionally, Mn, Cu, and Cr are transition metals available for a significantly lower cost than PGMs. [260]

Due to improved reducibility, demonstrated with TPR, Raman spectroscopy, and XPS, it is shown that doping ceria with Cu or Mn improves CO oxidative activity, but these dopants are less helpful for NO reduction. Conversely, doping ceria with Cr does not improve the catalytic activity for CO oxidation but does result in a catalyst with better low-temperature performance for NO reduction. The use of Cu and Cr as simultaneous co-dopants resulted in a significant synergetic improvement in catalytic activity, particularly for CO oxidation. Doping ceria nanorods with just 1 wt. % each Cu and Cr resulted in a catalyst with CO oxidative activity close to that of 7 wt. % Cu-doped ceria nanorods, while retaining good activity for NO reduction. These results are noteworthy because they show that large improvements in the catalytic activity of ceria-based materials are possible with the inclusion of small amounts of transition metals, which are cheaper than the PGMs used in catalytic converter designs.

5.1 Characterisation of doped nanorod catalysts

Undoped and doped ceria nanorods were hydrothermally synthesized, filtered and washed, and dried under vacuum. The undoped ceria synthesis produced a pale yellow powder product, while Mn, Cu, and Cr-doped ceria produced varying shades of brown. TEM images of undoped ceria, Mn-doped ceria, Cu-doped ceria, and Cr-doped ceria are shown in Figure 28. In all cases, there is a range of nanorod sizes: with nanorod widths generally below 50 nm and nanorod lengths ranging from 100 to several hundred nm. In the Cu-doped ceria sample, small nanoparticles and nanocubes can be seen in addition to nanorods. In all cases, there is no evidence of formation of Mn, Cu, and/or Cr particles outside the rod structure.

Powder XRD diffraction patterns of doped and undoped ceria nanorods are shown in Figure 29. In all cases, the main diffraction peaks of ceria's fluorite-type unit cell are observed (JCPDS 34–0394). For copper-doped ceria nanorods between 1 and 7 wt. % Cu and all dopant loadings for Mn and Cr-doped ceria, only ceria diffraction peaks are seen. This is an indication of dopant substitution into the ceria lattice and formation of a homogeneous fluorite structure. [135] However, it is possible that Cu or Cr particles are present that are too small to be visible in XRD patterns. For the co-dopant material – 1 wt. % each Cu and Cr – only ceria can be identified in the diffraction pattern as well. For Cu-doped ceria with 9 wt. % Cu, two additional diffraction peaks are seen at 36.9 and 43.5° 2θ – likely CuO and Cu_2O (Figure 30). [261] Therefore, it is likely that at 7 wt. % Cu and below, copper atoms are introduced within the ceria lattice, substituting cerium with copper ions, but above 7 wt. %, additional copper atoms are unable to be substituted into the lattice and agglomerate into copper oxide particles.

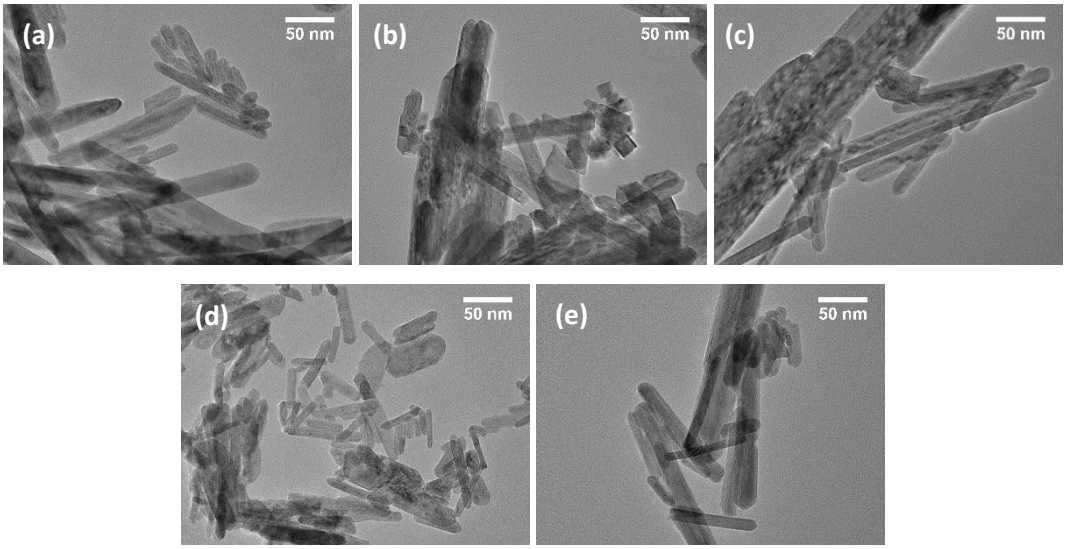

Figure 28. TEM micrographs of (a) undoped ceria nanorods, (b) 7 wt. % Cu-doped ceria nanorods, (c) 4 wt. % Mn-doped ceria nanorods, (d) 5 wt. % Cr-doped ceria nanorods, and (e) 1 wt. % each Cu/Cr-doped nanorods.

A small shift to higher 2θ values can be seen in the diffraction patterns with all dopants, shown in Figure 31. For Mn, Cu, and Cr-doped ceria, a higher level of dopant corresponds with a larger peak shift, indicative of increasing levels of incorporation into the crystal lattice. [135] In the case of copper, this shift only continues up to 7 wt. % copper – at higher copper dopant levels, there is no further shift which further support the formation of

external copper oxide particles at high loading levels. The Ce^{4+} ionic radius is 0.97 Å, compared with 0.73 Å for Cu^{2+} and 0.615 Å for Cr^{3+}. [262] Therefore, it is expected that increasing levels of dopant will decrease the unit cell size if the dopant is successfully integrated into the lattice structure. Correspondingly, unit cell values calculated using Bragg's Law for the doped ceria materials show a decrease in the size of ceria's unit cell with increasing levels of dopant (Figure 32a).

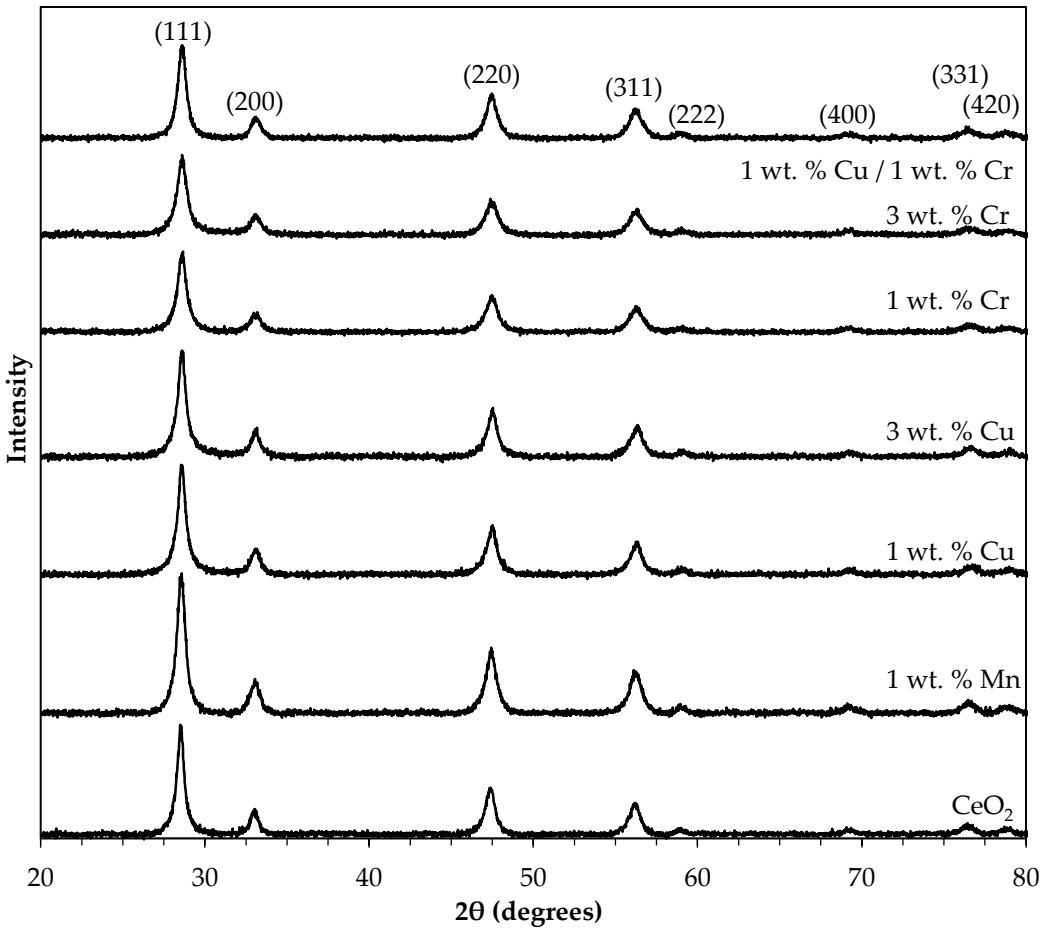

Figure 29. Powder XRD patterns of undoped, Mn-doped, Cu-doped, and Cr-doped ceria nanorods. Ceria diffraction peaks are labelled with their Miller indices.

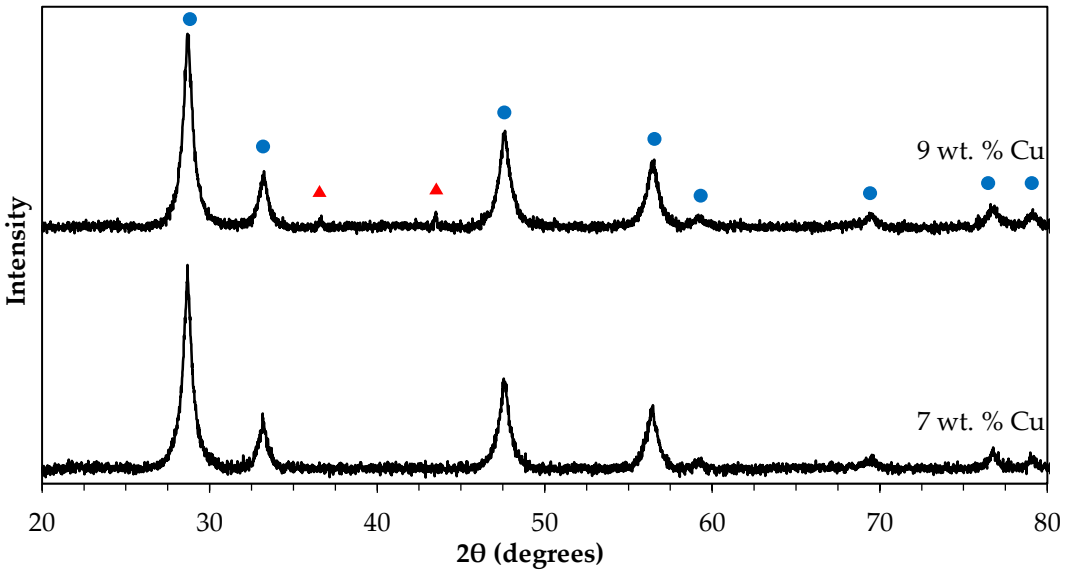

Figure 30. Powder XRD patterns of 7 and 9 wt. % Cu-doped ceria nanorods. ● indicates ceria diffraction peaks and ▲ indicates copper oxide diffraction peaks.

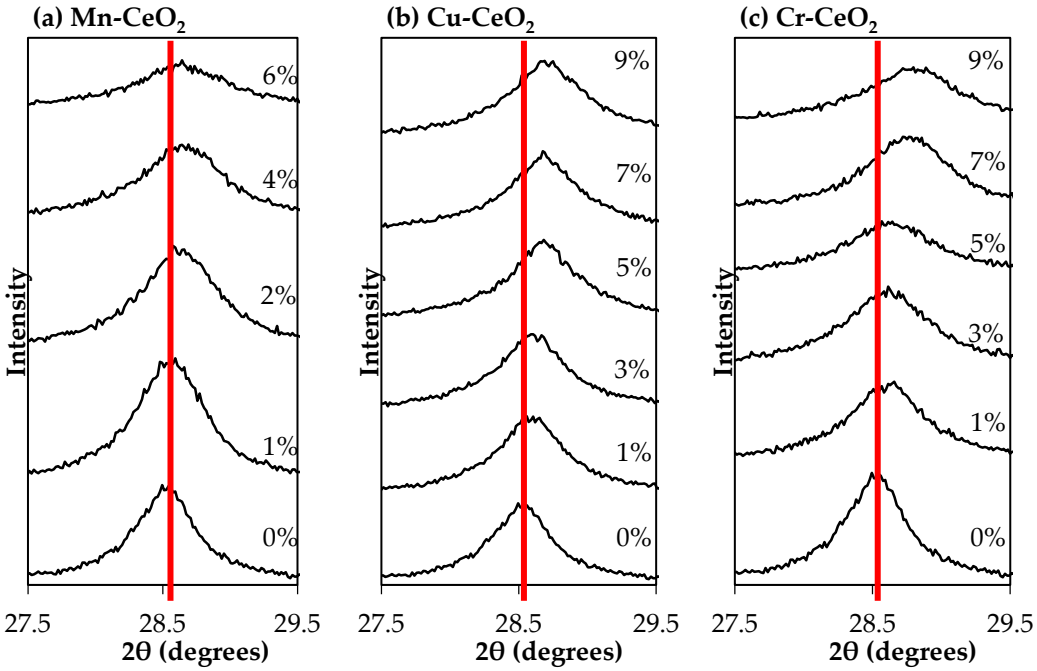

Figure 31. (111) diffraction peak shift for (a) Mn-doped, (b) Cu-doped, and (c) Cr-doped ceria nanorods prepared with different dopant concentrations.

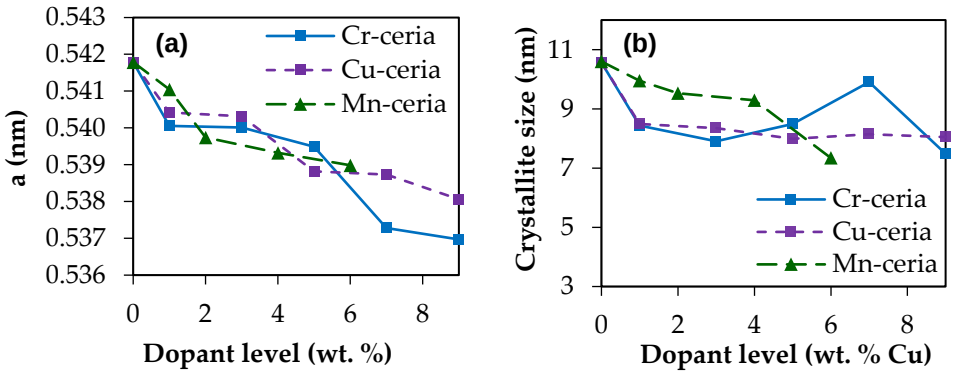

Figure 32. (a) Unit cell parameter 'a' vs. dopant wt. % and (b) crystallite size vs. dopant wt. % for Mn, Cu, and Cr-doped ceria nanorods.

In addition to unit cell dimensions, crystallite size calculations using the Scherrer equation show that increasing the amount of dopant decreases the crystallite size, shown in Figure 32b. This is potentially related to the preparation method used for nanorod synthesis. When the cerium precursor is added to the NaOH solution, $Ce(OH)_3$ nuclei are formed. During hydrothermal synthesis, these nuclei dissolve and then recrystallize into nanorods, growing anisotropically. [37] High levels of additional ions in the solution can interfere with this process – which would explain the nanoparticles and small nanocubes seen in Figure 28 in addition to ceria nanorods. However, Cr-doped ceria does not follow this trend of decreasing crystallite size past a dopant level of 5 wt. %.

Representative Raman spectra of undoped and doped ceria nanorod samples are shown in Figure 33. Ceria has a characteristic Raman band at approximately 465 cm^{-1} (F_{2g} mode), which is attributed to the symmetric vibrational breathing of oxygen surrounding the cerium ions in the fluorite-type crystal lattice. [263] This band is prominent in all spectra, but for the doped ceria samples is shifted. There are two main contributions to this shift. First, the substitution of Ce ions with the dopant ions changes the lattice parameters and the oxygen-metal bond length, affecting lattice vibration, and second, differences in oxygen vacancy concentration affect the vibrational mode as well. [264,265] Additionally, Raman peak broadening is visible in the doped ceria materials, which is associated with changes in crystallite size. [266] This correlates well with the crystallite size data calculated from the XRD spectra in Figure 29, which showed a crystallite size decrease upon doping. An additional band at approximately 600 cm^{-1} is visible in the doped ceria

samples, more prominently than in the case of undoped ceria. This band is generally attributed either to the quantity of oxygen vacancies in the sample or point defects related to the presence of Ce^{3+} ions. [263] Therefore, it can be concluded that the use of copper or chromium dopants increases the quantity of oxygen vacancies in the ceria nanorod samples.

In addition to the characteristic ceria bands, chromium-doped ceria samples had a prominent band at 860 cm^{-1} and a weak one at 1010 cm^{-1}. Both of these are indicative of the presence of CrO_3, suggesting that some chromium is present as a separate oxide phase instead of being incorporated into ceria's lattice structure. [267] This contrasts with the powder XRD spectrum of Cr-ceria, in which only ceria diffraction peaks are visible – however, Cr particles may be present that are not visible with powder XRD.

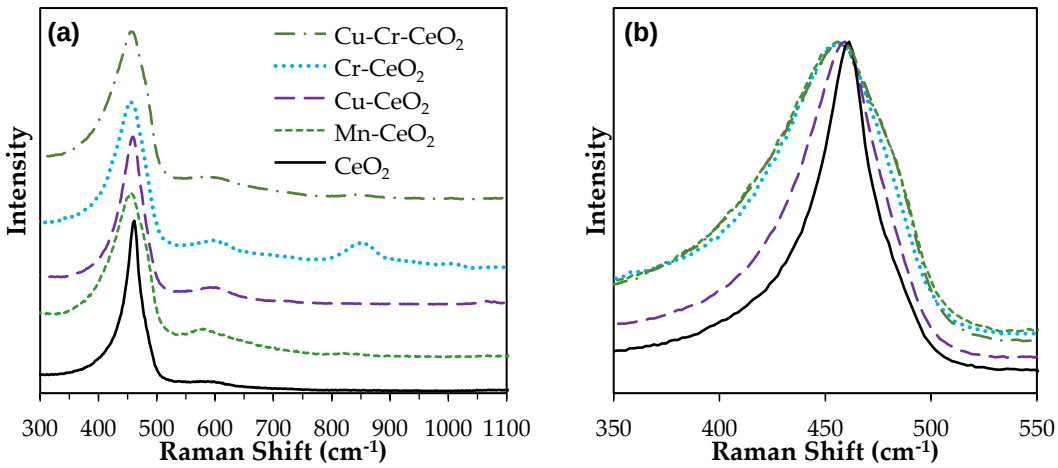

Figure 33. (a) Raman spectra of undoped and doped (1 wt. % Mn, 1 wt. % Cu, 1 wt. % Cr, and 1 wt. % each co-doped Cu+Cr) ceria nanorods. (b) F_{2g} Raman band for same ceria samples.

To understand how Cu and Cr dopants affect the reducibility of the ceria nanorod catalysts, TPR experiments were performed on the undoped and doped materials (Figure **34**). For nanosized ceria materials, two areas of reduction are typically seen – a low temperature area (200 to 500 °C) representing consumption of hydrogen due to readily available surface oxygen, and a higher temperature area (>600 °C) representing reduction of the bulk lattice oxygen. [37,268] In most cases, the deconvolution of the lower temperature reduction area (between 200 and 500 °C) can be represented with two Gaussian peaks (percentage peak fitting error inferior to 3%). For copper doped ceria

nanorods, the position of these two low-temperature peaks shifts to the left, from 359 and 467 °C corresponding to undoped ceria nanorods to 275 and 338 °C for the 5 wt. % Cu-doped ceria, indicating an increase in surface reducibility at lower temperatures with increasing levels of copper dopant (Table 1). Additionally, the ratio of areas of these two peaks shifts in favour of the second peak in the presence of Cu as dopant which suggests a decrease in the readily available surface oxygen. For chromium-doped ceria nanorods, while the same trend in peak areas is present, increasing the quantity of Cr dopant does not improve surface reducibility at lower temperatures. There is a shift to lower temperature reduction from undoped ceria to 1 wt. % Cr-doped ceria (303 and 418 °C respectively), but no further shift to lower temperatures with increasing levels of Cr.

In addition to the deconvolution of the low-temperature reduction area, the ratio of low-temperature to high-temperature areas can be used as a qualitative assessment of the reducibility of the bulk lattice structure, relative to the surface. Doping ceria with other metals generally changes bulk properties, not just those of the surface. [18] While reactions such as CO oxidation and NO reduction occur on the surface of ceria catalysts, improvements in bulk properties can also improve catalyst performance due to the mobility of oxygen vacancies and vacancy hopping mechanisms. [96,269] For undoped ceria the ratio of low-temperature to high-temperature areas is 0.47 (Table 2). With increasing levels of copper dopant, this ratio shifts in favour of the high-temperature area, indicating that relative to the surface, the bulk structure becomes more reducible. However, for chromium-doped ceria, the opposite trend is seen – the bulk becomes *less* reducible relative to the surface. This could be due to improvement of the surface reducibility and not the bulk.

Two additional sharp and intense reduction peaks appear in the 7 wt. % copper-doped ceria nanorods, centred at 197 and 222 °C. These peaks can be attributed to the reduction of copper particles, segregated from the ceria phase due to the high dopant content. [270–272] While this slightly conflicts with XRD analysis (Figure 30), in which separate copper oxide diffraction peaks were not seen until dopant levels reached 9 wt. %, these particles may just be too small and dispersed to be visible in powder XRD diffraction patterns.

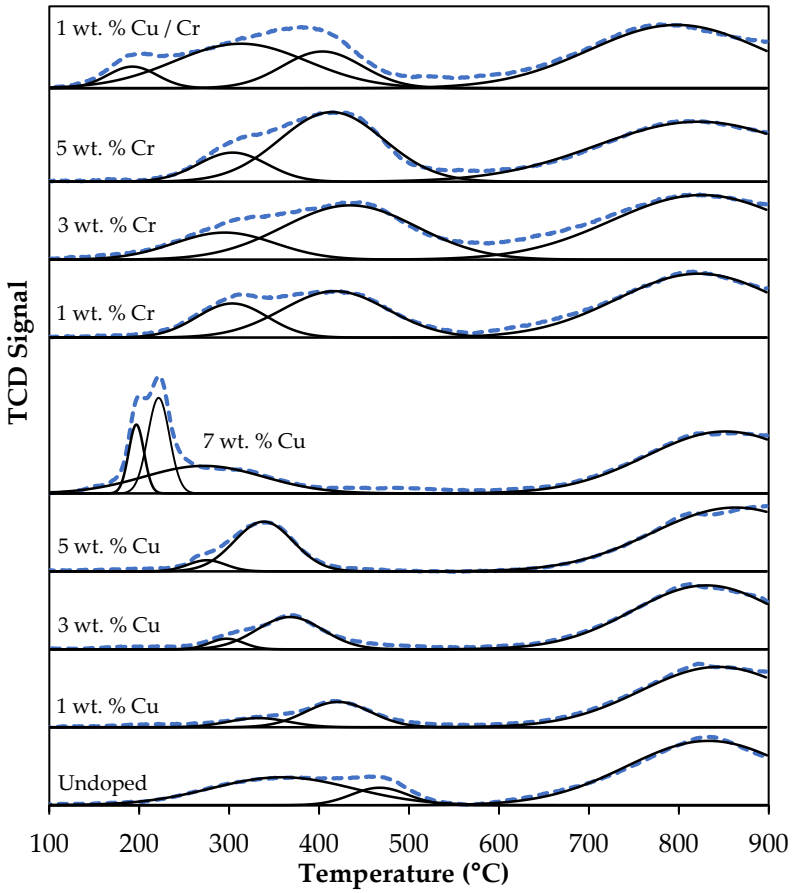

Figure 34. TPR analysis of undoped, Cu, Cr, and Cu+Cr-doped ceria nanorods. Dashed lines indicate experimental data and solid lines indicate fitted deconvolutions.

The TPR reduction profile of the simultaneous Cu- and Cr-doped ceria nanorods differs from the single-dopant materials – while there are still distinct low-temperature and high-temperature areas of reduction, the low-temperature reduction area is wider and extends further to lower temperature values in the case of the Cu-Cr doped ceria. Unlike the single-dopant nanorod samples, to keep the fitting error inferior to 3%, the deconvolution of this region is represented by three Gaussian peaks instead of two. The lowest-temperature peak is centred at 192 °C. This is a strong indication that the two-dopant material has much-improved surface reducibility compared to the single copper-doped ceria nanorods – a synergistic improvement that cannot be explained by the cumulative or average effect of the single-dopant contributions. Additionally, the ratio of the surface to bulk oxygen reduction areas is 1.2. This could also indicate an improvement in surface reducibility, or instead, similarly to Cr-doped ceria materials, the two-dopant system might not have improved the oxygen bulk reducibility but only that of the surface.

Table 1. TPR peak locations and areas for undoped and doped ceria nanorods.

Peak	Centre (°C)	Area
Undoped ceria nanorods		
Low temperature 1	359	14.1
Low temperature 2	467	3.5
High temperature 1	833	37.6
1 wt. % Cu		
Low temperature 1	333	3.1
Low temperature 2	421	9.2
High temperature 1	844	52.1
3 wt. % Cu		
Low temperature 1	297	1.8
Low temperature 2	367	10.5
High temperature 1	831	46.2
5 wt. % Cu		
Low temperature 1	275	2.0
Low temperature 2	338	13.7
High temperature 1	863	49.8
7 wt. % Cu		
Low temperature 1	197	4.7
Low temperature 2	222	9.3
Low temperature 3	272	14.7
High temperature 1	852	43.8
1 wt. % Cr		
Low temperature 1	303	6.0
Low temperature 2	418	12.1
High temperature 1	822	25.9
3 wt. % Cr		
Low temperature 1	295	7.3
Low temperature 2	435	19.4
High temperature 1	826	31.2
5 wt. % Cr		
Low temperature 1	304	4.5
Low temperature 2	414	16.2
High temperature 1	822	27.2
1 wt. % each Cu and Cr		
Low temperature 1	192	2.4
Low temperature 2	313	13.2
Low temperature 3	404	6.5
High temperature 1	798	18.5

Table 2. Ratio of low-temperature to high-temperature peak areas for ceria nanorod TPR profiles.

Material	Low T / High T area ratio
Undoped CeO_2	0.47
1 wt. % Cu	0.24
3 wt. % Cu	0.27
5 wt. % Cu	0.31
7 wt. % Cu	0.34
1 wt. % Cr	0.70
3 wt. % Cr	0.86
5 wt. % Cr	0.76
1 wt. % each Cu/Cr	1.20

XPS analysis was used to gain further insight into the surface state of the ceria nanorods. XPS spectra of Ce 3d, O 1s, Cu 2p, and Cr 2p are shown in Figure 35, Figure 37, and Figure 38. In Figure 35, the Ce 3d XPS spectra consist of five peaks (U_o, U, U', U'', and U''') representing $3d_{3/2}$ and five peaks (V_o, V, V', V'', and V''') representing $3d_{5/2}$. According to previously published methods, V_o + V' + U_o + U' can be assigned to Ce^{3+}, while the remaining peaks (V, V'', V''', U, U'', and U''') can be assigned to Ce^{4+}, and the relative ratio of peak areas can be used to determine the percentage concentration of Ce^{3+} and Ce^{4+} at the surface. [257,263,268] This is shown in Figure 36. This analysis reveals that undoped ceria nanorods have a nonstoichiometric surface, with 22 % of Ce 3d photoemission due to Ce^{3+} and 78 % due to Ce^{4+}. The addition of low levels of Cu dopant (1 and 3 wt. %) only slightly increases the concentration of Ce^{3+}, but higher levels of Cu (5 and 7 wt. %) result in a higher level of surface reduction, with the percentage of Ce^{3+} increasing to 26 and 27 %, respectively. In contrast, the addition of Cr dopant decreases the percentage of Ce^{3+} at the surface. Both results corroborate the TPR analysis above – generally speaking, Cu improves ceria's surface reducibility while Cr does not have a relevant effect. Cu-Cr co-doped ceria nanorods demonstrate the highest level of surface reduction, with the concentration of Ce^{3+} calculated to be 33 %. This phenomenon of enhanced surface reducibility with low levels of both Cu and Cr dopant also supports the TPR analysis in Figure 34.

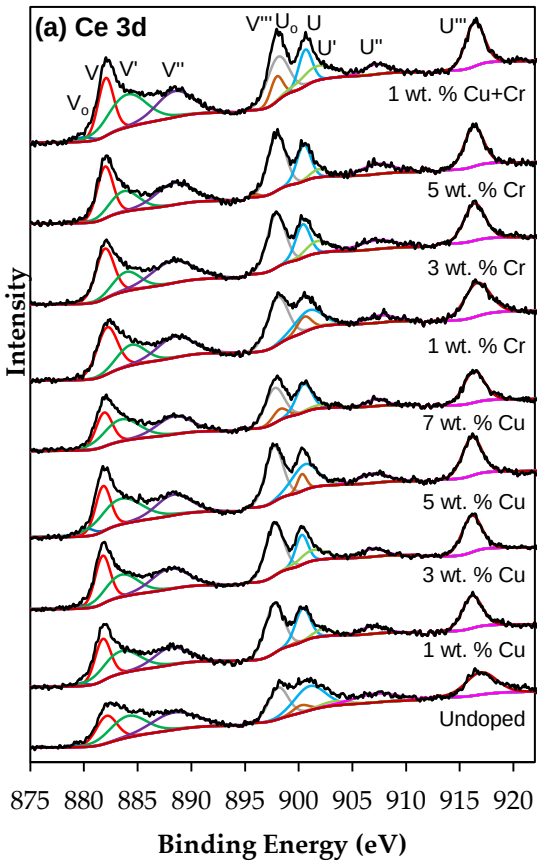

Figure 35. Ce 3d XPS spectra for undoped, Cu, Cr and Cu+Cr-doped ceria nanorods.

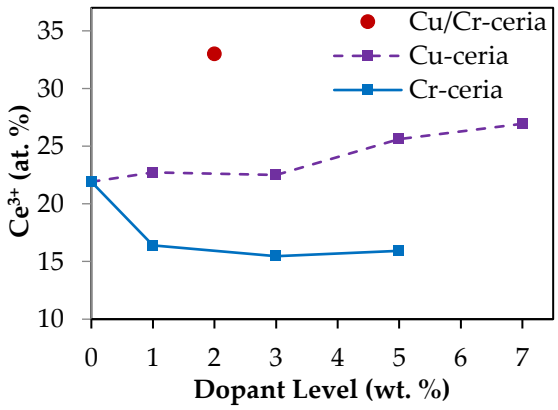

Figure 36. Surface concentration of Ce^{3+} at the surface of undoped and doped ceria nanorods, determined from Ce 3d XPS spectra.

XPS spectra in the O 1s region are shown in Figure 37 for the undoped and doped ceria nanorods, while relative peak areas are reported in Table 3. The O 1s spectrum is broad and consists of peak contributions from the various oxygen species at the surface of ceria. These spectra were resolved with three Gaussian-Lorentzian peaks. The peak at approximately 529 eV (O_α) can be attributed to the lattice oxygen of Ce^{4+}, while the peak

at 531 eV (O_β) can be attributed to oxygen vacancies or the lattice oxygen of Ce^{3+}. However, O_β can also be associated with surface adsorbed oxygen and hydroxyl groups. The broad peak at 533 eV (O_γ) is also associated with these surface oxygen species. [257,263] No shift in binding energy is evident when comparing the undoped and doped ceria samples. However, the undoped ceria spectrum has a larger contribution from stoichiometric lattice oxygen (O_α) than the doped materials – approximately 50 % of the total area of the three peaks compared with 38, 34, and 43 % for 1 wt. % Cu, 1 wt. % Cr, and 1 wt. % each Cu-Cr doped ceria, respectively.

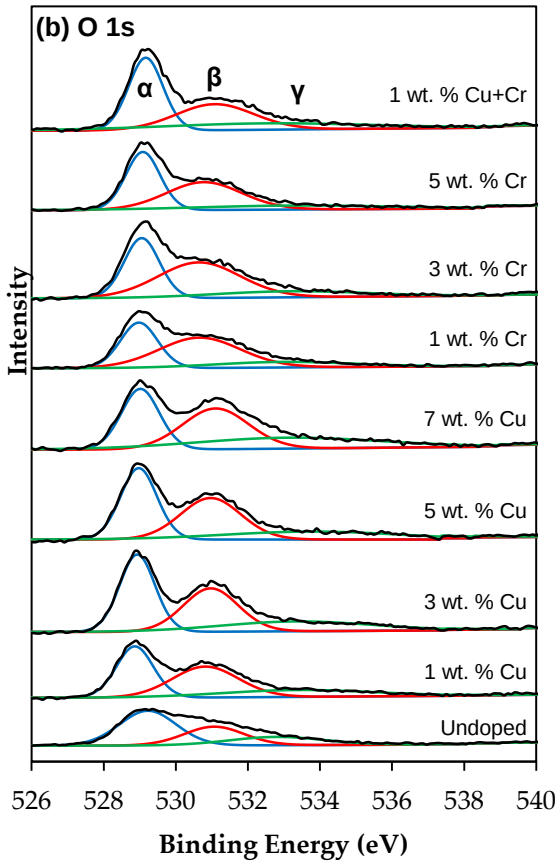

Figure 37. O 1s XPS spectra for undoped, Cu, Cr and Cu+Cr-doped ceria nanorods.

As shown in Figure 38a, no Cu 2p peaks are observable in the 1 wt. % Cu-doped ceria sample by XPS. Weak Cu $2p_{1/2}$ and Cu $2p_{3/2}$ peaks are visible in the 3 and 5 wt. % Cu-doped ceria materials, while the 7 wt. % Cu ceria material shows strong Cu $2p_{1/2}$ and Cu $2p_{3/2}$ peaks at 933.0 and 952.8 eV, respectively. Due to the lack of a clear shakeup satellite peak at 942 eV, such additional peaks in the 7 wt. % Cu sample can be tentatively assigned to Cu^+ or Cu^0. While the Cu 2p region is unable to distinguish between Cu^+ and metallic Cu,

TPR analysis (Figure 34) indicates that metallic Cu is likely present in the copper-doped ceria samples at a loading of 7 wt. % or higher. Because metallic Cu is not seen in the TPR analysis at Cu dopant levels below 7 wt. %, the Cu 2p peaks for these catalysts can be assigned to Cu^{+}. In contrast to 1 wt. % Cu-doped ceria, the sample simultaneously doped with 1 wt. % each Cu and Cr has observable Cu $2p_{1/2}$ and Cu $2p_{3/2}$ peaks, indicating that the co-doped ceria has a higher concentration of Cu at the surface than the single-dopant 1 wt. % Cu-ceria material. This corroborates other reports in the literature, which show that in Cu- and Cr-loaded ceria nanoparticles, the presence of Cr can enhance the surface concentration of Cu, but due to Cr's somewhat better solubility in the ceria lattice, Cr surface concentration is not enhanced. [273]

Figure 38b shows the Cr 2p XPS spectra for Cr and Cu/Cr-doped ceria nanorods. The visible Cr 2p peaks at approximately 576 and 587 eV indicate that Cr is in an oxidized state and can be assigned to Cr^{3+}. Intensity is higher for the 3 and 5 wt. % Cr samples. Unlike Cu, the XPS spectrum for co-doped 1 wt. % each Cu and Cr-doped ceria shows a weaker Cr intensity than 1 wt. % Cr-doped ceria.

Table 3. Relative peak areas for ceria nanorod O 1s spectra.

Material	O_α	O_β	O_γ
Undoped CeO_2	50.8	28.9	20.2
1 wt. % Cu	37.9	40.9	21.3
3 wt. % Cu	41.4	36.0	22.6
5 wt. % Cu	39.8	38.5	21.7
7 wt. % Cu	32.5	38.3	29.2
1 wt. % Cr	34.2	50.1	15.8
3 wt. % Cr	35.5	49.0	15.5
5 wt. % Cr	40.5	42.8	16.7
1 wt. % each Cu/Cr	42.5	34.4	23.1

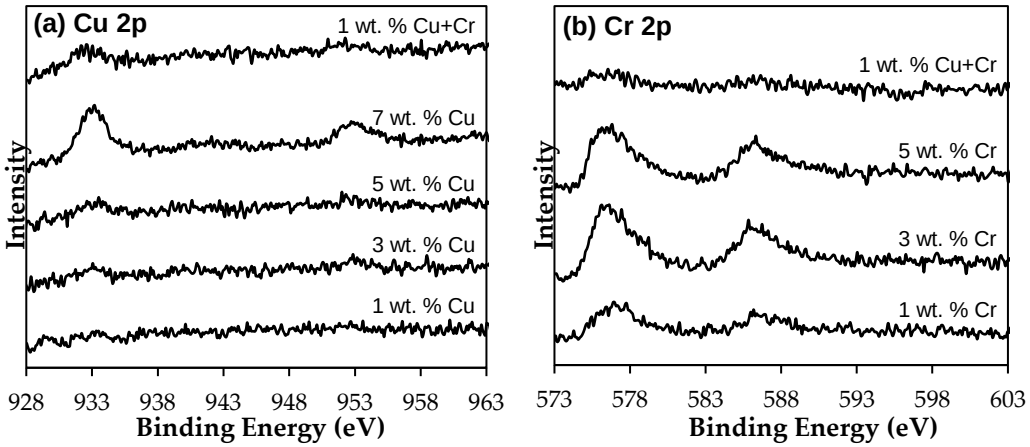

Figure 38. (a) Cu 2p and (b) Cr 2p XPS spectra for undoped, Cu, Cr, and Cu+Cr-doped ceria nanorods.

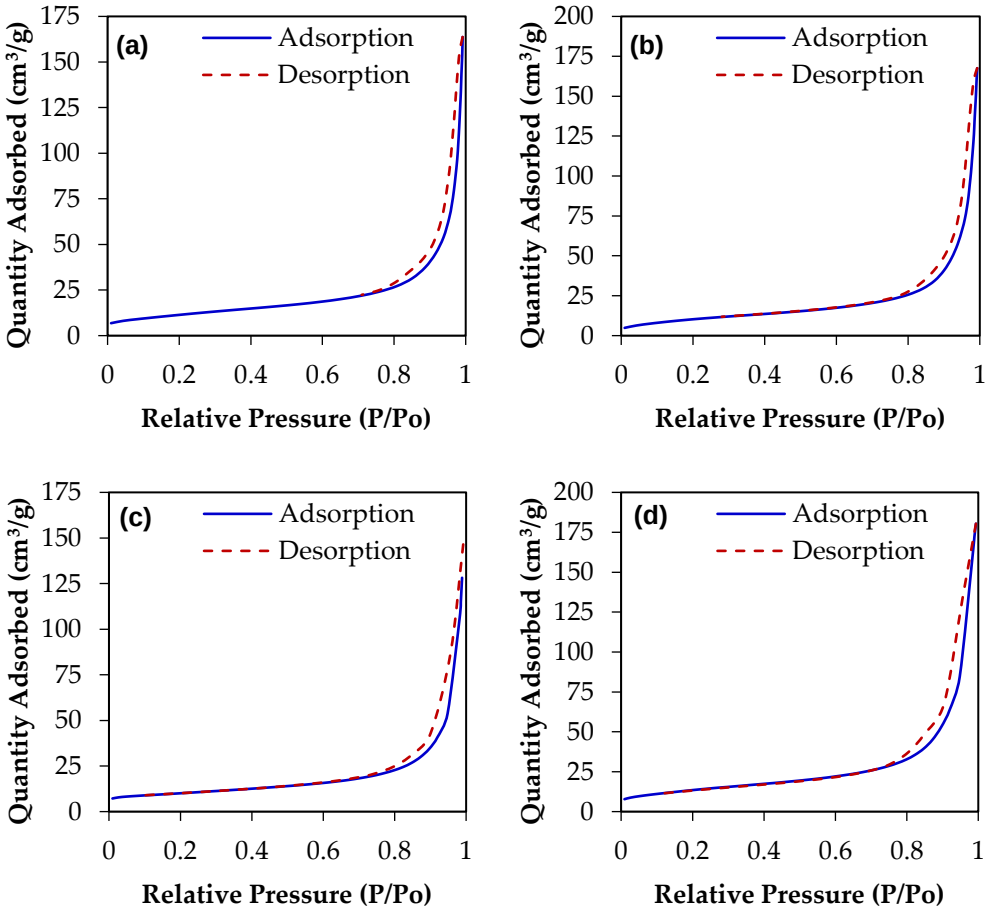

Figure 39. Nitrogen isotherms for (a) undoped, (b) 1 wt. % Mn-doped, (c) 1 wt. % Cu-doped, and (d) 1 wt. % Cr-doped ceria nanorods.

Nitrogen adsorption experiments show that the ceria nanorods, both undoped and doped, are non-porous but mesoporosity is observed due to interparticle voids, with a type IV isotherm in all cases (Figure 39). [274] BET surface area, measured at low relative

pressures, is in the range 29 to 55 m^2 g^{-1} (Figure 40). The presence of Cu has a negligible effect on the surface area, with no clear overall trend. For Cr-doped ceria, all doped samples had higher surface areas than undoped ceria nanorods. This is potentially due to the method of synthesis for ceria nanorods. The dissolution-recrystallisation rate of cerium in the reaction medium, dictated by the temperature and pressure inside the autoclave, as well as the time of the reaction, are the key parameters in determining product morphology. [37] Because of this, it is possible for the presence of other ions such as chromium to interfere with the nanorod growth process. As seen in Figure 28, TEM micrographs of the Cr-doped ceria nanorods show a lower range of nanorod lengths than are present in the other nanorod materials.

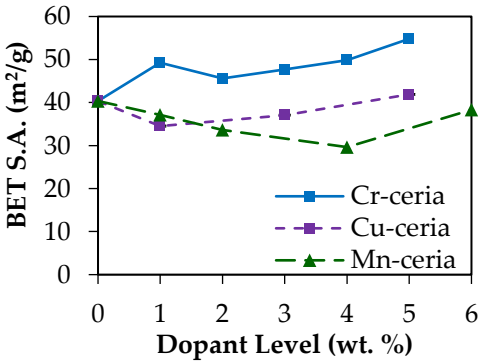

Figure 40. BET surface area vs. dopant level for Mn, Cu, and Cr-doped ceria nanorods.

5.2 Catalytic activity for CO oxidation and NO reduction

Catalytic activity of doped ceria nanorods for CO oxidation is shown in Figure 41-42. The addition of Mn improves low-temperature catalytic activity for CO oxidation with respect to undoped ceria nanorods, but improvements are only seen up to a loading of 2 wt. % Mn. Copper doping of ceria significantly improves the low-temperature catalytic activity for CO oxidation, with activity increasing as the Cu loading increases up to 7 wt. % Cu, above which no further improvements are observed. Based on previously published literature, this was expected – transition metal doping has been widely reported to improve the oxidative activity of ceria catalysts, particularly for CO oxidation. [275–277] The large jump in activity between the 5 wt. % Cu and 7 wt. % Cu-doped ceria catalysts can be explained with the appearance of the separate copper oxide phase at 7 wt. % Cu

loading (and at 9 wt. % in powder XRD), seen in the TPR analysis. Ceria-supported copper is known to be an effective low-temperature oxidative catalyst. [278] However, copper and other base metals are not used in automotive catalysis due to sulphur poisoning and thermal durability issues, so despite the enhanced activity, a separate copper phase is not desirable. [6]

A further increase in copper loading from 7 to 9 wt. % did not result in an improvement in low-temperature activity. This can be attributed to the doping limit being reached somewhere between 5 and 7 wt. % Cu, and the larger, agglomerated copper oxide particles in the 9 wt. % sample (visible in XRD and TPR) not providing more catalytic activity than the copper oxide particles present in the 7 wt. % Cu-ceria nanorod material (only visible in TPR). In contrast to manganese and copper, doping ceria nanorods with chromium reduced its catalytic activity for CO oxidation compared with undoped ceria nanorods. This also correlates with TPR and XPS results, which suggest that chromium doping of ceria decreased the reducibility of the material.

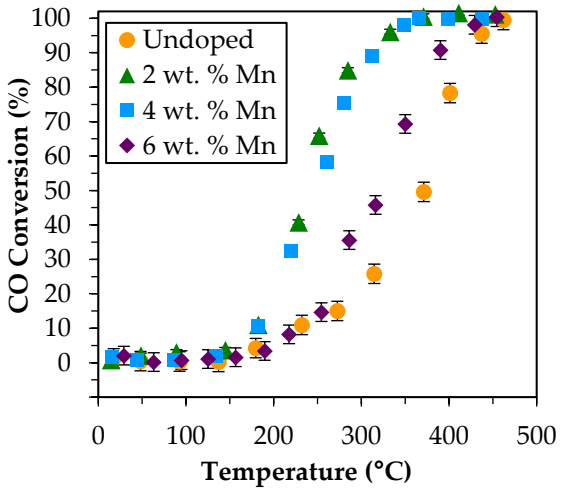

Figure 41. CO oxidation catalytic performance for Mn-doped ceria nanorods.

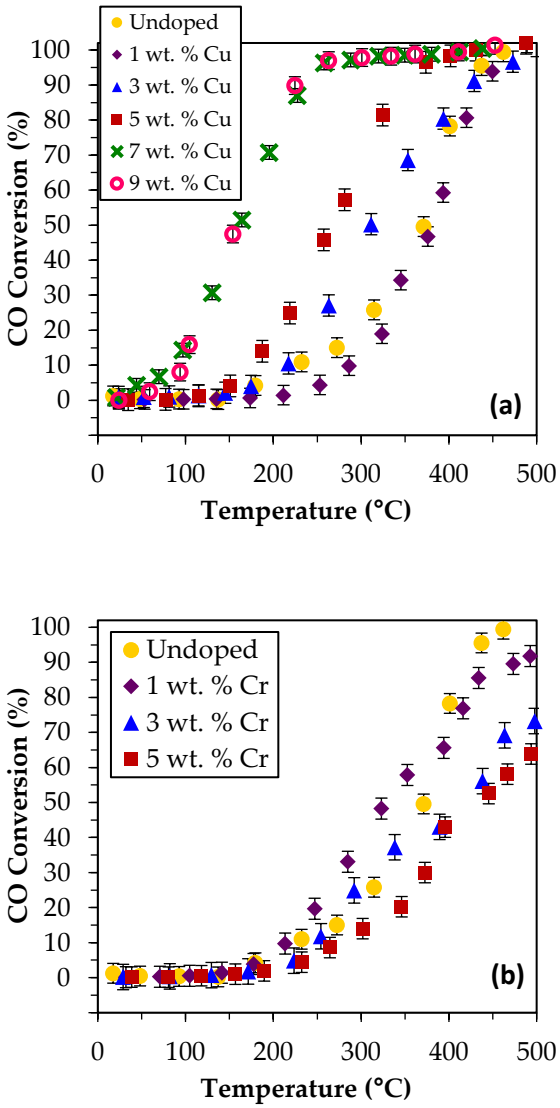

Figure 42. CO oxidation catalytic performance for (a) Cu-doped and (b) Cr-doped ceria nanorods.

The catalytic activity of Cu and Cr-doped ceria nanorods for NO reduction is shown in Figure 43. Cr-doped ceria nanorods are effective at improving catalytic activity beyond that of pure ceria, while Cu-doped ceria shows no improvement compared with pure ceria nanorods. This is expected in view of the characterisation – Cu doping improves ceria's oxidative catalytic activity by increasing the reducibility of ceria, but this is not helpful for reducing reactions. [113] In contrast, chromium demonstrates the opposite effect. However, chromium doping at levels above 1 wt. % do not show further improvement, with activity similar to that of 1 wt. % Cr-doped ceria. As with CO oxidation, this activity matches the analysis of the Ce 3d XPS spectra – ceria nanorods doped with 1, 3, and 5 wt. % Cr showed very similar levels of surface reduction.

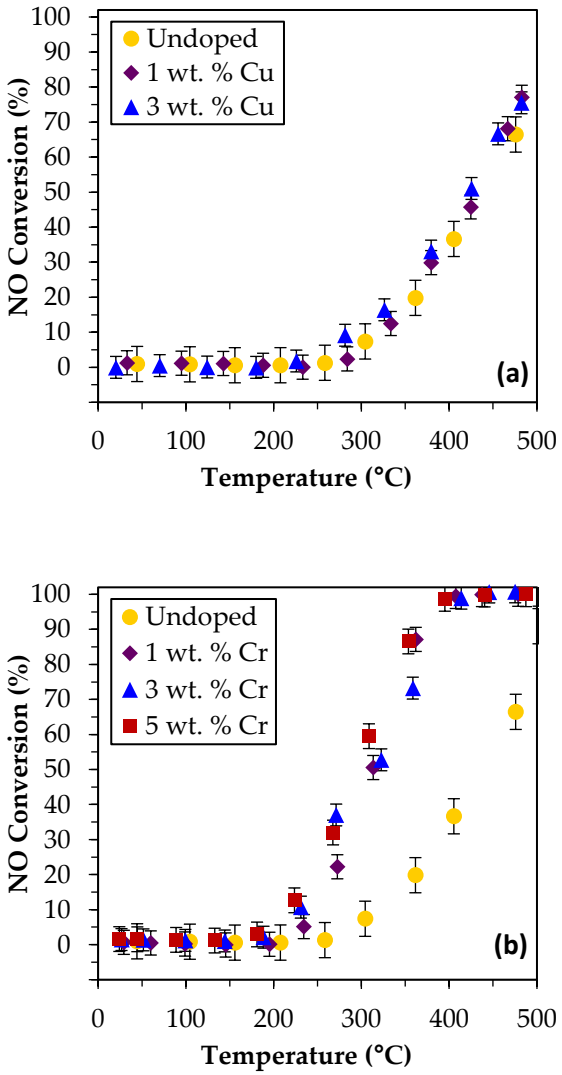

Figure 43. NO reduction catalytic performance for (a) Cu-doped and (b) Cr-doped ceria nanorods.

Catalyst performance of the 1 wt. % Cu and Cr co-doped ceria nanorod material is shown in Figure 44a for CO oxidation and Figure 44b for NO reduction. Despite containing only 1 wt. % Cu and Cr, the two-dopant ceria nanorods show activity for CO oxidation that is comparable to the activity of the 7 and 9 wt. % Cu-ceria nanorods. Therefore, co-doped Cu-Cr ceria appears to provide a unique synergistic effect, with an activity close to the one of 7 wt. % Cu-doped ceria nanorods for CO oxidation, despite only containing 1 wt. % Cu (2 wt. % total dopant content) and not having a separate copper phase. At the same time, the two-dopant catalyst retains activity for NO reduction that is similar to that of the Cr-doped ceria nanorods, with a slightly improved T_{10} value.

DFT simulations by Koizumi *et al* and Yoshida *et al* can explain such synergy. [273,279] They report that when Ce on the (111) surface of ceria is substituted with Cu, the dominant species is Cu^{2+}. However, the substitution of Ce with Cu and Cr results in the dominant Cu species being Cu^{+}. The presence of Cu^{+} in doped ceria is known to enhance CO chemisorption on the catalyst surface and catalytic activity for CO oxidation. [280] Conversely, for the reduction of NO, the presence of Cr enhances electron density on neighbouring Ce sites and lowers the barrier for oxygen vacancy formation, both of which improve NO adsorption on the doped ceria surface. [114,281] This corroborates the enhanced reducibility of the Cu/Cr-doped ceria seen in TPR and XPS analysis as well as the significantly improved catalytic performance for CO oxidation compared with single-dopant ceria. However, it should be noted that synergistic enhancement in the co-doped ceria nanorod catalyst for NO reduction was quite minor.

Therefore, while doping ceria with copper improves CO oxidation activity but not NO reduction activity and doping ceria with chromium improves NO reduction activity but reduces CO oxidation activity, the simultaneous co-doping of ceria nanorods with both Cu and Cr retains the benefits of each single dopant while significantly enhancing oxidative activity, a phenomenon that has not yet been reported in the literature for this doped system. These results also show that the improved reducibility provided by copper doping does not necessarily have a negative effect on the healing of oxygen vacancies. Doping the same ceria catalyst with both Cu and Cr is necessary for this synergistic effect – a physical mixture of Cu-doped ceria and Cr-doped ceria shows much lower catalytic activity (Figure 45).

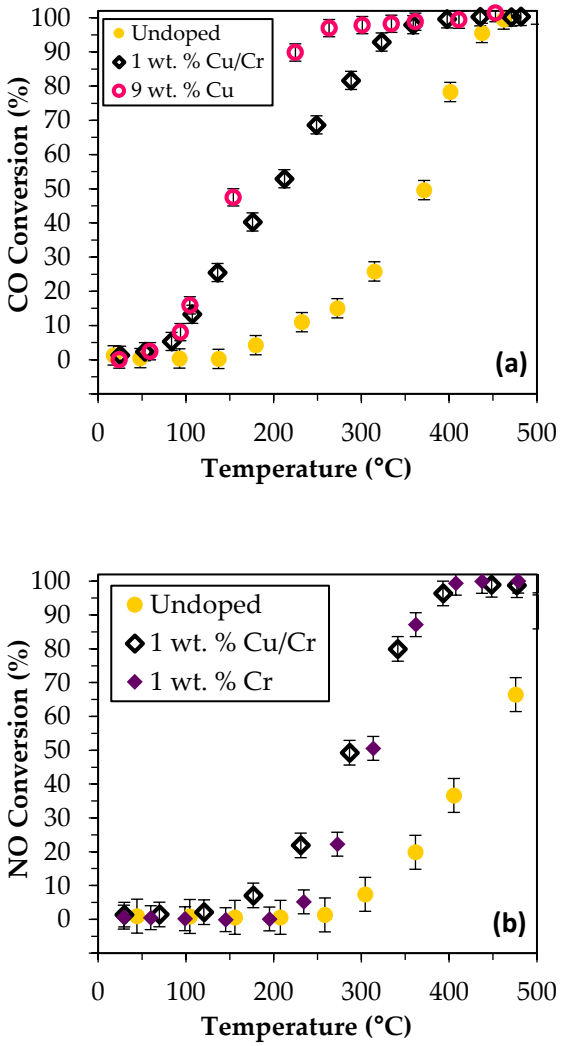

Figure 44. (a) CO oxidation and (b) NO reduction catalytic performance for undoped and Cu/Cr co-doped ceria nanorods.

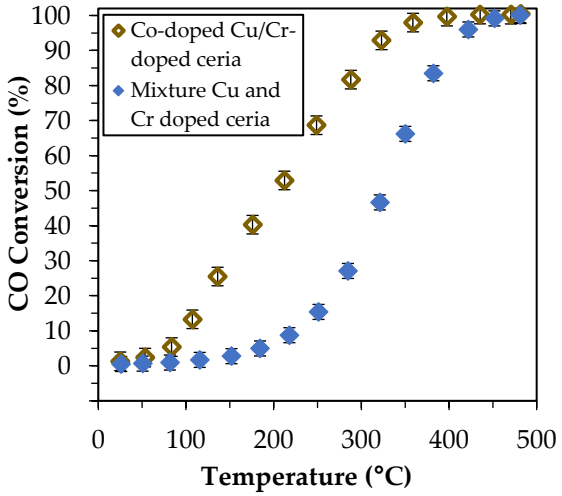

Figure 45. CO oxidation catalytic performance for ceria nanorods co-doped with 1 wt. % each Cu+Cr (15 mg catalyst weight), compared with a physical mixture of 2 wt. % Cu-doped ceria and 2 wt. % Cr-doped ceria (7.5 mg each, to achieve equal amounts of Ce, Cr, and Cu).

Various other ceria catalysts doped with copper or chromium have recently been reported. [131,180,282–284] Direct comparisons with other papers is difficult due to differences in reaction conditions such as catalyst loading and reactant flowrates or ratios, which wildly vary between different research groups. Nevertheless, activities can be normalized in terms of turnover frequency, shown in Table 4 for CO oxidation and Table 5 for NO reduction, along with T_{10} and T_{50} values (the temperature at which 10% and 50% conversion of CO is achieved). While the Cu- and Cu/Cr-doped catalyst materials reported in this work do not match the low-temperature performance of 10 mol % Cu-doped ceria nanorods for CO oxidation reported by Li *et al*, their performance does exceed that of other catalysts reported in Table 4. [131] Moreover, this was achieved with a much lower dopant level – only 1 wt. % Cu and 2 wt. % total Cu+Cr dopant content. In contrast, for NO reduction, our Cu/Cr-doped ceria nanorods performed slightly better at 150 °C but somewhat worse at 200 °C compared with a Cr-doped ceria catalyst ($Ce_{20}Cr_1O_x$) or a 0.14 wt. % Cu/Cr deposited on ceria (Table 1). [180] In any case, the latter uses a pulsed cathodic arc plasma technique in vacuum, much more complicated than our hydrothermal approach.

Table 4. Comparison of copper-ceria catalysts for CO oxidation.

Catalyst	T_{10} (°C)	T_{50} (°C)	Rate (μmol g^{-1} min^{-1})		Ref.
			At 50 °C	At 100 °C	
1 wt. % each Cu/Cr co-doped ceria nanorods	100	206	8.2	27.3	This work
3.9 wt. % Cu-doped ceria nanorods	65	122	61.3	352.7	[131]
3.9 wt. % Cu-doped ceria nanospheres	142	232	0.0	13.1	[282]
2.0 wt. % Cu-doped ceria nanopolyhedra	113	161	0.0	1.2	[283]
8.5 wt. % Cu deposited on ceria nanorods	40	73	16.4	90.0	[284]
0.14 wt. % Cu/Cr deposited on ceria	86	120	0.0	18.0	[279]

Table 5. Comparison of chromium-ceria catalysts for NO reduction.

Catalyst	T_{10} (°C)	T_{50} (°C)	Rate (μmol g^{-1} min^{-1})		Ref.
			At 150 °C	At 200 °C	
1 wt. % each Cu/Cr co-doped ceria nanorods	194	243	6.1	26.6	This work
$Ce_{20}Cr_1O_x$	202	216	0.0	40.9	[180]
0.14 wt. % Cu/Cr deposited on ceria	143	300	17.2	45.4	[285]

5.3 Kinetics

The apparent activation energy (E_a) of the doped ceria nanorod catalysts discussed in Section 5.2 have been calculated for further comparison (Table 6 and Table 7). Arrhenius plots used to calculate E_a values are shown in Figure 46 and Figure 47. It has been reported in the literature that when the concentration of CO is low and there is an excess of O_2, CO oxidation is a first-order reaction with respect to CO, and zero-order with respect to O_2. [286,287] With a low CO concentration of 0.2 % and 2x excess of O_2, the reaction conditions used in our paper meet these conditions. Therefore, the reaction rate and Arrhenius equations can be simplified:

$$r = -kc = -A\left(e^{-E_a/RT}\right)c \tag{16}$$

Where r is the reaction rate (mol s^{-1}), k is the rate constant (s^{-1}), c is the concentration of CO, A is the pre-exponential factor, E_a is the apparent activation energy (J/mol), R is the ideal gas constant (J mol^{-1} K^{-1}), and T is temperature (K). This equation can be rewritten in the following form:

$$\ln(k) = -\frac{E_a}{RT} + \ln(A) \tag{17}$$

And used to derive E_a values. Calculations were performed with conversion levels below 10 %.

NO reduction by CO has been reported to be modelled as first-order with respect to both NO and CO and second-order overall. [288,289] Therefore, the reaction rate can be expressed in terms of NO and CO concentration (Equation 18), or just NO concentration (Equation 19)

$$r = k[\mathrm{NO}][\mathrm{CO}] \tag{18}$$

$$r = k[\mathrm{NO}](1-x)[\mathrm{CO}](\varepsilon - x) \tag{19}$$

Where k is the second-order rate constant (L mol^{-1} s^{-1}), x is the conversion level of NO, and ε is the ratio of CO to NO. Similarly to CO oxidation, Equation 17 was used to determine E_a values with conversion levels below 10 %.

The Arrhenius plots in Figure 46 and E_a values in Table 6 show that doping ceria with copper reduces the value of E_a for CO oxidation, with an increasing effect up to 7 wt. % Cu. Calculated values ranged from 44.0 kJ mol^{-1} for undoped ceria nanorods to 31.4 kJ mol^{-1} for 7 wt. % Cu-doped ceria. In contrast, doping ceria with chromium results in an increase in E_a (52.8 kJ mol^{-1} for 5 wt. % Cr-doped ceria). The ceria sample doped with 1 wt. % each Cu and Cr has a lower E_a value, 32.8 kJ mol^{-1}, comparable to that of 7 wt. % Cu.

The E_a value for NO reduction with an undoped ceria nanorod catalyst was 118.6 kJ mol^{-1}, higher than that for CO oxidation. This value did not significant change with the addition of copper, but decreased to 97.5 kJ mol^{-1} for 1 wt. % Cr-doped ceria. The Cu and Cr co-doped ceria material showed a further decrease to 58.1 kJ mol^{-1}. These values corroborate the analysis in Section 5.2, which show that co-doping ceria nanorods with 1 wt. % each Cu and Cr is much more beneficial than doping with a similar level of a single transition metal.

Table 6. Apparent activation energy (E_a), Weisz-Prater criterion (C_{WP}), and Mears criterion (MR) for ceria nanorod catalysts and CO oxidation.

Sample	E_a (kJ mol^{-1})	$C_{WP,\ 150\ °C}$	$MR_{10\%}$
Undoped ceria nanorods	44.0	0.014	$6.16 \cdot 10^{-6}$
3 wt. % Cu-doped ceria	43.5	0.034	$6.11 \cdot 10^{-6}$
5 wt. % Cu-doped ceria	40.5	0.055	$5.83 \cdot 10^{-6}$
7 wt. % Cu-doped ceria	31.4	0.647	$5.19 \cdot 10^{-6}$
1 wt. % Cr-doped ceria	47.1	0.014	$6.10 \cdot 10^{-6}$
3 wt. % Cr-doped ceria	51.7	0.014	$6.45 \cdot 10^{-6}$
5 wt. % Cr-doped ceria	52.8	0.014	$6.45 \cdot 10^{-6}$
1 wt. % Cu+Cr doped ceria	32.8	0.454	$5.33 \cdot 10^{-6}$

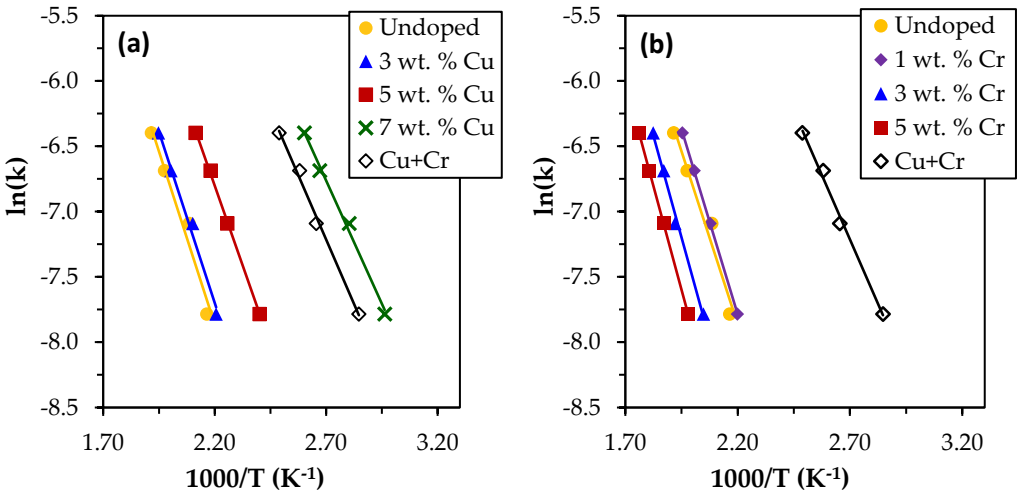

Figure 46. Arrhenius plots for CO oxidation over (a) undoped and Cu-doped ceria nanorods, and (b) undoped and Cr-doped ceria nanorods. Cu+Cr nanorods are doped at 1 wt. % each.

Table 7. Apparent activation energy (E_a), Weisz-Prater criterion (C_{WP}), and Mears criterion (MR) of ceria nanorod catalysts for NO reduction.

Sample	E_a (kJ mol^{-1})	$C_{WP,\ 300\ °C}$	$MR_{10\%}$
Undoped ceria nanorods	118.6	0.065	$5.61 \cdot 10^{-6}$
1 wt. % Cu-doped ceria	118.7	0.065	$5.68 \cdot 10^{-6}$
1 wt. % Cr-doped ceria	97.5	0.371	$5.32 \cdot 10^{-6}$
1 wt. % Cu+Cr doped ceria	58.1	0.510	$4.96 \cdot 10^{-6}$

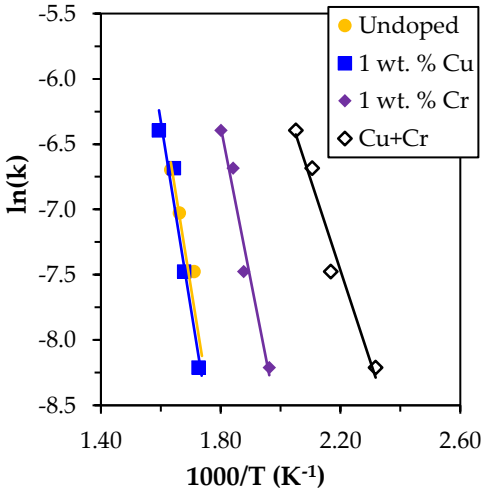

Figure 47. Arrhenius plots for NO reduction over undoped and doped ceria nanorods.

While excessively low apparent activation energy values may be a potential indication that a reaction is not under kinetic control, similar E_a values have been reported for ceria

catalysts elsewhere in the literature. [290,291] Additionally, Weisz-Prater and Mears criteria were employed to determine if the CO oxidation and NO reduction reactions were limited by internal and external diffusion, respectively. The Weisz-Prater criterion, shown in Equation 20, is a method used to determine if heterogeneous catalytic reactions are limited by internal pore diffusion. [292–295] If $C_{WP} < 1$, the reaction is not limited by internal diffusion, and there are no concentration gradients within catalyst particles. Here, $r_A(obs)$ is the observed rate of reaction (mol g^{-1} s^{-1}), ρ_c is the solid catalyst density (g m^{-3}), R is the catalyst particle radius (m), D_e is the effective diffusivity of the reacting species (m^2 s^{-1}), and C_{As} is the reactant concentration (mol m^{-3}). In Table 6 and 7, C_{WP} values are shown for CO oxidation at 150 °C and NO reduction at 300 °C, and are below a value of 1 for all doped and undoped ceria catalysts. In general, the C_{WP} values of these catalysts does not approach 1 until full conversion is almost achieved. Therefore, comparisons of catalyst performance at lower conversion levels are still valid.

$$C_{\mathrm{WP}} = \frac{-r_{\mathrm{A}}(\mathrm{obs})\rho_{\mathrm{c}}R^2}{D_{\mathrm{e}}C_{\mathrm{As}}} \tag{20}$$

The Mears criterion, shown in Equation 21, is a method used to determine if external mass transfer of the reacting species from the bulk gas flow to the surface of the catalyst can be ignored. [292,294–298] If MR < 0.15, external mass transfer effects can be neglected and are not rate-limiting. Here, $r_A(obs)$ is the observed rate of reaction (mol g^{-1} s^{-1}), ρ_b is the catalyst bed density (g m^{-3}), R is the catalyst particle radius (m), n is the order of reaction, k_c is the mass transfer coefficient (m s^{-1}), and C_{Ab} is the reactant concentration in the bulk (mol m^{-3}).

$$MR = \frac{-r_{\mathrm{A}}(\mathrm{obs})\rho_{\mathrm{b}}Rn}{k_{\mathrm{c}}C_{\mathrm{Ab}}} \tag{21}$$

As shown in Table 6 and 7, MR < 0.15 for all undoped and doped ceria catalysts, calculated at 10 % conversion. This is true for both CO oxidation and NO reduction. Therefore, external mass transfer can be neglected and no concentration gradient exists between the bulk gas flow and the catalyst surface.

5.4 Conclusions

Copper, manganese, and chromium have been utilized as dopants for ceria nanorod catalysts produced via a hydrothermal synthesis method. Manganese doping is shown to improve the activity for CO oxidation compared with undoped ceria nanorods. Copper doping significantly enhances activity for CO oxidation but not for NO reduction. The opposite is true for chromium-doped ceria. However, simultaneously doping a ceria nanorod catalyst with both Cu and Cr dopants results in a catalyst which shows improved activity for both CO oxidation and NO reduction. Additionally, the use of dual dopants appears to provide a somewhat synergistic effect, with only 1 wt. % Cu and 1 wt. % Cr required to provide activity for CO oxidation similar to that of the 7 wt. % Cu-doped ceria nanorods. This behaviour is supported by TPR and XPS analysis, which shows that the co-doped ceria nanorods show improved low-temperature surface reducibility compared to either Cu or Cr single-dopant ceria materials.

This research demonstrates the potential effectiveness of co-doping with transition metals as a strategy for improving the low-temperature performance of ceria-based automotive catalysts. While future research, such as optimisation of dopant levels, examination of other dopant metals, and testing the catalyst under more typical real-world conditions, will be necessary, Cu/Cr-doped ceria nanorods show promise as an improved catalyst for both oxidative and reductive reactions in three-way catalysis.

Chapter 6

Ceria-Based Catalysts for High-Temperature Vehicle Exhaust Conditions

This chapter reports on the synthesis, characterisation, and catalytic data of catalysts designed for high-temperature automotive catalysis. Graphene oxide (GO) templated ceria nanoflakes and copper-loaded ceria nanoflakes are examined as catalysts for CO oxidation and NO reduction. Additionally, ceria-zirconia mixed oxide catalyst materials – both GO-templated nanoflakes and hydrothermally synthesised nanorods – are characterised and tested.

Many ceria applications involve heterogeneous surface-catalysed reactions, so the ability to synthesize high surface area ceria is critical to improve performance. Surface areas over 200 $m^2\ g^{-1}$ are often reported for nanostructured ceria materials synthesized via a variety of methods such as hydrothermal or sol-gel, and surface areas of 345 $m^2\ g^{-1}$ has been obtained in ceria aerogel materials. [299–301] However, while the morphology of nanoceria and the nature of its exposed crystal planes can affect catalytic activity, ceria must also present a high thermal stability to maintain a useable surface area even when exposed to high temperatures. [33,37,302,303] Automotive catalysts can be exposed to vehicle exhaust temperatures of 850 °C, and close-coupled automotive catalysts can reach 1050 °C. [8,304] Therefore, the ability of ceria and ceria-based catalysts to resist sintering and maintain catalytic activity after high-temperature is critical to their long-term performance.

Template-based synthetic methods have been used to produce ceria-based catalysts with a variety of different morphologies. [33] Examples of this include soft template syntheses using surfactants or modifiers such as PVP, CTAB, glycol, or benzyl alcohol to produce rods, spheres, plates, nanoflowers, and octahedra, amongst other shapes. Hard template synthetic methods utilise templates such as carbon nanotubes, ZnO nanorods, or

polystyrene or carbon spheres to replicate their morphology with CeO_2. These morphologies, particularly at the nano scale, can strongly influence stability and catalytic activity. Therefore, the development of convenient and facile synthetic methods using templates will be useful in improving the performance of ceria-based catalysts. The use of GO as a template offers an attractive alternative route for synthesizing high surface area nanostructured catalysts. GO consists of a two-dimensional monolayer of carbon atoms, analogous to graphene, but interrupted by a range of oxygen-containing groups. GO's surface functional oxygen-containing groups allow it to be easily dispersed in a variety of solvents, unlike graphene, enabling its utilization in processes involving liquid suspensions or solutions. [305]

In previous work by Eslava *et al*, a method for producing large amounts of graphene oxide (10-20 g) was developed. [244] The graphene oxide was used as a support for polyoxotitanium clusters to produce a two-dimensional arrangement of polyoxotitanium on graphene oxide. When this material was calcined at 450 °C, this resulted in the synthesis of titania nanoflakes, consisting of smaller titania crystallites arranged in flat two-dimensional flakes. The same synthesis without GO produced larger, three-dimensional crystallite agglomerations. Compared to untemplated titania, the titania nanoflakes demonstrated smaller crystallite size and improved hydrogen production rate in the photocatalytic evolution of hydrogen from water.

Herein, the potential of GO for use as a template to produce ceria-based nanoflakes and how the two-dimensional nanoflake morphology would affect material and catalytic properties is examined. A simple precipitation reaction was used, and, similarly to the titania synthesis described above, the addition of GO resulted in the synthesis of two-dimensional ceria nanoflakes, while performing the reaction without GO provided large three-dimensional ceria agglomerations. These materials were characterised to determine the physical differences between GO-templated and untemplated ceria (surface area, morphology, crystallite size, etc.) as well as factors relevant for catalytic activity (surface reducibility and concentration of oxygen vacancies).

In addition to bare ceria nanoflakes, copper-loaded ceria nanoflakes were also tested for CO oxidation and NO reduction. And finally, ceria-zirconia mixed oxide catalysts were synthesised and characterised to improve sintering behaviour at high temperatures.

6.1 Ceria nanoflakes – synthesis and characterisation

Ceria particles and nanoflakes were prepared via a room temperature precipitation synthesis in the absence and presence of GO respectively, followed by a calcination in air at 400 °C to remove the GO template. An SEM micrograph of the GO used is shown in Figure 48. Prior to calcination, the nanoflakes are a brown powder, while after calcination at 400 °C, the product is yellow, similar to other ceria syntheses (Figure 49). The untemplated ceria particles were bright yellow both pre- and post-calcination. The GO-templated ceria nanoflakes were much more loosely packed than the untemplated ceria particles. Without any further treatment, the nanoflakes had a bulk density of 0.34 g mL^{-1}, while the untemplated particles had a bulk density of 0.65 g mL^{-1}.

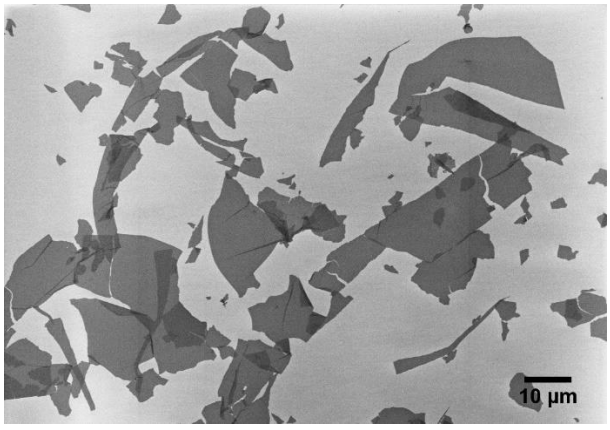

Figure 48. SEM micrograph of graphene oxide used as the template for ceria nanoflakes synthesis. The size distribution of GO flakes was approximately 1-20 µm.

Figure 50 shows TEM images of GO-templated ceria nanoflakes and untemplated ceria particles calcined in air at different temperatures between 400 to 1000 °C. The difference between the two materials is significant - while the GO-templated synthesis provided a two-dimensional arrangement of ceria crystallites, the untemplated synthesis resulted in much larger unstructured agglomerations. Typical ceria flakes calcined at 400 °C were a

few hundred nanometres in diameter and less than 10 nm in thickness, while the size of the untemplated ceria particle agglomerations was significantly larger, in the micrometre range.

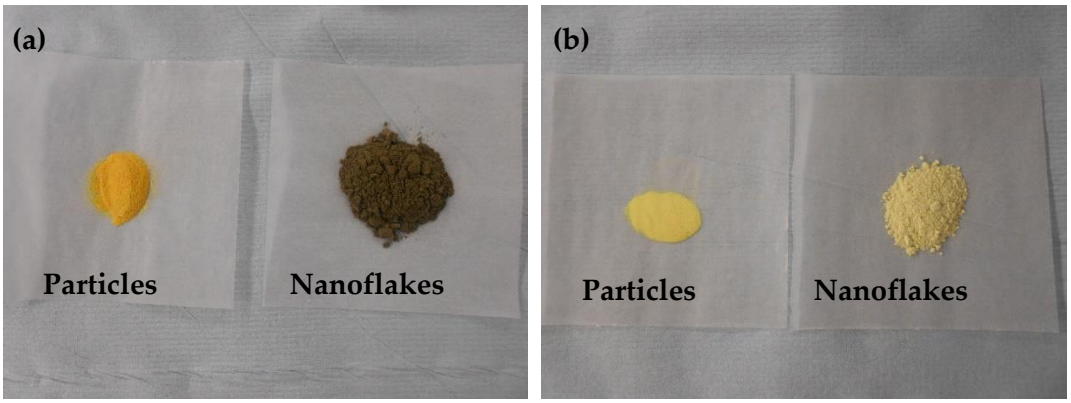

Figure 49. Photos of untemplated ceria particles and GO-templated ceria nanoflakes (a) after synthesis and freeze drying and (b) after calcination at 400 °C.

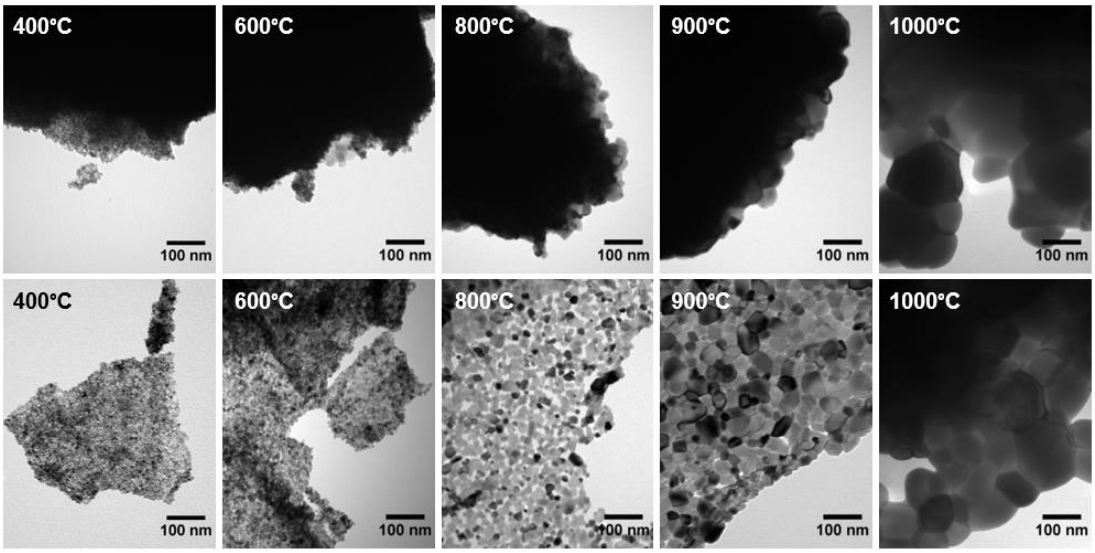

Figure 50. (above) TEM micrographs of untemplated ceria particles, calcined in air between 400 and 1000 °C. (below) TEM micrographs of GO-templated ceria flakes, calcined in air between 400 and 1000°C. Two-dimensional morphology is clearly retained for GO-templated ceria after thermal treatment.

Subsequent calcinations in air at 600, 800, 900, or 1000 °C to assess thermal stability also show differences between GO-templated ceria flakes and untemplated ceria particles. While both the ceria nanoflakes and particles show crystallite growth with increasing calcination temperature, the ceria nanoflakes retained their two-dimensional morphology even at high calcination temperatures (1000 °C).

Powder XRD patterns of the calcined ceria particles and nanoflakes crystallite sizes show that both are very similar. Figure 51 shows that the diffraction peaks get narrower and taller with increasing calcination temperature, indicating a growth in crystallite size. However, this trend is more prominent for the untemplated ceria particles compared to the GO-templated ceria nanoflakes for any calcination temperature. Crystallite size calculations using the ceria (111) peaks clearly show this trend in Table 8. When calcined at 400 °C, the ceria particles and flakes have a similar crystallite size, slightly smaller for the flakes (6.7 and 6.0 nm, respectively). But upon calcination at higher temperatures, crystallite size increases more quickly for the untemplated particles than for the GO-templated nanoflakes. This observation indicates that the two dimensional high aspect ratio arrangement of crystallites of the GO-templated nanoflakes replicating the GO morphology limits the diffusion of atoms at high temperature to a two dimensional plane which is translated into a low sintering degree. In contrast, diffusion of atoms at high temperature in untemplated particles takes place in three dimensions, favouring the sintering.

CHN analysis indicates that the GO is eliminated from the templated ceria material after the initial calcination at 400 °C. Pre-calcination, the ceria flakes and untemplated ceria particles contain 1.64 and 0.38 wt. % carbon, respectively, confirming the presence of GO. After calcination at 400 °C, the ceria flakes and untemplated ceria particles contain 0.39 and 0.34 wt. % carbon, respectively. These comparable values confirm the volatisation of GO during the calcination in air at 400 °C. Visual analysis of the materials support this – before calcination, the GO-templated ceria flakes are dark brown, but after calcination, they are pale yellow, more typical for ceria powders (Figure 49). Numerous examples of GO-ceria composite materials have been reported in the literature. For instance, hydrothermal methods have been used to synthesize ceria nanoparticles dispersed on the surface of graphene oxide for the oxidation of uric acid, degradation of methylene blue, and removal of arsenic species from water. [306–308] However, because calcination at 400 °C is sufficient to completely remove GO from such composite materials, there is quite a low upper temperature limit for such catalysts to be useful. In contrast, the GO-templated ceria flakes retain useful properties at much higher temperatures.

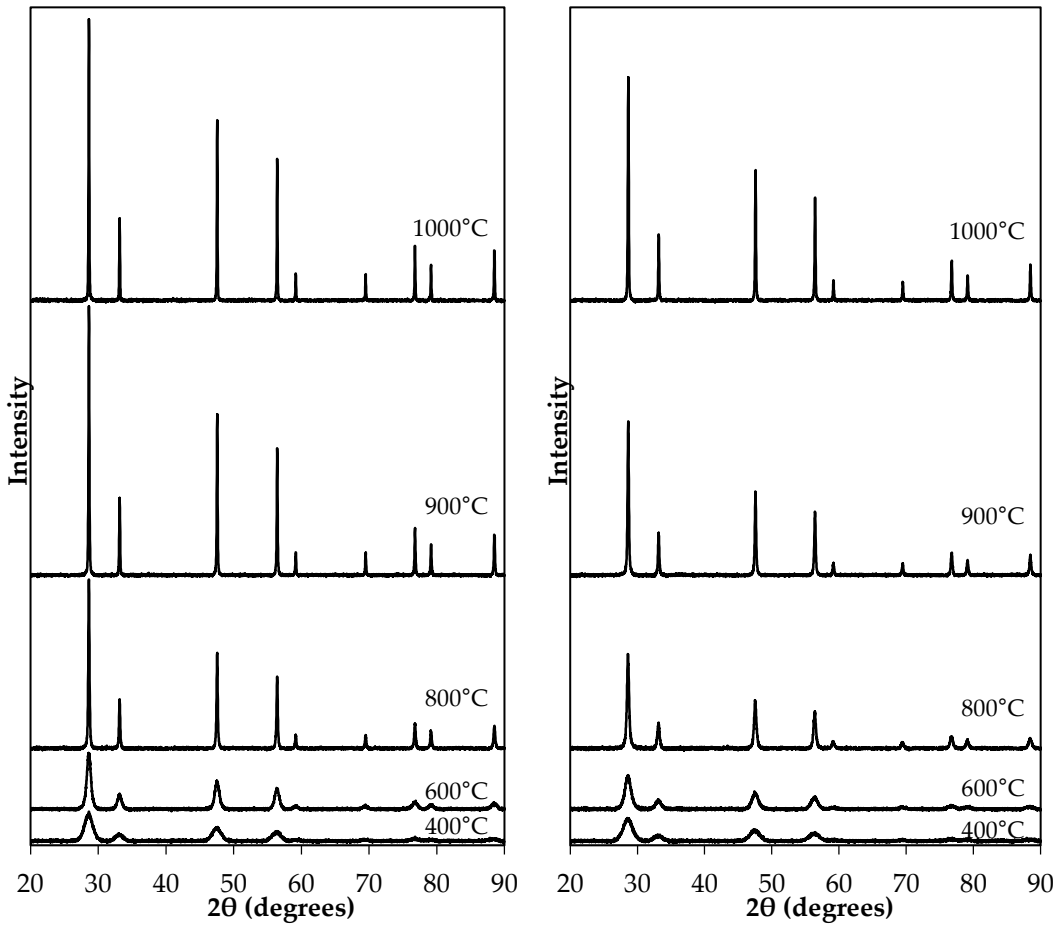

Figure 51. Powder X-ray diffraction patterns for (left) untemplated ceria particles and (right) GO-templated ceria flakes, calcined between 400 and 1000 °C.

Table 8. Structural properties of ceria particles and GO-templated ceria nanoflakes.

Calcination T (°C)	Crystallite size (nm)[a]	BET surface area (m^2/g)	Avg. pore diameter (cm^3/g)[b]	Oxygen vacancies (%)[c]
Untemplated ceria particles				
400	5.9	116	33.9	2.7
600	10.7	18	33.3	1.3
800	35.4	1		0.8
900	48.7	<1		0.9
1000	56.8	<1		0.6
GO-templated ceria flakes				
400	5.4	113	29.1	3.3
600	7.1	43	38.8	3.2
800	21.4	9	49.8	1.4
900	30.5	6	41.5	0.9
1000	42.1	6	47.0	1.0

[a] Calculated using Scherrer equation using ceria (111) peak in XRD pattern

[b] Calculated using Barret-Joyner-Halenda (BJH) method on desorption curves

[c] Calculated from Raman spectra F_{2g} band shift

Both the ceria particles and templated flakes were analysed with Raman spectroscopy, shown in Figure 52. In both cases, ceria's characteristic F_{2g} band at approximately 466 cm^{-1}, attributable to the vibrational characteristics of oxygen atoms surrounding cerium in the fluorite crystal structure, is clearly visible. [309] An additional defect band at 595 cm^{-1} is also visible in both samples calcined at 400 °C. This defect band can be attributed to the presence of Ce^{3+} related defects in the ceria lattice, or to defects caused by crystallite size effects – in general, in pure ceria it can be related to oxygen vacancy concentration due to non-stoichiometry of the CeO_2 lattice. [264,310] Shifts in the 466 cm^{-1} band can be attributed to differences in oxygen vacancy levels or lattice contraction, and this would also be indicated in a difference in intensity in the 595 cm^{-1} band. [187,263,311] While the GO templated and untemplated samples calcined at 400 °C appear to be similar, the 595 cm^{-1} band disappears in the untemplated ceria particle spectrum at calcination temperatures > 600°C, while it is retained in the GO-templated ceria spectrum even after treatments at 1000 °C, although its magnitude is considerably decreased.

Oxygen vacancy quantities can be calculated via correlation with a shift in the main F_{2g} band at ~466 cm^{-1}. [77,84] Results are shown in Table 8. For pure ceria, $\Delta\omega = -\gamma\omega/(\Delta V/V_0)$, where ω is the shift in Raman frequency, γ is the Grüneisen parameter (1.24 for this mode), and ΔV is the volume change from the reference volume. Volume changes of the unit cell are due to expansion of Ce^{4+} to Ce^{3+} (ionic radii 0.970 Å and 1.143 Å, respectively), which is only partially offset by the replacement of O^{2-} with oxygen vacancies (ionic radii 1.380 and 1.164 Å, respectively). Assuming pure ceria with no other contributing defects, the relationship between oxygen vacancy concentration δ and change in volume $\Delta V/V_0$ is relatively linear: $\delta = -10(\Delta a/a_0) = -3.3(\Delta V/V_0)$, where $(\Delta a/a_0)$ is the change in the lattice constant. Therefore, $\delta = 2.66(\Delta\omega/\omega_0)$. [84,312] It should be noted that the peak shift in these samples is quite small (<4 cm^{-1}), creating a degree of uncertainty. Furthermore, depending how far the Raman laser penetrates through the catalyst materials, this is a measure of oxygen vacancies at or near the surface of the particles. Nevertheless, the trend is clear – untemplated ceria particles show lower levels of oxygen vacancies than GO-templated ceria nanoflakes.

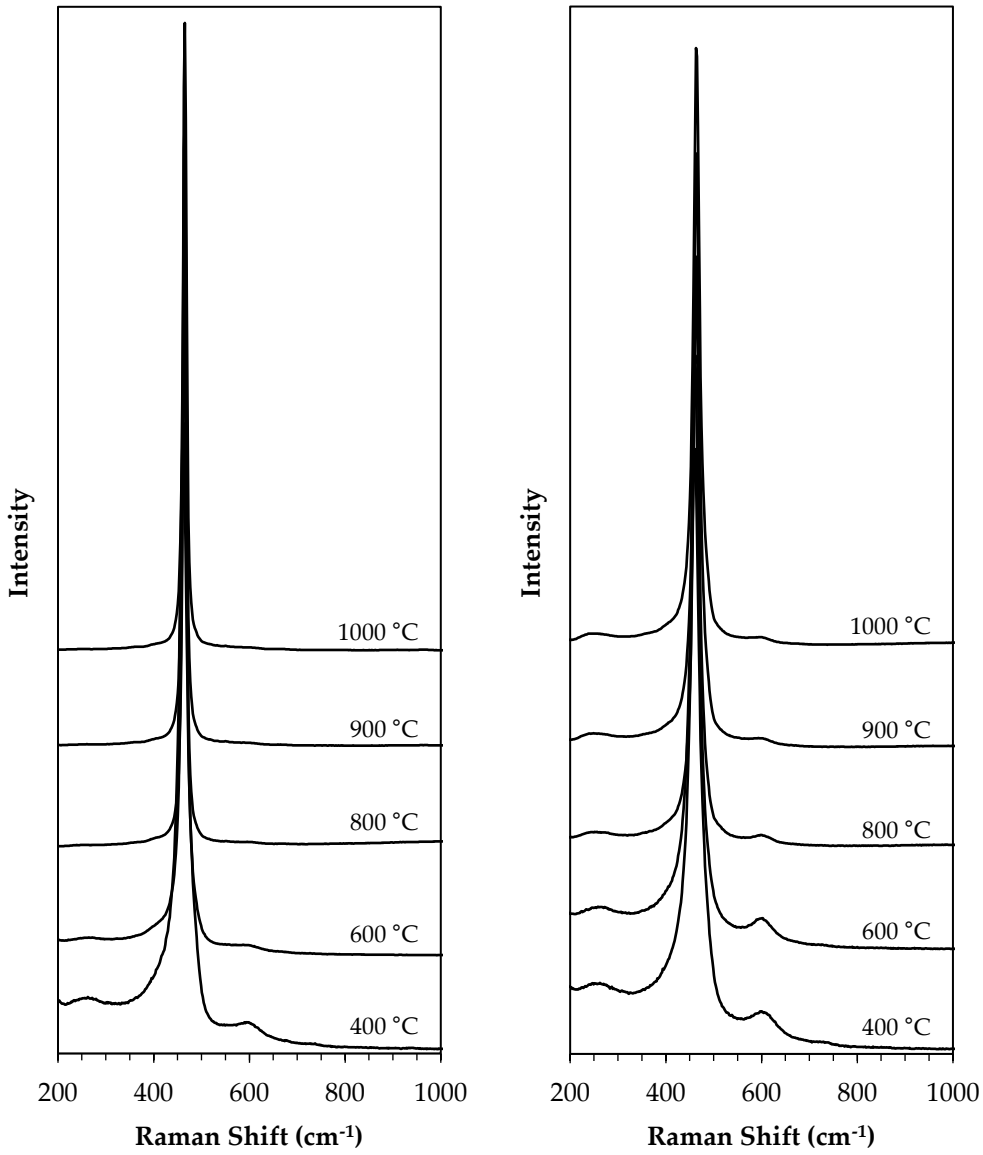

Figure 52. Raman spectra of (left) untemplated ceria particles and (right) GO-templated ceria flakes, calcined between 400 and 1000 °C.

To further quantify oxygen vacancy levels in the ceria materials, temperature-programmed reduction was performed, shown in Figure 53. Typically, two TPR peaks are associated with nanostructured ceria - a lower-temperature peak associated to readily available surface oxygen reduction, and a higher-temperature peak representing the reduction of the bulk lattice oxygen. [6,51] As shown in Figure 53a-b, both the GO-templated and untemplated ceria calcined at 400 and 600 °C clearly show both peaks. However, for the 800 °C calcination, this is greatly reduced for both samples. Table 9 shows the fraction of peaks intensities, clearly showing that the ceria flakes appear

to retain more low-temperature surface reducibility than the untemplated ceria particles for all three calcination temperatures in agreement with the Raman spectra analysis.

The physical properties of both materials were also characterised by nitrogen adsorption. Both the GO-templated ceria flakes and untemplated ceria particles calcined at 400 °C show a type IV isotherm (Figure 54), characteristic of mesoporous materials. [274] The type H2 hysteresis loop displayed is characteristic of a non-uniform network of pores, in both size and shape. [313] In both cases, the type IV isotherm is maintained upon calcination at 600 °C. As shown in Figure 54a, nitrogen adsorption and desorption from untemplated ceria particles calcined at 800 °C and above is negligible. GO-templated ceria nanoflakes calcined at 400 °C show a pore size distribution with narrower pore diameters than untemplated ceria particles, shown in Figure 55. However, upon calcination at 600 °C, both materials show a similar pore size distribution.

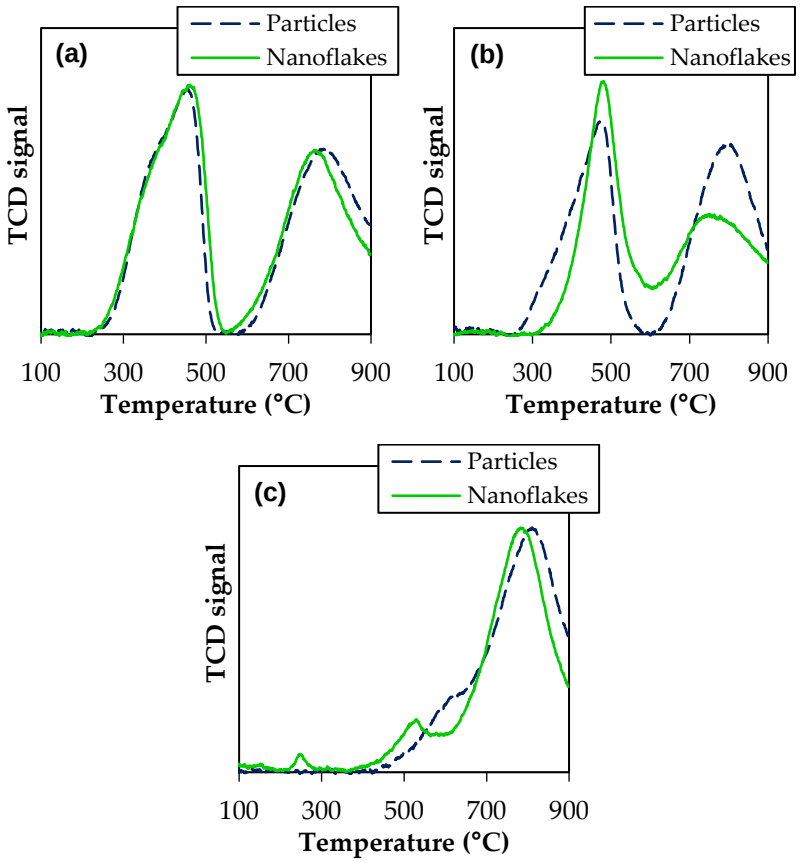

Figure 53. TPR profiles for GO-templated ceria flakes and untemplated ceria particles calcined at (a) 400 °C, (b) 600 °C, and (c) 800 °C.

Table 9. Fraction of peak areas in TPR profiles for untemplated ceria particles and GO-templated ceria flakes.

Calcination T (°C)	Surface oxygen peak (fraction)	Bulk oxygen peak (fraction)
Untemplated ceria particles		
400	0.64	0.36
600	0.53	0.47
800	0.03	0.97
GO-templated ceria flakes		
400	0.71	0.29
600	0.65	0.35
800	0.06	0.94

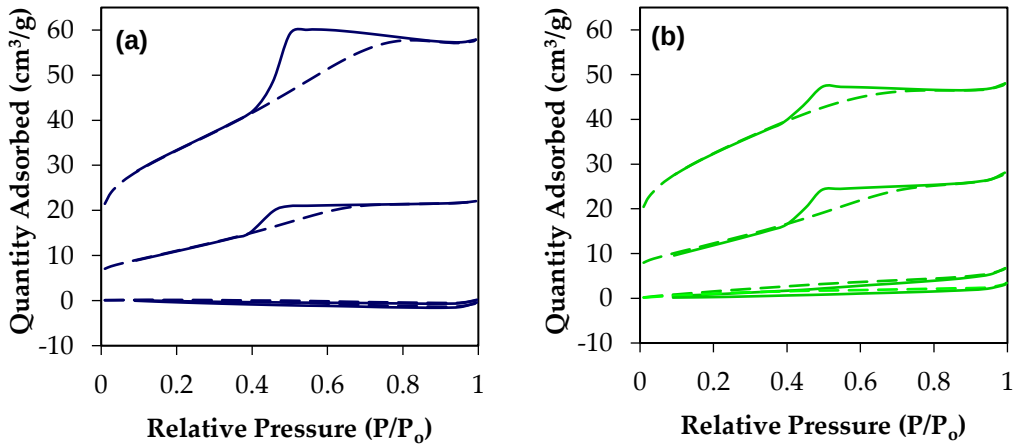

Figure 54. Nitrogen isotherms for (a) untemplated ceria particles calcined between 400-900 °C and (b) GO-templated ceria nanoflakes, calcined between 400-900 °C. The nitrogen isotherm for ceria samples calcined at 1000 °C is not shown, as it is unchanged from the 900 °C isotherm.

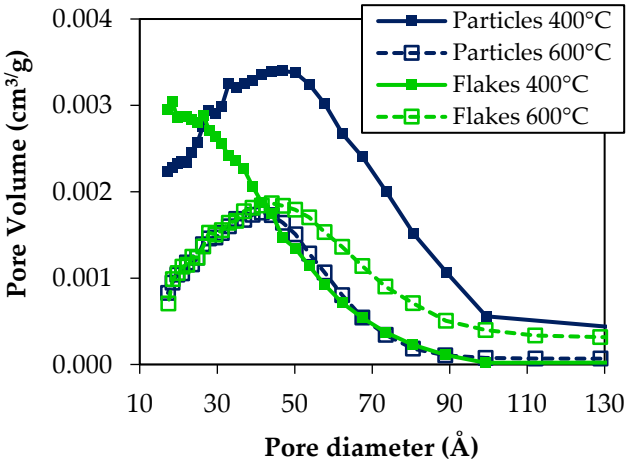

Figure 55. Pore size distribution for untemplated ceria particles and GO-templated ceria nanoflakes, calcined at 400 and 600 °C. Pore size calculations were not possible for the untemplated ceria particles calcined at 800 °C or above, due to a lack of available data points.

While both materials experience severe sintering at high temperatures, the GO-templated ceria nanoflakes maintain a higher BET surface area compared to untemplated ceria particles after calcination at the same temperature (Figure 56 and Table 8). This improved thermal stability of the flake materials is in agreement with the crystallite sizes derived from powder XRD data.

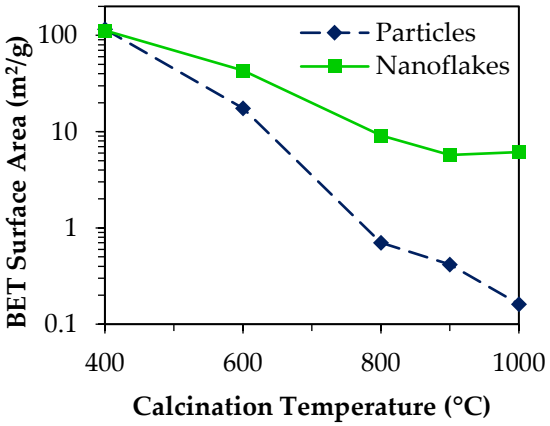

Figure 56. BET surface area vs. calcination temperature and for GO-templated ceria flakes and untemplated ceria particles.

6.2 Ceria nanoflakes – catalytic activity

The catalytic activity of GO-templated ceria flakes and untemplated ceria particles for CO oxidation is shown in Figure 57. Catalysts were calcined in static air at 400, 600, or 800 °C respectively prior to testing. The GO-templated ceria flakes calcined at 400 °C achieves similar although slightly superior activity than the untemplated ceria particles up to 400 °C reaction conditions. At higher reaction temperatures (400 to 500 °C), considerably higher conversions are achieved with the ceria flakes compared to the particles due to their considerably lower in-situ sintering as shown by the smaller reduction on surface area above 400 °C (Table 8). At 500 °C, the ceria flakes achieve full conversion of CO to CO_2, while the untemplated ceria particles only reach approximately 80% conversion. GO-templated ceria flakes also outperformed the untemplated particles when calcined at 600 °C - at this calcination temperature the GO-templated ceria flakes are capable of maintaining a high surface area and high concentration of their initial surface oxygen concentration, critical for the CO oxidation reaction. This is shown in terms of rate

calculations at 450 °C (Figure 58). These results demonstrate that templating ceria with sacrificial GO results in more thermally stable catalysts.

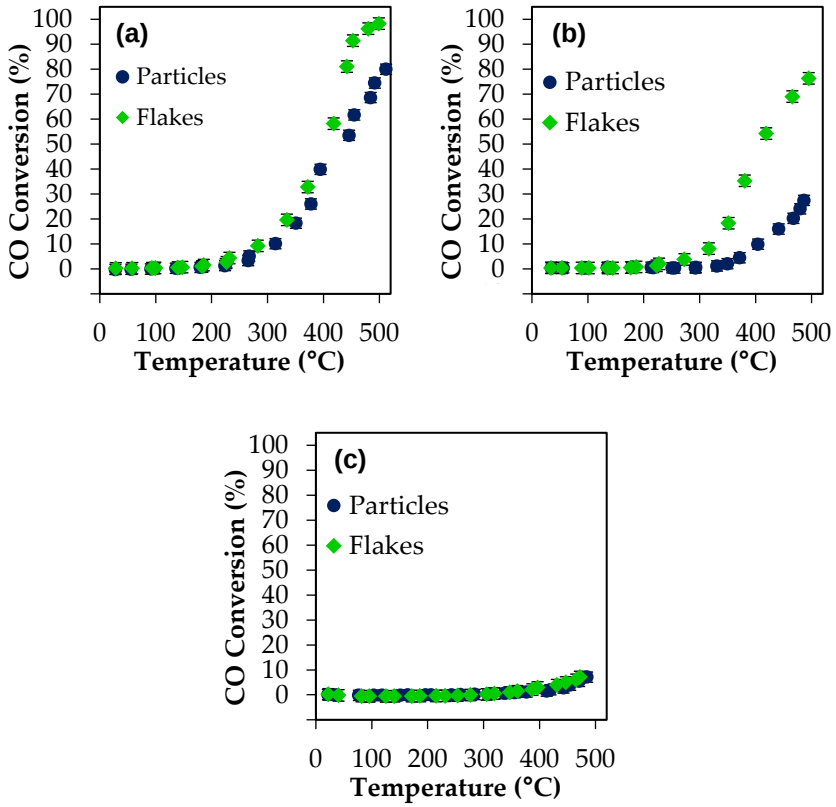

Figure 57. Catalytic activity for CO oxidation of GO-templated ceria flakes and untemplated ceria particles, calcined at (a) 400 °C, (b) 600 °C, and (c) 800 °C.

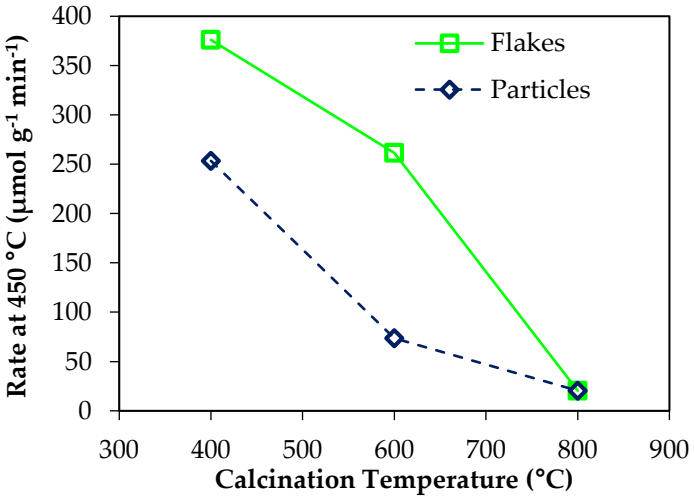

Figure 58. Rate of untemplated ceria particle and GO-templated ceria flake catalysts for CO oxidation, calculated with conversion rates at 450 °C.

Templated ceria nanoflakes perform comparably to or slightly better than some nanostructured ceria catalysts recently reported in the literature for CO oxidation. At 250 °C, the rate of these ceria nanoflakes for CO oxidation (in terms of μmol of CO converted per g of catalyst) is 19.1 μmol g^{-1} min^{-1}, while other papers show catalyst performance corresponding to 14 to 20 μmol g^{-1} min^{-1}. [314,315] Other papers report catalysts with conversion rates corresponding to much higher rate values; 53 and 163 μmol g^{-1} min^{-1} for solvothermally prepared 'cauliflower-like' ceria and microwave-assisted hydrothermally synthesized ceria nanocubes, respectively. [66,316] However, it should be noted that variations in reaction conditions can limit comparability; in particular, significantly different O_2:CO ratios in reaction gas mixtures.

CO oxidation is a surface-catalysed reaction, proceeding via the Mars-Van Krevelen mechanism. [86] Nevertheless, higher surface areas do not necessarily correlate with better catalytic performance, because, among other reasons, the nature of the exposed ceria crystal planes can influence activity. [317] In any case, prevention of excessive sintering is very important, as demonstrated with these ceria samples - where GO templating leads to smaller crystallite sizes and larger surface area upon calcination at 400-1000 °C, resulting in more active and thermally stable catalysts. [37,318,319] In addition, CO oxidation over ceria-based catalysts is rather sensitive to oxygen vacancy concentration in such a way that the greater the population of oxygen defects, the better the CO oxidation performance. [320,321] The observed catalytic trends correlate well with the Raman and TPR experiments, which show how ceria nanoflakes retain a higher population of oxygen defects after thermal treatment compared to ceria nanoparticles and thus improved reducibility, exhibiting improved oxidation activity.

The use of GO-templated ceria nanoflakes in TWC applications was further explored by testing their catalytic activity in NO reduction, shown in Figure 59. Similarly to CO oxidation (Figure 57), the GO-templated ceria flakes demonstrate somewhat improved catalytic activity compared to the untemplated ceria particles. The nanoflakes achieve full conversion of NO at a reaction temperature of approximately 500 °C, while the particles only achieve a conversion of approximately 70%.

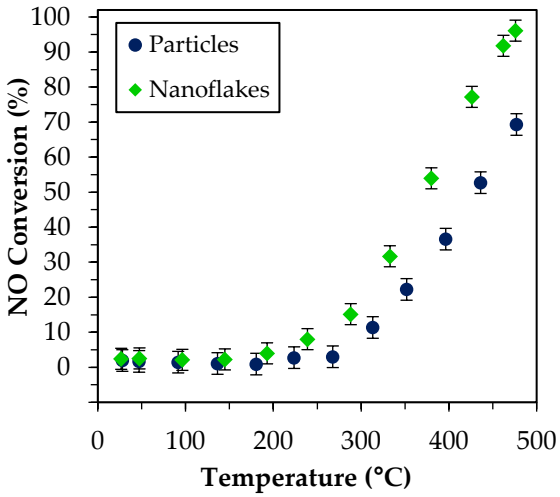

Figure 59. Catalytic activity for NO reduction of GO-templated ceria nanoflakes and untemplated ceria particles, calcined at 400 °C.

The apparent activation energies of templated ceria nanoflakes and untemplated ceria particles for CO oxidation and NO reduction were calculated using the method outlined in Section 5.3 and Equations 16-17 (Figure 60, Table 10). For both CO oxidation and NO reduction, the GO-templated ceria nanoflakes show a lower value of E_a than untemplated ceria particles. Furthermore, upon calcination at 600 °C, the E_a value of ceria nanoflakes increases much less than that of untemplated ceria particles. These results corroborate the rate and conversion data shown in Figure 57-59.

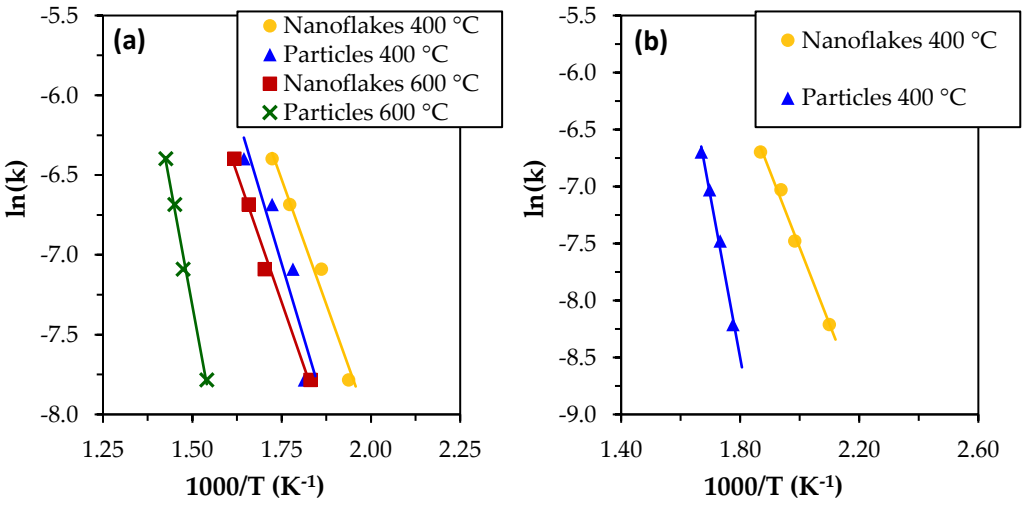

Figure 60. Arrhenius plots of ceria nanoflake and particle catalysts calcined at 400 or 600 °C for (a) CO oxidation and (b) NO reduction.

Weisz-Prater and Mears criteria (Equations 20 and 21, Section 5.3) were used to determine if these reactions were mass transfer or diffusion-limited. For the Weisz-Prater criterion, if the value of $C_{WP} < 1$, a reaction is not limited by internal pore diffusion, and for the Mears criterion, if MR < 0.15, the reaction is not limited by external bulk diffusion. As shown in Table 10, both of these conditions were met in all cases, and therefore mass transfer limitations are negligible with the conditions used in these expeirments.

Table 10. Apparent activation energy (E_a), Weisz-Prater criterion (C_{WP}), and Mears criterion (MR) for ceria nanoflake and particle catalysts calcined at 400 or 600 °C.

Sample	E_a (kJ mol^{-1})	$C_{WP,\ 300\ °C}$	$MR_{10\%}$
CO oxidation			
Nanoflakes 400 °C	52.0	0.151	$6.53 \cdot 10^{-6}$
Particles 400 °C	62.1	0.124	$6.70 \cdot 10^{-6}$
Nanoflakes 600 °C	53.7	0.083	$6.75 \cdot 10^{-6}$
Particles 600 °C	101.4	0.014	$7.23 \cdot 10^{-6}$
NO reduction			
Nanoflakes 400 °C	55.7	0.186	$5.21 \cdot 10^{-6}$
Particles 400 °C	117.8	0.083	$5.56 \cdot 10^{-6}$

6.3 Copper-loaded ceria nanoflakes

Three-way catalysts consist of metal particle catalysts loaded on a ceria-based oxygen storage medium. In order for the ceria nanoflake materials discussed in Sections 6.1 and 6.2 to improve TWC designs, they should show the capability to inhibit the sintering of these loaded metal particles as well as resist high temperature sintering themselves. Therefore, copper-loaded ceria nanoflakes and particles were also synthesised and tested for catalytic performance in CO oxidation (Figure 61) and NO reduction (Figure 62). Copper was added to ceria nanoflakes and particles at a loading of 1 wt. %, and the copper-ceria catalysts were calcined at 400 °C prior to testing.

For CO oxidation, while both the Cu-nanoflakes and Cu-particles appeared to have similar activities in initial tests (Figure 61a), a longer-term 20 h stability test at 500 °C (Figure 61b) showed that the Cu-loaded ceria nanoflakes retained higher activity after 20 h than the untemplated Cu-loaded ceria particles. Cu-loaded ceria nanoflakes show

higher activity for the reduction of NO than Cu-loaded ceria particles. (Figure 62a) Compared with CO oxidation, in the 20 h stability test (Figure 62b), there is a smaller difference between the two catalysts. However, Cu-nanoflakes still demonstrate improved performance and stability.

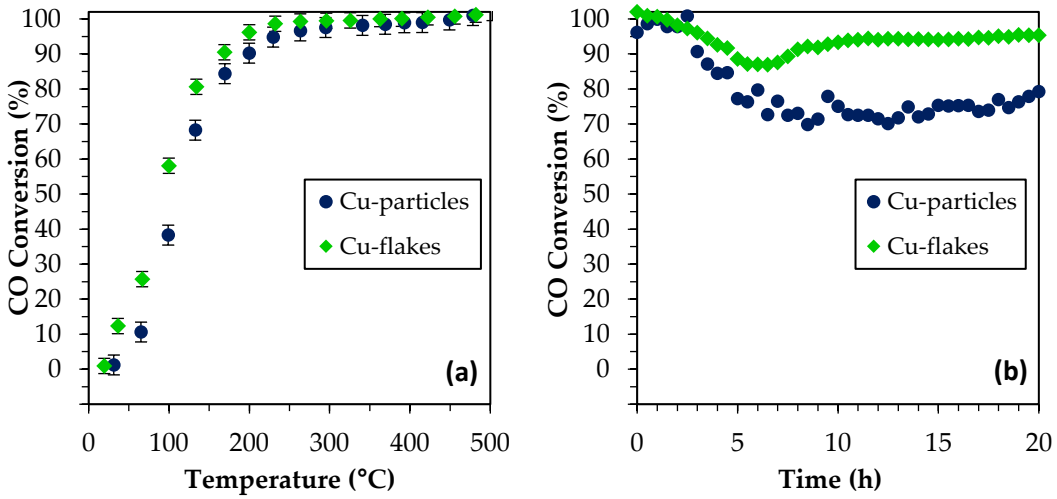

Figure 61. (a) Catalytic activity for CO oxidation of templated ceria nanoflakes and untemplated ceria nanoparticles loaded with 1 wt. % Cu and calcined at 400 °C. (b) Long-term catalytic activity at 500 °C.

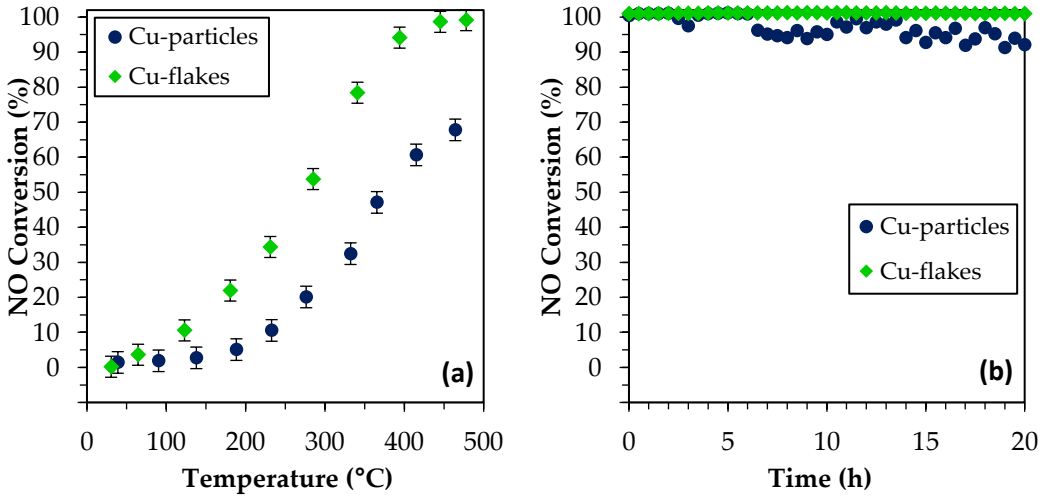

Figure 62. (a) Catalytic activity for NO reduction of templated ceria nanoflakes and untemplated ceria nanoparticles loaded with 1 wt. % Cu and calcined at 400 °C. (b) Long-term catalytic activity at 500 °C.

Characterisation of the Cu-loaded ceria catalysts (powder XRD spectra, Raman spectra, EDX mapping) was undertaken to examine differences between the GO-templated

nanoflakes and untemplated particles. In the XRD spectra (Figure 63), no significant differences were seen between the Cu-nanoflake and Cu-particle samples, and copper diffraction peaks were not visible. This is likely due to the low copper loading (1 wt. %). In the Raman spectra (Figure 64), both Cu-loaded samples have a more prominent band at 600 cm^{-1} than the bare ceria samples, indicative of a higher concentration of oxygen vacancies. [264] However, as with XRD, there were no significant differences between the Cu-nanoflakes and Cu-particles. Elemental mapping (Figure 65) also did not show significant differences between the two catalysts.

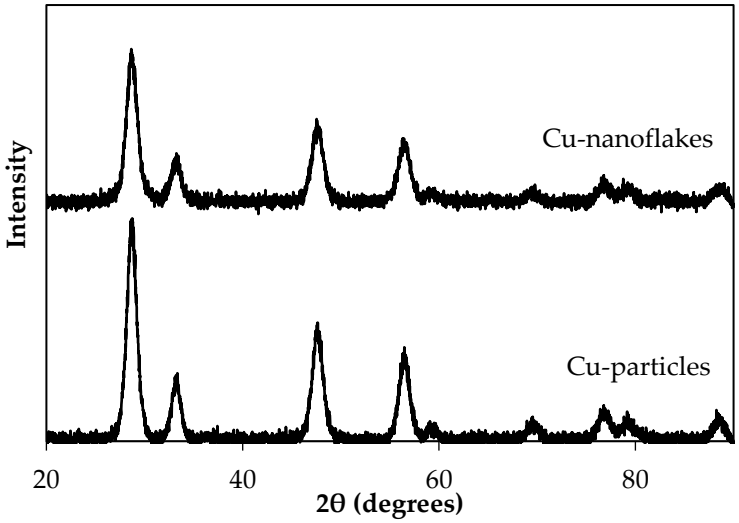

Figure 63. Powder XRD patterns of 1 wt. % Cu-loaded ceria nanoflakes and particles.

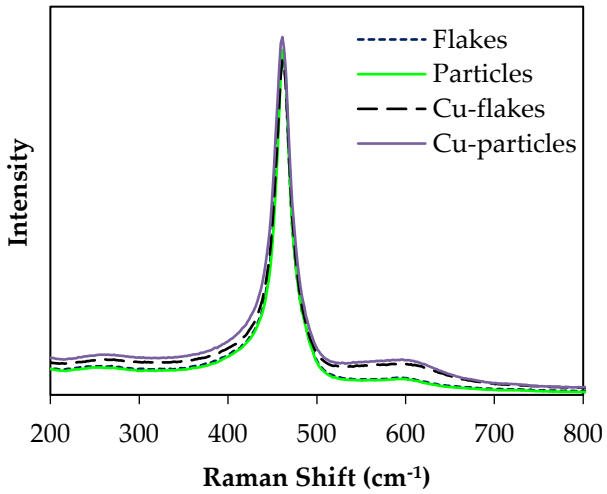

Figure 64. Raman spectra of bare and 1 wt. % Cu-loaded ceria nanoflakes and ceria particles.

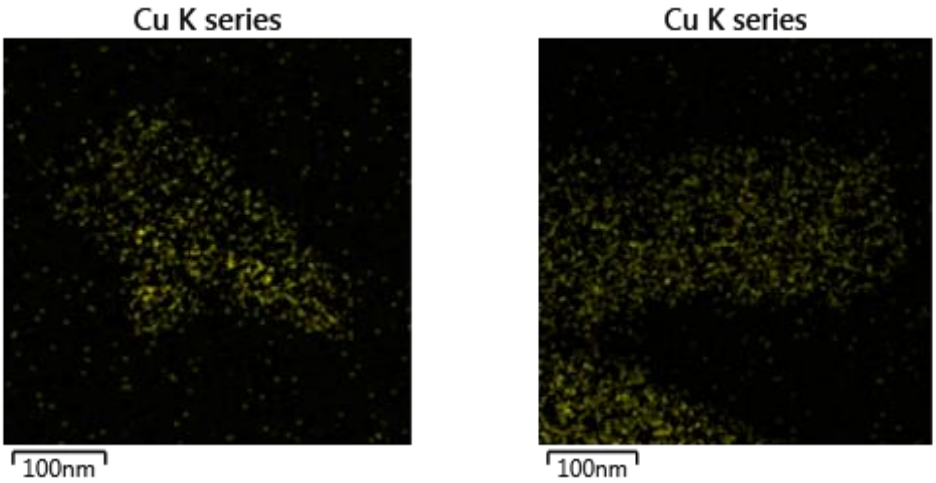

Figure 65. Elemental maps showing copper distribution on GO-templated ceria nanoflakes (left) and untemplated ceria particles (right).

6.4 Ceria-zirconia nanoflakes

Mixed oxides such as ceria-zirconia show enhanced resistance to sintering and retention of catalytic activity compared with pure ceria catalysts for three-way catalysis. [184] To investigate the applicability of the nanoflake morphology for automotive catalytic applications, a series of GO-templated ceria-zirconia mixed oxide catalysts with varying Ce/Zr ratios were synthesised, tested for catalytic activity in the oxidation of CO to CO_2, and characterised. When calcined at 400 °C, ceria-zirconia nanoflakes with zirconia content of 10 to 30 mol % all slightly outperform pure ceria nanoflakes – with a T_{10} value of approximately 235 °C for $Ce_{0.9}Zr_{0.1}O_2$ compared with 280 °C for CeO_2 nanoflakes (Figure 66a). After calcination at 600 °C, the $Ce_{0.9}Zr_{0.1}O_2$ sample showed similar performance to the samples calcined at 400 °C, while pure ceria and samples with 20 to 30 mol % Zr lost some activity (Figure 66b). After calcination at 800 °C, pure ceria nanoflakes lost almost all catalytic activity, while the 10 mol % Zr material retained significantly higher activity (Figure 66c).

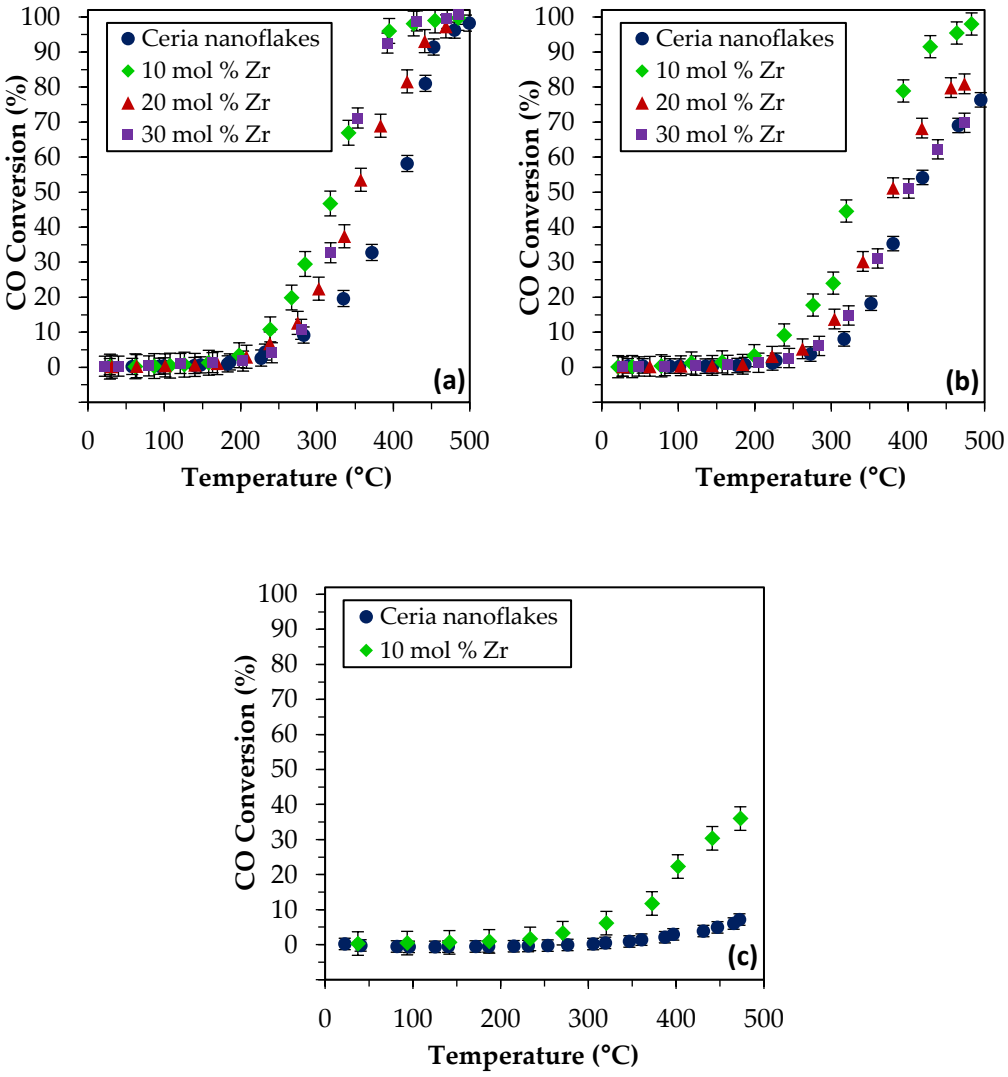

Figure 66. Catalytic activity for CO oxidation of ceria and ceria-zirconia nanoflakes calcined at (a) 400 °C, (b) 600 °C, and (c) 800 °C.

XRD spectra of the ceria-zirconia materials show full incorporation of Zr into the ceria lattice. All spectra show the characteristic diffraction peaks of ceria's fluorite lattice structure, with no visible Zr diffraction peaks at any Zr loading or calcination temperature. This is a good indication that Zr is well-incorporated within ceria instead of being segregated into a separate Zr phase. Representative spectra are shown in Figure 67.

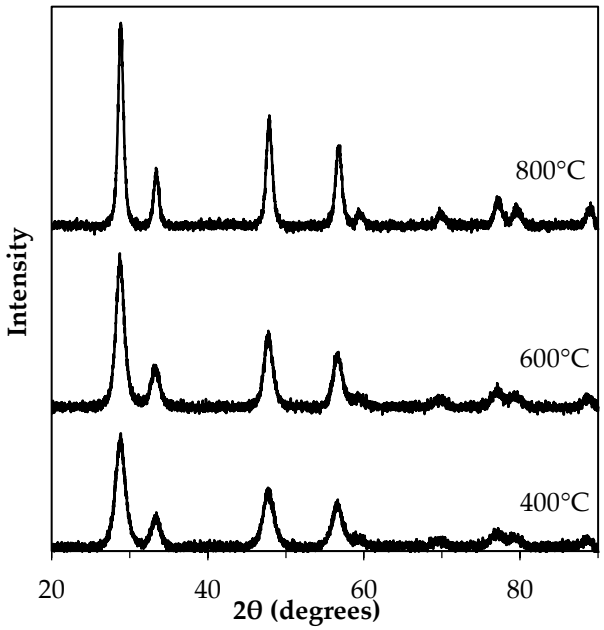

Figure 67. XRD spectra of $Ce_{0.9}Zr_{0.1}O_2$ nanoflakes calcined at 400, 600, and 800 °C.

Crystallite size calculations using the Scherrer equation (Figure 68a) show that the ceria-zirconia materials resist sintering much more strongly than pure ceria nanoflakes. Ceria nanoflakes calcined at 400 °C have a crystallite size of 6.0 nm, which increases to 20.3 nm when calcined at 800 °C. In contrast, the ceria-zirconia catalyst crystallite sizes range from 4 to 5 nm when calcined at 400 °C and 6.5 to 8.3 nm when calcined at 800 °C. Nitrogen adsorption analysis also confirm this anti-sintering behaviour. BET surface area measurements (Figure 68b) show that when calcined at 400 °C, CeO_2 and $Ce_{0.9}Zr_{0.1}O_2$ nanoflakes have similar specific surface areas, but at higher calcination temperatures, the pure ceria nanoflakes lose much more surface area than the nanoflakes incorporating zirconia.

Finally, TEM analysis confirms that the nanoflake morphology seen in Figure 50 for pure ceria nanoflakes has been retained with the addition of zirconium (Figure 69).

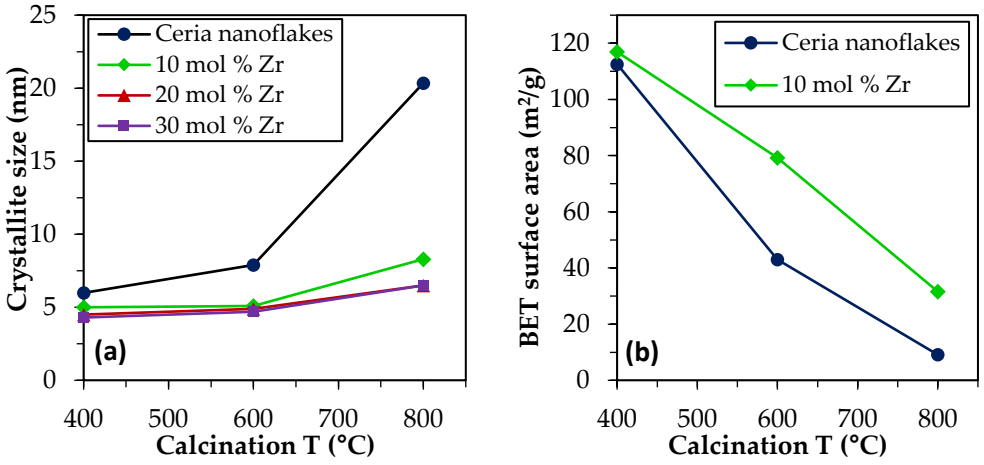

Figure 68. (a) Crystallite size of ceria and ceria-zirconia nanoflakes calculated with the Scherrer equation. (b) BET surface area measurements of ceria and ceria-zirconia nanoflakes.

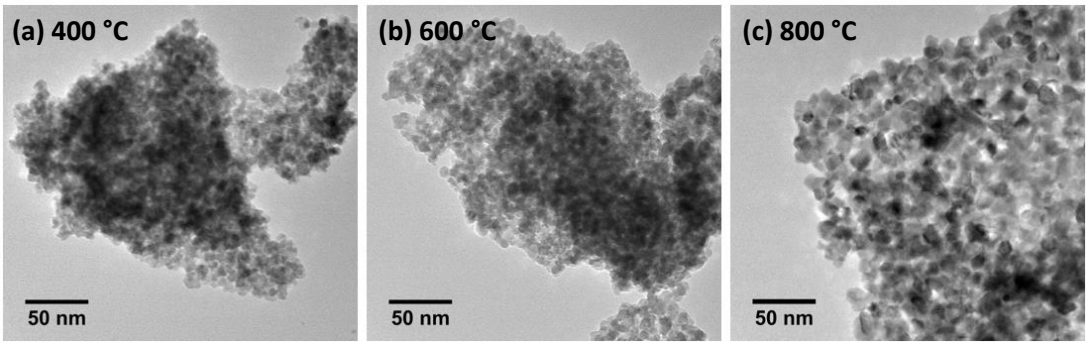

Figure 69. TEM micrographs of $Ce_{0.9}Zr_{0.1}O_2$ nanoflakes calcined at 400, 600, and 800 °C.

6.5 Ceria-zirconia nanorods

Continuing the work with hydrothermally produced ceria nanorods discussed in Chapter 5, ceria-zirconia mixed oxide nanorods were also synthesised. While doped ceria nanorod catalysts showed good low-temperature catalytic activity, this activity is of limited use for automotive catalyst applications if it cannot be retained after exposure to the high temperatures catalytic converters are exposed to. [8] Pure ceria and transition metal-doped ceria catalysts will not typically retain much catalytic activity after exposure to high temperatures. For instance, Venkataswamy *et al* report that the T_{10} value for CO oxidation of a Mn-ceria catalyst almost doubles (from 77 to 147 °C) when comparing samples calcined at 500 and 800 °C. [155] Therefore, a series of ceria-zirconia mixed oxide

nanorods were synthesised hydrothermally with a varying Ce/Zr ratio (10 to 40 mol % Zr). TEM images of these nanorods are shown in Figure 70.

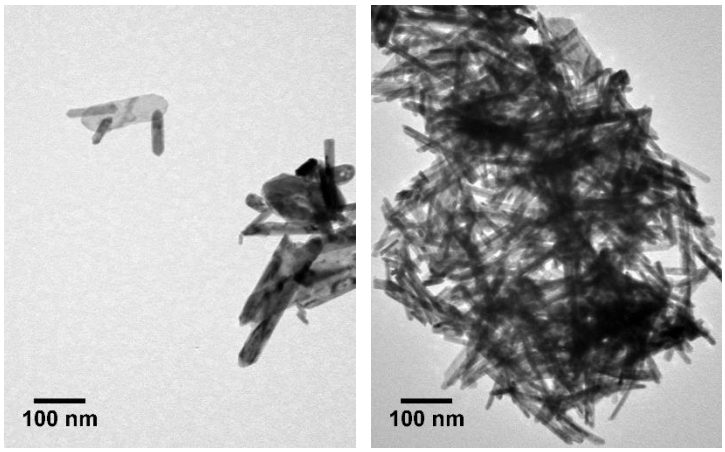

Figure 70. TEM images for (left) $Ce_{0.9}Zr_{0.1}O_2$ and (right) $Ce_{0.7}Zr_{0.3}O_2$ nanorods.

The catalytic activity of ceria and ceria-zirconia nanorods for CO oxidation are shown in Figure 71. All catalysts were tested uncalcined and calcined between 600 and 1000 °C. The calcined samples were heated in static air conditions for 4 hours.

For uncalcined samples, the addition of Zr reduced catalytic activity at low conversion levels. For uncalcined ceria, the T_{10} value was 228 °C, while for the ceria-zirconia nanorods, it ranged from 286 to 303 °C. However, at higher conversion levels, activity was similar, with only minor differences in T_{50} values (365 to 371 °C).

Upon calcination at higher temperatures (particularly 900 and 1000 °C), catalytic activity was severely degraded for all the tested samples. However, differences were apparent between the pure ceria and ceria-zirconia nanorods. For the pure ceria nanorods, catalytic activity was insignificant after calcination at 900 °C, and the sample calcined at 1000 °C was not tested. For all three ceria-zirconia catalysts, the samples calcined at 900 and 1000 °C retained a much larger degree of catalytic activity. The T_{10} value of the samples calcined at 1000 °C decreased with increasing Zr content – from 400 °C for $Ce_{0.9}Zr_{0.1}O_2$ to 325 °C for $Ce_{0.7}Zr_{0.3}O_2$ (a sample with 40 mol % Zr showed similar results to 30 mol %, with a T_{10} value of 330 °C). Therefore, after high-temperature calcination, the ceria-zirconia catalyst with 30 mol % Zr showed the best activity for CO oxidation.

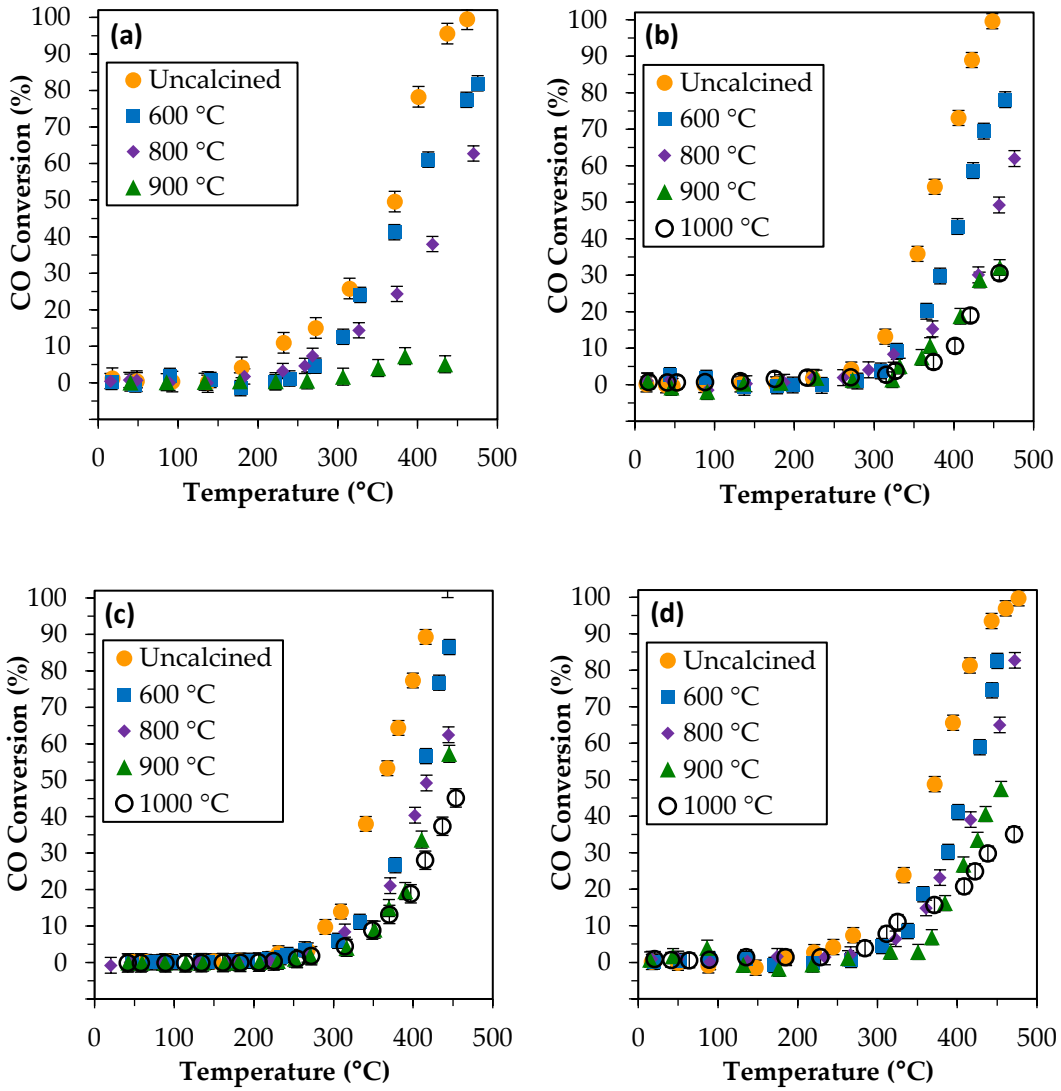

Figure 71. CO oxidation catalytic activity of (a) CeO_2, (b) $Ce_{0.9}Zr_{0.1}O_2$, (c) $Ce_{0.8}Zr_{0.2}O_2$, and (d) $Ce_{0.7}Zr_{0.3}O_2$, uncalcined and calcined at 600, 800, 900, or 1000 °C.

The results above demonstrate that ceria-zirconia nanorods show enhanced resistance to sintering and loss of catalytic activity after high-temperature calcination. To examine the effect of zirconia on the improved low-temperature activity demonstrated by the doped ceria nanorod catalysts in Chapter 5, a Mn-doped ceria-zirconia catalyst (4 wt. % Mn-doped $Ce_{0.7}Zr_{0.3}O_2$ nanorods) was synthesised. This material was also calcined at 600, 800, 900, and 1000 °C and tested as catalysts for CO oxidation, shown in Figure 72. Uncalcined Mn-doped ceria nanorods initially showed good catalytic activity (with a T_{10} of 180 °C) compared with undoped ceria nanorods (Figure 71a) and retained much of this activity after calcination at 600 °C. However, at higher calcination temperatures, activity quickly drops – for instance, the T_{10} of the Mn-ceria catalyst calcined at 900 °C was 360 °C.

In contrast, the uncalcined Mn-ceria/zirconia nanorods, with a T_{10} value of 242 °C, did not show improved catalytic activity compared with undoped, uncalcined ceria or ceria-zirconia nanorods. However, no loss of catalytic activity was seen after calcination at 600 or 800 °C. For the Mn-ceria/zirconia catalyst calcined at 900 °C, the T_{10} value was 270 °C, and for the sample calcined at 1000 °C, it was 326 °C. This demonstrates an enhanced catalytic performance compared with the Mn-ceria and undoped ceria/zirconia materials when calcined at high temperatures – but a loss of low-temperature catalytic activity when uncalcined.

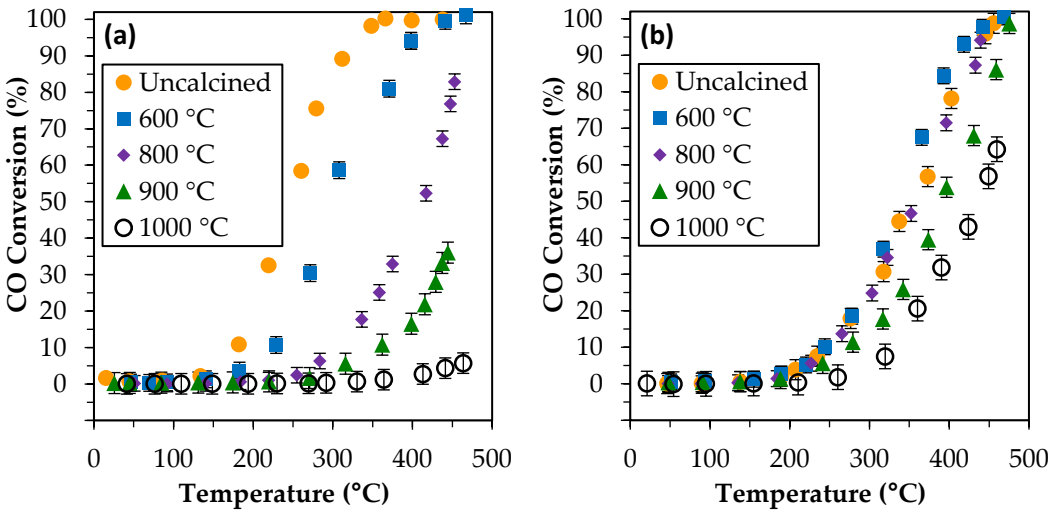

Figure 72. CO oxidation catalytic activity of 4 wt. % Mn-doped (a) CeO_2 and (b) $Ce_{0.7}Zr_{0.3}O_2$ nanorods, uncalcined and calcined at 600, 800, 900, or 1000 °C.

Representative powder XRD patterns for $Ce_{0.7}Zr_{0.3}O_2$ nanorods are shown in Figure 73, uncalcined and calcined between 600 and 1000 °C. For the uncalcined sample, only ceria's fluorite diffraction peaks are visible. However, after calcination at 800 °C or above, additional diffraction peaks appear, indicative of zirconia. This indicates that there is a degree of phase separation between ceria and zirconia after high-temperature calcination. The diffraction peak at 30.3° can be attributed to either the cubic or tetragonal phase of zirconia, while the others (24.1, 28.3, 31.7, and 38.9°) can be attributed to monoclinic zirconia. XRD patterns of the other ceria-zirconia nanorod samples show similar behaviour.

However, a shift in the ceria diffraction peaks is seen with increasing Zr content, indicating that despite the partial phase separation of ZrO_2, Zr has successfully substituted for Ce ions in the ceria fluorite lattice structure. This can be more clearly seen at higher calcination temperatures, and is shown in Figure 74 for uncalcined ceria and ceria-zirconia samples as well as samples calcined at 800 °C. Incorporation of Zr into the ceria crystal lattice is further confirmed by unit cell parameter calculations, shown in Figure 75a for the uncalcined samples and samples calcined at 800 °C. Because Zr^{4+} has a smaller ionic radius (0.84 Å) than Ce^{4+} (0.97 Å), higher levels of Zr result in smaller unit cell dimensions. Crystallite sizes were calculated using the Scherrer equation (Figure 75b), but no clear trend was seen.

BET surface area measurements for uncalcined and calcined ceria-zirconia nanorods are shown in Figure 76. Uncalcined samples have specific surface areas of 31 to 41 $m^2 g^{-1}$. Interestingly, while pure ceria nanorods retained much of this surface area after calcination at 600 and 800 °C, both ceria-zirconia samples tested lost the majority of their surface area. Therefore, for ceria and ceria-zirconia nanorods, surface area alone does not necessarily correlate with catalytic activity for CO oxidation.

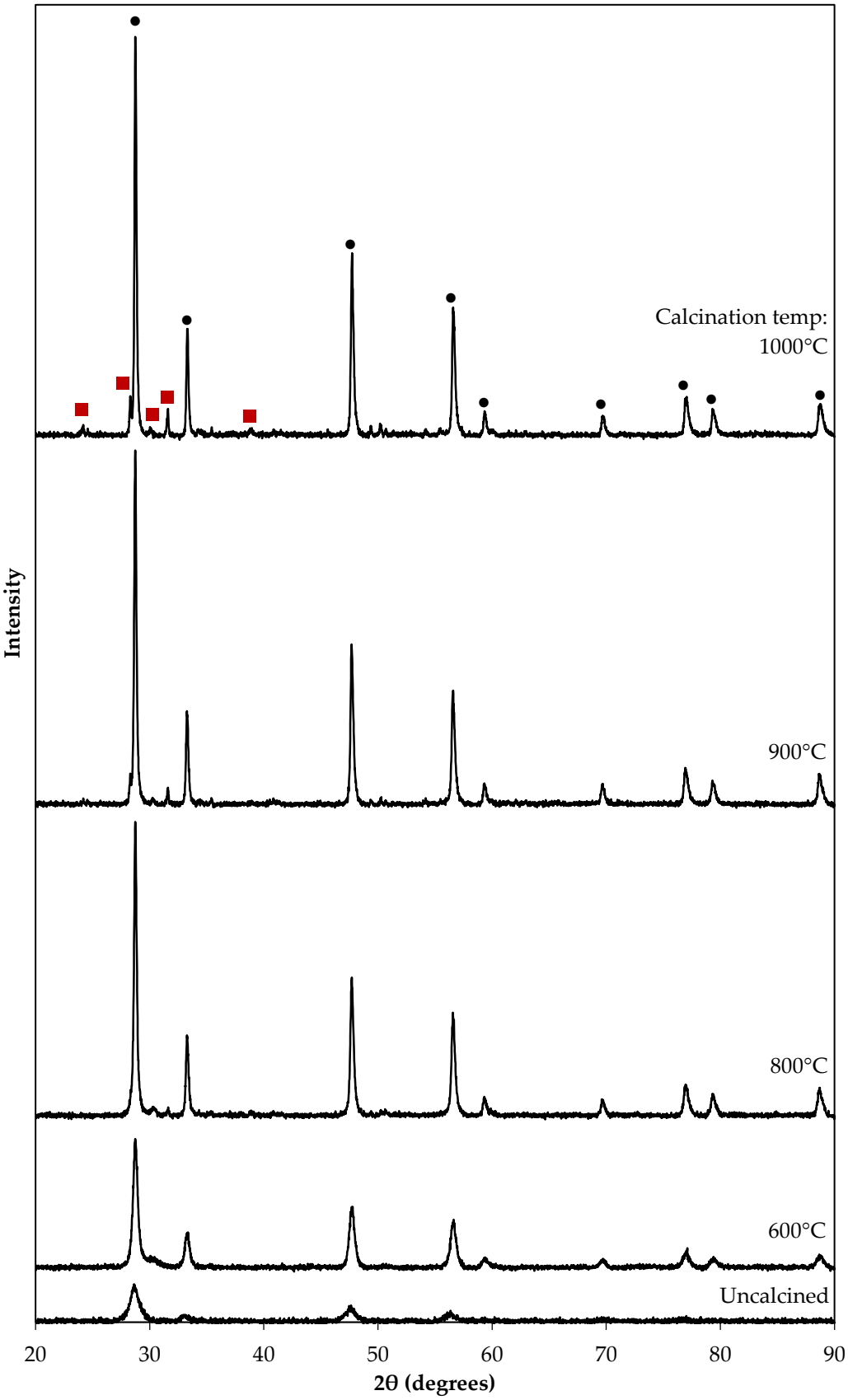

Figure 73. Powder XRD patterns for $Ce_{0.7}Zr_{0.3}O_2$ nanorods, uncalcined and calcined between 600 and 1000 °C. ● = CeO_2, ■ = ZrO_2

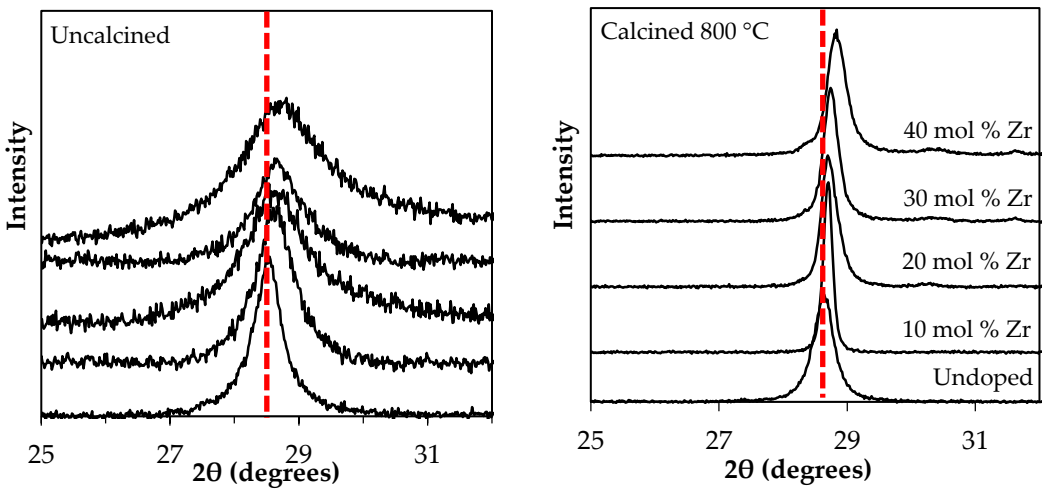

Figure 74. Powder XRD patterns of the Ce (111) diffraction peak for uncalcined samples and samples calcined at 800 °C.

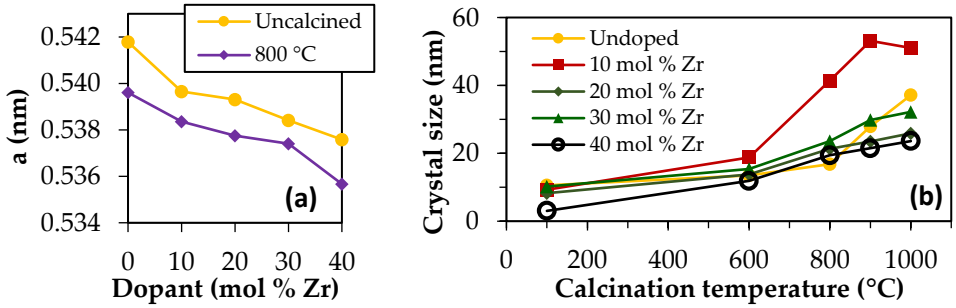

Figure 75. (a) Unit cell parameter and (b) crystallite size for uncalcined and calcined ceria-zirconia nanorods, calculated using powder XRD patterns.

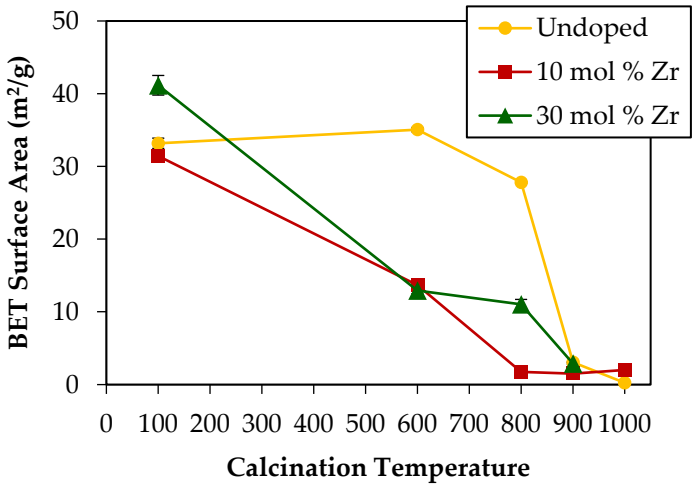

Figure 76. BET surface area for ceria and ceria-zirconia nanorods.

6.6 Conclusions

Sintering-resistant GO-templated ceria nanoflakes have been successfully synthesized via a room-temperature precipitation reaction. The improved textural properties provided by GO templating result in a ceria catalyst capable of maintaining a higher surface area than untemplated ceria particles when calcined above 400 °C, demonstrating lower crystallite growth and improved resistance to sintering. Furthermore, Raman and TPR analysis show that GO-templated ceria flakes have a higher level of oxygen vacancies than untemplated ceria particles. For these reasons, GO-templated ceria flakes demonstrate improved catalytic activity for CO oxidation and NO reduction. Ceria nanoflakes also inhibited loss of activity in a copper-loaded ceria catalyst, compared with Cu-loaded untemplated ceria particles.

The synthesis of GO-templated ceria-zirconia mixed oxide catalysts has shown that this nanoflake morphology can be maintained, providing additional resistance to sintering and loss of catalytic activity at high temperatures. This is an important step in showing the potential of GO templating for improving sintering behaviour in TWC oxygen storage materials. Using a combination of ceria and zirconia for hydrothermally synthesised nanorods also provided similar benefits. However, while the ceria-zirconia nanorods doped with Mn showed improved activity after high-temperature calcination, the addition of zirconia resulted in a loss of low-temperature activity, with no benefits compared with Mn-free nanorods.

It should be noted that, while more sintering-resistant than pure ceria, the ceria-zirconia materials discussed in this chapter do still lose specific surface area with exposure to high temperatures. This also holds true for ceria nanoflakes, compared with untemplated ceria particles. Future research will include steps to mitigate this behaviour further – for example, by investigating the applicability of GO templating with the inclusion of other promoters such as Nd, Pr, La, etc. which are known to improve thermal stability in automotive catalysis.

The capability to produce thermally stable ceria-based materials which limit high-temperature sintering is critical for ceria's further development across a range of environmentally applications. The use of GO as a sacrificial template offers a potential route for synthesizing thermally stable ceria catalysts, one in which a simple precipitation reaction is utilised and the template easily removed post-synthesis.

Chapter 7

Ceria Nanoflake Catalysts for Dry Methane Reformation

This chapter reports on the use of GO-templated ceria nanoflakes, discussed in Chapter 6, as a catalyst support for nickel in dry reforming of methane (DRM). While ceria is a critical component of automotive three-way catalysts, ceria-based materials are well-known for their use as a catalyst or catalyst support in a variety of other environmentally sensitive applications as well. Some of these include solid oxide fuel cells, steam reformation, photocatalysis, and thermochemical water splitting. [181,322–325] In dry methane reforming for the production of syngas, ceria has been utilised as a catalyst support or promoter of nickel catalysts, where it enhances activity. [326,327] The use of ceria in DRM as a catalyst support for nickel, instead of other supports such as Al_2O_3 or SiO_2, also inhibits coke formation, otherwise a significant potential source of deactivation in this reaction. [328,329] This is due to ceria's unique redox properties.

Dry reforming of methane is a reaction used to convert CH_4 and CO_2 to CO and H_2 (syngas):

$$CH_4 + CO_2 \rightarrow 2CO + 2H_2 \qquad (22)$$

This process both prevents greenhouse gases (methane and carbon dioxide) from being emitted into the atmosphere and produces syngas, which is a useful starting material for the production of various chemicals. [330] While the environmental incentives for DRM are strong, economically viable processes for DRM have not yet been developed. One reason for this is the high temperatures (typically 800 to 1000 °C) required to activate methane's C-H bonds and achieve good conversion – the overall enthalpy of reaction is +247 kJ mol^{-1}. [331] Therefore, ceria nanoflakes are an ideal potential candidate for use as

a catalyst support in the DRM reaction, due to their improved thermal stability and resistance to sintering.

While DRM theoretically results in syngas with a H_2/CO ratio of 1:1, the reverse water-gas shift reaction (Equation 23) can consume some of the hydrogen, resulting in a ratio of <1.

$$CO_2 + H_2 \rightarrow CO + H_2O \quad (23)$$

Additional side reactions can occur which cause the formation of coke, such as CH_4 decomposition (Equation 24) and the Boudouard reaction (Equation 25):

$$CH_4 \rightarrow C + 2H_2 \quad (24)$$

$$2CO \rightarrow C + CO_2 \quad (25)$$

Therefore, potential DRM catalysts must be stable under the harsh, high-temperature conditions required to achieve the reaction and inhibitory to the production of solid carbon. While noble metals may be used, nickel-based catalysts are also commonly reported in literature due to Ni's lower cost and higher availability. [330] Similarly to automotive catalysis, noble metals such as Pt, Pd, or Rh typically demonstrate enhanced stability, activity and resistance to coke formation than non-noble alternatives. However, interactions between the metal catalyst and support can play an important role in modifying metal dispersion and electronic effects – and thus overall catalyst performance. [332–334]

In this work, GO-templated ceria nanoflakes and untemplated ceria particles are used as a catalyst support for Ni/ceria DRM catalysts. GO-templated ceria nanoflakes and untemplated ceria particles were loaded with 10 wt. % Ni and analysed with XRD, H_2-TPR, TEM, TGA, and EDX mapping. Catalyst tests for DRM were tested with a temperature ramp between 550 and 850 °C as well as a longer-term stability test at 800 °C. Characterisation was undertaken on both fresh and post-reaction catalysts to analyse the physical changes and differences in side product carbon formation between the two Ni-ceria catalysts.

7.1 Ni-ceria nanoflakes – fresh catalyst characterisation

Powder XRD patterns of 10 wt. % Ni-loaded ceria samples are shown in Figure 77. After nickel deposition and calcination at 700 °C, but pre-reaction, NiO is visible in the diffraction pattern. Using the Scherrer equation, the sizes of the ceria crystallites are calculated to be 6.6 and 5.7 nm on templated ceria flakes and untemplated ceria particles, respectively, while the size of NiO particles is calculated to be 20 and 24 nm, respectively. These values are broadly similar, given the limitations of Scherrer equation calculations, indicating that both templated Ni-ceria flakes and untemplated Ni-ceria particles initially have similar crystallite sizes for both the ceria and NiO components of the catalyst.

Additionally, TPR experiments were conducted on the Ni-deposited ceria nanoflakes and particles, shown in Figure 78. The TPR profiles are similar to the ones of the bare ceria materials (Figure 53) with the addition of low temperature peaks (<400 °C), attributable to NiO reduction. For the NiO peaks, the NiO-ceria nanoflake TPR profile shows a shift to higher reduction temperatures compared with the NiO-ceria particle sample. There are two possible explanations for this. The size of NiO particles can affect the reduction temperature, so this is possibly indicative of different NiO particle sizes on the ceria nanoflake sample. [335,336] Alternatively, metal-support interactions can influence the reduction temperature as well. In the case of nickel-ceria, stronger interaction between NiO and the ceria, which can be influenced by oxygen vacancies acting as nucleation points, support results in higher reduction temperatures. [337,338] XRD analysis showed that the NiO crystallite sizes in the nanoflake and untemplated particle systems were similar, so the shift to a higher reduction temperature is likely due to differences in NiO-ceria interaction in the two catalysts. A shoulder extending from approximately 450 to 500 °C is visible for the NiO/ceria nanoflake TPR profile, but not the NiO/ceria particle sample, attributed to readily available surface oxygen in the ceria flakes.

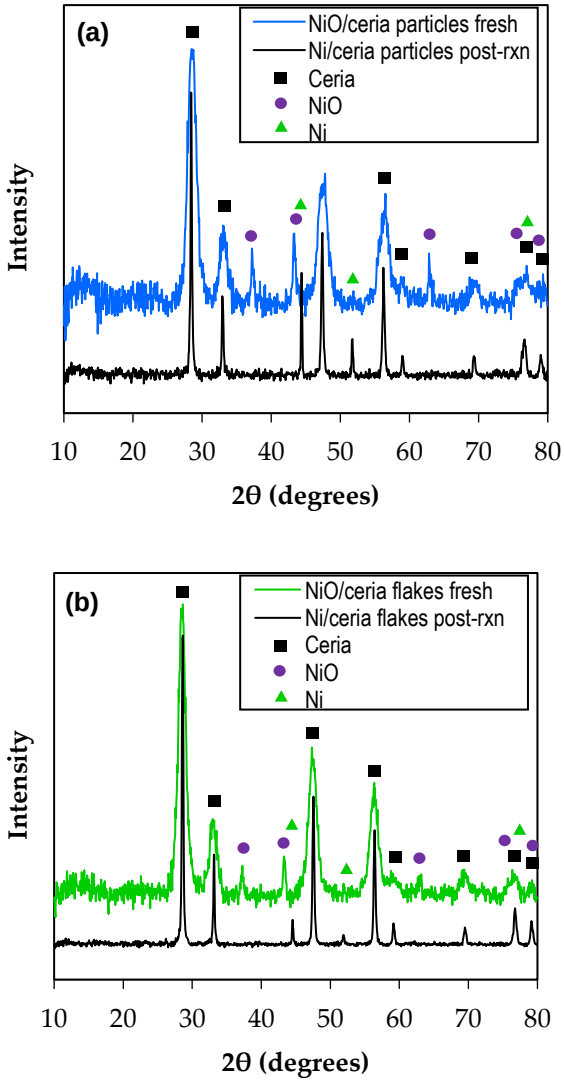

Figure 77. Powder XRD patterns of Ni-ceria catalysts, pre- and post-reaction (rxn). (a) Untemplated Ni-ceria particles. (b) GO-templated Ni-ceria flakes.

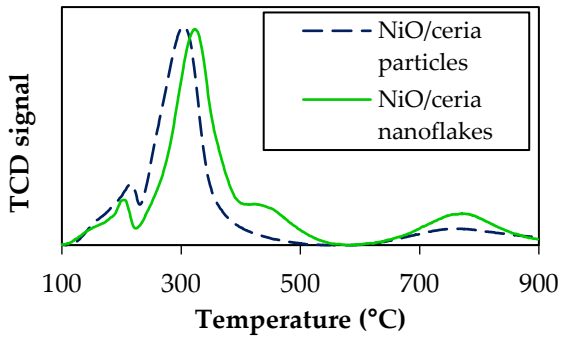

Figure 78. TPR profiles for nickel-deposited GO-templated ceria flakes and untemplated ceria particles.

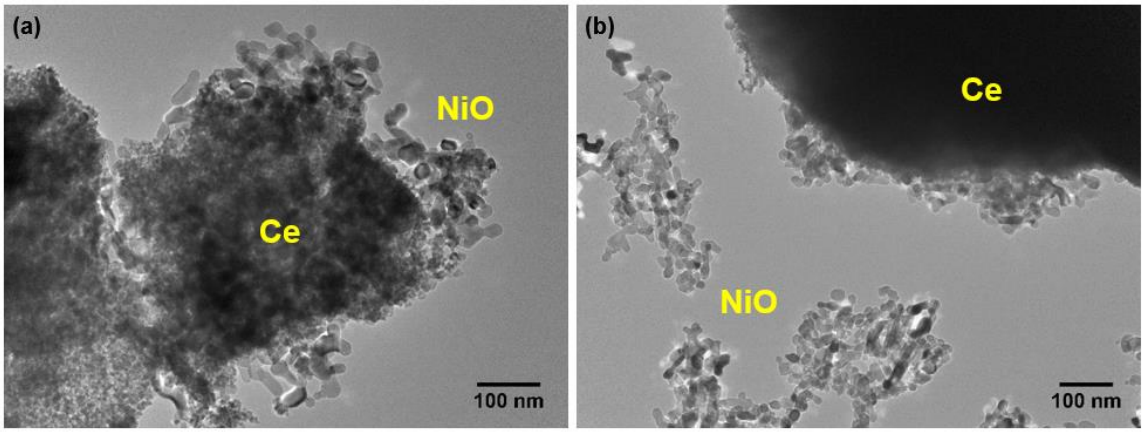

Figure 79. TEM micrographs of fresh Ni-ceria catalysts. (a) Fresh Ni-ceria flake catalyst after calcination at 700 °C. (b) Fresh Ni-ceria particle catalyst after calcination at 700 °C.

TEM micrographs of the fresh Ni-loaded ceria flakes and particles are shown in Figure 79a-b. EDX analyses and maps (Figure 80-83) show that the smaller (<10 nm) crystallites are primarily ceria, while the larger (20-40 nm) crystallites are nickel (NiO according to XRD). These ceria crystallite sizes match those calculated using Scherrer equation analysis using the ceria XRD patterns in Figure 51 (~6 nm for both materials, Table 8), and Ni-loaded ceria XRD patterns in Figure 77. In Figure 79a, of the fresh Ni-loaded ceria flakes, NiO particles can be seen clustering around the edges of ceria crystallite agglomerations. However, for the fresh untemplated Ni-loaded ceria particles, shown in Figure 79b, while some NiO particles appear to be similarly deposited on the edge of ceria crystallite agglomerations, much of the visible nickel is not deposited on ceria. These unsupported NiO particles were evenly dispersed across the TEM sample grid, a phenomenon not observed with the Ni-ceria flake sample. This observation suggests that NiO particles have a better interaction with the ceria support when supported on ceria flakes than ceria particles in agreement with the TPR data. Surface defects such as oxygen vacancies are known to be preferential nucleation sites for metal particle formation. [339,340] Therefore, the ceria flakes promote better nickel dispersion and stronger Ni-ceria interaction than the ceria particles, in agreement with the higher surface oxygen vacancy concentration of the nanoflakes, seen in Raman and TPR analysis (Figure 52-53).

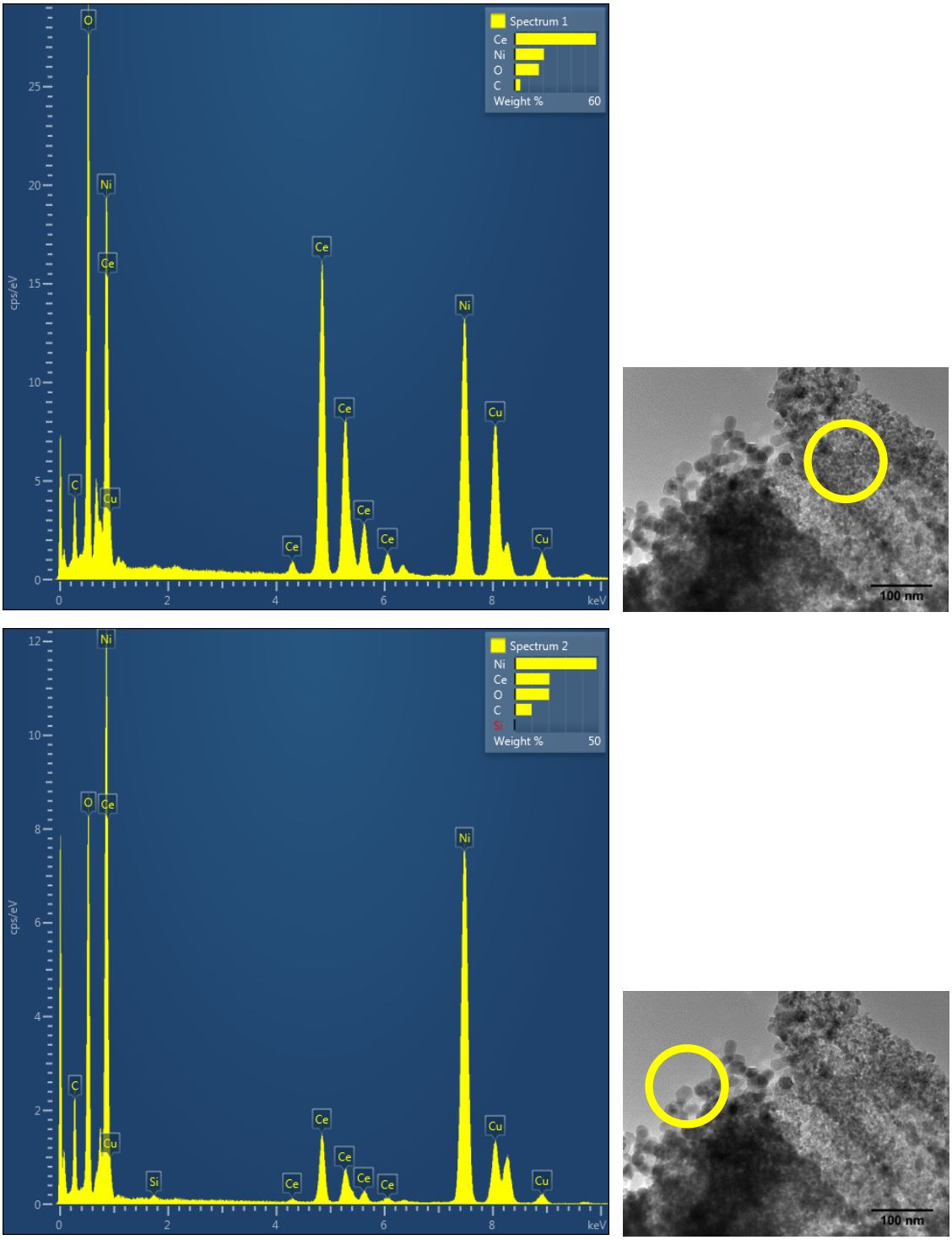

Figure 80. EDX analysis of fresh GO-templated nickel/ceria nanoflakes.

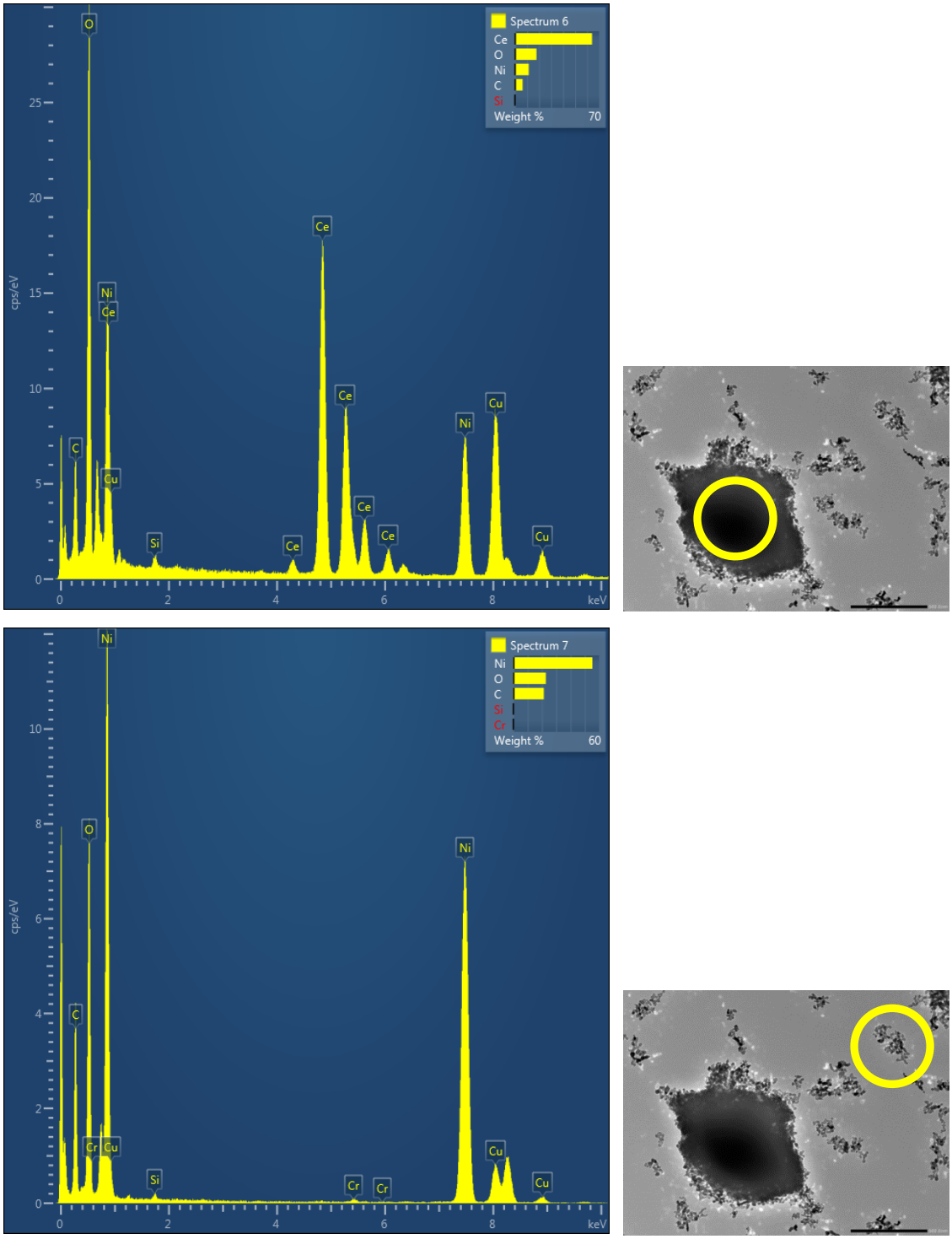

Figure 81. EDX analysis of fresh untemplated nickel/ceria particles.

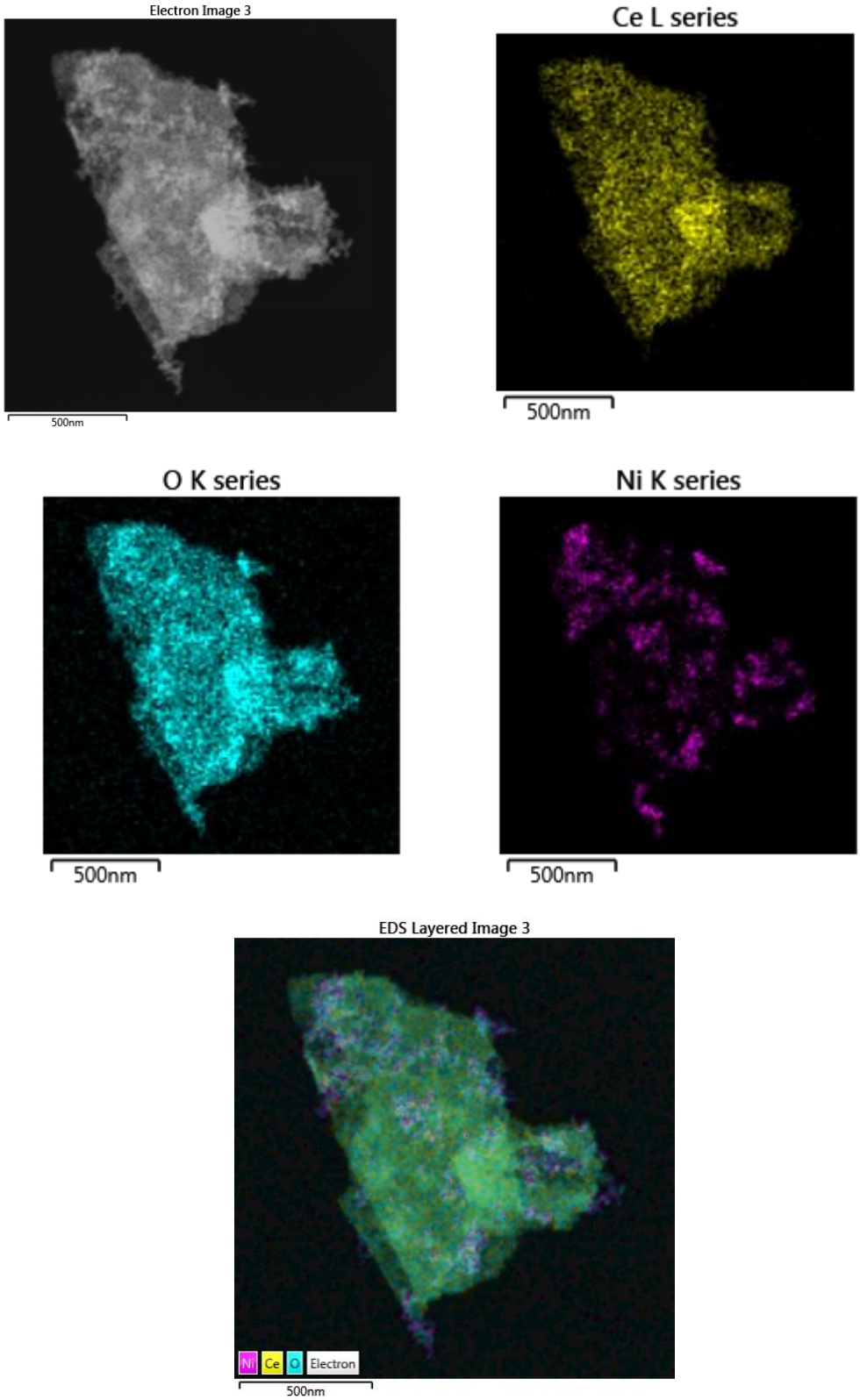

Figure 82. Elemental map of fresh GO-templated nickel/ceria nanoflakes.

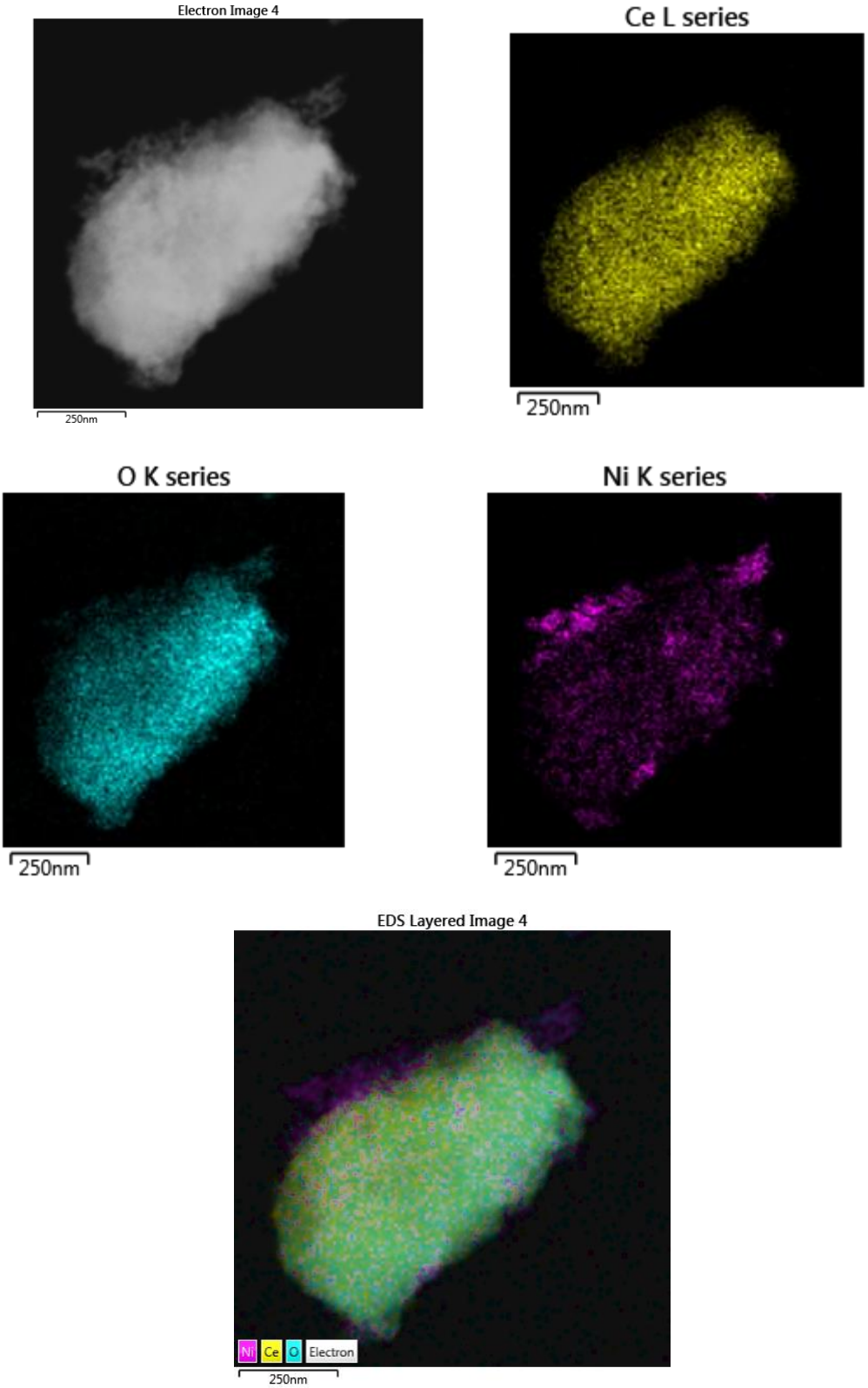

Figure 83. Elemental map of fresh untemplated nickel/ceria particles.

7.2 Ni/ceria nanoflakes – DRM catalytic activity

Catalytic activity of the Ni-loaded ceria particles and flakes for the dry reforming of methane (DRM) is shown in Figure 84a-b. In both cases, conversion of CH_4 is lower than conversion of CO_2 across the temperature range tested, a common observation in DRM because methane activation is the rate-limiting step. [341] For CO_2, conversion levels range from approximately 20% at 550 °C to 90% at 850 °C, while CH_4 conversion levels are less than 5% and 60-65% at 550 and 850 °C, respectively. The ratio of H_2 to CO produced ranges from 0.5 to 0.8 across the same temperature range. While this is promising, conversion levels do not appear to be as high as other nickel-based DRM catalysts recently reported in the literature. However, with papers reporting wide variation in Ni loading (1 to 63.5 %), reduction temperatures, space velocity and gas ratios, results are not always directly comparable. [342] The Ni supported on ceria flakes and particles perform similarly, although there are small differences. In both cases, the syngas H_2/CO ratio is close to 1 at high reaction temperatures, which is the limit imposed by the stoichiometry of the reaction.

Longer-term studies of the dry reforming reaction were undertaken at 800 °C, shown in Figure 84c-d. In contrast with the short-term temperature curve experiment shown in Figure 84a, where there were only small differences between the GO-templated and untemplated materials, in a long-term experiment the difference in activity between the two catalysts is quite dramatic. Untemplated Ni-ceria particles experience severe deactivation after approximately 5 hours, while the Ni-ceria flakes demonstrated much higher stability for both CH_4/CO_2 conversion and maintaining a high H_2/CO ratio. This can also be seen in the rate values (Figure 85) – for both CH_4 and CO_2 conversion over the 20-hour reaction, the activity of the Ni-ceria particles decreases significantly more than the activity of the Ni-ceria flakes. After 20 hours, the Ni-ceria flakes experience a reduction in activity of 18% for CO_2 conversion and 40% for CH_4 conversion, while the activity of Ni-ceria particles is reduced by 66% and 89%, respectively. Although only small improvements in activity are initially achieved with the ceria flakes compared with ceria particles, the main benefit of utilizing GO-templated ceria flakes is the improved thermal

stability and resistance to sintering that is due to the stronger nickel-ceria interaction of the ceria flakes.

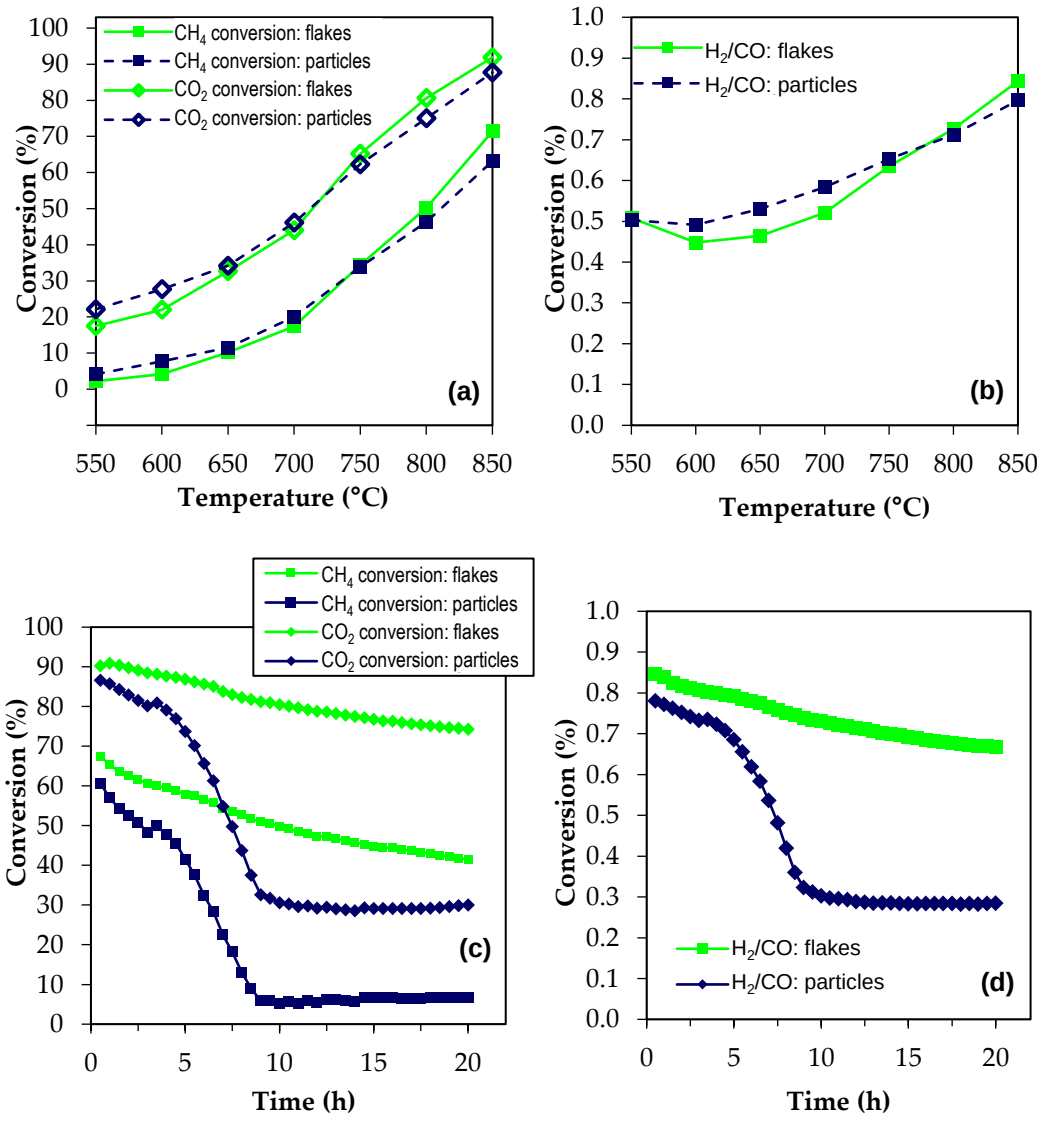

Figure 84. (a) Catalytic activity of Ni-loaded ceria flakes and particles for the dry reforming of methane, showing both CH_4 and CO_2 conversion. (b) The ratio of H_2 to CO produced as a function of temperature. (c) 20 h catalytic activity of Ni-loaded ceria flakes and particles at 800 °C for the dry reforming of methane, showing both CH_4 and CO_2 conversion. (d) The ratio of H_2 to CO produced as a function of time at 800 °C.

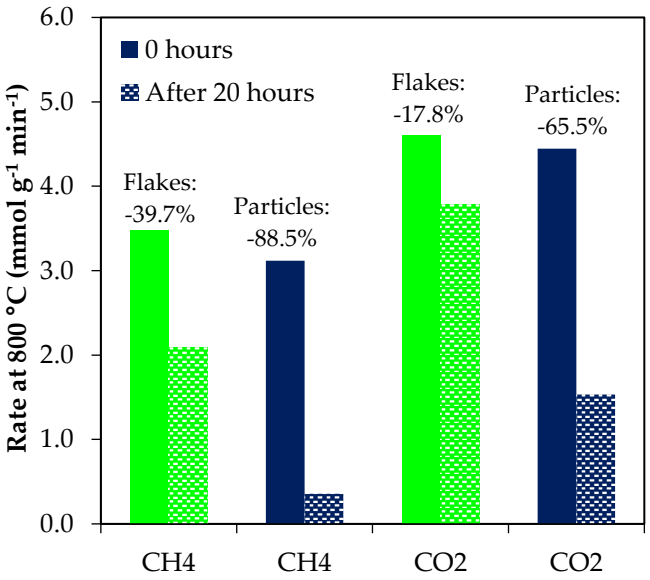

Figure 85. Rate of Ni/ceria flake and particle catalysts for dry reforming of methane over 20 hours. Reaction temperature: 800 °C.

7.3 Ni/ceria nanoflakes – post-DRM analysis

Nickel sintering and carbon deposition are the two major causes of catalyst deactivation of Ni based catalysts for dry methane reforming. [343] Post-reaction analysis was undertaken to determine the significance of these factors. Characterisation of the Ni-ceria materials prior to reaction, but after treatment with hydrogen to reduce the NiO particles to Ni, was not undertaken. This is because this step was performed in-situ immediately prior to catalyst testing. However, such characterisation does exist elsewhere in the literature. Horvath *et al* report that after reducing nickel-ceria-zirconia materials with hydrogen, XPS show the majority of Ni reduced to Ni^0, but approximately 30 % remains as Ni^{2+}. Additionally, Ce is reduced from Ce^{4+} to Ce^{3+}. [344] Kambolis *et al* report that reduction of such materials up to 900 °C reduces the specific surface area, typically by around 20 to 45 %. Aw *et al* report that when comparing calcination in air vs. calcination in a reducing environment, no significant difference is seen in terms of nickel particle sintering. [345] This means that differences in particle size pre-and post-reaction are likely due to sintering during the dry methane reforming reaction, not the pre-reduction step.

Post-reaction powder XRD patterns are shown in Figure 77. Compared with the fresh pre-reaction patterns, nickel is now present as Ni instead of NiO. Similarly to the pre-reaction NiO-ceria samples, the ceria crystallite sizes are similar in the spent catalysts – 34.4 and 33.1 nm for flakes and particles, respectively. In contrast, the Ni metal particles deposited on the post-reaction ceria particles are calculated to be 56 nm, compared with 43 nm for post-reaction ceria nanoflakes. This is an indication that while ceria nanoflakes do not entirely prevent nickel sintering, they do hinder sintering in comparison to nickel particles deposited on untemplated ceria and shows that the Ni particles are better dispersed on ceria flakes than ceria particles post-reaction, in agreement with the TPR results.

TEM micrographs of post-reaction spent Ni-ceria catalysts are shown in Figure 86a-b. After the 20 h stability experiment, the Ni-ceria flake catalyst, shown in Figure 86a, has retained its two-dimensional structure. However, the nickel particles have sintered, showing a wide range of sizes. Additionally, the ceria flakes are surrounded by a network of carbon nanotubes. In comparison, the Ni-loaded ceria particle catalyst is shown in Figure 86b. While the large ceria agglomerations seen in Figure 79b are still evident, the nickel is now also present in very large agglomerations being difficult to distinguish any structure at the nanoscale. Furthermore, no carbon nanotubes are visible.

While both the Ni-ceria flake and Ni-ceria particle catalysts show sintering of the nickel particles in EDX analysis (Figure 87-90), the sintering appears to be more severe for the untemplated Ni-ceria particle catalyst. The nanoflake catalyst shows a wide range of Ni particle sizes, from <100 nm to ~500 nm, while the untemplated particle catalyst only shows 300-500 nm and larger Ni particles. Additionally, while the elemental mapping analysis for the Ni-ceria flakes (Figure 89) still show distributed Ni particles, the map for Ni-ceria particles (Figure 90) shows one large Ni agglomeration.

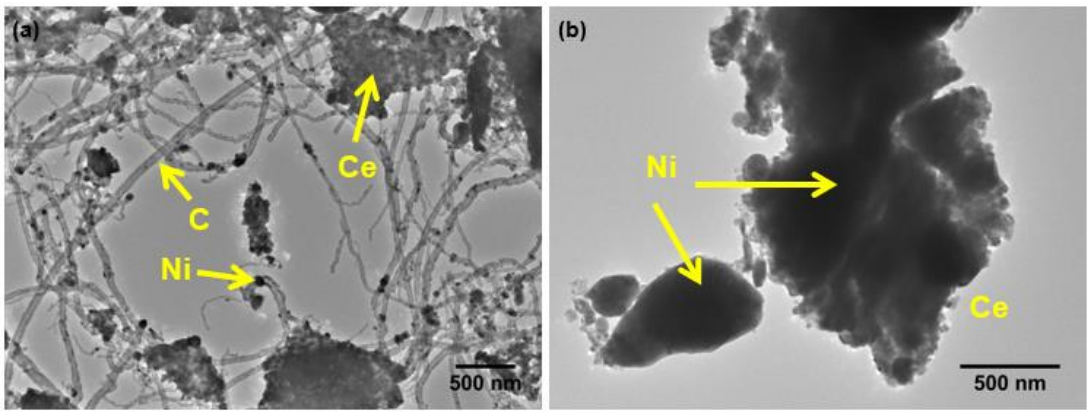

Figure 86. TEM micrographs of post-DRM Ni-ceria catalysts (a) Post-20 h, 800 °C reaction Ni ceria flake catalyst. (b) Post 20 h, 800 °C reaction Ni-ceria particle catalyst.

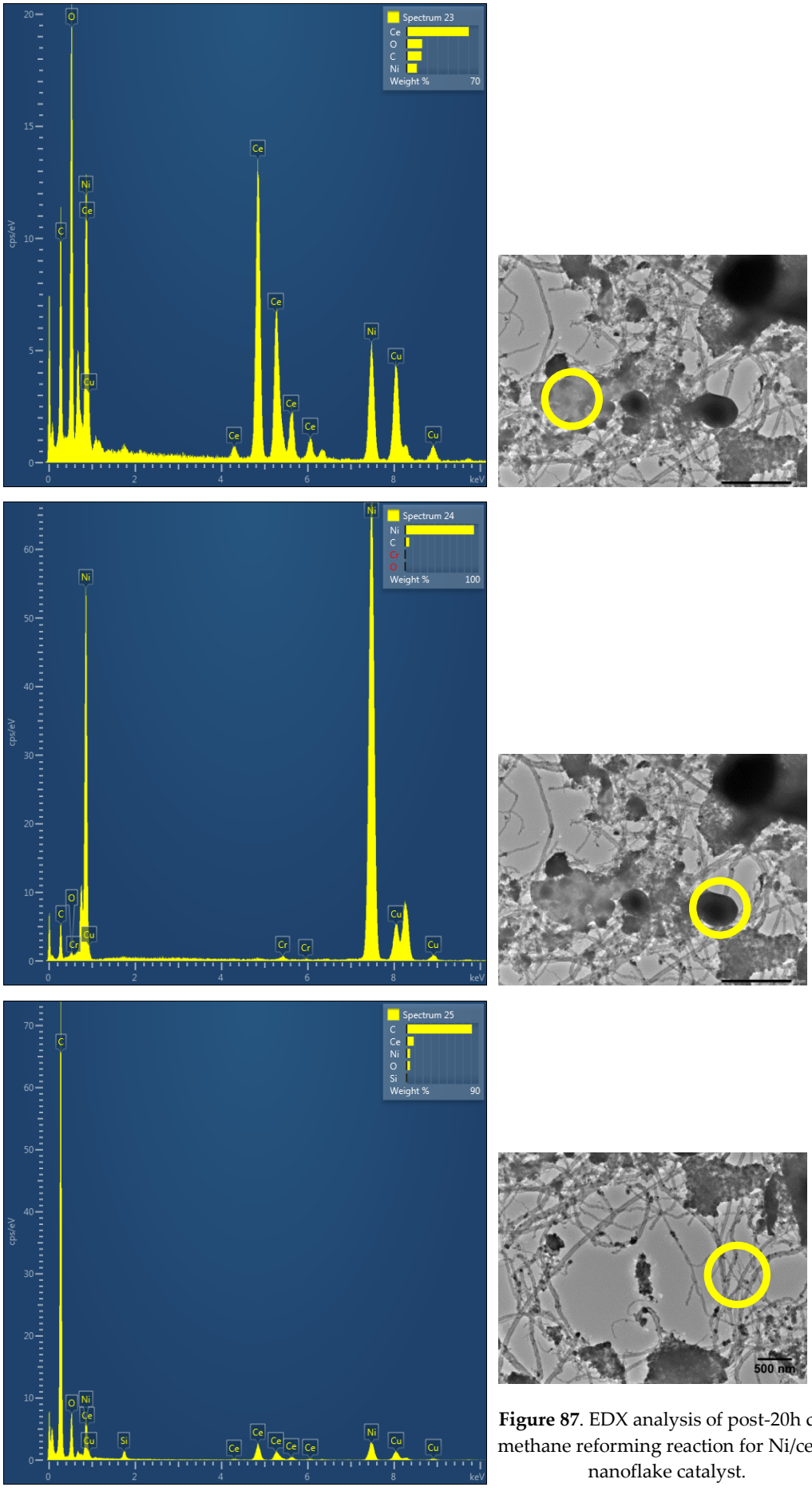

Figure 87. EDX analysis of post-20h dry methane reforming reaction for Ni/ceria nanoflake catalyst.

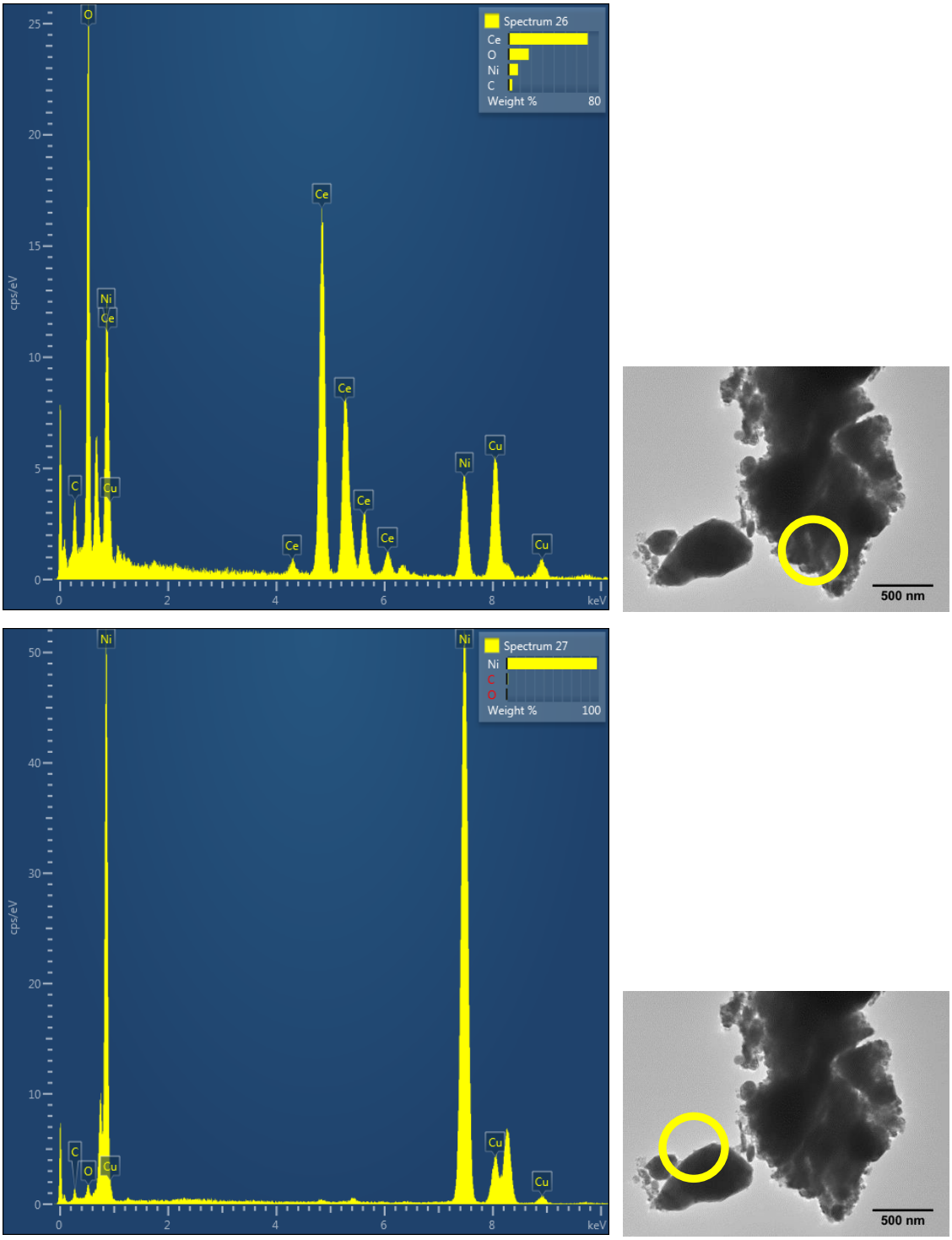

Figure 88. EDX analysis of post-20h dry methane reforming reaction for Ni/ceria particle catalyst.

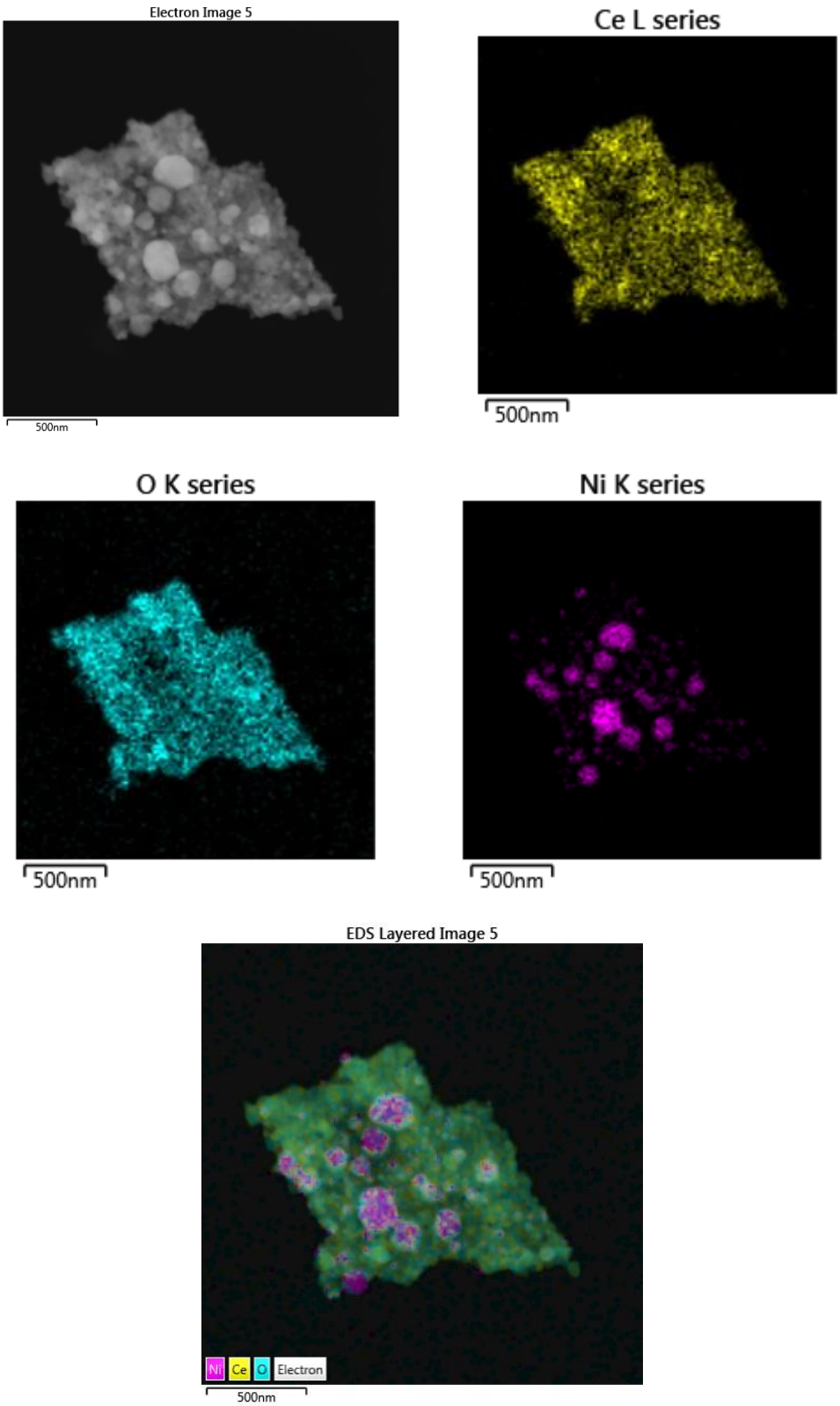

Figure 89. Elemental map of post-DRM reaction for GO-templated nickel/ceria flake catalyst.

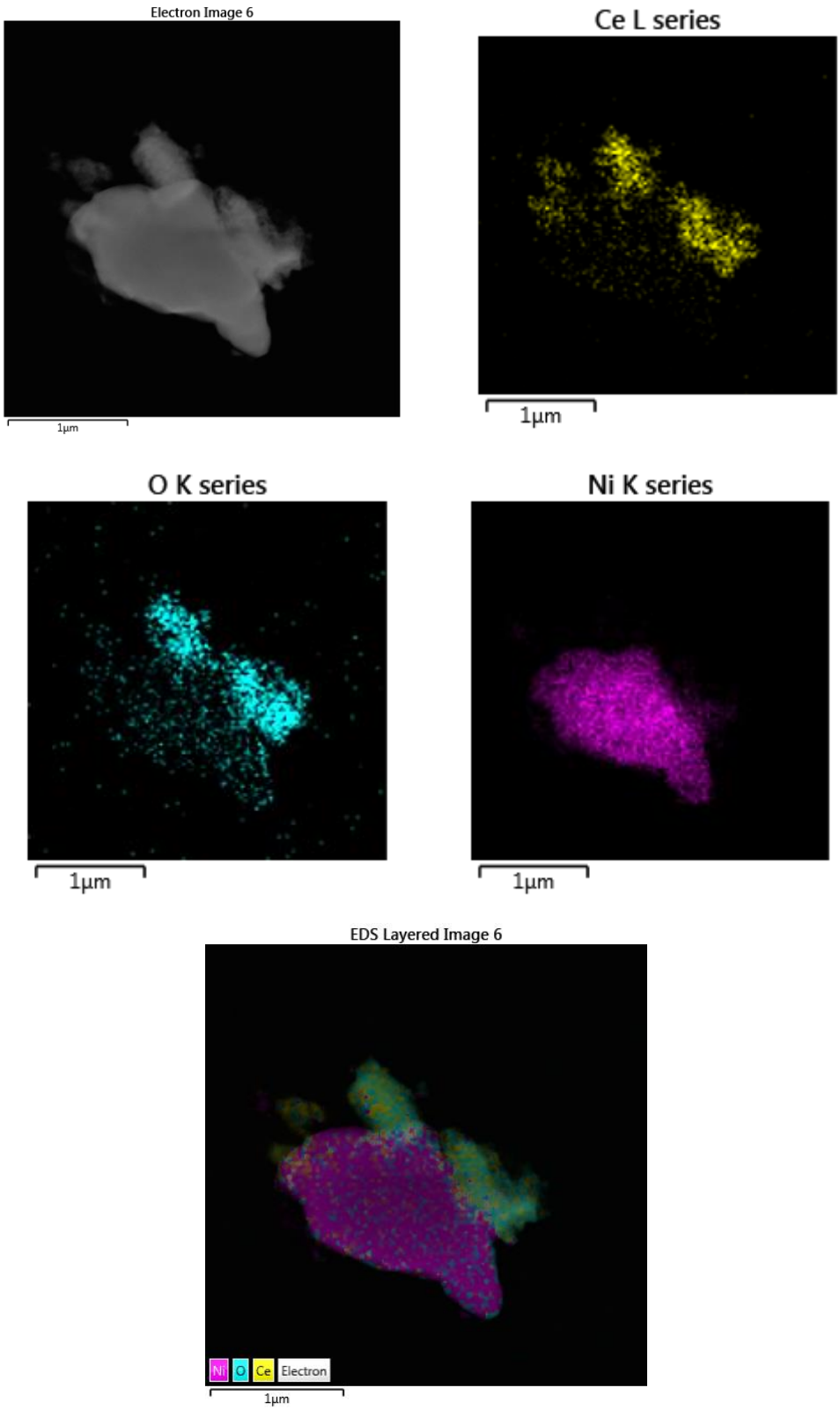

Figure 90. Elemental map of post-DRM reaction for untemplated nickel/ceria particle catalyst.

TGA was also performed on the post-20 h reaction Ni-ceria catalysts, shown in Figure 91. The TGA curve of the Ni-ceria flakes shows a sharp decrease in mass at approximately 500-600 °C, indicative of the presence of deposited carbon on the catalyst after reaction. However, the Ni-ceria particles do not show a similar decrease in mass. This indicates that significant carbon deposition occurred on the Ni-ceria flakes, but not the Ni-ceria particles, confirming a different reaction behaviour, and correlates well with TEM post-reaction analysis. The gain in weight seen in both samples could be due to several reasons: buoyancy effects in the TGA instrument at high temperatures, oxidation of the nickel particles, or a small effect due to the healing of oxygen vacancies in the ceria support.

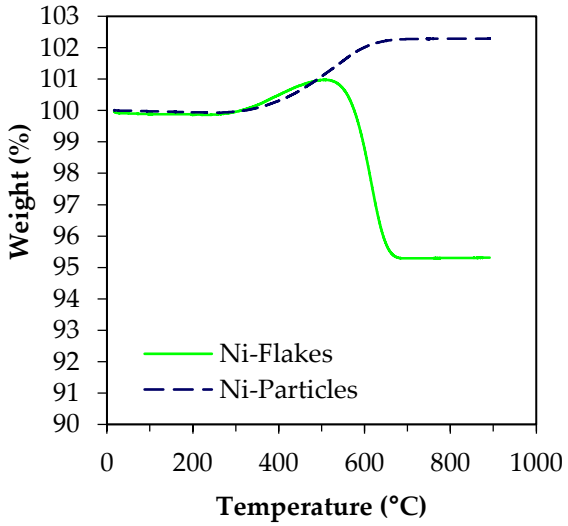

Figure 91. TGA curves for post-20 h reaction Ni-ceria flakes and particles in air.

In summary, the post-reaction analysis indicates that nickel sintering, and not carbon deposition, is responsible for the significant difference in catalyst deactivation in the long-term DRM experiment between the GO-templated and untemplated Ni-ceria catalysts. While both catalysts experienced nickel sintering, the untemplated Ni-ceria particle catalyst suffered from more severe sintering (Figure 86, Figure 89-90). While TGA analysis (Figure 91) showed carbon formation for the Ni-ceria flake catalyst and not the Ni-ceria particle catalyst, the TEM images (Figure 86a) showed that this was a network of filamentous carbon. Carbon deposition has often been reported to be a significant factor in nickel catalyst deactivation. [346–348] However, the type of carbon deposit –

encapsulating, filamentous, or other – affects methane reforming catalysts in different ways, if at all, and the relationship between catalytic activity and quantity of carbon deposited on the catalyst is not always straightforward. [344] While the formation of amorphous carbon can coat and deactivate catalysts, filamentous carbon growth can lead to structural modifications within the catalyst (such as forced separation of the nickel and ceria crystallites) which reduces activity. [349] Nevertheless, not all filamentous carbon growth appears to be harmful to catalytic activity. Additionally, it should be underlined that carbon formation is difficult to avoid for Ni-based materials during methane reforming reaction and the formation of carbon (soft or hard) is an indication of catalytic activity. [63] The key is developing Ni-based materials which lead to soft carbon formation, which is possible if Ni sintering is hindered, since large Ni clusters are more prone to forming hard carbon deposits than small Ni clusters. [332,350] In this scenario, Ni-ceria nanoflakes are excellent materials due to their resistance towards metallic sintering.

7.4 Conclusions

Nickel-loaded and GO-templated Ni/ceria nanoflakes outperform untemplated Ni/ceria particles for the dry reforming of methane. As with the performance of bare ceria nanoflakes in Chapter 6, their improved resistance to sintering, higher BET surface area after exposure to high temperatures, and higher surface reducibility leads to a clear stability advantage in high-temperature reactions. GO-templated ceria nanoflakes have shown that they not only hinder sintering of ceria particles, but of deposited nickel particles as well. Additionally, after a 20 h reaction stability test, no encapsulating hard carbon deposits are seen, only filamentous carbon which does not inhibit catalytic activity. Overall, these results show that the use of GO-templated ceria nanoflakes as a support for nickel DRM catalysts is a promising option for designing catalysts which are more stable at the high temperatures required by the reaction.

Chapter 8

Thesis Conclusions

The potential of different nanostructured ceria-based catalysts for eventual use in automotive catalysis has been explored in detail in the results presented in this thesis. In Chapter 1, the review of the scientific literature has emphasised the importance of the role ceria in catalytic converters plays in the removal of several pollutants from vehicle exhaust which significantly impact air quality. Doping and nanostructuring strategies can be used to improve the oxygen storage capacity of ceria and ceria-based materials, improving catalytic performance. This offers a potential route for the development of ceria-based catalyst materials with a reduced dependence on scarce and expensive platinum-group metals, important from a sustainability perspective.

Furthermore, this literature review has examined the reported performance of a wide range of doped ceria materials described in the literature for the reactions relevant to automotive three-way catalysis. While the effectiveness of doped ceria catalysts for CO oxidation has been widely reported, other reactions such as NO reduction are less thoroughly studied. The lack of literature regarding the efficacy of doped ceria materials in NO reduction catalysis shows that this area of research needs more attention, particularly due to this reaction's importance in completing the catalytic cycle of three-way catalysis – healing oxygen vacancies caused by the oxidation of CO and hydrocarbons to CO_2.

In Chapter 5, the effectiveness of doped ceria nanorods for CO oxidation and NO reduction reactions has been examined. Building on prior work demonstrating that ceria nanorods show advantages compared with other ceria morphologies due to selective exposure of the (110) crystal plane, and other doped ceria experiments reported in the literature, it is shown that doping ceria with copper or chromium improves catalytic activity for CO oxidation and NO reduction, respectively. In particular, copper doping improves the light-off temperature for CO oxidation to below that of common PGM-based

catalysts. Furthermore, simultaneously co-doping ceria nanorods with low levels of both copper and chromium results in a synergistic phenomenon – a ceria doped with 1 wt. % each Cu and Cr has enhanced catalytic performance for both CO oxidation and NO reduction, beyond that of ceria nanorods doped with an equivalent level of just copper or chromium. These results offer a potential route for the synthesis of ceria-based catalysts doped with low levels of transition metals instead of relying on deposited platinum group metal catalysts, as current catalytic converter designs do.

The use of graphene oxide as a sacrificial template for the production of ceria nanoflakes was investigated in Chapter 6. Due to their two-dimensional morphology, these nanoflakes have significantly improved resistance to sintering at high temperatures compared with similarly prepared untemplated ceria particles, and also demonstrate enhanced reducibility. Ceria nanoflakes are a better catalyst for CO oxidation compared with untemplated ceria particles due to their higher surface area and higher concentration of oxygen vacancies. Ceria nanoflakes loaded with copper also provide enhanced performance for CO oxidation than copper-loaded ceria particles, showing improved stability over time, and ceria-zirconia mixed oxide nanoflakes were synthesised to further enhance high-temperature stability.

In Chapter 7, ceria nanoflakes are used as a catalytic support for nickel particles in the dry reforming of methane for the production of syngas. Similarly to the bare ceria nanoflakes, nickel particles deposited on the nanoflakes show improved resistance to high-temperature sintering than nickel loaded on untemplated ceria particles. The nickel-ceria nanoflake catalyst shows improved catalytic activity in dry reforming of methane and, due to their resistance to sintering, a slower decline in activity over time. These results demonstrate the versatility of ceria nanoflakes as a catalyst support and for use in other high temperature catalytic applications that can also be impacted by sintering.

During the course of this thesis, two potential strategies for improving the catalytic performance of ceria-based materials have been explored. These strategies are doping ceria nanorods with transition metals to improve low-temperature activity, and using

graphene oxide to modify ceria's morphology for enhanced high-temperature stability. This work offers two routes for the further development of catalytic converter design:

One, the complete or partial replacement of platinum group metal particles in present-day three-way catalyst formulations with transition metals doped directly into the catalyst's ceria component, and potentially incorporating the nanorod morphology as well. This approach would be a more radical departure from current automotive catalyst formulations and would require a significant amount of additional research to become practical.

Two, using graphene oxide as a template to synthesise catalytic converter washcoat materials with enhanced high-temperature sintering resistance, which could reduce the decline in catalyst performance over a vehicle's lifetime. In terms of modifications to current three-way catalyst designs, this is a more conservative approach than replacing platinum group metals with doped transition metals.

Future directions in research for doped ceria materials will need to focus on improving sintering resistance and maintenance of catalytic activity at high temperatures. While the results reported in this thesis and elsewhere in the scientific literature show that good low-temperature performance can be achieved with doped ceria catalysts, this is of little practical use if these materials sinter and degrade upon exposure to high temperature vehicle exhaust. As a replacement for platinum group metal-based catalyst formulations, doped ceria catalysts need to demonstrate they can retain good performance even after high temperature exposure and over long periods of time. For the graphene oxide synthesis, further work should be conducted to produce templated nanoflake materials that more closely replicate the oxygen storage materials used in present-day three-way catalyst washcoat materials. While these oxygen storage materials are usually predominantly ceria and zirconia, they may also contain lower levels of various other metals (such as Al_2O_3, La, Pr, Nd, Ba) to improve stability and enhance performance.

Overall, the results reported in this thesis show promise in improving three-way catalyst performance for the remediation of vehicle exhaust. While battery electric vehicles are

becoming a more prominent part of the automotive market, vehicles powered by fossil fuels are projected to be in significant use for decades to come. Therefore, the further development of catalytic converter technology will be highly significant in continuing efforts to improve air quality, particularly in dense urban areas.

Chapter 9

References

[1] Defra, Air Pollution in the UK 2014, London, 2014.
[2] Rcp, Rcpch, Every Breath We Take - The Lifelong Impact of Air Pollution, London, 2016.
[3] UNEP, Air Pollution: World's Worst Environmental Health Risk, 2014.
[4] M.V. Twigg, Progress and future challenges in controlling automotive exhaust gas emissions, Appl. Catal. B-Environ. 70 (2007) 2–15. doi:10.1016/j.apcatb.2006.02.029.
[5] World Health Organization (WHO), WHO Global Urban Ambient Air Pollution Database (update 2016), 2016.
[6] M.V. Twigg, Catalytic control of emissions from cars, Catal. Today. 163 (2011) 33–41. doi:10.1016/j.cattod.2010.12.044.
[7] C.H. Bartholomew, R.J. Farrauto, Fundamentals of Industrial Catalytic Processes, 2nd ed., Wiley-Blackwell, 2006.
[8] J.-J. He, C.-X. Wang, T.-T. Zheng, Y.-K. Zhao, Thermally Induced Deactivation and the Corresponding Strategies for Improving Durability in Automotive Three-Way Catalysts, Johnson Matthey Tech. 60 (2016) 196–203. doi:10.1595/205651316x691960.
[9] E. Alonso, F.R. Field, R.E. Kirchain, A case study of the availability of platinum group metals for electronics manufacturers, in: IEEE, 2008: pp. 1–6. doi:10.1109/ISEE.2008.4562902.
[10] M.S. Reiter, K.M. Kockelman, The problem of cold starts: A closer look at mobile source emissions levels, Transport Res. D-Tr. E. 43 (2016) 123–132. doi:10.1016/j.trd.2015.12.012.
[11] A. Cao, R. Lu, G. Veser, Stabilizing metal nanoparticles for heterogeneous catalysis, Physical Chemistry Chemical Physics : PCCP. 12 (2010) 13499–510. doi:10.1039/c0cp00729c.
[12] N. Guillén-Hurtado, V. Rico-Pérez, A. García-García, D. Lozano-Castelló, A. Bueno-López, Three-Way Catalysts: Past, Present, and Future, Dyna. 79 (2012) 114–121.
[13] C.L.S. Wiseman, F. Zereini, Airborne particulate matter, platinum group elements and human health: a review of recent evidence, Sci. Total Environ. 407 (2009) 2493–500. doi:10.1016/j.scitotenv.2008.12.057.
[14] M. Buchert, D. Schuler, D. Bleher, Critical Metals for Future Sustainable Technologies and their Recycling Potential, 2009.
[15] M. Johnson, PGM Market Report May 2016, 2016.
[16] D. Friedman, T. Masciangioli, S. Olson, Replacing Critical Materials with Abundant Materials, in: National Academies Press (US), Washington, DC, 2012.
[17] T.E. Graedel, L. Erdmann, Will metal scarcity impede routine industrial use?, MRS Bull. 37 (2012) 325–331.
[18] M. Mogensen, Physical, chemical and electrochemical properties of pure and doped ceria, Solid State Ionics. 129 (2000) 63–94. doi:10.1016/S0167-2738(99)00318-5.
[19] Z.L. Wang, X. Feng, Polyhedral Shapes of CeO 2 Nanoparticles, The Journal of Physical Chemistry B. 107 (2003) 13563–13566. doi:10.1021/jp036815m.
[20] D. Schweke, Y. Mordehovitz, M. Halabi, L. Shelly, S. Hayun, Defect Chemistry of Oxides for Energy Applications, Advanced Materials. 30 (2018) 1706300. doi:10.1002/adma.201706300.
[21] C. Sun, H. Li, L. Chen, Nanostructured ceria-based materials: synthesis, properties, and applications, Energy Environ. Sci. 5 (2012) 8475–8475. doi:10.1039/c2ee22310d.
[22] F.S. da Silva, T.M. de Souza, Novel materials for solid oxide fuel cell technologies: A literature review, International Journal of Hydrogen Energy. 42 (2017) 26020–26036. doi:10.1016/j.ijhydene.2017.08.105.
[23] G. Eranna, B.C. Joshi, D.P. Runthala, R.P. Gupta, Oxide Materials for Development of Integrated Gas Sensors—A Comprehensive Review, Critical Reviews in Solid State and Materials Sciences. 29 (2004) 111–188. doi:10.1080/10408430490888977.
[24] L.M. Cook, Chemical processes in glass polishing, J. Non-Cryst. Solids. 120 (1990) 152–171. doi:10.1016/0022-3093(90)90200-6.
[25] R. Benzaid, J. Chevalier, M. Saâdaoui, G. Fantozzi, M. Nawa, L.A. Diaz, R. Torrecillas, Fracture toughness, strength and slow crack growth in a ceria stabilized zirconia–alumina nanocomposite for medical applications, Biomaterials. 29 (2008) 3636–3641. doi:10.1016/j.biomaterials.2008.05.021.
[26] Z. Tian, J. Li, Z. Zhang, W. Gao, X. Zhou, Y. Qu, Highly sensitive and robust peroxidase-like activity of porous nanorods of ceria and their application for breast cancer detection, Biomaterials. 59 (2015) 116–124. doi:10.1016/j.biomaterials.2015.04.039.
[27] K.J. Warren, J. Reim, K. Randhir, B. Greek, R. Carrillo, D.W. Hahn, J.R. Scheffe, Theoretical and Experimental Investigation of Solar Methane Reforming through the Nonstoichiometric Ceria Redox Cycle, Energy Technology. 5 (2017) 2138–2149. doi:10.1002/ente.201700083.
[28] I.D. Iglesias, G. Baronetti, F. Mariño, Nickel-based doped ceria-supported catalysts for steam reforming of methane at mild conditions, Energy Sources, Part A: Recovery, Utilization, and Environmental Effects. 39 (2017) 129–133. doi:10.1080/15567036.2016.1214639.
[29] A. Wolfbeisser, O. Sophiphun, J. Bernardi, J. Wittayakun, K. Föttinger, G. Rupprechter, Methane dry reforming over ceria-zirconia supported Ni catalysts, Catalysis Today. 277 (2016) 234–245. doi:10.1016/j.cattod.2016.04.025.

[30] S. Xie, Z. Wang, F. Cheng, P. Zhang, W. Mai, Y. Tong, Ceria and ceria-based nanostructured materials for photoenergy applications, Nano Energy. 34 (2017) 313–337. doi:10.1016/j.nanoen.2017.02.029.
[31] N.A.M. Fadzil, M.H.A. Rahim, G.P. Maniam, Brief review of ceria and modified ceria: synthesis and application, Mater. Res. Express. 5 (2018) 085019. doi:10.1088/2053-1591/aad2b5.
[32] V. Ivanov, O. Ivanova Polezhaeva, Y. Tretyakov, Nanocrystalline ceria: Synthesis, structure-sensitive properties, and promising applications, Russian Journal of General Chemistry. 80 (2010) 604–617. doi:10.1134/S1070363210030412.
[33] D. Zhang, X. Du, L. Shi, R. Gao, Shape-controlled synthesis and catalytic application of ceria nanomaterials, Dalton Trans. 41 (2012) 14455–14475. doi:10.1039/C2DT31759A.
[34] J. Baneshi, M. Haghighi, N. Jodeiri, M. Abdollahifar, H. Ajamein, Homogeneous precipitation synthesis of CuO–ZrO2–CeO2–Al2O3 nanocatalyst used in hydrogen production via methanol steam reforming for fuel cell applications, Energy Conversion and Management. 87 (2014) 928–937. doi:10.1016/j.enconman.2014.07.058.
[35] G. Dell'Agli, L. Spiridigliozzi, A. Marocco, G. Accardo, D. Frattini, Y. Kwon, S.P. Yoon, Morphological and crystalline evolution of Sm-(20mol%)–doped ceria nanopowders prepared by a combined co-precipitation/hydrothermal synthesis for solid oxide fuel cell applications, Ceramics International. 43 (2017) 12799–12808. doi:10.1016/j.ceramint.2017.06.169.
[36] H.-X. Mai, L.-D. Sun, Y.-W. Zhang, R. Si, W. Feng, H.-P. Zhang, H.-C. Liu, C.-H. Yan, Shape-selective synthesis and oxygen storage behavior of ceria nanopolyhedra, nanorods, and nanocubes, J. Phys. Chem. B. 109 (2005) 24380–5. doi:10.1021/jp055584b.
[37] L. Torrente-Murciano, A. Gilbank, B. Puertolas, T. Garcia, B. Solsona, D. Chadwick, Shape-dependency activity of nanostructured CeO2 in the total oxidation of polycyclic aromatic hydrocarbons, Appl. Catal. B-Environ. 132–133 (2013) 116–122. doi:10.1016/j.apcatb.2012.10.030.
[38] X. Jiang, J. Zhang, L. Yu, R. Chen, X. Xu, Synthesis of mono-dispersed ceria hollow nanospheres by a hydrothermal method, IET Micro Nano Letters. 11 (2016) 137–141. doi:10.1049/mnl.2015.0455.
[39] G. Shen, M. Liu, Z. Wang, Q. Wang, Hierarchical Structure and Catalytic Activity of Flower-Like CeO2 Spheres Prepared Via a Hydrothermal Method, Nanomaterials. 8 (2018) 773. doi:10.3390/nano8100773.
[40] R.I. Walton, Solvothermal synthesis of cerium oxides, Prog. Cryst. Growth Charact. Mater. 57 (2011) 93–108. doi:10.1016/j.pcrysgrow.2011.10.002.
[41] O.S. Hammond, K.J. Edler, D.T. Bowron, L. Torrente-Murciano, Deep eutectic-solvothermal synthesis of nanostructured ceria, Nature Communications. 8 (2017) 14150. doi:10.1038/ncomms14150.
[42] A. Kumar, N. Yadav, M. Bhatt, N.K. Mishra, P. Chaudhary, R. Singh, Sol-Gel Derived Nanomaterials and It's Applications: A Review, Res. J. Chem. Sci. 5 (2015) 98–105.
[43] T. Yu, J. Joo, Y.I. Park, T. Hyeon, Large-scale nonhydrolytic sol-gel synthesis of uniform-sized ceria nanocrystals with spherical, wire, and tadpole shapes, Angewandte Chemie (International Ed. in English). 44 (2005) 7411–4. doi:10.1002/anie.200500992.
[44] C. Laberty-Robert, J.W. Long, E.M. Lucas, K.A. Pettigrew, R.M. Stroud, M.S. Doescher, D.R. Rolison, Sol−Gel-Derived Ceria Nanoarchitectures: Synthesis, Characterization, and Electrical Properties, Chem. Mater. 18 (2006) 50–58. doi:10.1021/cm051385t.
[45] G. Chen, F. Rosei, D. Ma, Template engaged synthesis of hollow ceria-based composites, Nanoscale. 7 (2015) 5578–5591. doi:10.1039/C4NR07674E.
[46] M. Wang, M.-F. Wang, Y.-M. Wang, J.-W. Shen, Z.-Y. Wang, H. Gao, L.-L. Wang, X. Ouyang, DNA assisted synthesis of CeO2 nanocrystals with enhanced peroxidase-like activity, CrystEngComm. 20 (2018) 4075–4079. doi:10.1039/C8CE00569A.
[47] A.B. Sifontes, G. Gonzalez, J.L. Ochoa, L.M. Tovar, T. Zoltan, E. Cañizales, Chitosan as template for the synthesis of ceria nanoparticles, Materials Research Bulletin. 46 (2011) 1794–1799. doi:10.1016/j.materresbull.2011.07.049.
[48] D. Zhu, D. Duan, Y. Han, J. He, Y. He, Y. Chen, W. Zhang, Z. Yan, J. Wang, F. Yuan, Noble Metal-Free Ceria-Zirconia Solid Solutions Templated by Tobacco Materials for Catalytic Oxidation of CO, Catalysts. 6 (2016) 135. doi:10.3390/catal6090135.
[49] P. Xu, R. Yu, H. Ren, L. Zong, J. Chen, X. Xing, Hierarchical nanoscale multi-shell Au/CeO 2 hollow spheres, Chemical Science. 5 (2014) 4221–4226. doi:10.1039/C4SC01882F.
[50] S.T. Aruna, A.S. Mukasyan, Combustion synthesis and nanomaterials, Current Opinion in Solid State and Materials Science. 12 (2008) 44–50. doi:10.1016/j.cossms.2008.12.002.
[51] A.S. Mukasyan, P. Epstein, P. Dinka, Solution combustion synthesis of nanomaterials, Proceedings of the Combustion Institute. 31 (2007) 1789–1795. doi:10.1016/j.proci.2006.07.052.
[52] C. Aliotta, L.F. Liotta, V. La Parola, A. Martorana, E.N.S. Muccillo, R. Muccillo, F. Deganello, Ceria-based electrolytes prepared by solution combustion synthesis: The role of fuel on the materials properties, Appl. Catal. B-Environ. 197 (2016) 14–22. doi:10.1016/j.apcatb.2016.02.044.
[53] B. Shri Prakash, V.K. William Grips, S.T. Aruna, A single step solution combustion approach for preparing gadolinia doped ceria solid oxide fuel cell electrolyte material suitable for wet powder and plasma spraying processes, Journal of Power Sources. 214 (2012) 358–364. doi:10.1016/j.jpowsour.2012.04.049.
[54] M.V. Ganduglia-Pirovano, A. Hofmann, J. Sauer, Oxygen vacancies in transition metal and rare earth oxides: Current state of understanding and remaining challenges, Surf. Sci. Rep. 62 (2007) 219–270. doi:10.1016/j.surfrep.2007.03.002.
[55] A. Gupta, U.V. Waghmare, M.S. Hegde, Correlation of Oxygen Storage Capacity and Structural Distortion in Transition-Metal-, Noble-Metal-, and Rare-Earth-Ion-Substituted CeO2 from First Principles Calculation, Chem. Mater. 22 (2010) 5184–5198. doi:10.1021/cm101145d.

[56] T.X.T. Sayle, S.C. Parker, C.R.A. Catlow, The role of oxygen vacancies on ceria surfaces in the oxidation of carbon monoxide, Surf. Sci. 316 (1994) 329–336. doi:10.1016/0039-6028(94)91225-4.
[57] M. Nolan, S.C. Parker, G.W. Watson, The electronic structure of oxygen vacancy defects at the low index surfaces of ceria, Surf. Sci. 595 (2005) 223–232. doi:10.1016/j.susc.2005.08.015.
[58] A.D. Mayernick, M.J. Janik, Methane Activation and Oxygen Vacancy Formation over CeO 2 and Zr, Pd Substituted CeO 2 Surfaces, The Journal of Physical Chemistry C. 112 (2008) 14955–14964. doi:10.1021/jp805134s.
[59] Z. Yang, T.K. Woo, M. Baudin, K. Hermansson, Atomic and electronic structure of unreduced and reduced CeO2 surfaces: a first-principles study, The Journal of Chemical Physics. 120 (2004) 7741–9. doi:10.1063/1.1688316.
[60] S. Fabris, G. Vicario, G. Balducci, S. de Gironcoli, S. Baroni, Electronic and atomistic structures of clean and reduced ceria surfaces, The Journal of Physical Chemistry. B. 109 (2005) 22860–7. doi:10.1021/jp0511698.
[61] K. Zhou, X. Wang, X. Sun, Q. Peng, Y. Li, Enhanced catalytic activity of ceria nanorods from well-defined reactive crystal planes, J. Catal. 229 (2005) 206–212. doi:10.1016/j.jcat.2004.11.004.
[62] Tana, M. Zhang, J. Li, H. Li, Y. Li, W. Shen, Morphology-dependent redox and catalytic properties of CeO2 nanostructures: Nanowires, nanorods and nanoparticles, Catal. Today. 148 (2009) 179–183. doi:10.1016/j.cattod.2009.02.016.
[63] S. Agarwal, L. Lefferts, B.L. Mojet, D.A.J.M. Ligthart, E.J.M. Hensen, D.R.G. Mitchell, W.J. Erasmus, B.G. Anderson, E.J. Olivier, J.H. Neethling, A.K. Datye, Exposed Surfaces on Shape-Controlled Ceria Nanoparticles Revealed through AC-TEM and Water–Gas Shift Reactivity, ChemSusChem. 6 (2013) 1898–1906. doi:10.1002/cssc.201300651.
[64] I. de C. Silva, F.A. Sigoli, I.O. Mazali, Reversible Oxygen Vacancy Generation on Pure CeO2 Nanorods Evaluated by in Situ Raman Spectroscopy, J. Phys. Chem. C. 121 (2017) 12928–12935. doi:10.1021/acs.jpcc.7b03155.
[65] G. Zhang, Y. Guo, L. Lu, Z. Zhang, L. Wang, L. Zhou, J. Shao, Synthesis and characterization of CeO 2 thin film with well-ordered step edges, Mater. Lett. 125 (2014) 162–166. doi:10.1016/j.matlet.2014.03.157.
[66] O.S. Bezkrovnyi, P. Kraszkiewicz, M. Ptak, L. Kepinski, Thermally induced reconstruction of ceria nanocubes into zigzag {111}-nanofacetted structures and its influence on catalytic activity in CO oxidation, Catalysis Communications. (2018). doi:10.1016/j.catcom.2018.08.005.
[67] G. Zhou, B. Gui, H. Xie, F. Yang, Y. Chen, S. Chen, X. Zheng, Influence of CeO2 morphology on the catalytic oxidation of ethanol in air, Journal of Industrial and Engineering Chemistry. 20 (2014) 160–165. doi:10.1016/j.jiec.2013.04.012.
[68] M. Nolan, Charge Compensation and Ce 3+ Formation in Trivalent Doping of the CeO 2 (110) Surface: The Key Role of Dopant Ionic Radius, The Journal of Physical Chemistry C. 115 (2011) 6671–6681. doi:10.1021/jp112112u.
[69] G. Balducci, M.S. Islam, J. Kašpar, P. Fornasiero, M. Graziani, Reduction Process in CeO 2 −MO and CeO 2 −M 2 O 3 Mixed Oxides: A Computer Simulation Study, Chem. Mater. 15 (2003) 3781–3785. doi:10.1021/cm021289h.
[70] M.D. Krcha, A.D. Mayernick, M.J. Janik, Periodic trends of oxygen vacancy formation and C–H bond activation over transition metal-doped CeO2 (111) surfaces, J. Catal. 293 (2012) 103–115. doi:10.1016/j.jcat.2012.06.010.
[71] Y. Liu, C. Wen, Y. Guo, G. Lu, Y. Wang, Modulated CO oxidation activity of M-doped ceria (M = Cu, Ti, Zr, and Tb): Role of the pauling electronegativity of M, J. Phys. Chem. C. 114 (2010) 9889–9897. doi:10.1021/jp101939v.
[72] N. Shehata, K. Meehan, M. Hudait, N. Jain, Control of oxygen vacancies and Ce+3 concentrations in doped ceria nanoparticles via the selection of lanthanide element, J. Nanopart. Res. 14 (2012) 1173–1173. doi:10.1007/s11051-012-1173-1.
[73] G. Xiao, S. Li, H. Li, L. Chen, Synthesis of doped ceria with mesoporous flowerlike morphology and its catalytic performance for CO oxidation, Micropor. Mesopor. Mat. 120 (2009) 426–431. doi:10.1016/j.micromeso.2008.12.015.
[74] M.S. Hegde, G. Madras, K.C. Patil, Noble Metal Ionic Catalysts, Acc. Chem. Res. 42 (2009) 704–712. doi:10.1021/ar800209s.
[75] M. Sugiura, Oxygen Storage Materials for Automotive Catalysts: Ceria-Zirconia Solid Solutions, Catal Surv Asia. 7 (2003) 77–87. doi:10.1023/A:1023488709527.
[76] P. Min, S. Zhang, Y. Xu, R. Li, Enhanced oxygen storage capacity of CeO2 with doping-induced unstable crystal structure, Applied Surface Science. 448 (2018) 435–443. doi:10.1016/j.apsusc.2018.04.103.
[77] Lan, Yuan-Pei, Sohn, Hong Yong, Effect of oxygen vacancies and phases on catalytic properties of hydrogen-treated nanoceria particles, Mater. Res. Express. 5 (2018) 035501. doi:10.1088/2053-1591/aaaff4.
[78] X. Wan, D. Goberman, L.L. Shaw, G. Yi, G.-M. Chow, Valence states of nanocrystalline Ceria under combined effects of hydrogen reduction and particle size, Appl. Phys. Lett. 96 (2010) 123108. doi:10.1063/1.3371687.
[79] B. Choudhury, P. Chetri, A. Choudhury, Annealing temperature and oxygen-vacancy-dependent variation of lattice strain, band gap and luminescence properties of CeO2 nanoparticles, Journal of Experimental Nanoscience. 10 (2015) 103–114. doi:10.1080/17458080.2013.801566.
[80] L. Qiu, F. Liu, L. Zhao, Y. Ma, J. Yao, Comparative XPS study of surface reduction for nanocrystalline and microcrystalline ceria powder, Applied Surface Science. 252 (2006) 4931–4935. doi:10.1016/j.apsusc.2005.07.024.
[81] C.M. Sims, R.A. Maier, A.C. Johnston-Peck, J.M. Gorham, V.A. Hackley, B.C. Nelson, Approaches for the quantitative analysis of oxidation state in cerium oxide nanomaterials, Nanotechnology. 30 (2018) 085703. doi:10.1088/1361-6528/aae364.

[82] D.R. Mullins, The surface chemistry of cerium oxide, Surf. Sci. Rep. 70 (2015) 42–85. doi:10.1016/j.surfrep.2014.12.001.
[83] L. Braglia, A.L. Bugaev, K.A. Lomachenko, A.V. Soldatov, C. Lamberti, A.A. Guda, Investigation of oxygen vacancies in CeO2/Pt system with synchrotron light techniques, J. Phys.: Conf. Ser. 712 (2016) 012064. doi:10.1088/1742-6596/712/1/012064.
[84] Y. Lee, G. He, A.J. Akey, R. Si, M. Flytzani-Stephanopoulos, I.P. Herman, Raman Analysis of Mode Softening in Nanoparticle CeO2−δ and Au-CeO2−δ during CO Oxidation, J. Am. Chem. Soc. 133 (2011) 12952–12955. doi:10.1021/ja204479j.
[85] A. Eltayeb, R.K. Vijayaraghavan, A. McCoy, A. Venkatanarayanan, A.A. Yaremchenko, R. Surendran, E. McGlynn, S. Daniels, Control and enhancement of the oxygen storage capacity of ceria films by variation of the deposition gas atmosphere during pulsed DC magnetron sputtering, Journal of Power Sources. 279 (2015) 94–99. doi:10.1016/j.jpowsour.2014.12.146.
[86] V. Shapovalov, H. Metiu, Catalysis by doped oxides: CO oxidation by AuxCe1−xO2, J. Catal. 245 (2007) 205–214. doi:10.1016/j.jcat.2006.10.009.
[87] K. Wu, L.-D. Sun, C.-H. Yan, Recent Progress in Well-Controlled Synthesis of Ceria-Based Nanocatalysts towards Enhanced Catalytic Performance, Advanced Energy Materials. 6 (2016) 1600501–1600501. doi:10.1002/aenm.201600501.
[88] Z. Abbasi, M. Haghighi, E. Fatehifar, N. Rahemi, Comparative synthesis and physicochemical characterization of CeO2 nanopowder via redox reaction, precipitation and sol-gel methods used for total oxidation of toluene, Asia-Pacific Journal of Chemical Engineering. 7 (2012) 868–876. doi:10.1002/apj.652.
[89] A. Aranda, E. Aylón, B. Solsona, R. Murillo, A.M. Mastral, D.R. Sellick, S. Agouram, T. García, S.H. Taylor, High activity mesoporous copper doped cerium oxide catalysts for the total oxidation of polyaromatic hydrocarbon pollutants, Chem. Commun. 48 (2012) 4704–4704. doi:10.1039/c2cc31206a.
[90] C. Hu, Q. Zhu, Z. Jiang, L. Chen, R. Wu, Catalytic combustion of dilute acetone over Cu-doped ceria catalysts, Chem. Eng. J. 152 (2009) 583–590. doi:10.1016/j.cej.2009.05.033.
[91] A.C. Gluhoi, N. Bogdanchikova, B.E. Nieuwenhuys, The effect of different types of additives on the catalytic activity of Au/Al2O3 in propene total oxidation: transition metal oxides and ceria, J. Catal. 229 (2005) 154–162. doi:10.1016/j.jcat.2004.10.003.
[92] C. Doornkamp, V. Ponec, The universal character of the Mars and Van Krevelen mechanism, J. Mol. Catal. A: Chem. 162 (2000) 19–32. doi:10.1016/S1381-1169(00)00319-8.
[93] R.J. Baxter, P. Hu, Insight into why the Langmuir–Hinshelwood mechanism is generally preferred, J. Chem. Phys. 116 (2002) 4379–4381. doi:10.1063/1.1458938.
[94] A. Trovarelli, P. Fornasiero, Catalysis by Ceria and Related Materials, Imperial College Press, 2013.
[95] A. Catlow, C. Richard, Atomistic mechanisms of ionic transport in fast-ion conductors, J. Chem. Soc., Faraday Trans. 86 (1990) 1167–1167. doi:10.1039/ft9908601167.
[96] M. Nolan, J.E. Fearon, G.W. Watson, Oxygen vacancy formation and migration in ceria, Solid State Ionics. 177 (2006) 3069–3074. doi:10.1016/j.ssi.2006.07.045.
[97] M. Zhao, M. Shen, J. Wang, Effect of surface area and bulk structure on oxygen storage capacity of Ce0.67Zr0.33O2, J. Catal. 248 (2007) 258–267. doi:10.1016/j.jcat.2007.03.005.
[98] M. Nolan, G.W. Watson, The surface dependence of CO adsorption on Ceria, J. Phys. Chem. B. 110 (2006) 16600–6. doi:10.1021/jp062499a.
[99] M. Huang, S. Fabris, CO Adsorption and Oxidation on Ceria Surfaces from DFT+U Calculations, The Journal of Physical Chemistry C. 112 (2008) 8643–8648. doi:10.1021/jp709898r.
[100] D.O. Scanlon, N.M. Galea, B.J. Morgan, G.W. Watson, Reactivity on the (110) Surface of Ceria: A GGA+ U Study of Surface Reduction and the Adsorption of CO and NO2, The Journal of Physical Chemistry C. 113 (2009) 11095–11103. doi:10.1021/jp9021085.
[101] M. Nolan, V.S. Verdugo, H. Metiu, Vacancy formation and CO adsorption on gold-doped ceria surfaces, Surf. Sci. 602 (2008) 2734–2742. doi:10.1016/j.susc.2008.06.028.
[102] M. Nolan, Molecular Adsorption on the Doped (110) Ceria Surface, The Journal of Physical Chemistry C. 113 (2009) 2425–2432. doi:10.1021/jp809292u.
[103] I. Yeriskin, M. Nolan, Effect of La doping on CO adsorption at ceria surfaces, J Chem Phys. 131 (2009) 244702–244702. doi:10.1063/1.3271910.
[104] H.-T. Chen, First-Principles Study of CO Adsorption and Oxidation on Ru-Doped CeO2 (111) Surface, The Journal of Physical Chemistry C. 116 (2012) 6239–6246. doi:10.1021/jp210864m.
[105] X.-S. Liu, X.-D. Wang, M. Yao, W. Cui, H. Yan, Effects of Fe doping on oxygen vacancy formation and CO adsorption and oxidation at the ceria(111) surface, Catal. Commun. 63 (2015) 35–40. doi:10.1016/j.catcom.2014.09.032.
[106] Z. Yang, Z. Fu, Y. Wei, Z. Lu, First-Principles Study on the Effects of Zr Dopant on the CO Adsorption on Ceria, The Journal of Physical Chemistry C. 112 (2008) 15341–15347. doi:10.1021/jp711154k.
[107] B. Liu, W. Li, W. Song, J. Liu, Carbonate-mediated Mars–van Krevelen mechanism for CO oxidation on cobalt-doped ceria catalysts: facet-dependence and coordination-dependence, Physical Chemistry Chemical Physics. 20 (2018) 16045–16059. doi:10.1039/C8CP01694A.
[108] D. Knapp, T. Ziegler, Methane Dissociation on the Ceria (111) Surface, The Journal of Physical Chemistry C. 112 (2008) 17311–17318. doi:10.1021/jp8039862.
[109] H. Wu, S. Ma, W. Song, E.J.M. Hensen, Density Functional Theory Study of the Mechanism of Formaldehyde Oxidation on Mn-Doped Ceria, J. Phys. Chem. C. 120 (2016) 13071–13077. doi:10.1021/acs.jpcc.6b03218.
[110] Z. Yang, T.K. Woo, K. Hermansson, Adsorption of NO on unreduced and reduced CeO2 surfaces: A plane-wave DFT study, Surf. Sci. 600 (2006) 4953–4960. doi:10.1016/j.susc.2006.08.018.

[111] M.Y. Mihaylov, E.Z. Ivanova, H.A. Aleksandrov, P.S. Petkov, G.N. Vayssilov, K.I. Hadjiivanov, Formation of N3- during interaction of NO with reduced ceria, Chem. Commun. 51 (2015) 5668–5671. doi:10.1039/C5CC00500K.
[112] M. Nolan, S.C. Parker, G.W. Watson, Reduction of NO2 on Ceria Surfaces, The Journal of Physical Chemistry B. 110 (2006) 2256–2262. doi:10.1021/jp055624b.
[113] M. Nolan, Healing of oxygen vacancies on reduced surfaces of gold-doped ceria, J Chem Phys. 130 (2009) 144702–144702. doi:10.1063/1.3110702.
[114] K. Koizumi, H. Yoshida, M. Boero, K. Tamai, S. Hosokawa, T. Tanaka, K. Nobusada, M. Machida, A detailed insight into the catalytic reduction of NO operated by Cr–Cu nanostructures embedded in a CeO 2 surface, Physical Chemistry Chemical Physics. 20 (2018) 25592–25601. doi:10.1039/C8CP04314K.
[115] D. Devaiah, L.H. Reddy, S.-E. Park, B.M. Reddy, Ceria–zirconia mixed oxides: Synthetic methods and applications, Catal. Rev. 60 (2018) 177–277. doi:10.1080/01614940.2017.1415058.
[116] E. Mamontov, T. Egami, R. Brezny, M. Koranne, S. Tyagi, Lattice Defects and Oxygen Storage Capacity of Nanocrystalline Ceria and Ceria-Zirconia, The Journal of Physical Chemistry B. 104 (2000) 11110–11116. doi:10.1021/jp0023011.
[117] G. Balducci, J. Kašpar, P. Fornasiero, M. Graziani, M.S. Islam, J.D. Gale, Computer Simulation Studies of Bulk Reduction and Oxygen Migration in CeO2−ZrO2 Solid Solutions, The Journal of Physical Chemistry B. 101 (1997) 1750–1753. doi:10.1021/jp962530g.
[118] C. Bozo, F. Gaillard, N. Guilhaume, Characterisation of ceria–zirconia solid solutions after hydrothermal ageing, Appl. Catal. A-Gen. 220 (2001) 69–77. doi:10.1016/S0926-860X(01)00710-4.
[119] G. Balducci, P. Fornasiero, R. Di Monte, J. Kaspar, S. Meriani, M. Graziani, An unusual promotion of the redox behaviour of CeO2-ZrO2 solid solutions upon sintering at high temperatures, Catal. Lett. 33 (1995) 193–200. doi:10.1007/BF00817058.
[120] D.M. Fernandes, C.F. Scofield, A.A. Neto, M.J.B. Cardoso, F.M.Z. Zotin, The influence of temperature on the deactivation of commercial Pd/Rh automotive catalysts, Process Saf. Environ. Prot. 87 (2009) 315–322. doi:10.1016/j.psep.2009.05.002.
[121] J.-P. Cuif, G. Blanchard, O. Touret, A. Seigneurin, M. Marczi, E. Quéméré, (Ce, Zr)O2 Solid Solutions for Three-Way Catalysts, SAE Technical Paper 970463. (1997). doi:10.4271/970463.
[122] G.W. Graham, H.-W. Jen, R.W. McCabe, A.M. Straccia, L.P. Haack, Characterization of model automotive exhaust catalysts: Pd on Zr-rich ceria–zirconia supports, Catal. Lett. 67 (2000) 99–105. doi:10.1023/A:1019086026110.
[123] G. Li, Q. Wang, B. Zhao, R. Zhou, Dynamic oxygen mobility and a new insight into the role of Ni doping in Pd/CeO2–ZrO2 three-way catalysts, Catal. Today. 175 (2011) 40–47. doi:10.1016/j.cattod.2011.04.043.
[124] C.-C. Chuang, H.-I. Hsiang, C.-C. Chen, F.-S. Yen, M. Yoshimura, Phase Separation Phenomenon and Mechanism of Ce0.6Zr0.4O2 Powders Prepared Using Chemical Coprecipitation Method, J. Am. Ceram. Soc. 96 (2013) 1629–1634. doi:10.1111/jace.12183.
[125] A. Morikawa, T. Suzuki, T. Kanazawa, K. Kikuta, A. Suda, H. Shinjo, A new concept in high performance ceria–zirconia oxygen storage capacity material with Al2O3 as a diffusion barrier, Appl. Catal. B-Environ. 78 (2008) 210–221. doi:10.1016/j.apcatb.2007.09.013.
[126] H.-L. Chang, H.-Y. Chen, K. Koo, J. Rieck, P. Blakeman, Gasoline Cold Start Concept (gCSC™) Technology for Low Temperature Emission Control, SAE Int. J. Fuels Lubr. 7 (2014) 2014-01–1509. doi:10.4271/2014-01-1509.
[127] Q. Dong, S. Yin, C. Guo, T. Sato, Aluminum-doped ceria-zirconia solid solutions with enhanced thermal stability and high oxygen storage capacity, Nanoscale Research Letters. 7 (2012) 542–542. doi:10.1186/1556-276X-7-542.
[128] E. Rohart, O. Larcher, S. Deutsch, C. Hédouin, H. Aïmin, F. Fajardie, M. Allain, P. Macaudière, From Zr-Rich to Ce-Rich: Thermal Stability of OSC Materials on the Whole Range of Composition, Top. Catal. 30/31 (2004) 417–423. doi:10.1023/B:TOCA.0000029784.75813.81.
[129] Y. Zhang, L. Zhang, J. Deng, H. Dai, H. He, Controlled Synthesis, Characterization, and Morphology-Dependent Reducibility of Ceria−Zirconia−Yttria Solid Solutions with Nanorod-like, Microspherical, Microbowknot-like, and Micro-octahedral Shapes, Inorg. Chem. 48 (2009) 2181–2192. doi:10.1021/ic802195j.
[130] M. Li, Z. Liu, Y. Hu, M. Wang, H. Li, Effect of doping elements on catalytic performance of CeO2-ZrO2 solid solutions, J. Rare Earths. 26 (2008) 357–361. doi:10.1016/S1002-0721(08)60095-2.
[131] S. Li, N. Wang, Y. Yue, G. Wang, Z. Zu, Y. Zhang, Copper doped ceria porous nanostructures towards a highly efficient bifunctional catalyst for carbon monoxide and nitric oxide elimination, Chem. Sci. 6 (2015) 2495–2500. doi:10.1039/C5SC00129C.
[132] S. Lin, X. Yang, L. Yang, R. Zhou, Three-way catalytic performance of Pd/Ce0.67Zr0.33O2–Al2O3 catalysts: Role of the different Pd precursors, Appl. Surf. Sci. 327 (2015) 335–343. doi:10.1016/j.apsusc.2014.11.176.
[133] J. Liu, M. Zhao, C. Xu, S. Liu, X. Zhang, Y. Chen, Hydrothermal Synthesis and Catalytic Activity of CeZrAl Oxide-Supported Pd for the Purification of Gasohol Exhaust, Synthesis and Reactivity in Inorganic, Metal-Organic, and Nano-Metal Chemistry. 45 (2015) 899–905. doi:10.1080/15533174.2013.843554.
[134] A. Satsuma, K. Ueda, Y. Ito, C.A. Ang, J. Ohyama, Automotive Three Way Catalytic Activity of Fe-Ni/Ceria, Chem. Lett. 44 (2015) 703–705. doi:10.1246/cl.150123.
[135] T. Vinodkumar, B.G. Rao, B.M. Reddy, Influence of isovalent and aliovalent dopants on the reactivity of cerium oxide for catalytic applications, Catal. Today. 253 (2015) 57–64. doi:10.1016/j.cattod.2015.01.044.
[136] A. Singhania, High Surface Area M (M = La, Pr, Nd, and Pm)-Doped Ceria Nanoparticles: Synthesis, Characterization, and Activity Comparison for CO Oxidation, Ind. Eng. Chem. Res. 56 (2017) 13594–13601. doi:10.1021/acs.iecr.7b03143.

[137] B.P. Mandal, V. Grover, M.R. Pai, A.K. Tyagi, Improvement of physico-chemical properties by addition of H2O2: An extensive case study on the RE-doped ceria system (RE = Gd, Sm), J. Mater. Res. 24 (2009) 2845–2854. doi:10.1557/jmr.2009.0352.
[138] W. Liu, M. Flytzanistephanopoulos, Total Oxidation of Carbon Monoxide and Methane over Transition Metal Fluorite Oxide Composite Catalysts, J. Catal. 153 (1995) 304–316. doi:10.1006/jcat.1995.1132.
[139] D. Mukherjee, B.G. Rao, B.M. Reddy, CO and soot oxidation activity of doped ceria: Influence of dopants, Applied Catalysis B: Environmental. 197 (2016) 105–115. doi:10.1016/j.apcatb.2016.03.042.
[140] Y. Zuo, L. Li, X. Huang, G. Li, Searching for cheaper catalysts with high activity and stability in Ce–M–O systems (M = Fe, Co, Ni), Catalysis Science & Technology. 4 (2014) 3368–3368. doi:10.1039/C4CY00526K.
[141] D. Jampaiah, P. Venkataswamy, V. Elizabeth Coyle, B. M. Reddy, S. K. Bhargava, Low-temperature CO oxidation over manganese, cobalt, and nickel doped CeO2 nanorods, RSC Advances. 6 (2016) 80541–80548. doi:10.1039/C6RA13577C.
[142] C. Xian, S. Wang, C. Sun, H. Li, S. Chan, L. Chen, Effect of Ni doping on the catalytic properties of nanostructured peony-like CeO2, Chinese Journal of Catalysis. 34 (2013) 305–312. doi:10.1016/S1872-2067(11)60466-X.
[143] H. Zhu, Y. Chen, Z. Wang, W. Liu, L. Wang, Catalytic oxidation of CO over mesoporous copper-doped ceria catalysts via a facile CTAB-assisted synthesis, RSC Adv. 8 (2018) 14888–14897. doi:10.1039/C8RA02327A.
[144] S.-L. Zhong, L.-F. Zhang, L. Wang, W.-X. Huang, C.-M. Fan, A.-W. Xu, Uniform and Porous Ce 1– x Zn x O 2−δ Solid Solution Nanodisks: Preparation and Their CO Oxidation Activity, The Journal of Physical Chemistry C. 116 (2012) 13127–13132. doi:10.1021/jp3017826.
[145] M. Kurnatowska, L. Kepinski, W. Mista, Structure evolution of nanocrystalline Ce1−xPdxO2−y mixed oxide in oxidizing and reducing atmosphere: Reduction-induced activity in low-temperature CO oxidation, Applied Catalysis B: Environmental. 117–118 (2012) 135–147. doi:10.1016/j.apcatb.2011.12.034.
[146] M. Nolan, Charge Compensation and Ce 3+ Formation in Trivalent Doping of the CeO 2 (110) Surface: The Key Role of Dopant Ionic Radius, The Journal of Physical Chemistry C. 115 (2011) 6671–6681. doi:10.1021/jp112112u.
[147] M.D. Krcha, A.D. Mayernick, M.J. Janik, Periodic trends of oxygen vacancy formation and C–H bond activation over transition metal-doped CeO2 (111) surfaces, Journal of Catalysis. 293 (2012) 103–115. doi:10.1016/j.jcat.2012.06.010.
[148] D.N. Durgasri, T. Vinodkumar, P. Sudarsanam, B.M. Reddy, Nanosized CeO2–Gd2O3 Mixed Oxides: Study of Structural Characterization and Catalytic CO Oxidation Activity, Catal. Lett. 144 (2014) 971–979. doi:10.1007/s10562-014-1223-7.
[149] M.F. Wilkes, P. Hayden, A.K. Bhattacharya, Catalytic studies on ceria lanthana solid solutions II. Oxidation of carbon monoxide, Journal of Catalysis. 219 (2003) 295–304. doi:10.1016/S0021-9517(03)00045-9.
[150] D. Devaiah, L.H. Reddy, B.M. Reddy, Design of novel ceria-based nano-oxides for CO oxidation and other catalytic applications, Indian Journal of Chemistry - Section A. 51A (2012).
[151] X. Zhou, J. Ling, W. Sun, Z. Shen, Fabrication of homogeneously Cu2+/La3+-doped CeO2 nanosheets and their application in CO oxidation, J. Mater. Chem. A. 5 (2017) 9717–9722. doi:10.1039/C7TA00924K.
[152] H. Dasari, S. Y Park, H.-I. Ji, H.-R. Kim, J.-W. Son, B.-K. Kim, H. Lee, J.-H. Lee, Structural Characterization and Catalytic Activity of Ce 0.65 Zr 0.25 RE 0.1 O 2−δ Nanocrystalline Powders Synthesized by the Glycine-Nitrate Process, The Journal of Physical Chemistry C. 116 (2012) 3467. doi:10.1021/jp207107j.
[153] J. Ke, J.-W. Xiao, W. Zhu, H. Liu, R. Si, Y.-W. Zhang, C.-H. Yan, Dopant-Induced Modification of Active Site Structure and Surface Bonding Mode for High-Performance Nanocatalysts: CO Oxidation on Capping-free (110)-oriented CeO2:Ln (Ln = La–Lu) Nanowires, J. Am. Chem. Soc. 135 (2013) 15191–15200. doi:10.1021/ja407616p.
[154] P. Venkataswamy, D. Jampaiah, D. Mukherjee, C.U. Aniz, B.M. Reddy, Mn-doped Ceria Solid Solutions for CO Oxidation at Lower Temperatures, Catal Lett. 146 (2016) 2105–2118. doi:10.1007/s10562-016-1811-9.
[155] P. Venkataswamy, K.N. Rao, D. Jampaiah, B.M. Reddy, Nanostructured manganese doped ceria solid solutions for CO oxidation at lower temperatures, Appl. Catal. B-Environ. 162 (2015) 122–132. doi:10.1016/j.apcatb.2014.06.038.
[156] T. Vinodkumar, D. Naga Durgasri, B.M. Reddy, I. Alxneit, Synthesis and Structural Characterization of Eu2O3 Doped CeO2: Influence of Oxygen Defects on CO Oxidation, Catal. Lett. 144 (2014) 2033–2042. doi:10.1007/s10562-014-1367-5.
[157] P. Sudarsanam, B. Mallesham, D.N. Durgasri, B.M. Reddy, Physicochemical characterization and catalytic CO oxidation performance of nanocrystalline Ce–Fe mixed oxides, RSC Adv. 4 (2014) 11322–11322. doi:10.1039/c3ra45778h.
[158] K. Kuntaiah, P. Sudarsanam, B.M. Reddy, A. Vinu, Nanocrystalline Ce1−xSmxO2−δ (x = 0.4) solid solutions: structural characterization versus CO oxidation, RSC Adv. 3 (2013) 7953–7953. doi:10.1039/c3ra23491f.
[159] L. Katta, T. Vinod Kumar, D.N. Durgasri, Nanosized Ce1−xLaxO2−δ/Al2O3 solid solutions for CO oxidation: Combined study of structural characteristics and catalytic evaluation, Catal. Today. 198 (2012) 133–139. doi:10.1016/j.cattod.2012.07.015.
[160] B.M. Reddy, G. Thrimurthulu, L. Katta, Design of Efficient CexM1−xO2−δ (M = Zr, Hf, Tb and Pr) Nanosized Model Solid Solutions for CO Oxidation, Catal. Lett. 141 (2011) 572–581. doi:10.1007/s10562-010-0484-z.
[161] J.-Y. Luo, M. Meng, J.-S. Yao, X.-G. Li, Y.-Q. Zha, X. Wang, T.-Y. Zhang, One-step synthesis of nanostructured Pd-doped mixed oxides MOx-CeO2 (M=Mn, Fe, Co, Ni, Cu) for efficient CO and C3H8 total oxidation, Appl. Catal. B-Environ. 87 (2009) 92–103. doi:10.1016/j.apcatb.2008.08.017.
[162] L.P. dos Santos Xavier, V. Rico-Pérez, A.M. Hernández-Giménez, D. Lozano-Castelló, A. Bueno-López, Simultaneous catalytic oxidation of carbon monoxide, hydrocarbons and soot with Ce–Zr–Nd mixed oxides in

simulated diesel exhaust conditions, Appl. Catal. B-Environ. 162 (2015) 412–419. doi:10.1016/j.apcatb.2014.07.013.
[163] J.-F. Tu, L.-H. Zhao, X. Hu, Catalytic combustion of methane on Ce1-xMxO2-delta (M=Si, Mg, Al) oxides, Indian Journal of Chemistry Section A - Inorganic, Bio-Inorganic, Physical, Theoretical & Analytical Chemistry. 53 (2014) 167–173.
[164] R. Dziembaj, M. Molenda, M.M. Zaitz, L. Chmielarz, K. Furczoń, Correlation of electrical properties of nanometric copper-doped ceria materials (Ce1−xCuxO2−δ) with their catalytic activity in incineration of VOCs, Solid State Ionics. 251 (2013) 18–22. doi:10.1016/j.ssi.2013.03.011.
[165] H.-F. Lu, Y. Zhou, W.-F. Han, H. Huang, Y.-F. Chen, Promoting effect of ZrO2 carrier on activity and thermal stability of CeO2-based oxides catalysts for toluene combustion, Appl. Catal. A-Gen. 464 (2013) 101–108. doi:10.1016/j.apcata.2013.05.036.
[166] A. Aranda, S. Agouram, J.M. López, A.M. Mastral, D.R. Sellick, B. Solsona, S.H. Taylor, T. García, Oxygen defects: The key parameter controlling the activity and selectivity of mesoporous copper-doped ceria for the total oxidation of naphthalene, Appl. Catal. B-Environ. 127 (2012) 77–88. doi:10.1016/j.apcatb.2012.07.033.
[167] R. Dziembaj, M. Molenda, L. Chmielarz, M.M. Zaitz, Z. Piwowarska, A. Rafalska-Łasocha, Optimization of Cu doped ceria nanoparticles as catalysts for low-temperature methanol and ethylene total oxidation, Catal. Today. 169 (2011) 112–117. doi:10.1016/j.cattod.2010.11.061.
[168] G. Picasso, M. Gutiérrez, M.P. Pina, J. Herguido, Preparation and characterization of Ce-Zr and Ce-Mn based oxides for n-hexane combustion: Application to catalytic membrane reactors, Chem. Eng. J. 126 (2007) 119–130. doi:10.1016/j.cej.2006.09.005.
[169] D. Terribile, A. Trovarelli, C. de Leitenburg, A. Primavera, G. Dolcetti, Catalytic combustion of hydrocarbons with Mn and Cu-doped ceria–zirconia solid solutions, Catal. Today. 47 (1999) 133–140. doi:10.1016/S0920-5861(98)00292-2.
[170] S. Zhao, R.J. Gorte, A comparison of ceria and Sm-doped ceria for hydrocarbon oxidation reactions, Appl. Catal. A-Gen. 277 (2004) 129–136. doi:10.1016/j.apcata.2004.09.003.
[171] X. Wu, Q. Liang, D. Weng, J. Fan, R. Ran, Synthesis of CeO2–MnOx mixed oxides and catalytic performance under oxygen-rich condition, Catal. Today. 126 (2007) 430–435. doi:10.1016/j.cattod.2007.06.014.
[172] A.E.C. Palmqvist, E.M. Johansson, S.G. Järås, M. Muhammed, Total oxidation of methane over doped nanophase cerium oxides, Catal. Lett. 56 (1998) 69–75. doi:10.1023/A:1019032306894.
[173] Y. Zuo, X. Huang, L. Li, G. Li, An ultra-stable nanosized Ce0.9Fe0.1O2 solid solution with an excellent catalytic performance towards CH4 oxidation, J. Mater. Chem. A. 1 (2013) 374–380. doi:10.1039/C2TA00167E.
[174] X. Zeng, R. Zhang, X. Xu, X. Wang, Study on ceria-modified SnO2 for CO and CH4 oxidation, J. Rare Earths. 30 (2012) 1013–1019. doi:10.1016/S1002-0721(12)60171-9.
[175] X. Yao, C. Tang, Z. Ji, Y. Dai, Y. Cao, F. Gao, L. Dong, Y. Chen, Investigation of the physicochemical properties and catalytic activities of Ce0.67M0.33O2 (M = Zr 4+, Ti 4+, Sn 4+) solid solutions for NO removal by CO, Catal. Sci. Technol. 3 (2013) 688–698. doi:10.1039/C2CY20610B.
[176] C.-Q. Zhu, H. Liang, S.-H. Li, Y.-X. Hong, D.-Q. Ye, Performance of Mn Doped Ce0.7Zr0.3O2 Catalysts for Simultaneous Removal of PM and NOx, Chinese Journal of Inorganic Chemistry. 6 (2011) 1093–1100.
[177] B. Weidenhof, M. Reiser, K. Stöwe, W.F. Maier, M. Kim, J. Azurdia, E. Gulari, E. Seker, A. Barks, R.M. Laine, High-Throughput Screening of Nanoparticle Catalysts Made by Flame Spray Pyrolysis as Hydrocarbon/NO Oxidation Catalysts, J. Am. Chem. Soc. 131 (2009) 9207–9219. doi:10.1021/ja809134s.
[178] I. Atribak, A. Bueno-López, A. García-García, Combined removal of diesel soot particulates and NOx over CeO2–ZrO2 mixed oxides, J. Catal. 259 (2008) 123–132. doi:10.1016/j.jcat.2008.07.016.
[179] C. Tang, B. Sun, J. Sun, X. Hong, Y. Deng, F. Gao, L. Dong, Solid state preparation of NiO-CeO2 catalyst for NO reduction, Catalysis Today. 281 (2017) 575–582. doi:10.1016/j.cattod.2016.05.026.
[180] C. Deng, M. Li, J. Qian, Q. Hu, M. Huang, Q. Lin, Y. Ruan, L. Dong, B. Li, M. Fan, A Study of Different Doped Metal Cations on the Physicochemical Properties and Catalytic Activities of Ce20M1Ox (M=Zr, Cr, Mn, Fe, Co, Sn) Composite Oxides for Nitric Oxide Reduction by Carbon Monoxide, Chemistry – An Asian Journal. 11 (2016) 2144–2156. doi:10.1002/asia.201600516.
[181] T. Montini, M. Melchionna, M. Monai, P. Fornasiero, Fundamentals and Catalytic Applications of CeO2-Based Materials, Chem. Rev. 116 (2016) 5987–6041. doi:10.1021/acs.chemrev.5b00603.
[182] J. Wang, H. Chen, Z. Hu, M. Yao, Y. Li, A Review on the Pd-Based Three-Way Catalyst, Catal. Rev. 57 (2014) 79–144. doi:10.1080/01614940.2014.977059.
[183] M. Shelef, R.W. McCabe, Twenty-five years after introduction of automotive catalysts: what next?, Catal. Today. 62 (2000) 35–50. doi:10.1016/S0920-5861(00)00407-7.
[184] H. Shinjoh, Noble Metal Sintering Suppression Technology in Three-way Catalyst: Automotive Three-way Catalysts with the Noble Metal Sintering Suppression Technology Based on the Support Anchoring Effect, Catal Surv Asia. 13 (2009) 184–190. doi:10.1007/s10563-009-9076-6.
[185] T. Johnson, Vehicular Emissions in Review, SAE Int. J. Engines. 9 (2016). doi:10.4271/2016-01-0919.
[186] R. Si, Y.-W. Zhang, L.-M. Wang, S.-J. Li, B.-X. Lin, W.-S. Chu, Z.-Y. Wu, C.-H. Yan, Enhanced Thermal Stability and Oxygen Storage Capacity for CexZr1-xO2 (x = 0.4−0.6) Solid Solutions by Hydrothermally Homogenous Doping of Trivalent Rare Earths, J. Phys. Chem. C. 111 (2007) 787–794. doi:10.1021/jp0630875.
[187] J.R. McBride, K.C. Hass, B.D. Poindexter, W.H. Weber, Raman and x-ray studies of Ce1−xRExO2−y, where RE=La, Pr, Nd, Eu, Gd, and Tb, J. Appl. Phys. 76 (1994) 2435–2435. doi:10.1063/1.357593.
[188] A. Satsuma, K. Osaki, M. Yanagihara, J. Ohyama, K. Shimizu, Low temperature combustion over supported Pd catalysts – Strategy for catalyst design, Catal. Today. 258 (2015) 83–89. doi:10.1016/j.cattod.2015.03.047.

[189] Y. Cao, R. Ran, X. Wu, X. Wu, J. Wan, D. Weng, Ageing resistance of rhodium supported on CeO2–ZrO2 and ZrO2: Rhodium nanoparticle structure and Rh–support interaction under diverse ageing atmosphere, Catal. Today. 281 (2017) 490–499. doi:10.1016/j.cattod.2016.07.001.
[190] W. Lang, P. Laing, Y. Cheng, C. Hubbard, M.P. Harold, Co-oxidation of CO and propylene on Pd/CeO2-ZrO2 and Pd/Al2O3 monolith catalysts: A light-off, kinetics, and mechanistic study, Appl. Catal. B-Environ. 218 (2017) 430–442. doi:10.1016/j.apcatb.2017.06.064.
[191] Q. Zheng, R. Farrauto, M. Deeba, I. Valsamakis, Part I: A Comparative Thermal Aging Study on the Regenerability of Rh/Al2O3 and Rh/CexOy-ZrO2 as Model Catalysts for Automotive Three Way Catalysts, Catalysts. 5 (2015) 1770–1796. doi:10.3390/catal5041770.
[192] M. Ozawa, T. Okouchi, M. Haneda, Three way catalytic activity of thermally degenerated Pt/Al2O3 and Pt/CeO2–ZrO2 modified Al2O3 model catalysts, Catal. Today. 242 (2015) 329–337. doi:10.1016/j.cattod.2014.06.013.
[193] H.-Y. Chen, H.-L. Chang, Development of Low Temperature Three-Way Catalysts for Future Fuel Efficient Vehicles, Johnson Matthey Tech. 59 (2015) 64. doi:10.1595/205651315x686011.
[194] M. Yamamoto, H. Tanaka, Influence of Support Materials on Durability of Palladium in Three-Way Catalyst, SAE International, Warrendale, PA, 1998. doi:10.4271/980664.
[195] S. Hideo, Development of Ceria-Zirconia Solid Solutions and Future Trends., R&D Review of Toyota CRDL. 37 (2002) 1–5.
[196] J. Li, X. Liu, W. Zhan, Y. Guo, Y. Guo, G. Lu, Preparation of high oxygen storage capacity and thermally stable ceria–zirconia solid solution, Catal. Sci. Technol. 6 (2016) 897–907. doi:10.1039/C5CY01571E.
[197] N.S. Priya, C. Somayaji, S. Kanagaraj, Optimization of Ceria-Zirconia Solid Solution based on OSC Measurement by Cyclic Heating Process, Procedia Engineer. 64 (2013) 1235–1241. doi:10.1016/j.proeng.2013.09.203.
[198] Y. Madier, C. Descorme, A.M. Le Govic, D. Duprez, Oxygen Mobility in CeO2 and CexZr(1-x)O2 Compounds: Study by CO Transient Oxidation and 18O/16O Isotopic Exchange, J. Phys. Chem. B. 103 (1999) 10999–11006. doi:10.1021/jp991270a.
[199] N.S. Priya, C. Somayaji, S. Kanagaraj, Optimization of Ce0.6Zr0.4−xAl1.3xO2 solid solution based on oxygen storage capacity, J Nanopart Res. 16 (2014) 2214. doi:10.1007/s11051-013-2214-0.
[200] L. Lan, S. Chen, Y. Cao, M. Zhao, M. Gong, Y. Chen, Preparation of ceria-zirconia by modified coprecipitation method and its supported Pd-only three-way catalyst, J Colloid Interface Sci. 450 (2015) 404–416. doi:10.1016/j.jcis.2015.03.042.
[201] Y. Aoki, S. Sakagami, M. Kawai, N. Takahashi, T. Tanabe, T. Sunada, Development of Advanced Zone-Coated Three-Way Catalysts, SAE International. (2011). doi:10.4271/2011-01-0296.
[202] J. Guo, Z. Shi, D. Wu, H. Yin, M. Gong, Y. Chen, Effects of Nd on the properties of CeO2–ZrO2 and catalytic activities of three-way catalysts with low Pt and Rh, J. Alloys Compd. 621 (2015) 104–115. doi:10.1016/j.jallcom.2014.09.189.
[203] Q. Wang, G. Li, B. Zhao, R. Zhou, The effect of Nd on the properties of ceria–zirconia solid solution and the catalytic performance of its supported Pd-only three-way catalyst for gasoline engine exhaust reduction, J. Hazard. Mater. 189 (2011) 150–157. doi:10.1016/j.jhazmat.2011.02.012.
[204] Q. Wang, G. Li, B. Zhao, R. Zhou, Investigation on properties of a novel ceria–zirconia–praseodymia solid solution and its application in Pd-only three-way catalyst for gasoline engine emission control, Fuel. 90 (2011) 3047–3055. doi:10.1016/j.fuel.2011.05.029.
[205] Q. Wang, G. Li, B. Zhao, M. Shen, R. Zhou, The effect of La doping on the structure of Ce0.2Zr0.8O2 and the catalytic performance of its supported Pd-only three-way catalyst, Appl. Catal. B-Environ. 101 (2010) 150–159. doi:10.1016/j.apcatb.2010.09.026.
[206] Q. Wang, G. Li, B. Zhao, R. Zhou, The effect of rare earth modification on ceria–zirconia solid solution and its application in Pd-only three-way catalyst, J. Mol. Catal. A-Chem. 339 (2011) 52–60. doi:10.1016/j.molcata.2011.02.011.
[207] B. Zhao, Q. Wang, G. Li, R. Zhou, Effect of rare earth (La, Nd, Pr, Sm and Y) on the performance of Pd/Ce0.67Zr0.33MO2−δ three-way catalysts, J. Environ. Chem. Eng. 1 (2013) 534–543. doi:10.1016/j.jece.2013.06.018.
[208] Y. Zhou, J. Deng, L. Xiong, J. Wang, S. Yuan, H. Zhang, Y. Chen, Synthesis and study of nanostructured Ce-Zr-La-RE-O (RE=Y, Nd and Pr) quaternary solid solutions and their supported three-way catalysts, Mater. Design. 130 (2017) 149–156. doi:10.1016/j.matdes.2017.05.059.
[209] G. Jiaxiu, S. Zhonghua, W. Dongdong, Y. Huaqiang, G. Maochu, C. Yaoqiang, Study of Pt–Rh/CeO2–ZrO2–MxOy (M=Y, La)/Al2O3 three-way catalysts, Appl. Surf. Sci. 273 (2013) 527–535. doi:10.1016/j.apsusc.2013.02.074.
[210] A. Papavasiliou, A. Tsetsekou, V. Matsouka, M. Konsolakis, I.V. Yentekakis, An investigation of the role of Zr and La dopants into Ce1−x−yZrxLayOδ enriched γ-Al2O3 TWC washcoats, Appl. Catal. A-Gen. 382 (2010) 73–84. doi:10.1016/j.apcata.2010.04.025.
[211] M. Haneda, Y. Tomida, T. Takahashi, Y. Azuma, T. Fujimoto, Three-way catalytic performance and change in the valence state of Rh in Y- and Pr-doped Rh/ZrO2 under lean/rich perturbation conditions, Catal. Commun. 90 (2017) 1–4. doi:10.1016/j.catcom.2016.11.009.
[212] M. Haneda, Y. Tomida, H. Sawada, M. Hattori, Effect of Rare Earth Additives on the Catalytic Performance of Rh/ZrO2 Three-Way Catalyst, Top Catal. 59 (2016) 1059–1064. doi:10.1007/s11244-016-0590-2.
[213] M. Haneda, H. Sawada, N. Kamiuchi, M. Ozawa, Promoting Effect of CeO2 on the Catalytic Activity of Rhodium Supported on Y-Stabilized ZrO2 for NO–CO–C3H6–O2 Reactions, Chem. Lett. 42 (2012) 60–62. doi:10.1246/cl.2013.60.

[214] L. Yang, X. Yang, S. Lin, R. Zhou, Insights into the role of a structural promoter (Ba) in three-way catalyst Pd/CeO2–ZrO2 using in situ DRIFTS, Catal. Sci. Technol. 5 (2015) 2688–2695. doi:10.1039/C5CY00117J.
[215] L. Lan, S. Chen, Y. Cao, S. Wang, Q. Wu, Y. Zhou, M. Huang, M. Gong, Y. Chen, Promotion of CeO2–ZrO2–Al2O3 composite by selective doping with barium and its supported Pd-only three-way catalyst, J. Mol. Catal. A: Chem. 410 (2015) 100–109. doi:10.1016/j.molcata.2015.09.016.
[216] L. Lan, H. Li, S. Chen, W. Yang, D. Liu, W. Wang, M. Gong, Y. Chen, CeO2-ZrO2-Al2O3 Modified by Selective Doping with SrO for Improved Pd-Only Three-Way Catalyst, Russ. J. Phys. Chem. 92 (2018) 696–705. doi:10.1134/S0036024418040179.
[217] L. Yang, S. Lin, X. Yang, W. Fang, R. Zhou, Promoting effect of alkaline earth metal doping on catalytic activity of HC and NOx conversion over Pd-only three-way catalyst, J. Hazard. Mater. 279 (2014) 226–235. doi:10.1016/j.jhazmat.2014.06.076.
[218] G.S. Bugosh, M.P. Harold, Impact of Zeolite Beta on Hydrocarbon Trapping and Light-Off Behavior on Pt/Pd/BEA/Al2O3 Monolith Catalysts, Emiss. Control Sci. Technol. 3 (2017) 123–134. doi:10.1007/s40825-017-0061-7.
[219] J.M. López, M.V. Navarro, T. García, R. Murillo, A.M. Mastral, F.J. Varela-Gandía, D. Lozano-Castelló, A. Bueno-López, D. Cazorla-Amorós, Screening of different zeolites and silicoaluminophosphates for the retention of propene under cold start conditions, Micropor. Mesopor. Mat. 130 (2010) 239–247. doi:10.1016/j.micromeso.2009.11.016.
[220] L. Kustov, V. Golubeva, A. Korableva, O. Anischenko, N. Yegorushina, G. Kapustin, Alkaline-modified ZSM-5 zeolite to control hydrocarbon cold-start emission, Micropor. Mesopor. Mat. 260 (2018) 54–58. doi:10.1016/j.micromeso.2017.06.050.
[221] N.R. Burke, D.L. Trimm, R.F. Howe, The effect of silica:alumina ratio and hydrothermal ageing on the adsorption characteristics of BEA zeolites for cold start emission control, Appl. Catal. B-Environ. 46 (2003) 97–104. doi:10.1016/S0926-3373(03)00181-4.
[222] A. Westermann, B. Azambre, Impact of the Zeolite Structure and Acidity on the Adsorption of Unburnt Hydrocarbons Relevant to Cold Start Conditions, J. Phys. Chem. C. 120 (2016) 25903–25914. doi:10.1021/acs.jpcc.6b08880.
[223] Y. Murata, T. Morita, K. Wada, H. Ohno, NOx Trap Three-Way Catalyst (N-TWC) Concept: TWC with NOx Adsorption Properties at Low Temperatures for Cold-Start Emission Control, SAE Int. J. Fuels Lubr. 8 (2015). doi:10.4271/2015-01-1002.
[224] N.R. Collins, M.V. Twigg, Three-way catalyst emissions control technologies for spark-ignition engines—recent trends and future developments, Top Catal. 42–43 (2007) 323–332. doi:10.1007/s11244-007-0199-6.
[225] M. Haneda, T. Kaneko, N. Kamiuchi, M. Ozawa, Improved three-way catalytic activity of bimetallic Ir–Rh catalysts supported on CeO2–ZrO2, Catal. Sci. Technol. 5 (2015) 1792–1800. doi:10.1039/C4CY01502A.
[226] J. Cooper, J. Beecham, A Study of Platinum Group Metals in Three-Way Autocatalysts, Platinum Metals Rev. 57 (2013) 281. doi:10.1595/147106713x671457.
[227] E.A. Alikin, A.A. Vedyagin, High Temperature Interaction of Rhodium with Oxygen Storage Component in Three-Way Catalysts, Top Catal. 59 (2016) 1033–1038. doi:10.1007/s11244-016-0585-z.
[228] J.R. Theis, A. Getsoian, C. Lambert, The Development of Low Temperature Three-Way Catalysts for High Efficiency Gasoline Engines of the Future, SAE Int. J. Fuels Lubr. 10 (2017) 583–592. doi:https://doi.org/10.4271/2017-01-0918.
[229] S.B. Kang, S.J. Han, S.B. Nam, I.-S. Nam, B.K. Cho, C.H. Kim, S.H. Oh, Activity function describing the effect of Pd loading on the catalytic performance of modern commercial TWC, Chem. Eng. J. 207–208 (2012) 117–121. doi:10.1016/j.cej.2012.06.003.
[230] J.-W. Jeong, B.-C. Choi, Improvement of Performance and Durability of Three-Way Catalyst for Low-Emission Vehicles, JSME Int. J B-Fluid T. 45 (2002) 392–398. doi:10.1299/jsmeb.45.392.
[231] D.Q. Phan, S. Kureti, CO Oxidation on Pd/Al2O3 Catalysts under Stoichiometric Conditions, Top Catal. 60 (2017) 260–265. doi:10.1007/s11244-016-0608-9.
[232] M.-A. A., H. A.B., F.-G. M., I.-J. A., A. J.A., C. J.C., Light-off behaviour of PdO/gamma-Al2O3 catalysts for stoichiometric CO-O-2 and CO-O-2-NO reactions: a combined catalytic activity-in situ DRIFTS study, J. Catal. 221 (2004) 85–92. doi:10.1016/S0021-9517(03)00277-X.
[233] R. Di Monte, P. Fornasiero, J. Kašpar, P. Rumori, G. Gubitosa, M. Graziani, Pd/Ce0.6Zr0.4O2/Al2O3 as advanced materials for three-way catalysts: Part 1. Catalyst characterisation, thermal stability and catalytic activity in the reduction of NO by CO, Appl. Catal. B-Environ. 24 (2000) 157–167. doi:10.1016/S0926-3373(99)00102-2.
[234] J.A. Anderson, R.A. Daley, S.Y. Christou, A.M. Efstathiou, Regeneration of thermally aged Pt-Rh/CexZr1−xO2-Al2O3 model three-way catalysts by oxychlorination treatments, Appl. Catal. B-Environ. 64 (2006) 189–200. doi:10.1016/j.apcatb.2005.12.007.
[235] A.A. Vedyagin, V.O. Stoyanovskii, P.E. Plyusnin, Y.V. Shubin, E.M. Slavinskaya, I.V. Mishakov, Effect of metal ratio in alumina-supported Pd-Rh nanoalloys on its performance in three way catalysis, J. Alloys Compd. 749 (2018) 155–162. doi:10.1016/j.jallcom.2018.03.250.
[236] H. Shinjoh, M. Hatanaka, Y. Nagai, T. Tanabe, N. Takahashi, T. Yoshida, Y. Miyake, Suppression of Noble Metal Sintering Based on the Support Anchoring Effect and its Application in Automotive Three-Way Catalysis, Top Catal. 52 (2009) 1967. doi:10.1007/s11244-009-9371-5.
[237] B. Harrison, A.F. Diwell, C. Hallett, Promoting Platinum Metals by Ceria, Platinum Metals Rev. 32 (1988) 73–83.

[238] A.A. Vedyagin, M.S. Gavrilov, A.M. Volodin, V.O. Stoyanovskii, E.M. Slavinskaya, I.V. Mishakov, Y.V. Shubin, Catalytic Purification of Exhaust Gases Over Pd–Rh Alloy Catalysts, Top Catal. 56 (2013) 1008–1014. doi:10.1007/s11244-013-0064-8.
[239] Johnson Matthey Base Prices in US$ per troy oz., (n.d.). http://www.platinum.matthey.com/prices/price-tables (accessed July 4, 2018).
[240] H. Santos, M. Costa, Evaluation of the conversion efficiency of ceramic and metallic three way catalytic converters, Energy Convers. Manage. 49 (2008) 291–300. doi:10.1016/j.enconman.2007.06.008.
[241] R.M. Heck, S. Gulati, R.J. Farrauto, The application of monoliths for gas phase catalytic reactions, Chem. Eng. J. 82 (2001) 149–156. doi:10.1016/S1385-8947(00)00365-X.
[242] S. Otsuka, Y. Suehiro, H. Koyama, Y. Matsuzono, C. Tanner, D. Bronfenbrenner, T. Tao, K. Twiggs, Development of a Super-Light Substrate for LEV III/Tier3 Emission Regulation, in: 2015. doi:10.4271/2015-01-1001.
[243] S. Kikuchi, S. Hatcho, T. Okayama, S. Inose, K. Ikeshima, High Cell Density and Thin Wall Substrate for Higher Conversion Ratio Catalyst, in: 1999. doi:10.4271/1999-01-0268.
[244] S. Eslava, A. Reynal, V.G. Rocha, S. Barg, E. Saiz, Using graphene oxide as a sacrificial support of polyoxotitanium clusters to replicate its two-dimensionality on pure titania photocatalysts, J Mater. Chem. A. 4 (2016) 7200–7206. doi:10.1039/C5TA09989G.
[245] D.C. Marcano, D.V. Kosynkin, J.M. Berlin, A. Sinitskii, Z. Sun, A. Slesarev, L.B. Alemany, W. Lu, J.M. Tour, Improved synthesis of graphene oxide, ACS Nano. 4 (2010) 4806–4814. doi:10.1021/nn1006368.
[246] R.E. Dinnebier, S.J.L. Billinge, Powder Diffraction: Theory and Practice, The Royal Society of Chemistry, Cambridge, UK, 2008.
[247] U. Holzwarth, N. Gibson, The Scherrer equation versus the "Debye-Scherrer equation," Nature Nanotechnology. 6 (2011) 534. doi:10.1038/nnano.2011.145.
[248] J.S.J. Hargreaves, Some considerations related to the use of the Scherrer equation in powder X-ray diffraction as applied to heterogeneous catalysts, Catalysis, Structure & Reactivity. 2 (2016) 33–37. doi:10.1080/2055074X.2016.1252548.
[249] ISO/TC 24/SC 4, ISO 9277:2010 Determination of the specific surface area of solids by gas adsorption -- BET method, International Organization for Standardization, 2010.
[250] K. Sing, The use of nitrogen adsorption for the characterisation of porous materials, Colloids Surf. Physicochem. Eng. Aspects. 187–188 (2001) 3–9. doi:10.1016/S0927-7757(01)00612-4.
[251] P. Larkin, Infrared and Raman Spectroscopy: Principles and Spectral Interpretation, Elsevier, 2017.
[252] University of Warwick, Transmission Electron Microscopy (TEM), Department of Physics. (n.d.). https://warwick.ac.uk/fac/sci/physics/current/postgraduate/regs/mpagswarwick/ex5/techniques/structural/tem/ (accessed February 8, 2019).
[253] D. Shindo, T. Oikawa, Analytical Electron Microscopy for Materials Science, Springer Science & Business Media, 2013.
[254] M. Fadonia, Temperature programmed desorption, reduction, oxidation and flow chemisorption for the characterisation of heterogeneous catalysts. Theoretical aspects, instrumentation and applications, in: 2006.
[255] National Physical Laboratory (NPL), Introduction to XPS: X-ray Photoelectron Spectroscopy, Surface & Nanoanalysis. (n.d.). http://www.npl.co.uk/science-technology/surface-and-nanoanalysis/surface-and-nanoanalysis-basics/introduction-to-xps-x-ray-photoelectron-spectroscopy (accessed February 9, 2019).
[256] M. Muthuvel, ABC's of Electrochemistry: X-Ray Photoelectron Spectroscopy (XPS), (2011). https://www.ohio.edu/engineering/ceer/research/upload/xps.pdf (accessed September 2, 2019).
[257] J.M. López, A.L. Gilbank, T. García, B. Solsona, S. Agouram, L. Torrente-Murciano, The prevalence of surface oxygen vacancies over the mobility of bulk oxygen in nanostructured ceria for the total toluene oxidation, Appl. Catal. B-Environ. 174 (2015) 403–412. doi:10.1016/j.apcatb.2015.03.017.
[258] L. Torrente-Murciano, R.S.L. Chapman, A. Narvaez-Dinamarca, D. Mattia, M.D. Jones, Effect of nanostructured ceria as support for the iron catalysed hydrogenation of CO2 into hydrocarbons, Phys. Chem. Chem. Phys. 18 (2016) 15496–15500. doi:10.1039/C5CP07788E.
[259] L. Torrente-Murciano, F.R. Garcia-Garcia, Effect of nanostructured support on the WGSR activity of Pt/CeO2 catalysts, Catalysis Communications. 71 (2015) 1–6. doi:10.1016/j.catcom.2015.07.021.
[260] The London Metal Exchange, (2019). https://www.lme.com/.
[261] H. Yu, J. Yu, S. Liu, S. Mann, Template-free hydrothermal synthesis of CuO/Cu2O composite hollow microspheres, Chem. Mater. 19 (2007) 4327–4334. doi:10.1021/cm070386d.
[262] R.D. Shannon, Revised Effective Ionic Radii and Systematic Studies of Interatomic Distances in Halides and Chalcogenides, Acta Crystallogr. A32 (1976) 751–767. doi:10.1107/S0567739476001551.
[263] A. Younis, D. Chu, Y.V. Kaneti, S. Li, Tuning the surface oxygen concentration of {111} surrounded ceria nanocrystals for enhanced photocatalytic activities, Nanoscale. 8 (2016) 378–387. doi:10.1039/C5NR06588G.
[264] Y. She, Q. Zheng, L. Li, Y. Zhan, C. Chen, Y. Zheng, X. Lin, Rare earth oxide modified CuO/CeO2 catalysts for the water–gas shift reaction, Int. J. Hydrogen Energy. 34 (2009) 8929–8936. doi:10.1016/j.ijhydene.2009.08.062.
[265] D. Mukherjee, B.G. Rao, B.M. Reddy, Characterization of Ceria-Based Nano-Oxide Catalysts by Raman Spectroscopy, Top. Catal. 60 (2017) 1673–1681. doi:10.1007/s11244-017-0846-5.
[266] S. Saitzek, J.F. Blach, S. Villain, J.R. Gavarri, Nanostructured ceria: a comparative study from X-ray diffraction, Raman spectroscopy and BET specific surface measurements, Phys. Status Solidi a. 205 (2008) 1534–1539. doi:10.1002/pssa.200723419.
[267] F.D. Hardcastle, I.E. Wachs, Raman spectroscopy of chromium oxide supported on Al2O3, TiO2 and SiO2: a comparative study, J. Mol. Catal. 46 (1988) 173–186. doi:https://doi.org/10.1016/0304-5102(88)85092-2.

[268] H. Sohn, G. Celik, S. Gunduz, D. Dogu, S. Zhang, J. Shan, F.F. Tao, U.S. Ozkan, Oxygen Mobility in Pre-Reduced Nano-and Macro-Ceria with Co Loading: An AP-XPS, In-Situ DRIFTS and TPR Study, Catal. Lett. 147 (2017) 2863–2876. doi:10.1007/s10562-017-2176-4.
[269] Z.-K. Han, Y.-G. Wang, Y. Gao, Catalytic role of vacancy diffusion in ceria supported atomic gold catalyst, Chemical Communications. 53 (2017) 9125–9128. doi:10.1039/C7CC04440B.
[270] D.G. Araiza, A. Gómez-Cortés, G. Díaz, Partial oxidation of methanol over copper supported on nanoshaped ceria for hydrogen production, Catalysis Today. 282 (2017) 185–194. doi:10.1016/j.cattod.2016.06.055.
[271] W.-P. Dow, Y.-P. Wang, T.-J. Huang, TPR and XRD studies of yttria-doped ceria/γ-alumina-supported copper oxide catalyst, Applied Catalysis A: General. 190 (2000) 25–34. doi:10.1016/S0926-860X(99)00286-0.
[272] J. Papavasiliou, M. Rawski, J. Vakros, G. Avgouropoulos, A Novel Post-Synthesis Modification of CuO-CeO2 Catalysts: Effect on Their Activity for Selective CO Oxidation, ChemCatChem. 10 (2018) 2096–2106. doi:10.1002/cctc.201701968.
[273] H. Yoshida, Y. Okabe, S. Misumi, H. Oyama, K. Tokusada, S. Hinokuma, M. Machida, Structures and Catalytic Properties of Cr–Cu Embedded CeO2 Surfaces with Different Cr/Cu Ratios, J. Phys. Chem. C. 120 (2016) 26852–26863. doi:10.1021/acs.jpcc.6b08785.
[274] K.S.W. Sing, D.H. Everett, R.A.W. Haul, L. Moscou, R.A. Pierotti, J. Rouquérol, T. Siemieniewska, Reporting Physisorption Data for Gas/Solid Systems with Special Reference to the Determination of Surface Area and Porosity, Pure Appl. Chem. 54 (1982) 2201–2218. doi:10.1515/iupac.57.0007.
[275] L. Zhou, X. Li, Z. Yao, Z. Chen, M. Hong, R. Zhu, Y. Liang, J. Zhao, Transition-metal doped ceria microspheres with nanoporous structures for CO oxidation, Sci. Rep. 6 (2016). doi:10.1038/srep23900.
[276] J.S. Elias, K.A. Stoerzinger, W.T. Hong, M. Risch, L. Giordano, A.N. Mansour, Y. Shao-Horn, In Situ Spectroscopy and Mechanistic Insights into CO Oxidation on Transition-Metal-Substituted Ceria Nanoparticles, ACS Catal. 7 (2017) 6843–6857. doi:10.1021/acscatal.7b01600.
[277] Y. Park, S.K. Kim, D. Pradhan, Y. Sohn, Surface treatment effects on CO oxidation reactions over Co, Cu, and Ni-doped and codoped CeO2 catalysts, Chem. Eng. J. 250 (2014) 25–34. doi:10.1016/j.cej.2014.03.070.
[278] M. Konsolakis, The role of Copper–Ceria interactions in catalysis science: Recent theoretical and experimental advances, Applied Catalysis B: Environmental. 198 (2016) 49–66. doi:10.1016/j.apcatb.2016.05.037.
[279] H. Yoshida, N. Yamashita, S. Ijichi, Y. Okabe, S. Misumi, S. Hinokuma, M. Machida, A Thermally Stable Cr–Cu Nanostructure Embedded in the CeO2 Surface as a Substitute for Platinum-Group Metal Catalysts, ACS Catal. 5 (2015) 6738–6747. doi:10.1021/acscatal.5b01847.
[280] Z.-Y. Pu, X.-S. Liu, A.-P. Jia, Y.-L. Xie, J.-Q. Lu, M.-F. Luo, Enhanced Activity for CO Oxidation over Pr- and Cu-Doped CeO2 Catalysts: Effect of Oxygen Vacancies, The Journal of Physical Chemistry C. 112 (2008) 15045–15051. doi:10.1021/jp805389k.
[281] K. Koizumi, K. Nobusada, M. Boero, An atomic-level insight into the basic mechanism responsible for the enhancement of the catalytic oxidation of carbon monoxide on a Cu/CeO 2 surface, Physical Chemistry Chemical Physics. 19 (2017) 3498–3505. doi:10.1039/C6CP05957K.
[282] F. Yang, J. Wei, W. Liu, J. Guo, Y. Yang, Copper doped ceria nanospheres: surface defects promoted catalytic activity and a versatile approach, Journal of Materials Chemistry A. 2 (2014) 5662–5667. doi:10.1039/C3TA15253G.
[283] M. Dosa, M. Piumetti, S. Bensaid, T. Andana, C. Novara, F. Giorgis, D. Fino, N. Russo, Novel Mn–Cu-Containing CeO2 Nanopolyhedra for the Oxidation of CO and Diesel Soot: Effect of Dopants on the Nanostructure and Catalytic Activity, Catal Lett. 148 (2018) 298–311. doi:10.1007/s10562-017-2226-y.
[284] M. Lykaki, E. Pachatouridou, S.A.C. Carabineiro, E. Iliopoulou, C. Andriopoulou, N. Kallithrakas-Kontos, S. Boghosian, M. Konsolakis, Ceria nanoparticles shape effects on the structural defects and surface chemistry: Implications in CO oxidation by Cu/CeO2 catalysts, Applied Catalysis B: Environmental. 230 (2018) 18–28. doi:10.1016/j.apcatb.2018.02.035.
[285] H. Yoshida, Y. Okabe, N. Yamashita, S. Hinokuma, M. Machida, Catalytic CO–NO reaction over Cr–Cu embedded CeO2 surface structure, Catalysis Today. 281 (2017) 590–595. doi:10.1016/j.cattod.2016.05.018.
[286] Y. Zheng, K. Li, H. Wang, Y. Wang, D. Tian, Y. Wei, X. Zhu, C. Zeng, Y. Luo, Structure dependence and reaction mechanism of CO oxidation: A model study on macroporous CeO2 and CeO2-ZrO2 catalysts, J. Catal. 344 (2016) 365–377. doi:10.1016/j.jcat.2016.10.008.
[287] X. Li, H. Dai, J. Deng, Y. Liu, S. Xie, Z. Zhao, Y. Wang, G. Guo, H. Arandiyan, Au/3DOM LaCoO3: High-performance catalysts for the oxidation of carbon monoxide and toluene, Chemical Engineering Journal. 228 (2013) 965–975. doi:10.1016/j.cej.2013.05.070.
[288] M. Tsujimura, T. Furusawa, D. Kunii, Catalytic reduction of nitric aid by carbon monoxide over calcined limestone, J Chem Eng Jpn. 16 (1983) 524–526. doi:10.1252/jcej.16.524.
[289] S. Li, J. Yu, X. Wei, X. Guo, Y. Chen, Catalytic reduction of nitric oxide by carbon monoxide over coal gangue hollow ball, Fuel Process. Technol. 125 (2014) 163–169. doi:10.1016/j.fuproc.2014.04.005.
[290] W. Liu, M. Flytzani-Stephanopoulos, Transition metal-promoted oxidation catalysis by fluorite oxides: A study of CO oxidation over Cu-CeO2, Chem. Eng. J. 64 (1996) 283–294. doi:10.1016/S0923-0467(96)03135-1.
[291] J.S. Elias, N. Artrith, M. Bugnet, L. Giordano, G.A. Botton, A.M. Kolpak, Y. Shao-Horn, Elucidating the Nature of the Active Phase in Copper/Ceria Catalysts for CO Oxidation, ACS Catal. 6 (2016) 1675–1679. doi:10.1021/acscatal.5b02666.
[292] H.S. Fogler, Elements of Chemical Reaction Engineering, 5 edition, Prentice Hall, Boston, 2016.
[293] Air - Diffusion Coefficients of Gases in Excess of Air, Engineering ToolBox. (2018). https://www.engineeringtoolbox.com/air-diffusion-coefficient-gas-mixture-temperature-d_2010.html (accessed June 29, 2019).

[294] M.J. Tang, R.A. Cox, M. Kalberer, Compilation and evaluation of gas phase diffusion coefficients of reactive trace gases in the atmosphere: volume 1. Inorganic compounds, Atmospheric Chemistry and Physics. 14 (2014) 9233–9247. doi:https://doi.org/10.5194/acp-14-9233-2014.
[295] M.J. Tang, M. Shiraiwa, U. Pöschl, R.A. Cox, M. Kalberer, Compilation and evaluation of gas phase diffusion coefficients of reactive trace gases in the atmosphere: Volume 2. Diffusivities of organic compounds, pressure-normalised mean free paths, and average Knudsen numbers for gas uptake calculations, Atmospheric Chemistry and Physics. 15 (2015) 5585–5598. doi:https://doi.org/10.5194/acp-15-5585-2015.
[296] D.Yu. Murzin, T. Salmi, Chapter 10 - Mass Transfer and Catalytic Reactions, in: D.Yu. Murzin, T. Salmi (Eds.), Catalytic Kinetics (Second Edition), Elsevier, Amsterdam, 2016: pp. 589–664. doi:10.1016/B978-0-444-63753-6.00010-5.
[297] J.R. Backhurst, J.H. Harker, J.F. Richardson, J.M. Coulson, Chemical Engineering Volume 1: Fluid Flow, Heat Transfer and Mass Transfer: Fluid Flow, Heat Transfer and Mass Transfer v. 1, 6 edition, Butterworth-Heinemann, Oxford ; Boston, 1999.
[298] Gases - Dynamic Viscosity, Engineering ToolBox. (2018). https://www.engineeringtoolbox.com/gases-absolute-dynamic-viscosity-d_1888.html (accessed June 30, 2019).
[299] J.L. Gasser-Ramirez, B.C. Dunn, D.W. Ramirez, E.P. Fillerup, G.C. Turpin, Y. Shi, R.D. Ernst, R.J. Pugmire, E.M. Eyring, K.A. Pettigrew, A simple synthesis of catalytically active, high surface area ceria aerogels, J. Non-Cryst. Solids. 354 (2008) 5509–5514. doi:10.1016/j.jnoncrysol.2008.09.011.
[300] S. Kurajica, I. Minga, M. Gulиš, V. Mandić, I. Simčić, High Surface Area Ceria Nanoparticles via Hydrothermal Synthesis Experiment Design, J. Nanomater. 2016 (2016). doi:10.1155/2016/7274949.
[301] J. Yang, L. Lukashuk, H. Li, K. Föttinger, G. Rupprechter, U. Schubert, High surface area ceria for CO oxidation prepared from cerium t-butoxide by combined sol–gel and solvothermal processing, Catal. Lett. 144 (2014) 403–412. doi:10.1007/s10562-013-1162-8.
[302] J. Han, J. Meeprasert, P. Maitarad, S. Nammuangruk, L. Shi, D. Zhang, Investigation of the Facet-Dependent Catalytic Performance of Fe2O3/CeO2 for the Selective Catalytic Reduction of NO with NH3, J. Phys. Chem. C. 120 (2016) 1523–1533. doi:10.1021/acs.jpcc.5b09834.
[303] P. Maitarad, J. Han, D. Zhang, L. Shi, S. Namuangruk, T. Rungrotmongkol, Structure–Activity Relationships of NiO on CeO2 Nanorods for the Selective Catalytic Reduction of NO with NH3: Experimental and DFT Studies, J. Phys. Chem. C. 118 (2014) 9612–9620. doi:10.1021/jp5024845.
[304] Z. Gao, L.V. Mogni, E.C. Miller, J.G. Railsback, S.A. Barnett, A perspective on low-temperature solid oxide fuel cells, Energy Environ. Sci. 9 (2016) 1602–1644. doi:10.1039/C5EE03858H.
[305] D.R. Dreyer, A.D. Todd, C.W. Bielawski, Harnessing the chemistry of graphene oxide, Chem. Soc. Rev. 43 (2014) 5288–5301. doi:10.1039/c4cs00060a.
[306] L. Jiang, M. Yao, B. Liu, Q. Li, R. Liu, H. Lv, S. Lu, C. Gong, B. Zou, T. Cui, Controlled synthesis of CeO2/graphene nanocomposites with highly enhanced optical and catalytic properties, J. Phys. Chem. C. 116 (2012) 11741–11745. doi:10.1021/jp3015113.
[307] K. Huang, Y.H. Li, S. Lin, C. Liang, X. Xu, Y.F. Zhou, D.Y. Fan, H.J. Yang, P.L. Lang, R. Zhang, One-step synthesis of reduced graphene oxide–CeO 2 nanocubes composites with enhanced photocatalytic activity, Mater. Lett. 124 (2014) 223–226. doi:10.1016/j.matlet.2014.03.023.
[308] T.S. Sakthivel, S. Das, C.J. Pratt, S. Seal, One-pot synthesis of a ceria–graphene oxide composite for the efficient removal of arsenic species, Nanoscale. 9 (2017) 3367–3374. doi:10.1039/C6NR07608D.
[309] M. Guo, J. Lu, Y. Wu, Y. Wang, M. Luo, UV and visible Raman studies of oxygen vacancies in rare-earth-doped ceria, Langmuir. 27 (2011) 3872–3877. doi:10.1021/la200292f.
[310] S.A. Acharya, V.M. Gaikwad, V. Sathe, S.K. Kulkarni, Influence of gadolinium doping on the structure and defects of ceria under fuel cell operating temperature, Appl. Phys. Lett. 104 (2014) 113508. doi:10.1063/1.4869116.
[311] T. Taniguchi, T. Watanabe, N. Sugiyama, A.K. Subramani, H. Wagata, N. Matsushita, M. Yoshimura, Identifying defects in ceria-based nanocrystals by UV resonance Raman spectroscopy, The Journal of Physical Chemistry C. 113 (2009) 19789–19793. doi:10.1021/jp9049457.
[312] S.R. Bishop, K.L. Duncan, E.D. Wachsman, Defect equilibria and chemical expansion in non-stoichiometric undoped and gadolinium-doped cerium oxide, Electrochim Acta. 54 (2009) 1436–1443. doi:10.1016/j.electacta.2008.09.026.
[313] G. Leofanti, M. Padovan, G. Tozzola, B. Venturelli, Surface area and pore texture of catalysts, Catal. Today. 41 (1998) 207–219. doi:10.1016/s0920-5861(98)00050-9.
[314] M. Lykaki, E. Pachatouridou, E. Iliopoulou, S.A. C. Carabineiro, M. Konsolakis, Impact of the synthesis parameters on the solid state properties and the CO oxidation performance of ceria nanoparticles, RSC Advances. 7 (2017) 6160–6169. doi:10.1039/C6RA26712B.
[315] M. Piumetti, T. Andana, S. Bensaid, N. Russo, D. Fino, R. Pirone, Study on the CO Oxidation over Ceria-Based Nanocatalysts, Nanoscale Res. Lett. 11 (2016) 165. doi:10.1186/s11671-016-1375-z.
[316] X. Zhang, F. Hou, Y. Yang, Y. Wang, N. Liu, D. Chen, Y. Yang, A facile synthesis for cauliflower like CeO2 catalysts from Ce-BTC precursor and their catalytic performance for CO oxidation, Applied Surface Science. 423 (2017) 771–779. doi:10.1016/j.apsusc.2017.06.235.
[317] A. Trovarelli, J. Llorca, Ceria Catalysts at Nanoscale: How Do Crystal Shapes Shape Catalysis?, ACS Catal. 7 (2017) 4716–4735. doi:10.1021/acscatal.7b01246.
[318] A. Trovarelli, C. de Leitenburg, M. Boaro, G. Dolcetti, The utilization of ceria in industrial catalysis, Catal. Today. 50 (1999) 353–367. doi:10.1016/S0920-5861(98)00515-X.
[319] E. Aneggi, D. Wiater, C. de Leitenburg, J. Llorca, A. Trovarelli, Shape-dependent activity of ceria in soot combustion, ACS Catal. 4 (2013) 172–181. doi:10.1021/cs400850r.

[320] T.R. Reina, S. Ivanova, O.H. Laguna, M.A. Centeno, J.A. Odriozola, WGS and CO-PrOx reactions using gold promoted copper-ceria catalysts: “Bulk CuOCeO2 vs. CuOCeO2/Al2O3 with low mixed oxide content,” Appl. Catal. B-Environ. 197 (2016) 62–72. doi:https://doi.org/10.1016/j.apcatb.2016.03.022.
[321] P. Boldrin, E. Ruiz-Trejo, J. Mermelstein, J.M. Bermúdez Menéndez, T. Ramírez Reina, N.P. Brandon, Strategies for Carbon and Sulfur Tolerant Solid Oxide Fuel Cell Materials, Incorporating Lessons from Heterogeneous Catalysis, Chem. Rev. 116 (2016) 13633–13684. doi:10.1021/acs.chemrev.6b00284.
[322] Z.P. Shao, S.M. Haile, A high-performance cathode for the next generation of solid-oxide fuel cells, Nature. 431 (2004) 170–173. doi:10.1038/nature02863.
[323] B. Zhang, X. Tang, Y. Li, Y. Xu, W. Shen, Hydrogen production from steam reforming of ethanol and glycerol over ceria-supported metal catalysts, Int. J. Hydrogen Energy. 32 (2007) 2367–2373. doi:10.1016/j.ijhydene.2006.11.003.
[324] G.R. Bamwenda, H. Arakawa, Cerium dioxide as a photocatalyst for water decomposition to O(2) in the presence of Ce(aq)(4+) and Fe(aq)(3+) species, J. Mol. Catal. A: Chem. 161 (2000) 105–113. doi:10.1016/s1381-1169(00)00270-3.
[325] F. Lin, M. Rothensteiner, I. Alxneit, J.A. van Bokhoven, A. Wokaun, First demonstration of direct hydrocarbon fuel production from water and carbon dioxide by solar-driven thermochemical cycles using rhodium–ceria, Energy Environ. Sci. 9 (2016) 2400–2409. doi:10.1039/C6EE00862C.
[326] M.-S. Fan, A.Z. Abdullah, S. Bhatia, Catalytic technology for carbon dioxide reforming of methane to synthesis gas, ChemCatChem. 1 (2009) 192–208. doi:10.1002/cctc.200900025.
[327] X. Du, D. Zhang, L. Shi, R. Gao, J. Zhang, Morphology Dependence of Catalytic Properties of Ni/CeO2 Nanostructures for Carbon Dioxide Reforming of Methane, J. Phys. Chem. C. 116 (2012) 10009–10016. doi:10.1021/jp300543r.
[328] C. Tang, L. Liping, L. Zhang, L. Tan, L. Dong, High Carbon-Resistance Ni@CeO2 Core–Shell Catalysts for Dry Reforming of Methane, Kinet Catal. 58 (2017) 800–808. doi:10.1134/S0023158418010123.
[329] X. Zhao, M. Lu, H. Li, J. Fang, L. Shi, D. Zhang, In situ preparation of Ni nanoparticles in cerium-modified silica aerogels for coking- and sintering-resistant dry reforming of methane, New J. Chem. 41 (2017) 4869–4878. doi:10.1039/C7NJ00115K.
[330] S. Arora, R. Prasad, An overview on dry reforming of methane: strategies to reduce carbonaceous deactivation of catalysts, RSC Advances. 6 (2016) 108668–108688. doi:10.1039/C6RA20450C.
[331] D. Pakhare, J. Spivey, A review of dry (CO 2) reforming of methane over noble metal catalysts, Chem. Soc. Rev. 43 (2014) 7813–7837. doi:10.1039/C3CS60395D.
[332] M. Usman, W.W. Daud, H.F. Abbas, Dry reforming of methane: influence of process parameters—a review, Renewable and Sustainable Energy Reviews. 45 (2015) 710–744. doi:10.1016/j.rser.2015.02.026.
[333] T.E. Bell, G. Zhan, K. Wu, H.C. Zeng, L. Torrente-Murciano, Modification of Ammonia Decomposition Activity of Ruthenium Nanoparticles by N-Doping of CNT Supports, Top Catal. 60 (2017) 1251–1259. doi:10.1007/s11244-017-0806-0.
[334] L. Torrente-Murciano, The importance of particle-support interaction on particle size determination by gas chemisorption, J Nanopart Res. 18 (2016). doi:10.1007/s11051-016-3385-2.
[335] J. Guo, H. Lou, H. Zhao, D. Chai, X. Zheng, Dry reforming of methane over nickel catalysts supported on magnesium aluminate spinels, Appl. Catal. A-Gen. 273 (2004) 75–82. doi:10.1016/j.apcata.2004.06.014.
[336] J.M. Rynkowski, T. Paryjczak, M. Lenik, On the nature of oxidic nickel phases in NiO/γ-Al2O3 catalysts, Appl. Catal. A-Gen. 106 (1993) 73–82. doi:10.1016/0926-860X(93)80156-K.
[337] M. Li, H. Amari, A.C. van Veen, Metal-oxide interaction enhanced CO2 activation in methanation over ceria supported nickel nanocrystallites, Applied Catalysis B: Environmental. 239 (2018) 27–35. doi:10.1016/j.apcatb.2018.07.074.
[338] A. Vita, C. Italiano, C. Fabiano, M. Laganà, L. Pino, Influence of Ce-precursor and fuel on structure and catalytic activity of combustion synthesized Ni/CeO2 catalysts for biogas oxidative steam reforming, Materials Chemistry and Physics. 163 (2015) 337–347. doi:10.1016/j.matchemphys.2015.07.048.
[339] Y. Zhou, J.M. Perket, A.B. Crooks, J. Zhou, Effect of ceria support on the structure of Ni nanoparticles, The Journal of Physical Chemistry Letters. 1 (2010) 1447–1453. doi:10.1021/jz1003044.
[340] M. Bäumer, H.-J. Freund, Metal deposits on well-ordered oxide films, Prog. Surf. Sci. 61 (1999) 127–198. doi:10.1016/S0079-6816(99)00012-X.
[341] T. Stroud, T.J. Smith, E. Le Saché, J.L. Santos, M.A. Centeno, H. Arellano-Garcia, J.A. Odriozola, T.R. Reina, Chemical CO2 recycling via dry and bi reforming of methane using Ni-Sn/Al2O3 and Ni-Sn/CeO2-Al2O3 catalysts, Appl. Catal. B-Environ. 224 (2018) 125–135. doi:https://doi.org/10.1016/j.apcatb.2017.10.047.
[342] Y. Wang, L. Yao, S. Wang, D. Mao, C. Hu, Low-temperature catalytic CO2 dry reforming of methane on Ni-based catalysts: A review, Fuel Processing Technology. 169 (2018) 199–206. doi:10.1016/j.fuproc.2017.10.007.
[343] X. Lv, J.-F. Chen, Y. Tan, Y. Zhang, A highly dispersed nickel supported catalyst for dry reforming of methane, Catal. Commun. 20 (2012) 6–11. doi:10.1016/j.catcom.2012.01.002.
[344] A. Horváth, G. Stefler, O. Geszti, A. Kienneman, A. Pietraszek, L. Guczi, Methane dry reforming with CO 2 on CeZr-oxide supported Ni, NiRh and NiCo catalysts prepared by sol–gel technique: relationship between activity and coke formation, Catal. Today. 169 (2011) 102–111. doi:10.1016/j.cattod.2010.08.004.
[345] M.S. Aw, I.G. Osojnik Črnivec, P. Djinović, A. Pintar, Strategies to enhance dry reforming of methane: Synthesis of ceria-zirconia/nickel–cobalt catalysts by freeze-drying and NO calcination, International Journal of Hydrogen Energy. 39 (2014) 12636–12647. doi:10.1016/j.ijhydene.2014.06.083.
[346] C. Liu, J. Ye, J. Jiang, Y. Pan, Progresses in the Preparation of Coke Resistant Ni-Based Catalyst for Steam and CO2 Reforming of Methane, ChemCatChem. 3 (2011) 529–541. doi:10.1002/cctc.201000358.

[347] A. Albarazi, M.E. Gálvez, P. Da Costa, Synthesis strategies of ceria–zirconia doped Ni/SBA-15 catalysts for methane dry reforming, Catal. Commun. 59 (2015) 108–112. doi:10.1016/j.catcom.2014.09.050.
[348] J.-M. Lavoie, Review on dry reforming of methane, a potentially more environmentally-friendly approach to the increasing natural gas exploitation, Front. Chem. 2 (2014). doi:10.3389/fchem.2014.00081.
[349] A.R. McFarlane, I.P. Silverwood, R. Warringham, E.L. Norris, R.M. Ormerod, C.D. Frost, S.F. Parker, D. Lennon, The application of inelastic neutron scattering to investigate the 'dry'reforming of methane over an alumina-supported nickel catalyst operating under conditions where filamentous carbon formation is prevalent, RSC Adv. 3 (2013) 16577–16589. doi:10.1039/C3RA42435A.
[350] T. Margossian, K. Larmier, S.M. Kim, F. Krumeich, A. Fedorov, P. Chen, C.R. Müller, C. Copéret, Molecularly Tailored Nickel Precursor and Support Yield a Stable Methane Dry Reforming Catalyst with Superior Metal Utilization, J. Am. Chem. Soc. 139 (2017) 6919–6927. doi:10.1021/jacs.7b01625.
[351] H. Yucai, Hydrothermal Synthesis of Nano Ce–Zr–Y Oxide Solid Solution for Automotive Three-Way Catalyst, J. Am. Ceram. Soc. 89 (2006) 2949–2951. doi:10.1111/j.1551-2916.2006.01130.x.
[352] P. Granger, J.F. Lamonier, N. Sergent, A. Aboukais, L. Leclercq, G. Leclercq, Investigation of the Intrinsic Activity of ZrxCe1−xO2 Mixed Oxides in the CO + NO Reactions: Influence of Pd Incorporation, Top. Catal. 16–17 (2001) 89–94. doi:10.1023/A:1016634915247.
[353] Z. Zhou, J. Ouyang, H. Yang, A. Tang, Three-way catalytic performances of Pd loaded halloysite-Ce0.5Zr0.5O2 hybrid materials, Appl. Clay Sci. 121–122 (2016) 63–70. doi:10.1016/j.clay.2015.12.017.

Chapter 10

Appendices

10.1 Appendix A – supporting information for TWC literature review

Table A11. Varying washcoat composition and reported T_{10} and T_{50} values from literature. (1/6)

Composition	CO		HC		NO		NO_2		Aging conditions	Ref.
	T10 (°C)	T50 (°C)	T10 (°C)	T50 (°C)	T10 (°C)	T50 (°C)	T10 (°C)	T50 (°C)		
1% Pd/(Al_2O_3) (0.5% CO/250ppm HC)	193	216	172	224	-	-	-	-	Not aged	[190]
1% Pd/($Ce_xZr_yO_2$) (0.5% CO/250ppm HC)	95	157	176	208	-	-	-	-		
1% Pd/(Al_2O_3) (1.0% CO/500ppm HC)	209	225	191	270	-	-	-	-		
1% Pd/($Ce_xZr_yO_2$) (1.0% CO/500ppm HC)	127	164	193	226	-	-	-	-		
0.5% Pt/(Al_2O_3)	453	530	453	510	400	350	-	-	1000 °C in air, 3 h	[192]
0.5% Pt/(0.3CeO_2 + Al_2O_3)	268	350	360	430	360	420	-	-		
0.5% Pt/(0.3($Ce_{0.8}Zr_{0.2}O_2$) + Al_2O_3)	289	350	351	420	340	440	-	-		
1% Pd/(Al_2O_3/CeO_2/ZrO_2)	282	308	287	308	309	-	-	-	1050 °C, redox, 36 h	[193]
1% Pd/(Al_2O_3 + CeO_2/ZrO_2)	282	323	292	323	350	-	-	-		
(120 g/L Al_2O_3)/(60 g/L CeZrY); Pt deposited on Al_2O_3	-	248	-	256	-	251	-	-	900 °C, redox conditions 50 h	[194]
(120 g/L Al_2O_3)/(60 g/L CeZrY); Pt deposited on CeZrY	-	241	-	247	-	251	-	-		
(120 g/L Al_2O_3)/(60 g/L CeZr; Pt deposited on CeZr	-	304	-	307	-	327	-	-		
(80 g/L Al_2O_3)/(60 g/L CeZrY)/(40 g/L ZrO_2); Pt dep. on ZrO_2	-	263	-	275	-	279	-	-		
(80 g/L Al_2O_3)/(60 g/L CeZrY)/(40 g/L TiO_2); Pt dep. on TiO_2	-	323	-	325	-	325	-	-		
0.5% Pd/($Ce_{0.2}Zr_{0.8}O_2$)	-	140	-	304	-	161	-	-	Not aged	[200]
0.5% Pd/($Ce_{0.5}Zr_{0.5}O_2$)	-	114	-	289	-	143	-	-		
0.5% Pd/($Ce_{0.8}Zr_{0.2}O_2$)	-	120	-	295	-	143	-	-		
0.5% Pd/($Ce_{0.2}Zr_{0.8}O_2$ + $Ce_{0.8}Zr_{0.2}O_2$)	-	110	-	289	-	131	-	-		
0.5% Pd/($Ce_{0.2}Zr_{0.8}O_2$)	-	215	-	432	-	266	-	-	1000 °C in air, 5 h	
0.5% Pd/($Ce_{0.5}Zr_{0.5}O_2$)	-	185	-	370	-	238	-	-		
0.5% Pd/($Ce_{0.8}Zr_{0.2}O_2$)	-	215	-	415	-	255	-	-		
0.5% Pd/($Ce_{0.2}Zr_{0.8}O_2$ + $Ce_{0.8}Zr_{0.2}O_2$)	-	178	-	347	-	220	-	-		

Table A11. Varying washcoat composition and reported T_{10} and T_{50} values from literature. (2/6)

Composition	CO		HC		NO		NO_2		Aging conditions	Ref.
	T10 (°C)	T50 (°C)	T10 (°C)	T50 (°C)	T10 (°C)	T50 (°C)	T10 (°C)	T50 (°C)		
0.4% PtRh/($Ce_{0.35}Zr_{0.60}Nd_{0.05}O_2$)	223	242	260	289	248	278	-	-	Not aged	[202]
0.4% PtRh/($Ce_{0.35}Zr_{0.55}Nd_{0.10}O_2$)	142	160	230	259	190	211	-	-		
0.4% PtRh/($Ce_{0.35}Zr_{0.50}Nd_{0.15}O_2$)	140	170	228	259	186	217	-	-		
0.4% PtRh/($Ce_{0.35}Zr_{0.45}Nd_{0.20}O_2$)	151	179	230	258	180	240	-	-		
0.4% PtRh/($Ce_{0.35}Zr_{0.40}Nd_{0.25}O_2$)	163	191	238	262	202	231	-	-		
0.5 % Pd/($Ce_{0.2}Zr_{0.8}O_2$)	-	159	-	229	-	205	-	180	Not aged	[203]
0.5 % Pd/($Ce_{0.2}Zr_{0.8}O_2$ 3 wt. % Nd)	-	167	-	226	-	210	-	174		
0.5 % Pd/($Ce_{0.2}Zr_{0.8}O_2$ 5 wt. % Nd)	-	184	-	218	-	206	-	170		
0.5 % Pd/($Ce_{0.2}Zr_{0.8}O_2$ 8 wt. % Nd)	-	186	-	224	-	188	-	165		
0.5 % Pd/($Ce_{0.2}Zr_{0.8}O_2$ 10 wt. % Nd)	-	188	-	227	-	187	-	160		
0.5 % Pd/($Ce_{0.2}Zr_{0.8}O_2$)	-	265	-	372	-	360	-	315	1100 °C, 4 h	
0.5 % Pd/($Ce_{0.2}Zr_{0.8}O_2$ 3 wt. % Nd)	-	259	-	340	-	347	-	275		
0.5 % Pd/($Ce_{0.2}Zr_{0.8}O_2$ 5 wt. % Nd)	-	254	-	307	-	316	-	263		
0.5 % Pd/($Ce_{0.2}Zr_{0.8}O_2$ 8 wt. % Nd)	-	226	-	333	-	330	-	220		
0.5 % Pd/($Ce_{0.2}Zr_{0.8}O_2$ 10 wt. % Nd)	-	218	-	337	-	335	-	216		
0.5 % Pd/($Ce_{0.2}Zr_{0.8}O_2$)	-	159	-	229	-	205	-	180	Not aged	[204]
0.5 % Pd/($Ce_{0.2}Zr_{0.8}O_2$ 3 wt. % Pr)	-	157	-	222	-	190	-	164		
0.5 % Pd/($Ce_{0.2}Zr_{0.8}O_2$ 5 wt. % Pr)	-	153	-	212	-	176	-	157		
0.5 % Pd/($Ce_{0.2}Zr_{0.8}O_2$ 8 wt. % Pr)	-	152	-	200	-	174	-	157		
0.5 % Pd/($Ce_{0.2}Zr_{0.8}O_2$ 10 wt. % Pr)	-	147	-	199	-	172	-	156		
0.5 % Pd/($Ce_{0.2}Zr_{0.8}O_2$)	-	265	-	372	-	360	-	315	1100 °C, 4 h	
0.5 % Pd/($Ce_{0.2}Zr_{0.8}O_2$ 3 wt. % Pr)	-	252	-	347	-	365	-	289		
0.5 % Pd/($Ce_{0.2}Zr_{0.8}O_2$ 5 wt. % Pr)	-	252	-	340	-	353	-	279		
0.5 % Pd/($Ce_{0.2}Zr_{0.8}O_2$ 8 wt. % Pr)	-	203	-	332	-	336	-	203		
0.5 % Pd/($Ce_{0.2}Zr_{0.8}O_2$ 10 wt. % Pr)	-	203	-	327	-	322	-	203		

Table A11. Varying washcoat composition and reported T_{10} and T_{50} values from literature. (3/6)

Composition	CO		HC		NO		NO_2		Aged?	Ref.
	T10 (°C)	T50 (°C)	T10 (°C)	T50 (°C)	T10 (°C)	T50 (°C)	T10 (°C)	T50 (°C)		
0.5 % Pd/($Ce_{0.2}Zr_{0.8}O_2$)	-	159	-	229	-	205	-	180	Not aged	[205]
0.5 % Pd/($Ce_{0.2}Zr_{0.8}O_2$ 3 wt. % La)	-	166	-	248	-	221	-	178		
0.5 % Pd/($Ce_{0.2}Zr_{0.8}O_2$ 5 wt. % La)	-	181	-	215	-	213	-	187		
0.5 % Pd/($Ce_{0.2}Zr_{0.8}O_2$ 8 wt. % La)	-	184	-	234	-	208	-	187		
0.5 % Pd/($Ce_{0.2}Zr_{0.8}O_2$ 10 wt. % La)	-	185	-	237	-	205	-	187		
0.5 % Pd/($Ce_{0.2}Zr_{0.8}O_2$)	-	265	-	372	-	360	-	315	1100 °C, 4 h	
0.5 % Pd/($Ce_{0.2}Zr_{0.8}O_2$ 3 wt. % La)	-	243	-	330	-	340	-	259		
0.5 % Pd/($Ce_{0.2}Zr_{0.8}O_2$ 5 wt. % La)	-	239	-	282	-	280	-	240		
0.5 % Pd/($Ce_{0.2}Zr_{0.8}O_2$ 8 wt. % La)	-	227	-	292	-	320	-	225		
0.5 % Pd/($Ce_{0.2}Zr_{0.8}O_2$ 10 wt. % La)	-	219	-	304	-	328	-	218		
0.5 % Pd/($Ce_{0.2}Zr_{0.8}O_2$ 5 wt. % Sm)	-	278	-	385	-	403	-	297	1100 °C, 4 h	[206]
0.5 % Pd/($Ce_{0.2}Zr_{0.8}O_2$ 5 wt. % Y)	-	288	-	412	-	466	-	309		
0.5% Pd/($Ce_{0.67}Zr_{0.33}O_2$)	-	-	-	250	-	228	-	187	Not aged	[207]
0.5% Pd/($Ce_{0.67}Zr_{0.33}O_2$, 11 mol % La)	-	-	-	241	-	214	-	185		
0.5% Pd/($Ce_{0.67}Zr_{0.33}O_2$, 11 mol % Nd)	-	-	-	252	-	211	-	185		
0.5% Pd/($Ce_{0.67}Zr_{0.33}O_2$, 11 mol % Pr)	-	-	-	252	-	204	-	171		
0.5% Pd/($Ce_{0.67}Zr_{0.33}O_2$, 11 mol % Sr)	-	-	-	241	-	218	-	180		
0.5% Pd/($Ce_{0.67}Zr_{0.33}O_2$, 11 mol % Y)	-	-	-	252	-	224	-	187		
0.5% Pd/($Ce_{0.67}Zr_{0.33}O_2$)	-	-	-	280	-	287	-	225	1100 °C, 4 h	
0.5% Pd/($Ce_{0.67}Zr_{0.33}O_2$, 11 mol % La)	-	-	-	276	-	282	-	209		
0.5% Pd/($Ce_{0.67}Zr_{0.33}O_2$, 11 mol % Nd)	-	-	-	267	-	267	-	198		
0.5% Pd/($Ce_{0.67}Zr_{0.33}O_2$, 11 mol % Pr)	-	-	-	273	-	278	-	186		
0.5% Pd/($Ce_{0.67}Zr_{0.33}O_2$, 11 mol % Sr)	-	-	-	276	-	278	-	207		
0.5% Pd/($Ce_{0.67}Zr_{0.33}O_2$, 11 mol % Y)	-	-	-	273	-	276	-	203		

Table A11. Varying washcoat composition and reported T_{10} and T_{50} values from literature. (4/6)

Composition	CO		HC		NO		NO_2		Aged?	Ref.
	T10 (°C)	T50 (°C)	T10 (°C)	T50 (°C)	T10 (°C)	T50 (°C)	T10 (°C)	T50 (°C)		
1% Pd/(0.4CeO_2/0.5ZrO_2/0.05La_2O_3/0.05Y_2O_3)	-	147	-	285	-	161	-	-	Not aged	[208]
1% Pd/(0.4CeO_2/0.5ZrO_2/0.05La_2O_3/0.05Nd_2O_3)	-	131	-	284	-	144	-	-		
1% Pd/(0.4CeO_2/0.5ZrO_2/0.05La_2O_3/0.05Pr_2O_3)	-	142	-	288	-	155	-	-		
1% Pd/(0.4CeO_2/0.5ZrO_2/0.05La_2O_3/0.05Y_2O_3)	-	190	-	300	-	215	-	-	1000 °C in air, 4 h	
1% Pd/(0.4CeO_2/0.5ZrO_2/0.05La_2O_3/0.05Nd_2O_3)	-	174	-	300	-	197	-	-		
1% Pd/(0.4CeO_2/0.5ZrO_2/0.05La_2O_3/0.05Pr_2O_3)	-	185	-	355	-	206	-	-		
0.7 g/L Pt+Rh/($Ce_{0.35}Zr_{0.55}Y_{0.1}O_2$)/(3 % La_2O_3+Al_2O_3)	<140	180	200	232	<160	199	-	-	Not aged	[209]
0.7 g/L Pt+Rh/($Ce_{0.35}Zr_{0.55}La_{0.1}O_2$)/(3 % La_2O_3+Al_2O_3)	<140	175	190	228	160	194	-	-		
0.7 g/L Pt+Rh/($Ce_{0.35}Zr_{0.50}Y_{0.075}La_{0.075}O_2$)/(3 % La_2O_3+Al_2O_3)	144	167	180	219	<160	190	-	-		
0.7 g/L Pt+Rh/($Ce_{0.35}Zr_{0.55}Y_{0.1}O_2$)/(3 % La_2O_3+Al_2O_3)	220	241	263	287	247	260	-	-	1000 °C, hydrothermal 5 h	
0.7 g/L Pt+Rh/($Ce_{0.35}Zr_{0.55}La_{0.1}O_2$)/(3 % La_2O_3+Al_2O_3)	<200	241	226	280	<220	257	-	-		
0.7 g/L Pt+Rh/($Ce_{0.35}Zr_{0.50}Y_{0.075}La_{0.075}O_2$)/(3 % La_2O_3+Al_2O_3)	<180	205	220	265	<200	237	-	-		
0.5 % Pt/(0.8Al_2O_3)(0.2$Ce_{0.4}Zr_{0.5}La_{0.1}O_{1.95}$)	-	344	-	365	-	365	-	-	Not aged	[210]
2.25% Pt/Rh commercial catalyst	-	300	-	318	-	328	-	-		
0.5 % Pt/(0.8Al_2O_3)(0.2$Ce_{0.4}Zr_{0.5}La_{0.1}O_{1.95}$) ($H_2O$/$CO_2$ in exhaust)	-	225	-	286	-	324	-	-		
2.25% Pt/Rh commercial catalyst (H_2O/CO_2 in exhaust)	-	225	-	305	-	305	-	-		
0.5 % Pt/(0.8Al_2O_3)(0.2$Ce_{0.4}Zr_{0.5}La_{0.1}O_{1.95}$)	-	453	-	500	-	500	-	-	900 °C in air, 5 h	
2.25% Pt/Rh commercial catalyst, aged	-	357	-	368	-	388	-	-		
0.5 % Pt/(0.8Al_2O_3)(0.2$Ce_{0.4}Zr_{0.5}La_{0.1}O_{1.95}$) ($H_2O$/$CO_2$ in exhaust)	-	357	-	282	-	516	-	-		
2.25% Pt/Rh commercial catalyst, aged (H_2O/CO_2 in exhaust)	-	388	-	429	-	525	-	-		
(1.2 g/L Pd)/($Ce_{0.6}Zr_{0.3}Y_{0.1}O_2$)	164	182	177	197	183	195	-	-	Not aged	[351]
0.5 % Rh/(ZrO_2)	177	232	226	306	200	261	-	-	900 °C in air, 5 h	[211]
0.5 % Rh/(5 mol% Y_2O_3/ZrO_2)	166	211	221	287	200	261	-	-		
0.5 % Rh/(5 mol% Pr_6O_{11}/ZrO_2)	266	432	335	575	291	443	-	-		

Table A11. Varying washcoat composition and reported T_{10} and T_{50} values from literature. (5/6)

Composition	CO		HC		NO		NO_2		Aged?	Ref.
	T10 (°C)	T50 (°C)	T10 (°C)	T50 (°C)	T10 (°C)	T50 (°C)	T10 (°C)	T50 (°C)		
0.5 % Rh/(3 mol% Y_2O_3/ZrO_2)	207	253	274	322	252	272			900 °C in air, 5 h	[213]
0.5 % Rh/(3 mol% Y_2O_3/5 mol % CeO_2/ZrO_2)	192	223	246	298	224	250				
0.5 % Rh/(3 mol% Y_2O_3/10 mol % CeO_2/ZrO_2)	192	223	274	322	280	309				
0.5 % Rh/(3 mol% Y_2O_3/20 mol % CeO_2/ZrO_2)	192	223	274	325	284	315				
0.5% Rh/CeO_2	192	253	294	330	267	309				
1% Pd/($Ce_{0.67}Zr_{0.33}O_2$)	90	104	277	354	254	365	150	207	Not aged	[214]
1% Pd/($Ce_{0.67}Zr_{0.33}O_2$, 3 wt. % BaO)	115	155	176	242	164	219	138	166		
1% Pd/($Ce_{0.67}Zr_{0.33}O_2$, 5 wt. % BaO)	125	170	202	250	164	209	124	157		
1% Pd/($Ce_{0.67}Zr_{0.33}O_2$, 9 wt. % BaO)	144	182	231	284	173	266	138	184		
1% Pd/($Ce_{0.67}Zr_{0.33}O_2$)	<150	182	290	239	218	348	<150	213	1100 °C in air, 4h	
1% Pd/($Ce_{0.67}Zr_{0.33}O_2$, 3 wt. % BaO)	<150	187	175	267	175	316	152	196		
1% Pd/($Ce_{0.67}Zr_{0.33}O_2$, 5 wt. % BaO)	150	199	214	260	190	247	<150	187		
1% Pd/($Ce_{0.67}Zr_{0.33}O_2$, 9 wt. % BaO)	<150	202	185	302	180	275	<150	192		
0.5% Pd/($Ce_{0.5}Zr_{0.5}O_2$/Al_2O_3)	<200	232	<220	249	223	248	-	-	Not aged	[215]
0.5% Pd/($Ce_{0.5}Zr_{0.5}O_2$/Al_2O_3, 4 wt. % BaO)	<200	226	<220	243	222	245	-	-		
0.5% Pd/($Ce_{0.5}Zr_{0.5}O_2$/Al_2O_3, 6 wt. % BaO)	<200	223	<220	241	<220	237	-	-		
0.5% Pd/($Ce_{0.5}Zr_{0.5}O_2$/Al_2O_3, 8 wt. % BaO)	<200	220	<220	235	<220	231	-	-		
0.5% Pd/($Ce_{0.5}Zr_{0.5}O_2$/Al_2O_3, 10 wt. % BaO)	<200	238	<220	245	225	250	-	-		
0.5% Pd/($Ce_{0.5}Zr_{0.5}O_2$/Al_2O_3)	<260	280	<280	320	<260	309	-	-	1000 °C for 5 h	
0.5% Pd/($Ce_{0.5}Zr_{0.5}O_2$/Al_2O_3, 4 wt. % BaO)	<260	276	<280	311	<260	294	-	-		
0.5% Pd/($Ce_{0.5}Zr_{0.5}O_2$/Al_2O_3, 6 wt. % BaO)	<260	270	<280	306	<260	283	-	-		
0.5% Pd/($Ce_{0.5}Zr_{0.5}O_2$/Al_2O_3, 8 wt. % BaO)	<260	268	<280	302	<260	260	-	-		
0.5% Pd/($Ce_{0.5}Zr_{0.5}O_2$/Al_2O_3, 10 wt. % BaO)	<260	297	<280	311	<260	300	-	-		

Table A11. Varying washcoat composition and reported T_{10} and T_{50} values from literature. (6/6)

Composition	CO		HC		NO		NO_2		Aged?	Ref.
	T10 (°C)	T50 (°C)	T10 (°C)	T50 (°C)	T10 (°C)	T50 (°C)	T10 (°C)	T50 (°C)		
0.5% Pd/($Ce_{0.5}Zr_{0.5}O_2$/Al_2O_3)	-	255	-	249	-	246	-	-	Not aged	[216]
0.5% Pd/($Ce_{0.5}Zr_{0.5}O_2$/Al_2O_3, 6 wt. % SrO)	-	238	-	240	-	241	-	-		
0.5% Pd/($Ce_{0.5}Zr_{0.5}O_2$/Al_2O_3)	-	300	-	318	-	309	-	-	1000 °C, air 5 h	
0.5% Pd/($Ce_{0.5}Zr_{0.5}O_2$/Al_2O_3, 6 wt. % SrO)	-	295	-	306	-	286	-	-		
1% Pd/($Ce_{0.67}Zr_{0.33}O_2$)	90	100	288	354	254	374	144	204	Not aged	[217]
1% Pd/($Ce_{0.67}Zr_{0.33}O_2$, 3 wt. % Mg)	164	172	185	275	188	275	152	180		
1% Pd/($Ce_{0.67}Zr_{0.33}O_2$, 3 wt. % Ca)	154	175	205	269	188	269	156	180		
1% Pd/($Ce_{0.67}Zr_{0.33}O_2$, 3 wt. % Sr)	126	164	181	250	188	250	141	171		
1% Pd/($Ce_{0.67}Zr_{0.33}O_2$, 3 wt. % Ba)	115	156	185	244	166	219	141	163		
1% Pd/($Ce_{0.67}Zr_{0.33}O_2$)	<150	181	296	332	225	351	<150	212	1100 °C in air, 4h	
1% Pd/($Ce_{0.67}Zr_{0.33}O_2$, 3 wt. % Mg)	212	238	288	387	289	400	224	243		
1% Pd/($Ce_{0.67}Zr_{0.33}O_2$, 3 wt. % Ca)	<150	186	190	310	166	330	150	180		
1% Pd/($Ce_{0.67}Zr_{0.33}O_2$, 3 wt. % Sr)	180	194	181	310	184	320	177	200		
1% Pd/($Ce_{0.67}Zr_{0.33}O_2$, 3 wt. % Ba)	159	186	181	301	178	317	150	194		

Table A12. TWC experimental parameters reported in literature.

CO	C_3H_6	C_3H_8	NO	NO_2	H_2O	CO_2	O_2	H_2	Balance gas	GHSV (h^{-1})	Ref.
0.60%	-	0.03%	0.06%	-	10%	12%	stoich.	-	N_2	38000	[200]
0.30%	0.04%	-	0.10%	-	2%	-	0.33%	0.10%	N_2	300000 mL g^{-1} h^{-1}	[192,225]
0.75%	0.067%	0.033%	0.10%	0.03%	-	-	0.75%	-	Ar	43000	[204–207,214,217,352]
1%	-	0.04%	0.05%	-	-	10%	a/f 14.0	-	-	200 L h^{-1}	[353]
0.646%	-	0.081%	0.10%	-	10%	12%	stoich.	-	N_2	34000	[202]
0.56%	0.024%	0.012%	0.10%	-	10%	12%	stoich.	0.19%	N_2	40000	[215,216]
0.56%	-	0.03%	0.06%	-	10%	12%	stoich.	-	N_2	40000	[208]
0.70%	0.067%	-	0.10%	-	-	-	0.78%	-	He	50500	[210]
0.86%	-	0.06%	0.12%	-	10%	12%	stoich.	-	N_2	34000	[209]
0.30%	0.035%	0.015%	0.15%	-	10%	-	0.31%	-	He	240000	[235,238]
1.15%	0.10%	0.025%	1.60%	-	10%	9.35%	1.15%	0.40%	N_2	70000	[227]
1%	0.05%	-	0.05%	-	10%	10%	1%	0.30%	Ar	100000	[229]

Table A13. Varying PGM loadings and reported T_{10} and T_{50} values from literature. (1/3)

Composition	CO		C_3H_6		C_3H_8		NO or NO_x		Aging conditions	Ref.
	T10 (°C)	T50 (°C)	T10 (°C)	T50 (°C)	T10 (°C)	T50 (°C)	T10 (°C)	T50 (°C)		
0 g/ft^3 Pt ; 35 g/ft^3 Pd ; 5.0 g/ft^3 Rh	-	-	-	365	-	371	-	-	Johnson Matthey 160000 km road equivalent aging program	[226]
0 g/ft^3 Pt ; 15 g/ft^3 Pd ; 5.0 g/ft^3 Rh	-	-	-	377	-	375	-	-		
0 g/ft^3 Pt ; 25 g/ft^3 Pd ; 5.0 g/ft^3 Rh	-	-	-	370	-	374	-	-		
0 g/ft^3 Pt ; 25 g/ft^3 Pd ; 7.5 g/ft^3 Rh	-	-	-	354	-	356	-	-		
0 g/ft^3 Pt ; 25 g/ft^3 Pd ; 2.0 g/ft^3 Rh	-	-	-	376	-	379	-	-		
35 g/ft^3 Pt ; 0 g/ft^3 Pd ; 5.0 g/ft^3 Rh	-	-	-	379	-	376	-	-		
15 g/ft^3 Pt ; 0 g/ft^3 Pd ; 5.0 g/ft^3 Rh	-	-	-	375	-	375	-	-		
25 g/ft^3 Pt ; 0 g/ft^3 Pd ; 5.0 g/ft^3 Rh	-	-	-	380	-	381	-	-		
25 g/ft^3 Pt ; 0 g/ft^3 Pd ; 7.5 g/ft^3 Rh	-	-	-	362	-	360	-	-		
25 g/ft^3 Pt ; 0 g/ft^3 Pd ; 2.0 g/ft^3 Rh	-	-	-	383	-	386	-	-		
0.01 % Rh/($ZrCeYLaO_2$)	-	305	-	-	-	-	-	324	Not aged	[227]
0.05 % Rh/($ZrCeYLaO_2$)	-	269	-	288	-	-	-	280		
0.10 % Rh/($ZrCeYLaO_2$)	-	254	-	269	-	-	-	263		
0.25 % Rh/($ZrCeYLaO_2$)	-	232	-	246	-	-	-	242		
0.50 % Rh/($ZrCeYLaO_2$)	-	214	-	228	-	-	-	226		
0.75 % Rh/($ZrCeYLaO_2$)	-	202	-	218	-	-	-	215		
1 % Rh/($ZrCeYLaO_2$)	-	197	-	208	-	-	-	206		
0.01 % Rh/($ZrCeYLaO_2$)	-	-	-	-	-	-	-	-	1000 to 1100 °C, 4 h	
0.05 % Rh/($ZrCeYLaO_2$)	-	382	-	-	-	-	-	-		
0.10 % Rh/($ZrCeYLaO_2$)	-	341	-	-	-	-	-	351		
0.25 % Rh/($ZrCeYLaO_2$)	-	337	-	372	-	-	-	323		
0.50 % Rh/($ZrCeYLaO_2$)	-	318	-	339	-	-	-	305		
0.75 % Rh/($ZrCeYLaO_2$)	-	304	-	323	-	-	-	294		
1 % Rh/($ZrCeYLaO_2$)	-	295	-	307	-	-	-	289		

Table A13. Varying PGM loadings and reported T_{10} and T_{50} values from literature. (2/3)

Composition	CO		C_3H_6		C_3H_8		NO or NO_x		Aging conditions	Ref.
	T10 (°C)	T50 (°C)	T10 (°C)	T50 (°C)	T10 (°C)	T50 (°C)	T10 (°C)	T50 (°C)		
0.10% Pd/commercial catalyst (20 g/ft^3 Pd)	202	234	218	243	-	-	-	-	GM 4000 mile equivalent aging program	[229]
0.26% Pd/commercial catalyst (50 g/ft^3 Pd)	194	222	201	228	-	-	-	-		
0.42% Pd/commercial catalyst (80 g/ft^3 Pd)	176	202	189	221	-	-	-	-		
0.86% Pd/commercial catalyst (160 g/ft^3 Pd)	166	199	183	207	-	-	-	-		
1.24% Pd/commercial catalyst (240 g/ft^3 Pd)	166	195	178	199	-	-	-	-		
Rh/Pd 1/9 (2.744 g/L total)	-	252	-	284	-	-	-	-	900 °C in air (2 h) cooled to 300, 900 °C in air+19% H_2O (2 h)	[230]
Rh/Pd 1/13.5 (3.98 g/L total)	-	260	-	272	-	-	-	-		
Rh/Pd 1/18 (5.214 g/L total)	-	216	-	261	-	-	-	-		
Rh/Pd 1/22.5 (6.45 g/L total)	-	232	-	295	-	-	-	-		
Rh/Pd/Pt 1/9/3.5 (3.706 g/L total)	-	270	-	304	-	-	-	-		
Rh/Pd/Pt 1/3.5/9 (3.706 g/L total)	-	300	-	330	-	-	-	-		
Rh/Pd 0.83/12.5 (3.55 g/L total)	-	260	-	284	-	-	-	-		
Rh/Pd 1.25/12.5 (3.67 g/L total)	-	245	-	284	-	-	-	-		
0.1 % Pd/($Al2O_3$)	193	214	-	-	-	-	-	-	Not aged	[231]
1 % Pd/($Al2O_3$)	166	182	-	-	-	-	-	-		
2 % Pd/($Al2O_3$)	159	173	-	-	-	-	-	-		
3 % Pd/($Al2O_3$)	159	171	-	-	-	-	-	-		
4 % Pd/($Al2O_3$)	159	171	-	-	-	-	-	-		
5 % Pd/($Al2O_3$)	159	171	-	-	-	-	-	-		
0.05% Pd/($Al2O_3$)	250	278	-	-	-	-	279	294	Not aged	[232]
0.5% Pd/($Al2O_3$)	192	220	-	-	-	-	162	220		
1.0% Pd/($Al2O_3$)	162	205	-	-	-	-	<27	140		
0.7% Pd/($Al2O_3$)	-	-	-	-	-	-	252	332	Not aged	[233]
0.7% Pd/(10% $Ce_{0.6}Zr_{0.4}O_2$ / 90% Al_2O_3)	-	-	-	-	-	-	180	327		
2.8% Pd/(10% $Ce_{0.6}Zr_{0.4}O_2$ / 90% Al_2O_3)	-	-	-	-	-	-	157	213		

Table A13. Varying PGM loadings and reported T_{10} and T_{50} values from literature. (3/3)

Composition	CO		C_3H_6		C_3H_8		NO or NO_x		Aging conditions	Ref.
	T10 (°C)	T50 (°C)	T10 (°C)	T50 (°C)	T10 (°C)	T50 (°C)	T10 (°C)	T50 (°C)		
0.6% Pt-Rh/($Ce_{0.5}Zr_{0.5}O_2$) (Pt/Rh ratio 1.6/1)	257	308	-	-	-	-	-	-	700 °C in air, 3 h	[234]
1.0% Pt-Rh/($Ce_{0.5}Zr_{0.5}O_2$) (Pt/Rh ratio 3/1)	183	214	-	-	-	-	-	-		
0.08% Rh/(Al_2O_3)	171	206	270	311	331	377	195	247	Not aged	[238]
0.12% Pd/(Al_2O_3)	288	350	311	362	373	405	325	351		
0.2 % Pd-Rh/(Al_2O_3) (Pd-Rh 3/2 mechanical mixture)	215	250	266	298	317	373	250	306		
0.2 % Pd-Rh/(Al_2O_3) (Pd-Rh 3/2 alloy)	177	234	270	311	327	394	228	275		
0.2 % Pd-Rh/(Al_2O_3) (Pd/Rh = 3/2)	245	387	293	329	336	439	289	329	Not aged	[235]
0.2 % Pd-Rh/(Al_2O_3) (Pd/Rh = 7/3)	245	300	287	342	356	419	306	380		
0.2 % Pd-Rh/(Al_2O_3) (Pd/Rh = 4/1)	254	344	293	346	356	415	316	389		
0.5 % Rh/($Ce_{0.2}Zr_{0.8}O_2$)	156	239	251	337	-	-	237	314	Not aged	[225]
0.5 % Ir-Rh/($Ce_{0.2}Zr_{0.8}O_2$) (Ir/Rh = 1/9)	135	200	200	254	-	-	185	223		
0.5 % Ir-Rh/($Ce_{0.2}Zr_{0.8}O_2$) (Ir/Rh = 1/4)	156	239	251	337	-	-	237	331		
0.5 % Ir-Rh/($Ce_{0.2}Zr_{0.8}O_2$) (Ir/Rh = 1/1)	187	246	251	337	-	-	220	289		
0.5 % Ir-Rh/($Ce_{0.2}Zr_{0.8}O_2$) (Ir/Rh = 4/1)	210	263	251	375	-	-	220	314		
0.5 % Ir/(Ce0.2Zr0.8O2)	210	295	291	388	-	-	220	289		
0.1 % Ir-Rh/($Ce_{0.2}Zr_{0.8}O_2$) (Ir/Rh = 1/9)	-	267	-	408	-	-	-	357		
0.2 % Ir-Rh/($Ce_{0.2}Zr_{0.8}O_2$) (Ir/Rh = 1/9)	-	240	-	379	-	-	-	323		
0.3 % Ir-Rh/($Ce_{0.2}Zr_{0.8}O_2$) (Ir/Rh = 1/9)	-	230	-	360	-	-	-	318		
0.4 % Ir-Rh/($Ce_{0.2}Zr_{0.8}O_2$) (Ir/Rh = 1/9)	-	220	-	341	-	-	-	282		

10.2 Appendix B – Copyright permissions

Table A14. Image permissions obtained from the Copyright Clearance Center.

Figure	Publisher	License Number
Figure 1	American Chemical Society	n/a *
Figure 3	Elsevier	4504710387489
Figure 4	Royal Society of Chemistry	4504711045652
Figure 5	Elsevier	4504720410699
Figure 6	Elsevier	4504720615421
Figure 7	American Chemical Society	n/a *
Figure 8	Royal Society of Chemistry	4504721216243
Figure 9	Royal Society of Chemistry	4504730077319
Figure 10	Elsevier	4504740538569
Figure 14	Elsevier	4526511153376
Figure 15	Springer Nature	4526520117794
Figure 17	Elsevier	4526540976985
Figure 19	Elsevier	4526541092402
Figure 20	Elsevier	4526541329102
Figure 21	Elsevier	4526541442236
Figure 22	American Chemical Society	n/a *
Figure 25	Royal Society of Chemistry	4526531232005

* See below for permissions from the American Chemical Society

Figure 1:

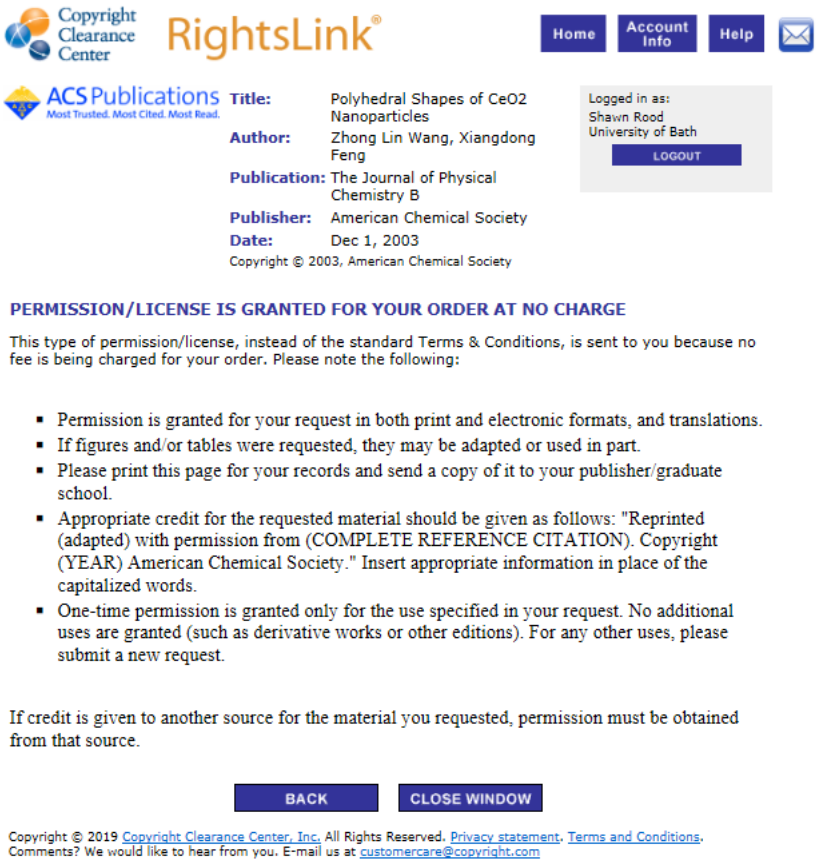

Copyright Clearance Center RightsLink®

Home | Account Info | Help

ACS Publications
Most Trusted. Most Cited. Most Read.

Title:	Polyhedral Shapes of CeO2 Nanoparticles
Author:	Zhong Lin Wang, Xiangdong Feng
Publication:	The Journal of Physical Chemistry B
Publisher:	American Chemical Society
Date:	Dec 1, 2003

Copyright © 2003, American Chemical Society

Logged in as:
Shawn Rood
University of Bath
LOGOUT

PERMISSION/LICENSE IS GRANTED FOR YOUR ORDER AT NO CHARGE

This type of permission/license, instead of the standard Terms & Conditions, is sent to you because no fee is being charged for your order. Please note the following:

- Permission is granted for your request in both print and electronic formats, and translations.
- If figures and/or tables were requested, they may be adapted or used in part.
- Please print this page for your records and send a copy of it to your publisher/graduate school.
- Appropriate credit for the requested material should be given as follows: "Reprinted (adapted) with permission from (COMPLETE REFERENCE CITATION). Copyright (YEAR) American Chemical Society." Insert appropriate information in place of the capitalized words.
- One-time permission is granted only for the use specified in your request. No additional uses are granted (such as derivative works or other editions). For any other uses, please submit a new request.

If credit is given to another source for the material you requested, permission must be obtained from that source.

BACK | CLOSE WINDOW

Figure 7:

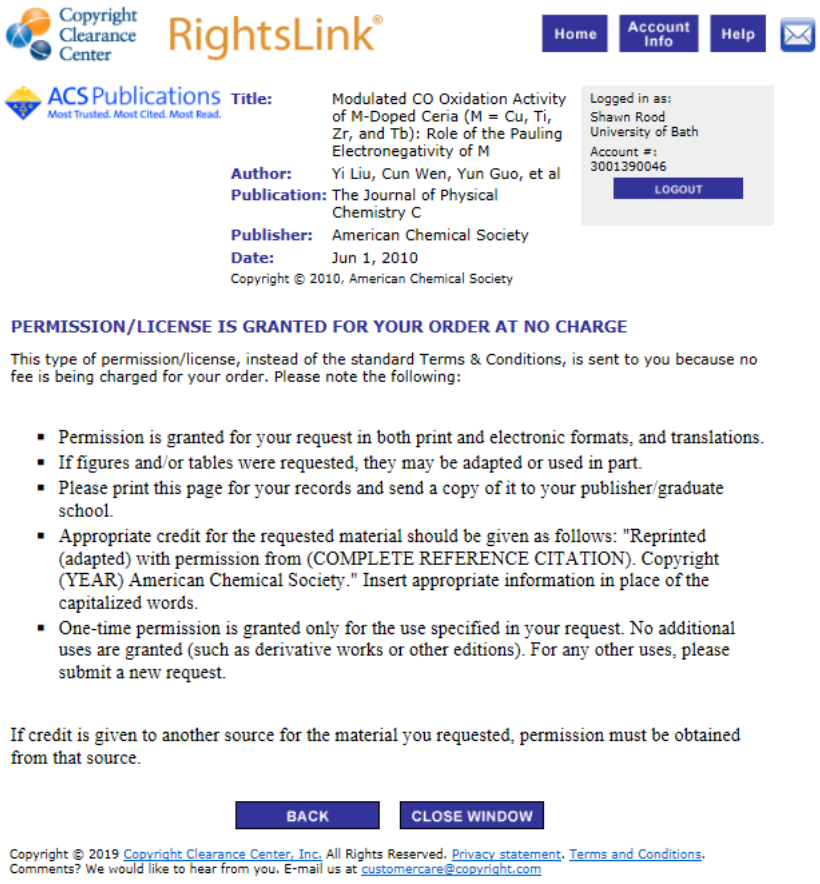

Copyright Clearance Center RightsLink®

Home | Account Info | Help

ACS Publications
Most Trusted. Most Cited. Most Read.

Title: Modulated CO Oxidation Activity of M-Doped Ceria (M = Cu, Ti, Zr, and Tb): Role of the Pauling Electronegativity of M

Author: Yi Liu, Cun Wen, Yun Guo, et al

Publication: The Journal of Physical Chemistry C

Publisher: American Chemical Society

Date: Jun 1, 2010

Copyright © 2010, American Chemical Society

Logged in as:
Shawn Rood
University of Bath
Account #:
3001390046
LOGOUT

PERMISSION/LICENSE IS GRANTED FOR YOUR ORDER AT NO CHARGE

This type of permission/license, instead of the standard Terms & Conditions, is sent to you because no fee is being charged for your order. Please note the following:

- Permission is granted for your request in both print and electronic formats, and translations.
- If figures and/or tables were requested, they may be adapted or used in part.
- Please print this page for your records and send a copy of it to your publisher/graduate school.
- Appropriate credit for the requested material should be given as follows: "Reprinted (adapted) with permission from (COMPLETE REFERENCE CITATION). Copyright (YEAR) American Chemical Society." Insert appropriate information in place of the capitalized words.
- One-time permission is granted only for the use specified in your request. No additional uses are granted (such as derivative works or other editions). For any other uses, please submit a new request.

If credit is given to another source for the material you requested, permission must be obtained from that source.

BACK | CLOSE WINDOW

Figure 22:

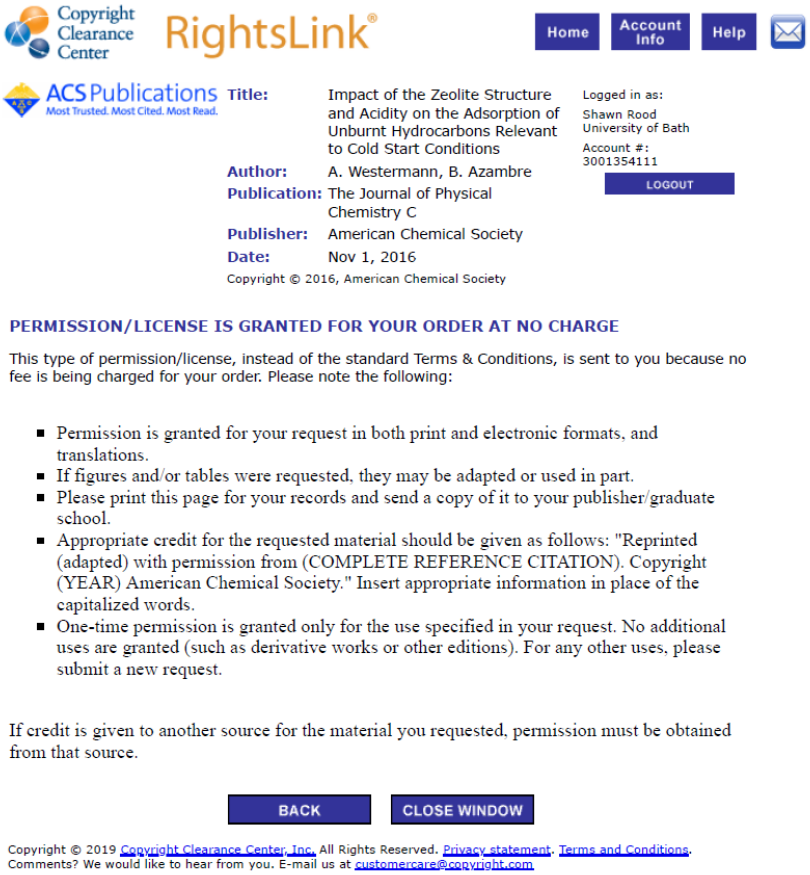

Copyright Clearance Center RightsLink®

Home | Account Info | Help

ACS Publications
Most Trusted. Most Cited. Most Read.

Title: Impact of the Zeolite Structure and Acidity on the Adsorption of Unburnt Hydrocarbons Relevant to Cold Start Conditions

Author: A. Westermann, B. Azambre

Publication: The Journal of Physical Chemistry C

Publisher: American Chemical Society

Date: Nov 1, 2016

Copyright © 2016, American Chemical Society

Logged in as:
Shawn Rood
University of Bath
Account #:
3001354111

LOGOUT

PERMISSION/LICENSE IS GRANTED FOR YOUR ORDER AT NO CHARGE

This type of permission/license, instead of the standard Terms & Conditions, is sent to you because no fee is being charged for your order. Please note the following:

- Permission is granted for your request in both print and electronic formats, and translations.
- If figures and/or tables were requested, they may be adapted or used in part.
- Please print this page for your records and send a copy of it to your publisher/graduate school.
- Appropriate credit for the requested material should be given as follows: "Reprinted (adapted) with permission from (COMPLETE REFERENCE CITATION). Copyright (YEAR) American Chemical Society." Insert appropriate information in place of the capitalized words.
- One-time permission is granted only for the use specified in your request. No additional uses are granted (such as derivative works or other editions). For any other uses, please submit a new request.

If credit is given to another source for the material you requested, permission must be obtained from that source.

BACK | CLOSE WINDOW

Copyright © 2019 Copyright Clearance Center, Inc. All Rights Reserved. Privacy statement. Terms and Conditions.
Comments? We would like to hear from you. E-mail us at customercare@copyright.com